Universidade de Trás-os-Montes e Alto Douro

# Automatic analysis of UAS-based multi-temporal data as support to a precision agroforestry management system

Tese de Doutoramento em Informática

**Luís Filipe Machado Pádua**

**Orientador:** Professor Doutor Joaquim João Moreira de Sousa

**Coorientadores:** Professor Doutor Emanuel Peres Soares Correia

Professor Doutor António Manuel Ribeiro de Sousa

Vila Real, 2021

Universidade de Trás-os-Montes e Alto Douro

# Automatic analysis of UAS-based multi-temporal data as support to a precision agroforestry management system

Tese de Doutoramento em Informática

**Luís Filipe Machado Pádua**

**Orientação**

Professor Doutor Joaquim João Moreira de Sousa

Professor Doutor Emanuel Peres Soares Correia

Professor Doutor António Manuel Ribeiro de Sousa

**Composição do júri:**

**Presidente:**

Doutor José Boaventura Ribeiro da Cunha, Professor Associado com Agregação (UTAD)

**Vogais:**

Doutor Mário Manuel de Miranda Furtado Campos Cunha, Professor Associado (UP)

Doutor Luís Gonzaga Mendes Magalhães, Professor Auxiliar com Agregação (UM)

Doutor António Manuel Trigueiros Cunha, Professor Auxiliar (UTAD),

Doutor Joaquim João Sousa, Professor Auxiliar com Agregação (UTAD)

Doutor Pedro Miguel do Vale Moreira, Professor Coordenador (IPVC)

Doutor Alessandro Matese, Investigador do Italian National Research Council (CNR)

Vila Real, 2021

# Abstract

Forest and agriculture ecosystems are prone to disturbances caused by human action or natural effects. For instance, climate change is projected to be a key influence on vegetation across the globe. Regarding agriculture, primary climate vectors with a significant impact include temperature, moisture stress, and radiation. Within this context, it is of foremost importance to monitor crops along time, as well as to detect pests, diseases, assess and control irrigation demands. Regular monitoring activities will enable timely measures that may trigger field interventions that are used to preserve health status of crops, achieving both time and economic gains, while assuring a more sustainable activity. Within this scope, precision agriculture (PA) techniques appear as an effective alternative to the traditional agronomy practices. In fact, the technological advances that promote PA are able to enhance support when making decisions, resulting in agronomical processes upgraded by employing site or plant specific management operations. In this regard, the capabilities of unmanned aerial vehicles (UAVs) to provide flexible, efficient, non-destructive, and non-invasive means of acquiring data on agricultural crops and the various agro-environmental factors of the parcel, can be used for PA applications. The high- temporal, radiometric and spatial resolutions achieved by UAV-based aerial imagery make possible to foresee new and important advances in PA practices.

In this study it is presented the development of a management support system for the agriculture and forestry sectors, based on the analysis of multi-temporal data obtained through different sensors coupled to UAVs. With a continuous monitoring, it is intended to monitor the vegetative development and to identify, in an early and (semi)automatic way, potential issues, allowing their localized mitigation, through methodologies and algorithms developed for this purpose. To meet these main objectives, two important agricultural crops from the region of Trás-os-Montes and Alto Douro (Portugal) economy, were identified: the grapevine (*Vitis vinifera* L.); and the European chestnut (*Castanea Sativa* Mill.). Both of these crops have a high socio-economic relevance for the population of this region and represent an important share of national production. Thus, the work is divided into two parts, one focuses on monitoring chestnut stands and the other focuses on vineyards. The several differences among these two species in the planting typology and their geometry, make the approaches to each of the sectors also different. However, this fact will allow the adaptation of the proposed methodologies to almost all agricultural species, regardless of the type and the way they are arranged, in a grid or in rows.

Although there are several approaches to detect and monitor vegetation through aerial imagery, most of them remain dependent of manual extraction of vegetation parameters. This work presents automatic methods that allow—with none or few parametrization—the individual detection of the trees/grapevines and their multi-temporal analysis. The approach for tree detection was applied to several chestnut stands, allowing the automatic estimation of several parameters, such as the number of trees, the canopy coverage, tree height, and crown diameter. A novel methodology that enables the identification of phytosanitary issues from multi-temporal analysis of chestnut stands, using UAV-based multispectral imagery, was also developed and it is presented in this thesis. This approach not only allows the absence or presence of phytosanitary issues but also the identification and the classification of biotic or abiotic factors affecting the trees. The developed methodology proved to be effective in automatically detecting and classifying phytosanitary issues in chestnut trees throughout the growing season.

Likewise, methods to automatically estimate and extract grapevine vegetation parameters are also proposed. A full pipeline for vineyards management was developed. First, a methodology able to differentiate grapevine canopy between inter-row vegetation cover and soil, and to identify independent vine row was built. Then, the outputs were provided but the former methods were used to create a multi-temporal data analysis of vineyards, enabling the monitoring of vegetation dynamics of a given vineyard plot along the growing season. This way, areas with canopy management operation needs, and with different vigour levels, are identified. The approaches proposed enable to fully exploit the advantages offered from the UAV-based multi-sensor data (RGB, multispectral and thermal infrared), by performing multi-temporal analysis of vineyards both at the plot and at the plant scales. Individual grapevine detection permits the estimation of geometrical and biophysical parameters, as well as missing grapevine plants.

Thus, the developed methodologies proved to be very effective and can be used in a single epoch, analyzing the data from one individual flight campaign to estimate different parameters (depending on the used sensors), both at parcel-level and at the plant-level. In terms of agricultural plot, the canopy coverage, the estimation of the number of trees/grapevines, and the estimation of other vegetation and bare soil can be reached, as well as mean values of the species under analysis. Regarding the plant-level monitoring, geometrical and biophysical

parameters as height, canopy volume, crown diameter, temperature and vegetation indices that correlate with yield, biomass, leaf density and phytosanitary issues are also possible to estimate.

Combining data from different flight campaigns, allows a multi-temporal analysis to be performed. Moreover, this multi-temporal analysis can be carried out over a single vegetative cycle and/or over different agricultural years, allowing, in any case, to obtain important management information. Hence, the original methods presented in this work have shown to be effective and have proved that their potential goes beyond vegetation detection, since they can be employed in an operational routine for the automatic monitoring of vineyard plots and chestnut stands. Thus, this work can be seen as an important contribution towards the substitution of time-consuming and costly field campaigns for managing plantations in a quicker and more sustainable way.

**Keywords**: multi-temporal data analysis, unmanned aerial vehicles, precision agriculture; precision viticulture; decision support system.

# Resumo

Os ecossistemas agroflorestais estão sujeitos a distúrbios causados por ação humana ou por efeitos naturais. Por exemplo, projeta-se que as alterações climáticas venham a ter grande impacto na vegetação a nível global. Em relação à agricultura, os parâmetros climáticos com maior impacto são a temperatura, a humidade e a radiação. Nesse contexto, a monitorização das culturas ao longo do tempo é de primordial importância, possibilitando a deteção de pragas e de doenças, assim como a avaliação e o controlo das necessidades de irrigação. Uma monitorização regular permitirá a adoção atempada de medidas que podem desencadear intervenções para preservar o estado das culturas agrícolas, obtendo-se, com isso, proveitos a vários níveis, nomeadamente ganhos económicos e um aumento na eficiência e na sustentabilidade. Nesse âmbito, a com vista a atingir esses desideratos, a utilização de técnicas de agricultura de precisão (AP) surge como uma alternativa eficaz às práticas tradicionais. De facto, os avanços tecnológicos que possibilitaram os recentes desenvolvimentos da AP, permitem, simultaneamente, melhorar o apoio à tomada de decisão, melhorando os processos agrícolas, através da aplicação de ações localizadas ao nível da planta ou de uma determinada zona do terreno. Neste sentido, a capacidade dos veículos aéreos não tripulados (VANT), para adquirirem dados de culturas agrícolas e outros fatores agroambientais, de forma flexível, eficiente, não destrutiva e não invasiva faz com que estes possam ser usados para aplicações de AP. As suas elevadas resoluções espacial, radiométrica e temporal fazem com que as imagens aéreas obtidas por VANT ajudem a atingir novos e importantes avanços nas práticas de AP.

O trabalho apresentado neste documento, teve por finalidade o desenvolvimento de um sistema de apoio à gestão dos setores agrícola e florestal, baseado na análise de dados multi-temporais obtidos por meio de diferentes sensores acoplados em VANT. Com um acompanhamento contínuo, demonstrou-se ser possível monitorizar o desenvolvimento vegetativo e identificar, de forma precoce e (semi)automática, potenciais problemas, permitindo a sua mitigação, através de metodologias e algoritmos desenvolvidos para o efeito. Para cumprir estes objetivos principais, foram identificadas duas culturas agrícolas com forte peso na economia da região de Trás-os-Montes e Alto Douro (Portugal): a videira (*Vitis vinifera* L.); e o castanheiro europeu (*Castanea Sativa* Mill.). Estas culturas representam uma elevada relevância socioeconómica para a população da região e uma importante parcela da produção nacional. Assim sendo, o trabalho realizado dividiu-se em duas partes, uma centrada na monitorização de soutos e outra

na monitorização de vinhas. As diferenças entre estas duas espécies são substanciais, a vários níveis, obrigando, necessariamente, ao recurso de abordagens distintas. No entanto, este facto permitirá a adaptação das metodologias propostas a quase todas as espécies agrícolas, independentemente da forma como estão dispostas no terreno, quer seja em grelha ou em linha.

Embora existam várias abordagens para detetar e monitorizar a vegetação através de imagens aéreas, a maioria permanece dependente da extração manual de parâmetros relacionados com a vegetação. Neste trabalho apresentam-se métodos automáticos que permitem—com poucas ou nenhumas parametrizações—a deteção individual de árvores/videiras e a sua análise numa perspetiva multi-temporal. A abordagem para deteção de árvores foi aplicada em vários soutos, permitindo estimar vários parâmetros de forma automática, tais como o número de árvores, a cobertura do solo pelo copado, a altura das árvores e o diâmetro da copa. É apresentada, também, uma nova metodologia para a identificação de problemas fitossanitários em castanheiros, a partir da análise multi-temporal usando imagens multiespectrais obtidas por VANT. Esta abordagem permite não só aferir a ausência ou presença de problemas fitossanitários, como também a identificação e a classificação de fatores bióticos ou abióticos específicos que possam afetar as árvores. A aplicação da metodologia desenvolvida mostrou ser eficaz na deteção e na classificação automática de problemas fitossanitários em castanheiros ao longo do período vegetativo.

Propõem-se, ainda, métodos para estimar e extrair, automaticamente, parâmetros de videiras. Foi desenvolvida uma *pipeline* específica para a gestão de vinhas. Primeiro, foi construída uma metodologia capaz de diferenciar o copado das videiras de vegetação que a envolve e do solo, e identificar os diferentes bardos. De seguida, estes resultados foram usados para criar uma análise multi-temporal da vinha, permitindo realizar a monitorização da dinâmica da vegetação de uma determinada parcela de vinha ao longo do período vegetativo. Desta forma, são identificadas áreas com necessidades de intervenção no copado e com diferentes níveis de vigor. As abordagens propostas permitem explorar as vantagens oferecidas pelos dados de diferentes sensores acoplados em VANT (RGB, multiespectral e térmico), através da realização de análises multi-temporais da vinha, tanto à escala da parcela como ao nível da planta. A deteção individual de videiras permite a estimativa de parâmetros geométricos e fisiológicos, bem como a contagem de videiras em falta.

As metodologias desenvolvidas neste trabalho revelaram-se eficazes e podem ser utilizadas numa única época (data), analisando os dados de uma única campanha de voo para estimar diferentes parâmetros (dependendo dos sensores utilizados), tanto ao nível da parcela quanto ao nível de planta. Ao nível da parcela, parâmetros como a cobertura do solo pelo copado, o número de árvores/videiras e a segmentação de outro tipo de vegetação e do solo podem ser obtidos, assim como valores médios da cultura em análise. Relativamente à monitorização ao nível da planta, vários parâmetros geométricos e fisiológicos podem ser estimados como altura, volume do copado, o diâmetro da copa, a temperatura e diferentes índices de vegetação, que se correlacionam com a produtividade, a biomassa, a densidade foliar e potenciais problemas fitossanitários.

A combinação de dados provenientes de diferentes campanhas de voo permite a realização de análises multi-temporais. Além disso, este tipo de análises pode ser realizado ao longo do período vegetativo e/ou ao longo de diferentes anos agrícolas, permitindo, em qualquer caso, obter informações importantes para a gestão das parcelas. Desta forma, os métodos apresentados neste trabalho revelaram-se eficazes, comprovando que o seu potencial vai muito para além da deteção de vegetação, uma vez que podem ser aplicados numa rotina operacional para a gestão automática de vinhas e soutos. Assim, este trabalho pode ser visto como uma importante contribuição para a substituição de campanhas de campo, demoradas e trabalhosas, logo muito dispendiosas, passando-se para uma gestão de parcelas agrícolas de forma mais rápida, integrada, otimizada e sustentável.

**Palavras-chave:** análise de dados multi-temporais; veículos aéreos não tripulados; agricultura de precisão; viticultura de precisão; sistemas de apoio à decisão.

# Agradecimentos

A realização deste trabalho, com sucesso, não seria possível sem o apoio de várias pessoas e/ou entidades. Assim, gostaria de agradecer:

À Universidade de Trás-os-Montes e Alto Douro, instituição que me acolheu em praticamente todo o meu percurso e me proporcionou condições para a minha formação académica.

Ao Centro de Robótica Industrial e Sistemas Inteligentes do Instituto de Engenharia de Sistemas e Computadores, Tecnologia e Ciência (INESC TEC), instituição que me acolheu durante parte do meu doutoramento.

À equipa de orientação, composta pelo Professor Doutor Joaquim João Moreira de Sousa, Professor Doutor Emanuel Peres Soares Correia e Professor Doutor António Manuel Ribeiro de Sousa, por todo o conhecimento transmitido, pela disponibilidade e apoio prestado durante a realização deste trabalho.

Aos Professores António Cunha e Luís Magalhães por me terem introduzido em atividades e projetos de investigação durante a realização do meu mestrado.

Aos Professores Raul Morais, Luís Martins, José Martinho Lourenço e João Paulo Castro pelo apoio prestado no trabalho de campo e pelos ensinamentos transmitidos nos seus domínios de conhecimento.

Aos colegas Telmo Adão, Jonáš Hruška, Pedro Marques e Nathalie Guimarães com quem privei durante o desenvolvimento desta tese, pelo auxílio e apoio prestados.

Ao Professor Doutor João Manuel Pereira Barroso e Professor Doutor José Benjamim Ribeiro da Fonseca, respetivamente, Diretor e Vice-diretor do curso de Doutoramento em Informática.

Ao Projeto "PARRA - Plataforma integrAda de monitoRização e avaliação da doença da flavescência douRada na vinhA" (referência 3447), cofinanciado pelo Fundo Europeu de Desenvolvimento Regional (FEDER), através do COMPETE 2020 – Programa Operacional Competitividade e Internacionalização (POCI), o qual integrei durante o meu doutoramento até à sua conclusão.

Um agradecimento à Fundação para a Ciência e Tecnologia (FCT) pelo financiamento parcial deste doutoramento (SFRH/BD/139702/2018), Ministério da Ciência, Tecnologia e Ensino

Superior (MCTES), cofinanciada pelo Fundo Social Europeu (FSE) através do NORTE 2020 (Programa Operacional Regional do Norte 2014/2020) e União Europeia (EU).

A todos os que direta ou indiretamente contribuíram para a concretização desta tese de doutoramento.

A todos os meus sinceros agradecimentos!

# Table of contents

# List of figures

# List of tables

# List of abbreviations

| Abbreviation | Expansion |
| --- | --- |
| **#** | |
| **3D** | — Three-dimensional |
| **A** | |
| **AGB** | — Above-ground biomass |
| **AOI** | — Area of interest |
| **AUVSI** | — Association of Unmanned Vehicle System International |
| **B** | |
| **BAI** | — Burn Area Index |
| **BGVI** | — Blue/Green Pigment Index |
| **BILISA** | — Bivariate local indicators of spatial association |
| **BRVI** | — Blue/Red Pigment Index |
| **C** | |
| **CG** | — Chestnut Growth |
| **CHM** | — Canopy Height Model |
| **CI** | — Canopy cover index |
| **CIR** | — Colour Infrared |
| **CMOS** | — Complementary Metal Oxide Semiconductor |
| **CSM** | — Crop Surface Model |
| **CWSI** | — Crop Water Stress Index |
| **D** | |
| **DBH** | — Diameter at Breast Height |
| **DDM** | — Digital Differential Model |
| **DDR** | — Douro Demarcated Region |
| **DEM** | — Digital Elevation Model |
| **DOY** | — Day of Year |
| **DSM** | — Digital Surface Model |

| Abbreviation | | Expansion |
|---|---|---|
| **DTM** | — | Digital Terrain Model |
| **DVI** | — | Difference Vegetation Index |
| **E** | | |
| **EM** | — | Electromagnetic |
| **EPSG** | — | European Petroleum Survey Group |
| **EVI** | — | Enhanced Vegetation Index |
| **ExG** | — | Excess Green |
| **ExG-R** | — | Excess Green-Red |
| **ExNIR** | — | Excess NIR |
| **ExRE** | — | Excess Red Edge |
| **F** | | |
| **FiND** | — | Fishing Net Dragging |
| **FIR** | — | Far Infrared |
| **FN** | — | False Negative |
| **FNR** | — | False Negative Rate |
| **FP** | — | False Positive |
| **G** | | |
| **G%** | — | Green Percentage Index |
| **GCP** | — | Ground Control Point |
| **GIS** | — | Geographical Information Systems |
| **GLI** | — | Green Leaf Index |
| **GNDVI** | — | Green Normalized Difference Vegetation Index |
| **GNSS** | — | Global Navigation Satellite System |
| **GRVI** | — | Green-Red Vegetation Index |
| **GSAVI** | — | Green Soil-Adjusted Vegetation Index |
| **GSD** | — | Ground Sample Distance |

| Abbreviation | | Expansion |
|---|---|---|
| **H** | | |
| **HH** | — | High–High |
| **HL** | — | High–Low |
| **HSV** | — | Hue Saturation and Value |
| **I** | | |
| **I3** | — | Stomatal conductance index I3 |
| **ICP** | — | Independent Check Points |
| **ID** | — | Identification |
| **IDW** | — | Inverse Distance Weighting |
| **Ig** | — | Stomatal conductance index Ig |
| **IQR** | — | Interquartile Range |
| **IPMA** | — | Instituto Português do Mar e da Atmosfera |
| **ITCD** | — | Individual Tree Crown Detection and Delineation |
| **L** | | |
| **LAI** | — | Leaf Area Index |
| **LDA** | — | Linear Discriminant Analysis |
| **LH** | — | Low–High |
| **LiDAR** | — | Light Detection And Ranging |
| **LISA** | — | Local Indicators of Spatial Association |
| **LL** | — | Low–Low |
| **LMI** | — | Local Moran’s index |
| **LST** | — | Land Surface Temperature |
| **M** | | |
| **MGRVI** | — | Modified Green Red Vegetation Index |
| **MI** | — | Moran’s index |
| **ML** | — | Machine Learning |
| **MNDWI** | — | Modified Normalized Difference Water Index |
| **MNGRDI** | — | Modified Normalized Green red difference index |

| Abbreviation | Expansion |
|---|---|
| **MSAVI** — | Modified Soil-Adjusted Vegetation Index |
| **N** | |
| **NBR** — | Normalized Burn Ratio |
| **NBRT** — | Normalized Burn Ratio - Thermal |
| **NDExNIR** — | Normalized Difference Excess NIR |
| **NDExRE** — | Normalized Difference Excess RE |
| **NDRE** — | Normalized Difference Red Edge |
| **NDSI** — | Normalized Difference Snow Index |
| **NDVI** — | Normalized Difference Vegetation Index |
| **NDWI** — | Normalized Difference Water Index |
| **NGBDI** — | Normalized Green Blue Difference Index |
| **NGRDI** — | Normalized Green-Red Difference Index |
| **NIR** — | Near infrared |
| **O** | |
| **OA** — | Overall accuracy |
| **OBIA** — | Object-Based Image Analysis |
| **OSAVI** — | Optimized Soil-Adjusted Vegetation Index |
| **OTB** — | Orfeo ToolBox |
| **P** | |
| **PA** — | Precision Agriculture |
| **PCDI** — | Plant Cell Density Index |
| **PET** — | Potential Evapotranspiration |
| **PPK** — | Post Processing Kinematic |
| **PRI** — | Photochemical Reflectance Index |
| **PV** — | Precision Viticulture |
| **R** | |
| $R^2$ — | Coefficient of determination |
| **RADAR** — | Radio Detection And Ranging |

| Abbreviation | | Expansion |
|---|---|---|
| **RDVI** | — | Renormalized Difference Vegetation Index |
| **RE** | — | Red edge |
| **RF** | — | Random Forest |
| **RFE** | — | Recursive Feature Elimination |
| **RGB** | — | Red-Green-Blue |
| **RGBVI** | — | Red Green Blue Vegetation Index |
| **RMSE** | — | Root mean square error |
| **RTK** | — | Real-Time Kinematic |
| **RVI** | — | Ratio Vegetation Index |
| **S** | | |
| **SAVI** | — | Soil-Adjusted Vegetation Index |
| **SfM** | — | Structure from Motion |
| **SIFT** | — | Scale-Invariant Feature Transform |
| **SKIZ** | — | Skeleton by zone of influence |
| **SR** | — | Simple Ratio |
| **SVM** | — | Support Vector Machine |
| **T** | | |
| **TCARI** | — | Transformed chlorophyll absorption ratio index |
| **TGI** | — | Triangular Greenness Index |
| **TIR** | — | Thermal Infrared |
| **TN** | — | True Negative |
| **TP** | — | True Positive |
| **U** | | |
| **UAS** | — | Unmanned Aerial System |
| **UAV** | — | Unmanned Aerial Vehicle |
| **UN** | — | United Nations |
| **UTAD** | — | University of Trás-os-Montes e Alto Douro |

| Abbreviation | | Expansion |
|---|---|---|
| **V** | | |
| **VARIg** | — | Vegetation Index Green |
| **VEG** | — | Vegetativen |
| **VI** | — | Vegetation Index |
| **VSP** | — | vertical shoot positioning |
| **VTOL** | — | Vertical Take-Off and Landing |
| **W** | | |
| **WGS** | — | World Geodetic System |
| **WI** | — | Woebbecke Index |

# Chapter 1.

## Introduction

## 1.1. Contextualization

The agriculture sector has considerably evolved due to technological developments achieved in the last decades, enabling improvements in the entire production chain (Floros et al., 2010). Despite these advances, the global context, where water scarcity will increase together with the global population, demands for optimization of agriculture processes and, at the same time, for environmental sustainability (United Nations, 2015). In fact, in most regions of the world, over 70% of freshwater is used for agriculture (Gilbert, 2012). By 2050, to sustain Earth's population an estimated 50% (at least) increase in agricultural production and a 15% increase in water withdrawals are expected (Bruinsma, 2011; Ercin & Hoekstra, 2014). This future demand on water will affect all sectors, requiring as much as 25 to 40% of water to be re-allocated from lower to higher productivity and employment activities, particularly in water stressed regions (McKinsey, 2009). Given the existing constraints, the agricultural water management sector is currently in the process of repositioning itself towards modern and sustainable service provision, optimized according to the crops demands (Vanham et al., 2013). On the other hand, the adverse effect of synthetic chemicals on human health and environment can only be reduced or eliminated by adopting new agricultural technological practices (Al-Samarrai et al., 2012). Finally, it cannot be forgotten that the nature of agriculture and farming practices, in any location, are strongly influenced by the long-term mean climate state. Changes in the mean climate away from current states, may require adjustments to current practices in order to maintain productivity, and in some cases, the optimum type of farming may change (Howden et al., 2007).

Given these factors, it is essential to develop new methods/approaches to better adapt to this changing and challenging context. Precision agriculture (PA) promotes the use of technology for the improvement of agronomical processes by means of data acquisition, processing and analysis to support decision making and crop management operations (Gebbers & Adamchuk, 2010; Pablo J Zarco-Tejada et al., 2014). With the implementation of PA approaches environmental impacts can be mitigated while increase yields and maintaining the crop health status, by adopting site-specific management practices (Baofeng et al., 2016).

In the Portuguese case, more specifically in the region of Trás-os-Montes and Alto Douro, the wine and the chestnut sectors are very relevant (Luís Martins et al., 2015), and for this reason, they are the focus crops of this work. Both chestnut trees (*Castanea sativa* Mill.)—wood and chestnut production—and grapevines (*Vitis vinifera* L.)—for wine production—are within the most important species in Portugal. Those are especially relevant in the northern region of the country. According to the 2018 Portuguese Agricultural Statistics (Instituto Nacional de Estatística, I. P., 2019), in this region, chestnut trees represent 89% of planted surface (34,504 ha) and 88% of yield (29,908 tons) while grapevines represent 47% of the planted surface (82,850 ha) and 33% of the wine production in Portugal (778,698 tons of grapes harvested to produce 1,918,369 hectolitres of wine). Both can be affected by several phytosanitary issues—due to biotic or abiotic factors—which can significantly impact the plant development and its yield (Luís Martins et al., 2014). This way, there is a need to efficiently monitor these species with a high and spatial resolution enabling an early detection of pests, diseases and nutritional deficiencies for a quick, site-specific and effective response, which will foster a more sustainable and more profitable management of these crops and natural resources.

The use of remote sensed data acquired from airborne or spaceborne platforms arises as an effective alternative for vegetation monitoring. More recently, the technological development has led to a size reduction of unmanned aerial vehicles (UAVs), to adapt to different usage contexts and at a more affordable cost (Pádua, Vanko, et al., 2017). Indeed, UAVs have become a highly flexible remote sensing platform to use in different areas (Jenkins & Vasigh, 2013; Juul, 2015). These allow the data acquisition from different sensor types, with greater versatility and lower cost (in small to medium sized project) when compared to other remote sensing platforms, such as satellites or manned aircrafts (Alessandro Matese et al., 2015). In the agriculture and forestry sectors its use extends, among others, to crop monitoring (Berni, Zarco-Tejada, Suárez, et al., 2009; D. Turner et al., 2011), weed mapping (D. Gómez-Candón et al., 2013), irrigation management (Baluja et al., 2012; Bellvert et al., 2013; Bellvert & Girona, 2012; Pablo J. Zarco-Tejada et al., 2012), estimation of biomass (Bendig et al., 2014; Eija Honkavaara et al., 2013; Pölönen et al., 2013), chlorophyll (Uto et al., 2013; Pablo J. Zarco-Tejada et al., 2012), or nutrients (Caturegli et al., 2016; Pölönen et al., 2013), vegetation height mapping (Mathews & Jensen, 2013; Suomalainen et al., 2014), helping in the decision making process to manage eventual problems (Yubin Lan et al., 2010).

In most of the studies found in the bibliography, the use of UAVs is not intended to acquire data of the crops vegetative state in a temporal context. Some studies have used multi-temporal data in different types of crops, such as barley (Bendig et al., 2013), sunflowers (Vega et al., 2015), silage maize (Castaldi et al., 2017), rice (Willkomm et al., 2016) and vineyards (Ballesteros et al., 2015). In these studies, the data obtained in the different periods allowed to achieve results, which, in some cases, were only visible from a certain phase of the vegetative cycle. Thus, the study of UAV-based data of the same area obtained in a multi-temporal approach can be advantageous, as it will allow to continuously assess the vegetative development and to identify possible problems, which will enable a more effective and localized response, to mitigate them.

Although the UAV data acquisition process is constantly evolving, it is reasonably established. However, concerning data processing and its interpretation for the extraction of valid and useful information for farmers, it is still primarily a manual process using geographical information systems (GIS). This thesis, presents the development of a management system for decision support for agriculture and forest, based on the automatic analysis of the acquired data at different periods, using different sensors aboard UAVs. Thus, in addition to the development and in-field validation of the necessary procedures for the different phases of the system, particular attention is given to the development of algorithms that allow automatic data processing and the extraction of useful information. Along these lines, it is intended a box-to-box management support system for the agriculture and forest sectors. In this context, the scientific work presented in this thesis contributes to crop sustainability and, at the same time, reduces chemical treatments and preserves water resources.

## 1.2. Objectives of the study

The main goal of this thesis is the development of a solution that can be used to support the management of agricultural and forest crops. This solution is supported by automatic data acquisition and analysis with high spatial and temporal resolution, using different sensors coupled to UAVs. This solution allows the assessment of crops temporal evolution, defining the probable causes of eventual problems—from biotic and/or abiotic origins—thus, allowing the most appropriate measures to be taken in order to solve or mitigate the detected issues. From this general objective, several specific objectives might be drawn up:

- Study the relevance of multiple source data fusion/combination for the extraction of the most relevant information on a specific crop;
- Importance of multi-temporal data for management of vineyards and chestnut plantations;
- Development of algorithms for automatic monitoring of the vegetative status and detection of possible crop phytosanitary and nutritional issues;

- Validation of the algorithms in monitoring and verification of crop development, when compared with traditional methods.

In this sense, the following research question has been formulated:

1) Can multi-temporal data from multi-sources be combined to provide better management of agricultural and forest crops, in particular in vineyards and chestnut plantations?

If the answer to the previous question is yes, it is necessary to understand if there is any obstacle to the development of a complete analysis process. It will then be necessary to answer the following question:

2) Can the agriculture and forest management process be automated based on the developed algorithms specifically for the extraction of valid information from data acquired from different types of sensors?

## 1.3. Structure of the thesis

This thesis is organized in ten Chapters, eight of which (Chapters 2-9) composed of original scientific research published in refereed international journals, subjected to blind peer reviews.

This introduction chapter is followed by a comprehensive state-of-the-art regarding the usage of UAVs and different sensors in agriculture and forestry. This review (Chapter 2) was published in an international scientific journal and describes the advantages of UAVs regarding other remote sensing platforms, highlighting the existent UAV types along with the different sensors that can be applied for data acquisition in agriculture and forestry sectors. Considerations towards the most suitable UAV type and sensor to a specific application are presented along with its potential costs.

Chapters 3 to 5 are mainly focused in the monitoring of chestnut trees, while Chapters 6 to 9 are related to vineyard monitoring. The main objective of Chapter 3 is to explore UAVs for aerial imagery acquisition for preservation and prevention contexts, for this purpose two studies were conducted, in an area were chestnut trees are predominant and in a coastal area. The monitoring of chestnut trees health and the assessment of phytosanitary issues from the acquired multi-temporal imagery enabled the identification of the tree canopy cover decline through the time.

In Chapter 4 a method for automatic multi-temporal analysis of chestnut stands is proposed. The UAV-based dataset from Chapter 3 was used. The method allows the single tree detection enabling to estimate its height, tree crown diameter and, by means of multi-temporal analysis, to estimate the canopy decline. The analysis of the tree canopy decline enables to estimate trees with potential phytosanitary problems. This method poses as a faster approach for chestnut trees monitoring and to assist in field inspections.

Chapter 5 presents a study where a chestnut stand was monitored along a growing season. The multi-temporal dataset acquired, using a multispectral sensor coupled to a UAV, along with a phytosanitary characterization of each individual tree, enabled to apply machine learning for the detection of phytosanitary issues. The method presented in Chapter 4 was used for the segmentation of each tree and several features were extracted for training a random forest classifier using data from each flight campaign. The results achieved in this study allow to understand the accuracy of the presence of phytosanitary issues in chestnut trees and to predict the specific issue affecting each one of them.

In Chapter 6 a method for vineyard vegetation detection is presented. For this purpose, different vineyards, mainly located in the Douro Demarcated Region, were surveyed using a low-cost UAV. The method relies in the use of RGB and height information driven from the photogrammetric processing of the UAV-based imagery. It allows, with high accuracy, to estimate the number of vine rows, grapevine vegetation, inter-row vegetation, bare soil and areas along the rows with potential missing vines. This way, new automatisms in vineyard monitoring are achieved for a better decision support.

Chapter 7 addresses a study using multi-temporal UAV-based RGB data acquisition with nine flight campaigns carried in two vineyard plots located at University of Trás-os-Montes e Alto Douro (UTAD). The data covers different phenological stages of the growing season of 2017. The vineyard vegetation segmentation method presented in Chapter 6 is applied to estimate the vineyard vegetation and the vine rows along with the grapevines canopy volume. The estimated height was validated with field measurements. This process enabled to characterize the vineyard vegetation evolution (grapevine and inter-row vegetation area and grapevine volume) throughout the season and allows to estimate areas were canopy management can be applied.

Chapter 8 presents a study that explores the relationship among different sensors coupled in UAVs and analyses different approaches to generate vineyard vigour maps. A vineyard plot at

UTAD was surveyed in the growing season of 2018 along five different flight campaigns of the vineyard vegetative development. UAV-based data is acquired from RGB, multispectral and thermal sensors. The vigour maps are classified in three levels (high, medium and low) using the whole vineyard or only grapevine vegetation. This approach enables a rapid vineyard characterization and provides knowledge to farmers and winegrowers of areas with lower and higher vigour within a vineyard plot.

Using the knowledge acquired and the methods presented in Chapters 6 and 7, a computer vision method for individual grapevine analysis from UAV-based data is presented in Chapter 8. This method is capable to estimate potential missing grapevines with a high accuracy when comparing to ground-truth data. A multi-temporal dataset composed of RGB, thermal infrared and multispectral data from two vineyard plots in two different wine regions is used to extract different biophysical grapevine parameters. The extracted parameters allow a better understanding of the vineyard dynamics along the growing season, possessing potential to be used for the computation prescription maps for plant-specific applications and to estimate the individual grapevine production.

Chapter 10 concludes the thesis with a synthesis of the significant achievements of this research and presents future research directions.

# Chapter 2.

## UAS, sensors, and data processing in agroforestry: a review towards practical applications

*International Journal of Remote Sensing*, 2017, *38*(8-10), 2349-2391

Journal Impact Factor – 2017: 1.782

5 Year Impact Factor – 2017: 2.003

**Luís Pádua**, Jakub Vanko, Jonáš Hruška, Telmo Adão,
Joaquim J. Sousa, Emanuel Peres and Raul Morais

Refer to https://doi.org/10.1080/01431161.2017.1297548 for online published version

## 2.1. Introduction

Recent years showed rapid socialization and an increased interest in unmanned aircraft system (UAS) for civilian applications. Unmanned aerial vehicles (UAVs), often referred as drone, are aircrafts without a human pilot on board. Instead, UAVs are controlled by a ground operator. This was achieved due to a variety of factors, ranging from the introduction of relatively low-cost systems and user-friendly controls to the general technological advances and to the miniaturization of individual components (main boards, micro-processors and motors, high-power density batteries, cheaper airframes, communication devices, and sensors). These advances led to the production of affordable off-the-shelf UAS suitable for civilian applications, easy to transport, mount, launch, and operate.

An UAS can be defined as a power-driven reusable aircraft operated without a human pilot on board (J. M. Sullivan, 2006). It can be remotely piloted or have a programmed route to perform an autonomous flight, using the embedded autopilot. Generally, it also requires a ground-control station, sensor suites and communication devices for carrying out flight missions (Pappalardo, 2003).

Apart from military applications (Austin, 2011; Gertler, 2012; Jenks, 2009), the European Parliamentary Research Service provided a list of potential applications in civil and commercial use consisting of disaster response, earth observation, the energy sector, infrastructures, maintenance monitoring, aerial mapping, filming, agriculture, forestry, fisheries, telecommunications, package delivery and non-military government authorities. Also, some concerns rose from the increased use of UAS in illegal activities, such as drug trafficking (Juul, 2015). The Association for Unmanned Vehicle Systems International (AUVSI) estimates that, among the aforementioned applications, agriculture is at the vanguard of the promising markets for the commercial use of UAS (Jenkins & Vasigh, 2013).

In the specific area of agriculture, every farmer’s goal is to efficiently apply the available resources to gain the maximum yield possible. To achieve this, they need a fast, reliable, cost-effective and easy method to scan their fields. The crop’s condition can be assessed by the stage of ripening, water status, pest attacks and nutritional requirements. UAS with remote sensing capabilities can provide this necessary data, so that the farmer is able to identify problems in early stages and rapidly select the appropriate interventions (George et al., 2013). Besides crop monitoring, farmers can also benefit from UAS in precision spraying. Similarly, agriculture, forestry and nature preservation can also greatly benefit from the use of UAS technology. Foresters can use them for inspection of forestry operations, wildfire detection, wildlife tracking, legal restrictions monitoring, woodland change detection and survey sites which are otherwise inaccessible or where trespassing is undesirable (Grenzdörffer et al., 2008).

There is a wide range of UAS and sensors that can be used in agroforestry, which leaves space for uncertainty among the professionals regarding the use of those devices and how they can actually help to cost-effectively leverage the production. Thereby, the purpose of this study is to help users selecting the proper UAS together with the proper imaging sensor to get the expected and needed results. Several authors already provided surveys regarding UAS and their applications (Colomina & Molina, 2014; Nex & Remondino, 2013; Pajares, 2015; Salamí et al., 2014; Watts et al., 2012; Zhang & Kovacs, 2012). However, in this study authors are focusing on the application of low-cost mini and micro UAS and imaging sensors that meet the interests of both farmers and foresters.

## 2.2. UAS as a remote sensing platform

Remote sensing platforms are useful to provide added value information for agroforestry applications. This section presents these platforms focusing on UAS which are classified according to their size. Emphasis is given on small, mini and micro UAS, which are divided in two types: fixed-wing and rotor-based.

### 2.2.1. Traditional remote sensing technologies and UAS

Traditional remote sensing technologies encompass satellite and manned aircraft platforms. These platforms are continuously improving in terms of spatial, spectral and temporal resolutions. Each of these technologies has benefits and constrains regarding technological, operational and economic factors. The high spatial and temporal resolutions, flexibility and much lower operational costs make UAS a good alternative to traditional remote sensing platforms for agroforestry applications (Muchiri & Kimathi, 2016; Salamí et al., 2014).

The use of professional civilian UAS is increasing rapidly around the world and it is expected to explode in the upcoming years. The main factors supporting this growth are related to the increasing awareness of the benefits that this technology can bring to a wide range of industries and non-commercial sectors, as well as to the introduction of relatively low-cost systems, user-friendly controls and the general technological advancements and the miniaturization of individual components.

According to the AUVSI, the foreseen integration of UAS in the United States national airspace, for the decade 2015–2025, is expected to create more than 100 000 jobs and generate an economic impact of $82 billion (Jenkins & Vasigh, 2013).

As a new method of geo-data collection, UAS complements existing techniques, filling the gap between large area imaging (satellites and manned aircrafts), and smaller coverage, time-consuming, but highly accurate terrestrial techniques (Figure 2.1). Compared to high altitude data, UAS data is fairly low cost, with the advantage that flights can be made often and quickly. UAS are thus very useful when portions of land must be quickly surveyed (quick response capability for, e.g. time-sensitive deliverables, disaster situations or search and rescue operations). Compared to laser scanning—a very good technique for most of the surveying operations—UAS have the advantage of being above the area to be monitored, which is often a requirement to get an accurate reading. However, and despite the aforementioned advantages of UAS, they are not really competing against traditional aerial photography, since they are seen as a complementary technology.

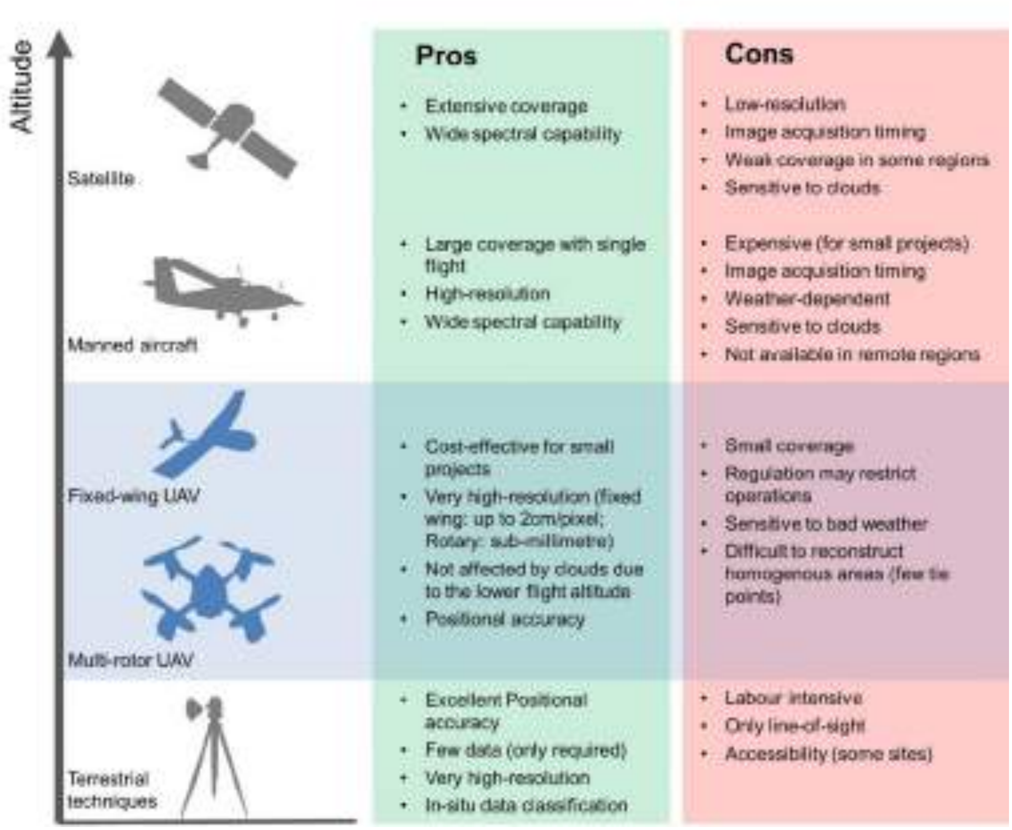


**Figure 2.1.** Pros and cons of the existing remote-sensing technologies Unmanned aerial system (UAS) technology complements existing techniques, filling the existing gap between large-area satellite and manned aircraft imagery and smaller coverage, time-consuming, but highly accurate collection using terrestrial surveying instruments with major pros and cons highlighted.

A technical comparison between multi-rotor UAS, manned aircraft and satellites was made by Matese et al. (2015), to evaluate their cost-effectiveness within the precision agricultural scope. UAS were classified with the best flexibility, optimal cloud cover independence and regarding the processing tasks, the resolution and precision were also classified as optimal. However, the coverage range, flight endurance, mosaicking and geocoding effort were classified as poor in comparison with the other two platforms. The case study was implemented in two different vineyards. In heterogeneous vineyards, low-resolution images fail in presenting part of the intra-vineyard variability. The referred study concluded that in small fields (5 hectares), rotor-based UAS proved to be the most cost-effective solution. However, and according to the authors' own experience with UAS, fixed-wing small UAVs can be used up to a square kilometre area—with a Ground Sample Distance (GSD) up to 5 cm/pixel—and up to 4 $km^2$ area for a GSD greater than 10 cm/pixel. Of course, these threshold values depend on the UAS autonomy (the eBee, from SenseFly, was used as reference). It is worth noting that imaging area-coverage is also influenced by flight altitude (directly influences the GSD), speed, endurance, and sensor resolution (low resolution sensor lead to lower altitude flights, which impacts on the imaging area).

Therefore, UAS represent an evolution in gathering agricultural and forest statistics data from small to medium areas. Commercial low-cost aerial platforms coupled with high resolution imaging sensors allow to collect accurate data regarding crop and trees' health at large scale with insignificant clouds' influence (Quiroz, 2015).

### 2.2.2. UAS main characteristics

The use of UAS equipped with small sensors has emerged as a promising alternative to assist modelling, mapping and monitoring applications in rangelands, forest and agricultural environments. UAS are also suitable to be used in dirty, dull and dangerous conditions as wildlife monitoring, ice cover, weather phenomena and climate change (Watts et al., 2012). However, flight regulations and legislation do not always engage technological advancements regarding UAS. Many countries still lack the proper legislation that regulates the use of UAS both for commercial and for leisure purposes. The sooner legislation safely integrates UAS in the airspace—clarifying requirements and conditions under which drones can be operated—the sooner UAS usage will increase. The legal situation with regard to flying a UAS in various different countries is discussed extensively in the paper by Cracknell and Hayes (2007) which is published in this special issue.

With UAS it is possible to acquire low-cost yet high precision images since they are acquired from lower altitudes. For agroforestry applications, such level of detail can reveal more information about crop condition, weeds, pests and other abnormalities, leading to an earlier detection. These advantages can help agroforestry professionals in short, medium- and long-term operations, due to the possibility of identifying problems faster and, consequently, react quickly, reducing losses and other economical outlays. Regarding farm management, it is possible to gather more accurate results on how crops are reacting to different treatments, leading to a more effective use of resources.

As previously mentioned, UAS differ in size, physical shape and operational endurance, which limit the supported payload carrying capacity, operating altitude and range. This subsection will address UAS of diverse dimensions but it is important to remind that the main focus of this study are mini and micro UAS, since these types are more affordable, easier to carry and simpler to use than the large and medium sized UAS.

Some authors classify UAS in terms of aerospace occupation, altitude and endurance (Austin, 2011; Nex & Remondino, 2013; Watts et al., 2012; Zhang & Kovacs, 2012).

The large UAS used for civilian applications are commonly adapted from military platforms. They are intended to be used on tasks where manned aircraft deployment would be potentially unsafe or inefficient (e.g. in forest wildfires monitoring). NASA's Ikhana UAS (Figure 2.2a) was used to collect and process data regarding fire detection, through a multispectral camera (Ambrosia et al., 2011). These types of platforms require high financial funding, due to the development, deployment and ground operations complexity.

Medium-sized UAS suffer basically from the same problems as large UAS. In comparison medium-sized UAS feature reduced overall costs and easier take-off/landing operations. An example of a medium-sized UAS is the NASA's SIERRA UAS (Figure 2.2b). It was applied in atmospheric composition, arctic surveys, land cover characterization, surface to air fluxes, disaster response and assessment, agriculture and ecosystem assessment, biological/physical oceanography, island and coastal remote sensing and coral reef monitoring (Watts et al., 2012). Another NASA's UAS, known as Pathfinder-Plus (Figure 2.2c), was applied for surveillance operations and decision support in agriculture, to detect weeds and inconsistencies in the fertilization delivery of coffee plantations, using image acquisition sensors, more specifically RGB and narrow-band multispectral (Herwitz et al., 2004). Due to costs, portability and required knowledge for controlling purposes, these types of UAS are not suitable or even affordable for most farmers and foresters.

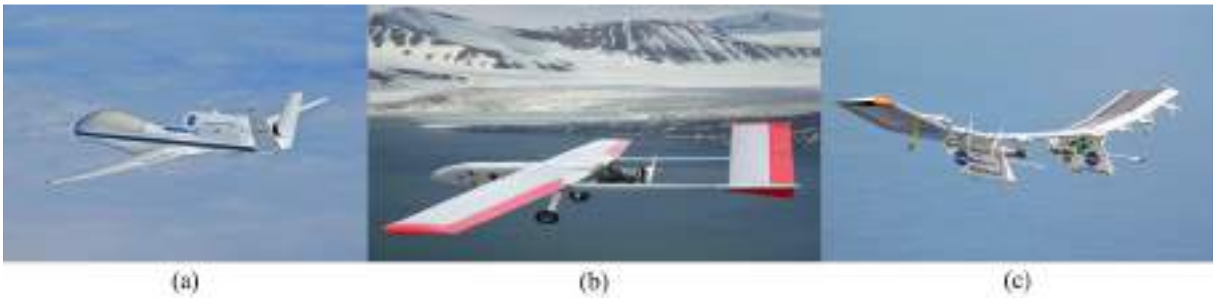


**Figure 2.2.** Large and medium-sized unmanned aerial vehicles (UAVs): (a) NASA's Ikhana; (b) NASA's SIERRA; and (c) NASA's Pathfinder-Plus. Image courtesy of NASA.

The small, mini and micro UAS built for civilian usage features user-friendly platforms, present a typical weight less than 20 kilograms with a flight time comprised between a couple of minutes and a few hours of autonomy within limited distance range (Hardin & Jensen, 2011). Technological advancements have enabled meaningful upgrades to these devices which are capable of acquiring spatial data in great detail using cost-effective platforms (Watts et al., 2012). The expansion of these devices has been facilitated by the miniaturization and the cost reduction of sensors and embedded computers (Berni, Zarco-Tejada, Suarez, et al., 2009).

There are two main types of small, micro and mini UAVs: fixed-wing and multi-rotor. Each type has its own advantages for different deploying environments and required tasks.

The size of the mapped area, its complexity, desired resolution, weather conditions and take-off/landing zone space are the necessary conditions that must be considered before acquiring an UAS. The minimal experience to program and to operate these platforms is an important advantage, given that flight planning and management can be controlled from a single interface.

Fixed-wing UAS can travel several kilometres from the launch point, being mainly suitable for mapping with applications in land surveying, agriculture, mining and environmental management. This type of UAS can achieve a high cruise altitude and speed, cover large areas and get a few centimetres of GSD. However, they are launched by hand or use a small launch ramp and require a large and soft corridor to land. After successful launch, the Global Navigation Satellite System (GNSS) receiver guides the UAS along a pre-defined path (Hardin & Jensen, 2011). The market offers a wide variety of commercial lightweight fixed-wing UAS. Some of the most successful are shown in Figure 2.3.


**Figure 2.3.** Some of the most representative fixed-wing UAVs: (a) QuestUAV Q-Pod; (b) SenseFly eBee; (c) Trimble UX5; (d) MAVinci Sirius Pro; and (e) PrecisionHawk Lancaster. The images were obtained from the manufacturers' websites.

The multi-rotor UAS rely on a set of propellers arranged around its core (Figure 2.4) being the most suitable for inspection, surveying, construction, emergency response, law enforcement and cinematography and videography. Their low cruise altitude and speed are adequate to cover small areas, obtaining spatial resolution up to a millimetre GSD. Moreover, their vertical take-off and landing (VTOL) only requires a few square metres of free terrain, contrarily to fixed-wing-based systems. The rotors can be arranged around the UAV or can be attached to a set of fixed arms. Multi-rotors are less prone to vibrations than fixed-wing (L. O. Wallace et al., 2011). As more rotors are added, the lesser is the crash risk and heavier payloads are supported, although the payload size limitation remains (Anderson & Gaston, 2013).


**Figure 2.4.** Some of the most representative rotor-based UAVs: (a) Topcon Falcon 8; (b) DJI Phantom 4; (c) 3DR SOLO Quadcopter; (d) SenseFly eXom; and (e) Yuneec Typhoon. The images were obtained from the manufacturers' websites.

Regarding mini and micro UAVs, a few considerations should be made before acquiring or deploying them. Anderson and Gaston (2013) presented the four main constraints for consideration: (1) platform; (2) sensor; (3) operating and; (4) environmental constrains. Table 2.1 summarizes the major differences between the fixed-wing and the multi-rotor UAVs.

**Table 2.1.** Comparison between mini and micro fixed-wing and rotor-based UAVs regarding specific parameters and examples of tasks that can be performed.

| | **Fixed-wing** | **Multi-rotor** |
|---|---|---|
| **Image resolution** | Up to centimetre level | Up to millimetre level |
| **Take-off** | Hand/small launch ramp | Vertical take-off |
| **Payload capacity** | Small | Depending on the number of rotors |
| **Flight time** | High (usually up to 1h) | Low (usually up to 30 min) |
| **Landing surface** | Several meters of extension | Approximately the UAV size |
| **Coverage** | | |
| **Cruise speed** | Fixed-wing outperforms multi-rotor, most of the times | |
| **Wind resistance** | | |
| **Main applications** | Land surveying, agriculture, GIS, mining, environmental management | Inspection, video, surveying (urban scale), construction and emergency |

There are two approaches to carry out a UAS mission: by autopilot according to a predefined flight path or manually with a remote controller operated by a pilot. An autonomous flight can be achieved in the following main steps: (1) flight plan—most of the recent UAS are released with a flight planning software, and there are also freely available smartphone applications that allow to specify the intended area of interest, mark the launch area (i.e. where the UAV will gain enough altitude to start the mission) and the landing area; (2) after planning—the flight path must be uploaded to the UAV, making it available to start the next step, the flight execution and data gathering. After a successful launch, the UAV will automatically capture images triggered using the GNSS location as reference. Sufficient overlap of the images ensures enough redundant data in case of distorted images; (3) after landing—the obtained data are downloaded and later processed in a software that provides the desired output; and (4) the last step is to evaluate the data, for the intended purpose (e.g. field issues, irrigation issues, water stressed crops, crop height).

As previously mentioned, lightweight UAVs have limited payload, which makes most of the available platforms unable of carrying a multi sensor system. In some cases, to acquire data from different sensors, the UAV must perform multiple flights over the same area.

The next section provides the different types of sensors used in UAS flight missions.

## 2.3. Sensors

The critical component for carrying out remote sensing activities is the imaging or sensing payload which defines the capabilities and the usability of the UAV (Siebert & Teizer, 2014). The current huge market offer of imaging sensors can be quite overwhelming at first glance for a non-expert user. To help farmers and foresters making their final decision, an overview of imaging sensor types is provided together with their main applications in precision agriculture and forestry. It is noteworthy that the development of UAVs and sensors occurs at a rapid rate which, expectedly should not slow down in the upcoming years (Wagner, 2015). In the near future most of the current systems will probably be discontinued, evolve or be replaced by entirely new systems. Therefore, potential buyers should always find up-to-date information about the current state of available UAVs and sensing instruments. UAVs as a remote sensing platform are capable of carrying a large variety of sensors, from low-cost commercial Digital Single-Lens Reflex (DSLR) cameras to expensive professional gear, such as hyperspectral cameras or LIght Detection And Ranging (LiDAR) sensors, specially designed for UAVs (Klemas, 2015).

Each remote sensing device detects a portion of the electromagnetic radiation. Gamma rays, x-rays, ultraviolet, visible light, infrared light, microwaves and radio waves are examples of electromagnetic radiation that differ from each other concerning wavelength. This range of electromagnetic radiation is called the electromagnetic (EM) spectrum. Only a very small portion of the EM spectrum is visible by the (naked) human eye. However, some sensors can detect different parts of the EM spectrum allowing humans beings to interpret it and therefore make the non-visible become visible. In this study, two types of imaging sensors will be discussed: passive and active sensors.

Passive sensors are used for natural emissions detection from the Earth's surface and its atmosphere whereas active sensors transmit their own pulses of radiation from their own source of energy and then detect the incoming reflected radiation. Passive sensors include RGB cameras, near infrared (NIR) cameras, thermal cameras and their combinations in multispectral and hyperspectral cameras, whilst LiDAR and RADAR (radio detection and ranging) are examples of active sensors (Richards, 2013; W. Turner et al., 2003).

### 2.3.1. RGB sensors

Visible light sensors are capable of capturing imagery perceptible to the human eye. Optical visible light cameras operate in the wavelength range, approximately, from 400 to 700 nm (Austin, 2011). UAS can benefit from a large scale of mass-market off-the-shelf cameras to professional grade cameras with prices varying accordingly. In their review, Colomina and Molina (2014), present a list of small and medium format visible band cameras with their basic parameters. In addition to this list, Figure 2.5 displays some currently used RGB cameras suitable for mini and micro drones, for agricultural and forestry applications.


**Figure 2.5.** Examples of optical cameras commonly used on UAVs for RGB image acquisition: (a) GoPro Hero 4 Black edition; (b) Canon G9X; (c) Panasonic Lumix DMC-TZ71; (d) Sony Alpha 7; and (e) Nikon D800.

RGB sensors mounted on UAVs are capable of providing high resolution imagery from a bird's eye perspective, as presented in Figure 2.6. These images can be processed into orthophoto mosaics, by stitching images together (Darren Turner et al., 2012), or to build digital surface models (DSM), using 3D reconstruction algorithms based on stereo vision or structure from motion (SfM) algorithms (Nex & Remondino, 2013). Possible uses of orthophoto mosaics include aerial mapping and imaging, plant counting, surveillance, emergency response, surveying and land use applications. DSMs can be useful for 3D surveying and mapping or volume computation.

**Figure 2.6.** RGB image sample obtained with Sensefly's eBee fixed-wing UAV over one vineyard of the University of-Trás-os-Montes e Alto Douro (UTAD).

Remote sensing applications also very often separate RGB channels and work with individual red, green and blue channels. Colour reassigning is used to create false colour images to enhance certain features that can be very useful in land analysis. While this kind of imagery might provide valuable visual information for farmers and foresters, it is not very suitable to assess vegetation properties due to the lack of information obtained in the NIR region, where the high reflectance of vegetation occurs (Nebiker et al., 2008).

### 2.3.2. Infrared sensors

The infrared spectrum covers longer wavelengths than the visible light spectrum, ranging from around 700 nm (NIR) to 1,000,000 nm (far infra-red, FIR). The boundaries between the visible and NIR, at one end, and between the FIR and microwaves, on the other end, are not precise and are open to different interpretations (Austin, 2011). The NIR band from 700 nm to approximately 8,500 nm represents the region where high plant reflectance occurs, thus being crucial for most of the agroforestry applications. A NIR image is displayed in Figure 2.7.

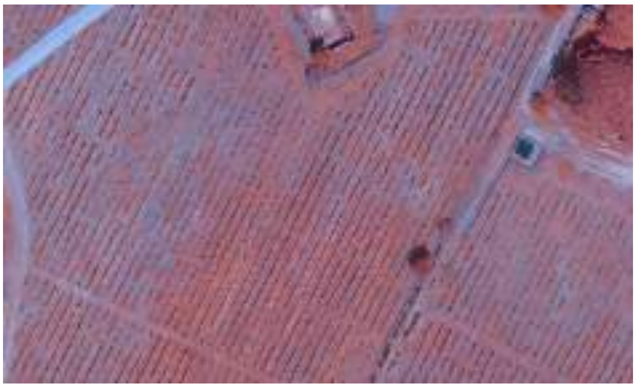

**Figure 2.7.** NIR image sample obtained with Sensefly's eBee fixed-wing UAV corresponding to the same area represented in Figure 2.6.

NIR sensors are frequently used in precision agriculture applications and constitute the basis for vegetation analysis. Healthy vegetation that is actively growing and producing energy from photosynthesis reflects more in the NIR region. When combined with RGB, it can be used for vegetation indices (VI) calculations which are based on the fact that vegetation reflects various wavelengths differently. Most of the common off-the-shelf cameras have filters blocking NIR. However, it is relatively easy to transform an RGB camera into a NIR camera, by removing the filter and replacing it by one that is filtering the visible red, green or blue bands. Figure 2.8 displays some of currently used cameras that were converted to NIR cameras by changing the filters. NIR and RGB sensors are often combined in multispectral sensors, which will be addressed later.


**Figure 2.8.** NIR cameras commonly used in UAVs: (a) Canon S110; (b) Panasonic Lumix 7; and (c) Fujifilm X-M1.

While the human eye is less sensitive to NIR, FIR is entirely invisible for us. With the intensity increase, this radiation can be experienced as heat. Thermal cameras operate approximately in the spectrum at wavelengths from 5,000 nm to 14,000 nm. Each pixel's intensity can be transformed into a temperature measurement.

When compared with conventional cameras, thermal cameras are much more expensive and the image resolution is much lower (Mejias et al., 2015). Thermal sensors allow to create full thermal maps (Lagüela et al., 2015), to check irrigation management (Gonzalez-Dugo et al., 2013), to assess the functionality of solar panels (Quater et al., 2014) and to detect wildlife or livestock (Israel, 2011). A couple of thermal cameras developed for UAS are depicted in Figure 2.9.


**Figure 2.9.** Common thermal cameras developed to be mounted on UAVs: (a) Workswell WIRIS and (b) FLIR Vue.

### 2.3.3. Multispectral and hyperspectral sensors

Until a few years ago multispectral and hyperspectral cameras were considered too heavy for mini and micro UAVs, whereas RGB and modified RGB cameras, for acquiring the NIR band, were considered as a standard tool coupled with UAVs for photogrammetric and remote sensing applications. Apart from early prototypes (Saari et al., 2011), such cameras only became commercially available in recent years. Just like NIR sensors, multispectral sensors are extensively used for vegetation analysis, since NIR is one of the multiple bands they can detect (usually R, G, B, NIR, Red Edge and sometimes ultra violet light and thermal bands are included in multispectral sensors). Red edge refers to the EM region between visible light spectrum and NIR. Some of the most used multispectral sensors are shown in Figure 2.10. Nebiker et al. (2016) made a comparison between a high-end multispectral camera and a low-cost off-the-shelf NIR camera showing significant differences. As expected, the multispectral sensor provided good results, consistent with the reference values obtained by a hyperspectral spectrometer whilst the low-cost camera showed a reasonable correlation with the multispectral system with some significant biases. However, the use of high spatial resolution low-cost cameras proved to be useful for qualitative monitoring of crops, including diseases detection.

While multispectral cameras sense broadbands, usually 4 to 12, hyperspectral cameras (Figure 2.11) are capable of sensing hundreds of narrow bands, up to 2 nm in wavelength (Bendig et al., 2015).


**Figure 2.10.** Some of the most commonly used multispectral cameras: (a) Parrot Sequoia; (b) multiSPEC 4C; (c) Tetracam ADC; and (d) MicaSense RedEdge.


Figure 2.11. Some of the most common used hyperspectral cameras: (a) the Headwall Photonics Micro-Hyperspec; (b) the Rikola Hyperspectral camera; and (c) the Surface Optics Corp. SOC710-GX.

Hyperspectral sensors produce images in which each pixel contains the whole spectrum of the sensed wavelengths. This means that hyperspectral outcomes provide much more information than the imagery produced by the previously referred devices. A simplified representation of a hyperspectral data cube is shown in Figure 2.12. A list of both multispectral and hyperspectral sensors used in conjunction with UAVs in several published works can be found in Colomina and Molina (2014).

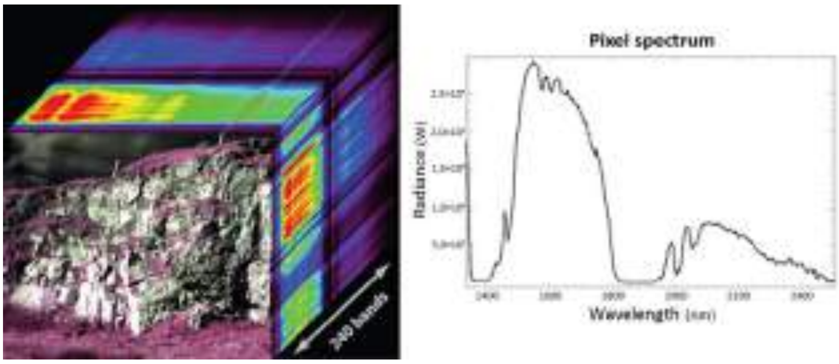


**Figure 2.12.** Two-dimensional projection of a hyperspectral data cube. The high number—typically, over 100—of narrow spectral bands results in a continuous range of reflectance values for each image pixel. The front of the cube shows a false colour image using the infrared spectral bands 1721, 2306, and 1565 nm in RGB (image from http://org.uib.no/cipr/Project/VOG/hyperspectral.htm).

### 2.3.4. LiDAR sensors

LiDAR is an active laser-based remote sensing technology that transmits to the surface optical laser pulses with a fast repeat rate. By measuring the double path time from the emitted pulse (transmitter-target-transmitter/receptor) it is possible to determine the distance to targets (objects, surface). By repeating this process with a fast sequence, LiDAR generates a 3D point cloud of the surface, as shown in Figure 2.13.

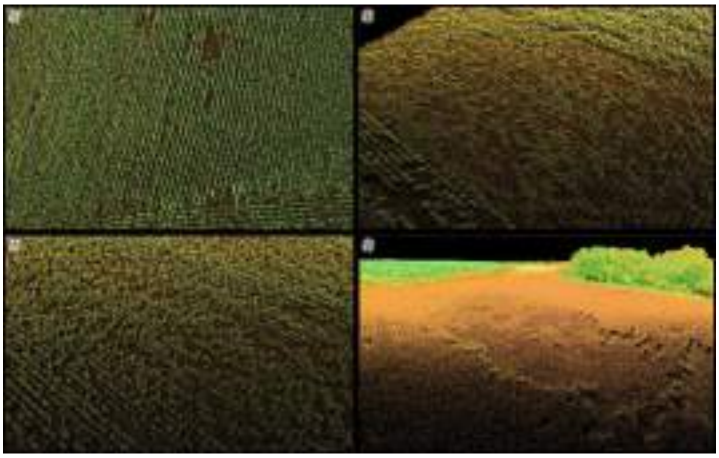

**Figure 2.13.** UAV-based lidar data of different agriculture features. Properly sparse surveys in time provide valuable data to detect cropland critical areas. © RIEGL LMS, www.riegl.com

The accuracy of these 3D point clouds allows them to be used for multiple applications in agroforestry, forest change detection (L. Wallace et al., 2014), flood mapping (Malinowski et al., 2016) or plant height measurements (Bareth et al., 2016). Short-range LiDAR sensors were also used on-board UAVs for obstacle detection and guidance (Ramasamy et al., 2016). In the near future, further miniaturization and cost reduction of LiDAR sensors is expected (Poulton & Watts, 2016). Figure 2.14 shows some currently available LiDAR systems suitable for UAS.

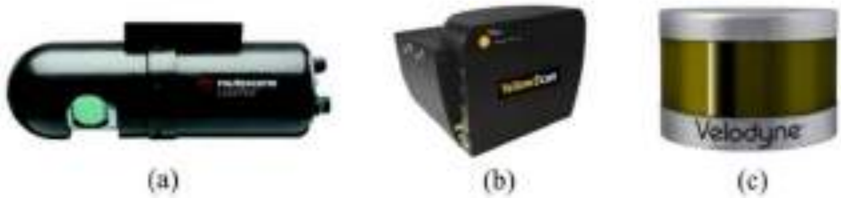


**Figure 2.14.** Examples of commonly used UAS lidar sensors: (a) the Routescene lidar Pod; (b) the Yellowscan Mapper; and (c) the Velodyne PUCK.

Table 2.2 presents some examples of application areas and studies in which the described sensors were used. Depending on the goal of certain applications, the sensor should be properly selected, considering the trade-off between characteristics and goals to reach. Thermal sensors provide spectral bands that are more suitable for applications that require temperature information invariant to light conditions as, for example, real-time animal detection. Disease detection, in early stages, can be performed by hyperspectral sensors since many of them only present slightly noticeable visible characteristics. On the other hand, and despite of the fact that some similar tasks can be achieved with thermal and hyperspectral sensors, such as water status assessment, other aspects need to be considered (e.g. spatial and spectral resolution and acquisition costs). These topics are addressed in Section 2.5 of this study, where the estimated budgets of UAS bundles for different agroforestry applications are also presented (including UAV platform, sensors and processing software).

The amount of data collected by sensors mounted on UAVs can be huge, prompting the need for methods able to transform them into valuable information. In the next section this topic is addressed.

## 2.4. Data processing

After each flight the sensors mounted on the UAV returns a large amount of data which is not yet suitable to extract information and to reach conclusions, since platforms are rarely designed to interact on-the-fly with the attached sensors. Thus, the desired results must be pursued in a post-flight processing stage (Geipel et al., 2013). This section intends to present the several operations that can be performed with the acquired data, in the referred post-flight processing stage.

**Table 2.2.** List of potential application areas with examples of scientific studies, grouped by sensor type.

| Sensors | Application areas | References |
|---|---|---|
| RGB | Forest canopy gaps inspection | Getzin et al, (2012) |
| | Biomass monitoring | Bendig et al. (2014) |
| | Volume characterization | Ballesteros et al. (2015) |
| | Vegetation segmentation | Nolan et al. (2015) |
| | Early-season crop monitoring | Torres-Sánchez et al. (2014); Gómez-Candón et al. (2013) |
| Thermal | Land-use classification | Lagüela et al. (2015) |
| | Water status assessment | Baluja et al. (2012); Zarco-Tejada et al. (2012); Park et al. (2015) |
| | Wildlife detection | Israel, (2011); Ward et al. (2016) |
| | Irrigation management | Bellvert and Girona (2012); Bellvert et al. (2013) |
| | Fire detection | Merino et al. (2011) |
| Multispectral | Vigour maps production based on vegetation indices | Primicerio et al. (2012); Candiago et al. (2015); Nebiker et al. (2008); Navia et al. (2016) |
| | Image segmentation | Comba et al. (2015) |
| | Weed mapping | Peña et al. (2013) |
| | Nitrogen status estimation | Caturegli et al. (2016) |
| | Biomass estimation | Bendig et al. (2015) |
| Hyperspectral | Biomass estimation | Honkavaara et al. (2012); Pölönen et al. (2013) |
| | Chlorophyll estimation | Uto et al. (2013) |
| | Nitrogen status estimation | Pölönen et al. (2013) |
| | Water status assessment | Zarco-Tejada et al. (2012) |
| | Early detection of plant disease | Calderón et al. (2015) |
| LiDAR | Bellow forest canopy mapping | Chisholm et al. (2013) |
| | Forest inventory and structural properties | Wallace et al. (2012); Wallace (2013); Wallace et al. (2016) |
| | Assessment of tree parameters | Park et al. (2015) |

### 2.4.1. Image pre-processing

Numerous issues may affect data quality. To enhance the data, a pre-processing stage is commonly used. Issues such as atmospheric distortions, spectral variability of the surface materials, altitude, wind turbulence, camera focal length and viewing angle are external factors that may contribute to image degradation. For these reasons, to detect changes as revealed by modifications in surface reflectance and to be able to compare acquired data in different epochs (time series analysis), it is necessary to carry out radiometric corrections. Two approaches to radiometric calibration are possible: (1) ground measurements at the time of data acquisition for atmospheric correction and sensor calibration; and (2) radiometric calibration target that allows the user to calibrate and correct the images' reflectance, considering the illumination and some of the sensor's characteristics. It is recommended to use such a target when generating index maps. Practically, the radiometric calibration target is a white balance card. The radiometric calibration target should cover enough pixels to get good statistics.

In most use cases a single image cannot cover the entire area of interest, which makes it necessary to capture several overlapping images of the area (Figure 2.15a). These images have to be stitched together into a single orthophoto mosaic (Figure 2.15b). Jia et al. (2016) describe the mosaicking process based on the Scale-Invariant Feature Transform (SIFT) algorithm. The process can be subdivided into the following steps: (1) image pre-processing; (2) image registration (feature extraction, feature matching, model transformation and parameter estimation); and (3) image fusion. Also, the correction of the image's geolocation can be achieved with Ground Control Points (GCP).

It should be noticed that the most common UAS limit the sensor payload in weight and dimension, imposing the selection of standard small format sensors for imaging. The sensor's characteristics (focal length changes, principal point offset, lens optical distortion, etc.) along with external factors produce image deformations. The cause of resolving the above parameters is called geometric calibration, which is critical to ensure UAS's data geolocation precision and significant for UAS quantitative remote sensing application.

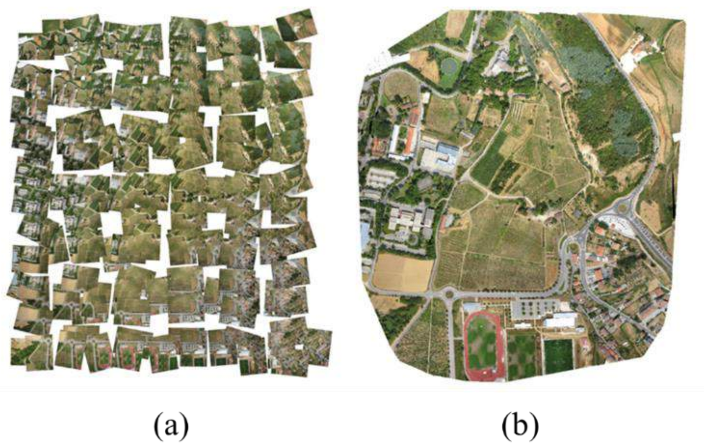


**Figure 2.15.** Orthophoto mosaic generation example. (a) Images gathered in a UAV flight over UTAD's campus. (b) Orthorectified image mosaic which is the result of the processing operations (involving homographic corrections and stitching) upon the acquired images.

## 2.4.2. Spectral indices

To easily extract information from the mosaic, there are different spectral indices that can be applied. These indices are calculated through the use of information about the surface's reflectance from two or more wavelengths or spectral bands. The results provide a relative abundance of certain features. The most used indices are VI. However other available types of indices can be useful for agroforestry professionals, e.g. burned areas and water or snow indices.

Vegetation indices are not recent and were used in the evaluation of data gathered by other remote sensing platforms (e.g. satellites) before being applied to UAS data. Its use extends from crop and vegetation monitoring to estimation of plant parameters.

There are broad and narrowband indices, both designed to measure the overall amount and quality of photosynthetic material, which is crucial for understanding vegetation's state. Broadband greenness VI are the simplest way to measure the general quantity and vigour of green vegetation. Narrowband greenness VI are intended for use with imaging spectrometers, making them suitable for precision agriculture since these can be used to identify, analyse and manage. Comparing both types, narrowband VI are more sensitive to smaller changes in vegetation health, mainly in areas with dense vegetation where broadband measures can saturate.

Vegetation detection through images is possible due to the absorption of red and blue channels and a higher reflectance of the green and NIR channels. Different spectral signatures are obtained from different vegetation types concerning size, shape and colour of leaves (Salamí et al., 2014).

Vegetation indices can also be used to calculate biomass, Leaf Area Index (LAI), disease detection, water stress presence and nitrogen content, assisting farmers and foresters in crop management, yield forecasting and environmental protection (Zhang & Kovacs, 2012). Series of used VIs can be found in (Baluja et al., 2012; Gnyp et al., 2014; López-López et al., 2016; Salamí et al., 2014; P. J. Zarco-Tejada, Ustin, et al., 2005). NIR vegetation indices are reported to have a good correlation with biomass and LAI (Thenkabail et al., 2000). López-López (2016) have separated some vegetation indices in different categories: structural indices, pigment indices or chlorophyll a+b indices, carotenoid indices, xanthophyll indices, R/G/B indices, chlorophyll fluorescence and plant disease index. Table 2.3 provides the necessary information about the most commonly used VI, including the formula allowing their calculation and their main applications. Theoretical basis regarding the VI are provided by Galiano (2012) mostly related to water stress vegetation indices.

Indices based on NIR and visible spectrum combine NIR and red bands for biomass estimation, canopy structure, and LAI. Among them, the most commonly used index is the Normalized Difference Vegetation Index (NDVI) (Zhang & Kovacs, 2012) proposed by Rouse et al., (1974). Figure 2.16 presents a false colour image obtained after NDVI calculation from a vineyard.

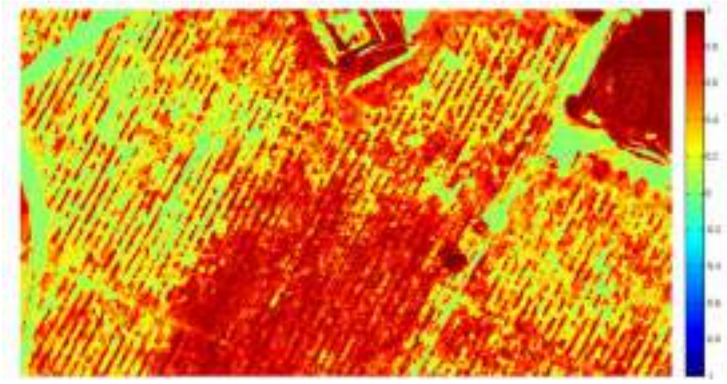

**Figure 2.16.** False-colour representation of a normalized difference vegetation index (NDVI) image composed of red and near-infrared (NIR) bands corresponding to Figure 2.6–Figure 2**.7**.

Wehrhan et al., (2016) compared different VI (NDVI, TSAVI and EVI) to the plant-related carbon dynamics in agricultural soils using a fixed-wing UAV with a multispectral camera array. EVI was pointed out as the best correlation index between ground-based measurements of fresh phytomass.

With the use of visible band indices, it is also possible to acquire vegetation parameters. Bendig et al., (2015) showed that the visible band indices (GRVI, MGRVI, RGBVI) presented a better ability to model biomass in early growth stages rather than later ones, achieving a cost-effective alternative for ground-based reflectance measurements.

Torres-Sánchez et al., (2014) compared different visible spectrum vegetation indices: ExG (Woebbecke et al., 1995), ExGR, Woebbecke Index (Woebbecke et al., 1995), Normalized Green-Red Difference Index (NGRDI) (Gitelson et al., 2002), Vegetativen (VEG) (Hague et al., 2006) and two VI combinations in two different flight altitudes (30 and 60 metres) using multiple flights during the early-season in a wheat field, among them ExG and VEG achieved the best performance.

The need to identify diseases in early stage is crucial to provide a proper crop protection. Regarding this topic, Salamí et al., (2014) concluded that indices based on crown temperature (CWSI) and visible ratio indices proved to be effective. Calderón et al. (2015) used classification methods (linear discriminant analysis—LDA—and support vector machine—SVM—to classify the verticillium wilt severity on olives through hyperspectral and thermal imagery data. SVM achieved better overall results than LDA. However, LDA is more effective for initial and low severity disease levels. The type of indices that suited better for verticillium wilt identification were normalized canopy temperature, chlorophyll fluorescence, structural, xanthophyll, chlorophyll, carotenoid and disease indices. A similar study was conducted by López-López et al. (2016) to evaluate disease incidence and severity in almond orchards affected by the red leaf blotch fungal. Several indices where described and used to detect disease symptoms: the better results were achieved by pigment indices (chlorophyll a+b indices) and chlorophyll fluorescence in disease and severity detection, making them appropriate for decision support and implementation of precision crop protection techniques. Thermal imagery can be used to detect low transpiration rates caused by root diseases.

Burn indices have been useful for forestry professionals, land resource managers and fire officials to estimate areas of potential fire hazards, fire perimeter mapping and study and measure post-fire burn and vegetation regrowth areas. In this type of indices, a pre-processing stage is needed in order to mask water presence in the images. Chuvieco et al. (2002) compared different spectral indices, including NDVI, SAVI and BAI to distinguish burned land. They have demonstrated that BAI provided a better discrimination than the other tested indices, with a consistent behaviour along a considerable variability of scorched areas.

Table 2.3 sums up the presented indices, bands needed for their computation, formulas and references. Regarding the symbology, NIR, Red, Green, Blue, SWIR are related with the spectral broadband and $R_n$ stands for the reflectance value, in nanometres, on a certain narrowband. Broadband indices can also be computed with narrowband reflectance values from each spectral band. In thermal indices there are different formulas that use temperature as T. There are also variables (e.g. L, G, a) representing parameterized features. Some authors use normalization schemes (J. Torres-Sánchez et al., 2014) as a pre-processing step before the use of values in the indices (e.g. green = Green/Red+Green+Blue; red = Red/ Red+Green+Blue; blue = Blue/ Red+Green+Blue).

**Table 2.3.** Case-study applications, grouped by VI and respective formulas, operating bands and literature references.

| Index | Name | Formula | Bands | Reference | Applications/Description |
|---|---|---|---|---|---|
| Vegetation Indices | | | | | |
| CWSI | Crop Water Stress Index | $CSWI = \frac{T_{canopy} - T_{wet}}{T_{dry} - T_{wet}}$ | Thermal | Idso et al. 1981 | Analysis of plant hydration, given by the difference between the measured canopy temperature and a non-water-stressed baseline and diseases identification in early stage (Salamí et al., 2014). Used for generate maps that help in precision irrigation management in vineyards (Bellvert et al., 2013) and to assess the spatial variability of tree water status on heterogeneous orchards (Bellvert et al., 2016; Park et al., 2015). |
| Ig | Stomatal conductance index Ig | $Ig = \frac{T_{dry} - T_{canopy}}{T_{canopy} - T_{wet}}$ | Thermal | Jones, 1999 | Uses thermal bands in combination with wet and dry surface references to address environmental variations. Depending on the humidity and canopy height the results cannot be notorious, i.e. small temperature variations. |
| I3 | Stomatal conductance index I3 | $I3 = \frac{T_{canopy} - T_{wet}}{T_{dry} - T_{canopy}}$ | Thermal | | |
| NDVI | Normalized Difference Vegetation Index | $NDVI = \frac{\text{NIR} - \text{Red}}{\text{NIR} + \text{Red}}$ | NIR RGB | Rouse et al. 1974 | Biomass estimation (Bendig et al., 2015), canopy structure, Leaf Area Index and crop management (Candiago et al., 2015). (Depending on the season of the year this may not be suitable due to leaf colour change, since the reflectance from the green band is not used in index calculation |
| SAVI | Soil-Adjusted Vegetation Index | $SAVI = \frac{\text{NIR} - \text{Red}}{\text{NIR} + \text{Red} + \text{L}} 1 + L$ | NIR RGB | Huete, 1988 | Biomass estimation (Bendig et al., 2015), canopy structure, Leaf Area Index and Crop management (Gitelson et al., 1996). (These indices are based on NDVI but aim the minimization of soil brightness variations). |
| MSAVI | Modified Soil-Adjusted Vegetation Index | $MSAVI = \frac{\text{NIR} - \text{Red1} + \text{L}}{\text{NIR} + \text{Red} + \text{L}}$ | NIR RGB | Qi et al. 1994 | |
| OSAVI | Optimized Soil-Adjusted Vegetation Index | $OSAVI = \frac{1.5\text{NIR} - \text{Red}}{\text{NIR} + \text{Red} + 0.6}$ | NIR RGB | Rondeaux et al. 1996 | |

(Continued)

**Table 2.3.** (Continued).

| Index | Name | Formula | Bands | Reference | Applications/Description |
|---|---|---|---|---|---|
| TCARI | Transformed chlorophyll absorption ratio index | $TCARI = 3\left[(R_{700} - R_{670}) - 0.2(R_{700} - R_{550})\left(\frac{R_{700}}{R_{670}}\right)\right]$ | RedEdge Red | Haboudane et al. 2002 | Access vine water status (Baluja et al., 2012), separating of vegetation from soil background, (Perez et al., 2000). If normalized by the optimized soil-adjusted vegetation index (TCARI/OSAVI) integrates advantages of the minimization of soil background effects (OSAVI) and chlorophyll concertation estimation (TCARI) (Haboudane et al. 2002) |
| GNDVI | Green Normalized Difference Vegetation Index | $GNDVI = \frac{\text{NIR} - \text{Green}}{\text{NIR} + \text{Green}}$ | NIR RGB | Gitelson et al. 1996 | Crop management (Gitelson et al., 1996). |
| DVI | Difference Vegetation Index | $DVI = \text{NIR} - \text{Red}$ | NIR RGB | Tucker, 1979 | |
| EVI | Enhanced Vegetation Index | $EVI = \text{G}\left(\frac{\text{NIR} - \text{Red}}{\text{NIR} + C_1\text{Red} - C_2 Blue + L}\right)$ | NIR RGB | Justice et al. 1998 | Leaf Area Index (where NDVI may saturate. It reduces atmospheric influences by adding the blue band combined with the red band and NIR reflectance). |
| RVI or PCDI | Ratio Vegetation Index or Plant Cell Density Index | $RVI\ or\ PCDI = \frac{\text{NIR}}{\text{Red}}$ | NIR RGB | Jordan, 1969 | Used to measure vine vigour (Bramley and Hamilton 2007). |
| GRVI NDI NGRVI | Green-Red Vegetation Index | $GRVI = \frac{\text{Green} - \text{Red}}{\text{Green} + \text{Red}}$ | RGB | Falkowski et al. 2005; Gitelson et al. 2002; Perez et al. 2000; Tucker, 1979 | Marker for green vegetation, soils, water/snow, phonological indicator, separating of vegetation from soil background (Motohka et al., 2010). |
| MGRVI | Modified Green Red Vegetation Index | $MGRVI = \frac{Green^2 - Red^2}{Green^2 + Red^2}$ | RGB | J. Bendig et al. 2015 | Barley biomass monitoring (Gnyp et al., 2014). |
| RGBVI | Red Green Blue Vegetation Index | $RGBVI = \frac{Green^2 - \text{BlueRed}}{Green^2 + \text{BlueRed}}$ | RGB | J. Bendig et al. 2015 | |

(Continued)

**Table 2.3.** (Continued).

| Index | Name | Formula | Bands | Reference | Applications/Description |
|---|---|---|---|---|---|
| BGVI | Blue/Green Pigment Index | $BGVI = \frac{\text{Blue}}{\text{Green}}$ | RGB | P. J. Zarco-Tejada et al. 2005 | Water stress detection |
| BRVI | Blue/Red Pigment Index | $BGVI = \frac{\text{Blue}}{Red}$ | RGB | P. J. Zarco-Tejada et al. 2005 | |
| ExG | Excess Green | $ExG = 2\text{Green} - \text{Red} - \text{Blue}$ | RGB | Woebbecke et al. 1995 | Early-season crop detection (Torres-Sánchez et al., 2015; Torres-Sánchez et al., 2014). |
| ExG-R | Excess Green-Red | $ExGR = \text{ExG} - 1.4\text{Red} - \text{Green}$ | RGB | Neto, 2004 | |
| VEG | Vegetativen | $VEG = \frac{\text{Green}}{Red^{a}Blue^{(1-a)}}$ with $a = 0.667$ | RGB | Hague et al. 2006 | Wheat field monitoring (Hague et al., 2006). |
| PRI | Photochemical Reflectance Index | $PRI = \frac{\text{R}_{531} - \text{R}_{570}}{\text{R}_{531} + \text{R}_{570}}$ | RGB | Gamon et al. 1992 | It uses visible range images and is related to changes in photosynthetic efficiency. PRI is computed by the use of narrowband reflectance (R) at 531 and 570 nm wavelength. Berni et al. (2009) used PRI to investigate water stress in citrus orchard. |
| PCDI | Plant Cell Density Index | $PCDI = \frac{\text{NIR}}{\text{Red}}$ | RGB | Bramley and Hamilton, 2007 | Represents the ratio between NIR and red bands and can be used to measure of vine vigour (Bramley and Hamilton 2007). It was also applied multispectral and thermal imagery to evaluate the relationship between grapevine water status and PCDI and CWSI Bellvert and Girona, 2012). PCDI can be useful to discriminate well-watered zones in a vineyard as well as acting as a tool for irrigation scheduling. |
| GnyLi Index | Named by the developers Gnyp and Li | $GnyLi = \frac{R_{900}R_{1050} - R_{955}R_{1220}}{R_{900}R_{1050} + R_{955}R_{1220}}$ | NIR | Gnyp et al. 2014 | Barley biomass monitoring (Gnyp et al., 2014). |

(Continued)

**Table 2.3.** (Continued).

| Index | Name | Formula | Bands | Reference | Applications/Description |
|---|---|---|---|---|---|
| Burn Indices | | | | | |
| BAI | Burn Area Index | $BAI = \frac{1}{0.1 - Red^2 + 0.06 - NIR^2}$ | NIR RGB | Martín Isabel and Chuvieco Salinero, 1998 | Uses the NIR and red spectrum bands to highlight the burned land in post-fire images (Martín Isabel and Chuvieco Salinero, 1998). |
| NBR | Normalized Burn Ratio | $NBR = \frac{\text{NIR} - \text{SWIR}}{\text{NIR} + \text{SWIR}}$ | NIR SWIR | García & Caselles, 1991 | Similar to NDVI index, but it uses the shortwave-infrared (SWIR) instead of the red band (García and Caselles, 1991) to identify the darker pixels representing burned areas. It is suitable to calculate burned parts in areas greater than 200 hectares. |
| NBRT | Normalized Burn Ratio - Thermal | $NBRT = \frac{\text{NIR} - \text{SWIR}\left(\frac{Thermal}{1000}\right)}{\text{NIR} + \text{SWIR}\left(\frac{Thermal}{1000}\right)}$ | Thermal NIR SWIR | Holden et al. 2005 | Uses the thermal band that improves the differentiation between burned and unburned land (Holden et al., 2005). |
| Miscellaneous indices | | | | | |
| NDSI | Normalized Difference Snow Index | $NDSI = \frac{\text{Green} - \text{NIR}}{\text{Green} + \text{NIR}}$ | RGB NIR | Riggs, Hall and Salomonson, 1994 | Used to detect snow. |
| NDWI | Normalized Difference Water Index | $NDWI = \frac{\text{NIR} - \text{SWIR}}{\text{NIR} + \text{SWIR}}$ | NIR SWIR | Gao, 1996 | Used to detect and enhance the presence of water in images: NDWI is similar to NBR, however, values close to 1 represent areas with a strong presence of water. |
| MNDWI | Modified Normalized Difference Water Index | $MNDWI = \frac{\text{Green} - \text{SWIR}}{\text{Green} + \text{SWIR}}$ | RGB SWIR | Xu, 2006 | MNDWI uses the green band instead of NIR to improve the NDWI results, enhancing water features. |

### 2.4.3. Segmentation

Image processing techniques are frequently used as a complement to the vegetation indices calculation. In this topic, segmentation is particularly important for agroforestry, agriculture and related areas inasmuch as it is responsible for the simplification of imagery data into subsets that enable an easier analysis regarding features of interest. Thresholding is a common segmentation method that can be applied to mask certain features and/or to highlight the desired information. Within this category, there is a noteworthy algorithm that relies in the Otsu's method (Otsu, 1979) and which can be applied to obtain two classes of pixels (e.g. to distinguish bare soil from vegetation). Summing up, this method calculates an optimal threshold requiring low computational costs.

Meyer and Neto (2008) used VI to determine a colour vegetation index with an automatic threshold and to determine their accuracy using plant-soil-residue images. They compared the ExG, ExG−ExR and NDV indices results with manual plant pixel extraction after applying Otsu's method. Among the tested indices, the ExG-ExR allow reaching the best results in the successful discrimination of plants from the bare soil.

Regarding early season vegetation detection, Torres-Sánchez et al. (2015) used two image acquisition sensors (RGB and Multispectral) in three different types of crops: maize; sunflower and wheat. The developed algorithm for object-based image analysis (OBIA) was based on a multiresolution segmentation algorithm whilst the Otsu's method was applied for thresholding two vegetation indices, more specifically ExG and NDVI.

Another used method is the watershed transform: a gradient magnitude-based method that consists in finding the pixels with the highest gradient intensity corresponding to region boundaries. It was successfully applied in the extraction of canopy from palm orchards (Cohen et al., 2005). Baluja et al. (2012)used watershed algorithm combined with NDVI image to identify rows in vineyard crops.

OBIA (Blaschke, 2010) relies in the reduction of intra-class spectral variability caused by crown textures, gaps and shadows. Firstly, a group of spatially adjacent pixels is aggregated into spectrally homogeneous features which are then classified using objects as the minimum processing units (Torres-Sánchez et al. 2015). OBIA was used to identify different types of plant canopy, in pure olive crowns detection (R. Calderón et al., 2013), in discontinuous and continuous olive orchards (Díaz-Varela et al. 2015) and also for weed map generation in maize fields (Peña et al. 2013).

In order to successfully detect vine rows using UAS imagery, Comba et al. (2015) used Hough Space Clustering and total least square. Their method can be applied to different types of images resulting from VI calculation (e.g. NDVI) or in a simple grayscale image, based on a single-band (e.g. NIR). Nolan et al. (2015) used skeletisation techniques to accurately segment vineyard rows to produce precise vine maps. The proposed algorithm uses as inputs single-band images from any type of sensor with the only requirement of having a high spatial resolution to distinguish vine rows and soil. The application of such an algorithm allowed Nolan et al. (2015) to achieve an accuracy of 97,1% regarding the identification of vineyard rows. The 2,9% failure rate occurred because of trees obscuring vine rows, shadows and also segmentation discontinuities. Bobillet et al. (2003) also classified vine rows; however, their method required manual adjustments in pre and post-processing stages to the achievement of valid results. Moreover, problems identifying vine rows with grass in between were reported.

### 2.4.4. 3D reconstruction

In agroforestry applications, vegetation can be accurately virtualized using 3D scanning methods. One of the most known of these methods involves the extraction of a point cloud from ground, crops and other field elements. As it was previously mentioned, LiDAR can be used for 3D scanning. For example, Wallace (2013) used this sensor to digitalize forest's canopy.

Another known technique is the Structure from Motion (SfM) which provides the ability to create 3D models from 2D images. Digital Surface Models (DSMs) and Crop Surface Models (CSMs) can be achieved using this technique. In turn, these models can be used to obtain important data regarding the elevation models and in crop development (Flener et al., 2013). The reconstruction process consists in the following steps: (1) matching the overlapping images containing the similar features; (2) extraction of geometry; (3) point cloud processing; and (4) 3D model and texture generation accordingly with the provided images. The main constraint of this method is the high demand of computational requirements and, consequently, the processing time. Bendig et al. (2014) conducted a study to monitor barley crops using the post-flight generated CSM computed by images acquired form an RGB camera mounted on a UAV. The study introduced a method to estimate biomass based on the plant height derived from CSM, demonstrating that RGB images are highly suitable for deriving barley plant height. Mathews and Jensen (2013) opted by applying SfM to compute a point cloud of vine canopy structure to estimate LAI. Figure 2.17 shows an example of a DSM obtained from 2D nadir images. Gatziolis et al. (2015) used a multi-rotor UAV to capture images and achieve 3D reconstructions of trees with SfM algorithms. SfM techniques are becoming increasingly used due to their cost-effectiveness in comparison with expensive systems such as LiDAR. More recently, Thiel and Schmullius (2017) compared point clouds from UAV images with those created from LiDAR systems over a forested area and showed that the photogrammetric accuracy compares well with LiDAR, yet the density of surface points is much higher from images, which is of particular importance for the detection of small trees. Alternatively, there are other valid techniques for 3D reconstruction that are getting increasingly accessible, like the ones based on stereo cameras (Frankenberger et al., 2008; Eija Honkavaara et al., 2013).

Wallace et al. (2016) carried out a comparison of airborne LiDAR scanning and SfM. Both methods proved to be capable of providing useful information about canopy and terrain in areas with low canopy closure. However, LiDAR outperformed SfM in capturing terrain under denser canopy cover. Díaz-Varela et al. (2015) worked with SfM-based DSMs to estimate olive crown parameters such as tree height and crown diameter, in continuous and discontinuous canopy cropping systems. The estimation of crown parameters presented a high compliance with the real measurements.

**Figure 2.17.** Digital surface model (DSM) of a UTAD’s vineyard determined in the post-processing stage of a flight with an UAV carrying an optical sensor.

Different applications are provided in the next section depending on the application area: agriculture, forestry or both.

# 2.5. Applications

UAS provide high-resolution aerial imagery opening new cost-effective horizons that are capable of tackling the traditional and expansive remote sensing platforms such as manned aircraft or satellites. In this section, some of the works that constitute the state of the art on applications relying on UAS will be reviewed to provide a better insight of the potential of these unmanned flight devices in agriculture, forestry and related areas, as presented in Table 2.4. In agriculture, the main applications include crop monitoring, invasive weed mapping, water status estimation, biomass estimation, chlorophyll estimation and nitrogen estimation. For forestry applications, bellow forest canopy mapping, forest inventory, measuring and monitoring structural forest properties, forest fire detection and monitoring have been explored by the use of UAS. There are also applications common to both areas such as land-use classification, wildlife detection and vegetation height maps.

## 2.5.1. Agriculture

UAS-based remote sensing can help determining plant parameters as leaf area index, canopy cover and volume. UAVs provide flexibility to assess crop parameters as vigour, quality and yield estimation which is needed to be measured during the whole growing season, as presented in Ballesteros et al. (2015). For parameters that are hard to detect with visible spectrum sensors, hyperspectral sensors are more suitable. These sensors enable the acquisition of imagery data with very high spectral and temporal resolutions, which is especially adequate for disease detection in early stages (Calderón et al. 2015) or precision agriculture (Candiago et al. 2015), reducing future losses. Farmers' interests are to have healthier crops and, at a same time, to manage resources (e.g. water and pesticides) in an efficient way. This can be provided by UAVs data to create maps for better crop management (Ballesteros et al. 2015). These maps are adequate to expose problems as irrigation, soil variation, fungal or pest investigation.

Usually, NIR sensors are not used separately, but in combination with RGB sensors or as a component in multispectral sensors. Navia et al. (2016) used multispectral imagery acquired from a multi-rotor UAV to generate multispectral mosaics computed with NDVI, to assist farmers in the assessment of plant health monitoring. Lukas et al. (2016) compared the basic growth parameters obtained from a fixed-wing UAV equipped with a NIR camera and from Landsat 8. Both methods showed a high correlation with ground spectrometer measurements of biomass and nitrogen content but the satellite data had a coarse resolution. Kalisperakis et al. (2015) used different UAS imaging sources, more specifically, hyperspectral, RGB orthophotos and 3D crop surface models to access LAI estimation in vineyards. The comparison between estimated LAI and ground truth LAI measurements showed that the lowest correlation rates occurred from RGB orthophotos. On the other hand, the highest correlation was noticed in hyperspectral data and 3D crop surface models.

**Table 2.4.** UAS-based remote sensing applications on agriculture, forestry and common to both areas.

| Application | Main objective | References |
|---|---|---|
| Agriculture | Crop monitoring | (Ballesteros et al., 2015; Berni, Zarco-Tejada, Suarez, et al., 2009; Rocío Calderón et al., 2015; Candiago et al., 2015; Comba et al., 2015; Díaz-Varela, de la Rosa, et al., 2015; Kalisperakis et al., 2015; Lukas et al., 2016, 2016; Navia et al., 2016, 2016; Nebiker et al., 2008; Jacopo Primicerio et al., 2012; Suomalainen et al., 2014; J. Torres-Sánchez et al., 2014, 2015; D. Turner et al., 2011) |
| | Invasive weed mapping | (D. Gómez-Candón et al., 2013; Peña et al., 2013) |
| | Water status estimation | (Baluja et al., 2012; Bellvert et al., 2013; Bellvert & Girona, 2012; Park et al., 2015; Pablo J. Zarco-Tejada et al., 2012) |
| | Biomass estimation | (Bendig et al., 2014, 2015; Eija Honkavaara et al., 2012, 2013, 2013; Pölönen et al., 2013) |
| | Chlorophyll estimation | (Uto et al., 2013; Pablo J. Zarco-Tejada et al., 2012) |
| | Nitrogen estimation | (Caturegli et al., 2016; Pölönen et al., 2013) |
| Forestry | Bellow forest canopy mapping | (Chisholm et al., 2013; Getzin et al., 2012) |
| | Forest inventory | (Rokhmana, 2015; Luke Wallace et al., 2012) |
| | Measuring and monitoring structural forest properties | (Gatziolis et al., 2015; L. Wallace, 2013; Luke Wallace et al., 2016) |
| | Forest fire detection and monitoring | (Merino et al., 2011) |
| Agriculture & Forestry | Land-use classification | (Lagüela et al., 2015) |
| | Wildlife detection | (Israel, 2011; Ward et al., 2016) |
| | Vegetation height maps | (Ballesteros et al., 2015; Bendig et al., 2015; Mathews & Jensen, 2013; Suomalainen et al., 2014; D. Turner et al., 2011) |

Another application area in agriculture is invasive weed mapping. A study to distinguish the invasive weeds from other crops was carried out by Peña et al. (2013). It consisted on detecting weed in early stages of maize using a six-band multispectral camera attached to an UAV in which the applied OBIA procedure computed multiple results and statistics that could be exported in the form of weed maps, vectors or table file format and provide relevant information. Another study to distinguish crops from invasive weed was carried out by Gómez-Candón et al. (2013) in wheat.

Water status estimation is a task that can be performed by UAVs with quick turnaround times. Bellvert et al. (2013) demonstrated the feasibility of using high resolution thermal imagery for irrigation management across vineyards for precision agriculture purposes (optimal irrigation). According to Bellvert et al. (2013) the best time of the day to acquire thermal images is around noon, because there is an almost complete absence of shadow effects and, consequently, the sensitiveness for the identification of water stress problems is higher. Multispectral and thermal imagery was applied by Baluja et al. (2012) and Bellvert and Girona (2012) to determine water status variability in vineyards. This data can be used for better irrigation management in a vineyard parcel scale. Zarco-Tejada et al. (2012) addressed the detection of water stress in a citrus orchard by using fluorescence, canopy temperature and narrow-band indices, from data acquired by a micro-hyperspectral and a thermal camera.

Biomass estimation was studied by Bendig et al. (2014) with vegetation indices and plant height maps derived from RGB imagery on barley. Three vegetation indices were computed, with the main issue of the visible band being reliable only in early growing stages. However, combining the vegetation indices with plant height by using multiple linear regression or non-linear regression models, a better performance was achieved, in comparison with the indices itself.

Chlorophyll estimation was addressed in the study carried out by Uto et al. (2013) focusing on the estimation of rice chlorophyll density, based on low altitude flights carried out by an UAV equipped with a hyperspectral sensor. Experimental results showed that the chlorophyll density can be estimated with high accuracy, even under unstable light conditions. Suomalainen et al. (2014) developed a hyperspectral sensor based on low-cost components, to apply it on multiple types of crops. Chlorophyll concentration was examined using Red Edge-based indices. Martín et al. (2015) used hyperspectral sensing to investigate the relation between leaves chlorophyll a+b concentration and grapes composition in vineyards affected by iron chlorosis and to assess if the leaves chlorophyll concentration acquired from hyperspectral images could be useful to map potential quality zones in these vineyards. The results suggest a promising application for predicting grapes' quality in vineyards affected by the iron chlorosis.

Caturegli et al. (2016) focused on the estimation of nitrogen status in turfgrass. This kind of knowledge can lead to both economic and environmental benefits inasmuch as it enables the balanced application of fertilizers. Also, pesticides are extensively applied for eliminating pests and weeds infesting the crops. Pölönen et al. (2013) were able to estimate both biomass and nitrogen content with a hyperspectral sensor and a machine learning approach.

### 2.5.2. Forestry

Getzin et al. (2012) used a fixed-wing UAV to take aerial images of a forest aiming the further examination of canopy gaps and the assessment of the floristic biodiversity existent in the forest understorey. The obtained images led the authors to conclude that detailed, spatially implicit information on gap shape metrics is sufficient to reveal strong dependency between disturbance patterns and plant diversity. Chisholm et al. (2013) conducted a trial with a LiDAR mounted on an UAV for mapping the forest below the canopy. The main goals were to map tree stems and to measure the diameter of trees at breast height (DBH). The LiDAR along with a developed algorithm enabled the detection of trees in flights of 3m that took place 20cm above the DBH.

To calculate wood stock of a teak wood forest in Indonesia, Rokhmana (2015) used orthophoto mosaics and 3D models. The main prerequisite for this task was to distinguish individual trees so its height could be measured as well as the canopy diameter. As it was previously mentioned in Section 2.4.4, LiDAR is a good tool for the accurate extraction of 3D data. The comparison between tree canopy mapping and photogrammetric SfM was already addressed in Wallace et al. (2012), showing that LiDAR outperforms SfM in bellow canopy mapping.

Gatziolis et al. (2015) were able to reconstruct 3D models using RGB cameras from UAV along with SfM algorithms. This methodology can be applied to individual or to a group of trees providing useful information related, with for instance tree growth among time.

Merino et al. (2011) developed an UAS for automatic forest fire monitoring and measurement. It was based on multiple UAVs and a central station. The main payload consisted in infrared and visual cameras which extract fire related features

### 2.5.3. Agroforestry

There are tasks that can be applied in both agriculture and forestry. The case of generation of thermographic mosaics and thermographic DSMs from thermal sensors attached on a low-cost multi-rotor UAV were used (Lagüela et al. 2015). Although agroforestry was not the primary focus, the methodology can be extended to land use classification and water management according to the thermal response of objects.

Industrialization of agriculture brought many benefits but also an increased danger for wild animals living in agroforestry areas. Israel (2011) presented a light weight infrared thermal sensor attached to an UAV which is capable of preventing many fatalities among the roe deer fawn communities on meadows and pastures, caused by machines. Ward et al. (2016) took the concept even further and created a system that can autonomously detect animals, determine their coordinates and generate maps displaying their locations ahead of the user. They have proved the effectiveness of UAS over ground-based techniques like camera traps or surveys on foot.

Vegetation height maps can be applied in agriculture or forestry areas. Several studies were conducted making good use of this information for creation of crop surface models (Bendig et al., 2014; Mathews and Jensen, 2013) or even to forest canopy cover (Wallace 2013).

### 2.5.4. Recommendations towards UAS platform selection

Table 2.5 presents budget estimations for the acquisition of an UAS according to the coverage area and the sensor type, which is influenced by the intended application. For large areas (greater than 50 ha) a fixed-wing UAV is recommended due to the ability of quicker area coverage; on the other hand, a multi-rotor UAV is more suitable for smaller area coverage. However, the usage of a fixed-wing UAV requires a large space to perform safe landing operations—at least an area of 20 by 100 metres (for linear landing)—which is a drawback of this type of UAV. A practical example is the Douro wine region in Portugal, where the vineyard layout disposed in slopes along the river Douro makes the landing task challenging due to the lack of secure areas to accomplish it. Complementary to Table 2.5, Figure 2.18 illustrates the process of selecting the most appropriate UAS and sensors for the required task.

Essentially, rotor-based UAS are used to cover small areas whereas the fixed-wing UASs are more suitable for being applied in wider areas, as detailed in Table 2.5. On the other hand, the use of sensors is highly dependent of the application's purpose.

On the subject of forestry applications such as inventory and canopy mapping, the usage of LiDAR sensors represents an effective tool capable of gathering data below canopy. When it comes to perform forest fire monitoring and wildlife detection, thermal sensors are a suitable option, while for determining burned areas in post-fire scenario multi-spectral sensors can be applied.

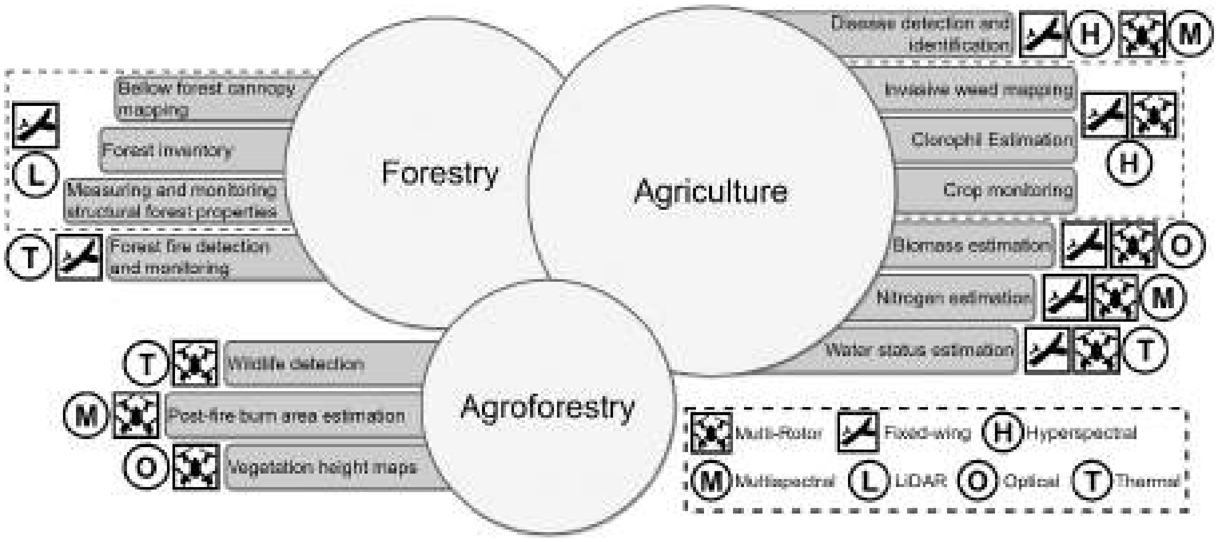


**Figure 2.18.** Diagram depicting an appropriate selection of a UAS platform—including UAV and sensor—depending on the area of application and the task.

To obtain vegetation height maps, optical sensors are a plausible choice, because of their ability to process the acquired images using SfM algorithms and the cost-effectiveness comparatively to sensors like LiDAR. Crop monitoring along the whole growth season can be performed through multispectral sensors which seem to present the most compromise between cost and effectiveness. In spite of it, other sensors can also be applied to do crop monitoring related tasks. For those who are interested in biomass estimation, optical sensors might be a good choice. Multispectral sensors can be applied to map invasive weeds and nitrogen estimation. Whilst the first results from post-flight image processing algorithms (e.g. OBIA), the latter is by providing fertilization maps.

Disease detection and identification have a significant importance in agricultural applications, either for resource optimization and/or timely actions for preventive purposes. Thus, and notwithstanding the costs, hyperspectral sensors are recommended even for early stage disease detection. Alternatively, depending on the crop type and disease, multispectral sensors can be used. Hyperspectral sensors are also suitable for chlorophyll estimation through narrow-band VI calculation on the acquired data, accordingly to the addressed studies.

Finally, water status can be estimated through a set of spectral VI that are calculated to determine vigour, based on data acquired from multispectral or optical sensors, yet thermal sensors can provide this type of data in a faster way, although some cautions concerning day time must be taken due to effects of shadows, according to Bellvert et al. (2013). Thereby, it is recommended to use these sensors when the sun heading is at, approximately, 180º (solar noon).

**Table 2.5.** Recommended UAV platforms for different agroforestry applications and respective estimated budgets. Each UAV platform considers a UAV type (fixed-wind or multi-rotor) and an attachable sensor (Optical, Multispectral, Hyperspectral, Thermal and LiDAR).

| Area of application | Coverage area | Recommended sensor(s) | Recommended UAV | Estimated budget (Euros) |
|---|---|---|---|---|
| Crop monitoring | Large | Multispectral | Fixed-wing | 25 000 |
| | Small | Multispectral | Multi-rotor | 10 000 |
| Disease detection and identification | Large | Hyperspectral | Fixed-wing | 120 000* |
| | Small | Multispectral | Multi-rotor | 10 000 |
| Invasive weed mapping | Large | Multispectral | Fixed-wing | 25 000 |
| | Small | Multispectral | Multi-rotor | 10 000 |
| Water status estimation | Large | Thermal | Fixed-wing | 35 000 |
| | Small | Thermal | Multi-rotor | 15 000 |
| Biomass estimation | Large | Optical | Fixed-wing | 20 000 |
| | Small | Optical | Multi-rotor | 2000 |
| Chlorophyll estimation | Large | Hyperspectral | Fixed-wing | 25 000 |
| | Small | Hyperspectral | Multi-rotor | 10 000 |
| Bellow forest canopy mapping | Large | LIDAR | Fixed-wing | 30 000 |
| Forest inventory | Large | LIDAR | Fixed-wing | 30 000 |
| Measuring and monitoring structural forest properties | Large | LIDAR | Fixed-wing | 30 000 |
| Forest fire detection and monitoring | Large | Thermal | Fixed-wing | 35 000 |
| Post-fire burn area estimation | Large | Multispectral | Fixed-wing | 25 000 |
| Wildlife detection | Small | Thermal | Multi-rotor | 8000 |
| Nitrogen estimation | Large | Multispectral | Fixed-wing | 25 000 |
| | Small | Multispectral | Multi-rotor | 10 000 |
| Vegetation height maps | Small | Optical | Multi-rotor | 3000 |

Small areas up to 50 ha; Large areas between 50 ha and 5km$^2$; The estimated budged includes UAV + sensor + processing software; * the prices have been decreasing

Table 2.6 provides an overview of the reviewed studies regarding the main objective and conclusions, along with the used UAV types and the used sensors. It is noteworthy that fixed-wing UAVs are widely applied to land use classification, water assessment or even to provide data towards the optimization of agricultural tasks (e.g. crop management and pesticide administration) through the use of optical, thermal, multi and hyperspectral sensors. Most of the reviewed studies preferred multi-rotor UAVs that can vary the specified set of sensors to perform fire monitoring, canopy development assessment, detection of vineyard rows, etc. and also because they are usually cheaper and more flexible for demonstrative/scientific studies. Notwithstanding the great number of successful approaches, there is an important aspect that should be retained: the specifications of each platform (in terms of area covering, flight time durability, payload capacity) should be attended along with the recommendations left on this paper inasmuch as they intend to represent general guidelines to prevent unnecessary costs for mission accomplishment or potential failure in performing the required surveys in demanding situations. In the way that a fixed-wing UAV for water status assessment in a small crop area could be exaggerated, a regular rotor-based UAV could be time-consuming at monitoring biodiversity in an extensive forestry area due to the lower autonomy in terms of flight time.

Regarding UAV sensors, whilst the RGB sensors are suitable to find features within a certain area (e.g. vineyard rows detection, tree crown size estimation), to estimate LAI for green vegetation and invasive weed mapping. The infrared, multispectral and hyperspectral sensors are specialized in identifying the presence/absence of certain components or materials (e.g. disease detection, water status estimation) within a scene through reflectance analysis and processing at certain wavebands that can range out of the visible spectrum. LiDAR sensors can provide accurate measurements through laser pulses targeting land objects (e.g. vegetation height determination). The cost/task-effectiveness binomial has a relevant role when it comes to select a tool for data extraction. If the precision on estimating the presence of a certain feature in the environment (e.g. vineyard disease) is required, the use of a hyperspectral sensor should be considered. In an alternative scenario, when a low-budget system is required, for instance to produce 3D models of a certain culture for analysing different development stages, an RGB camera allied to photogrammetric techniques will be sufficient (despite the probable loss of information—e.g. soil—over the obvious, but usually expensive, LiDAR sensor).

**Table 2.6.** Compilation of the reviewed studies presenting their respective main objectives and conclusions and UAV type and sensors used in each case.

| Reference | Objective | Main conclusion | UAV type | | Used sensors | | | | |
|---|---|---|---|---|---|---|---|---|---|
| | | | FW | RB | O | T | M | H | L |
| (Lagüela et al., 2015) | Land-use classification | Successful land use classification (buildings, tall vegetation, short vegetation). | | ● | | ● | | | |
| (Jacopo Primicerio et al., 2012) | Producing of vigor maps of vineyards based on NDVI | Results highly correlated with ground truth spectrometer. | | ● | | | ● | | |
| (Getzin et al., 2012) | Use canopy gaps in forests to assess floristic biodiversity of the forest understory | High-resolution imagery can effectively assess biodiversity in temperate forests. | ● | | ● | | | | |
| (D. Gómez-Candón et al., 2013) | Assess the parameters that affect the accuracy of orthomosaics. Early weed mapping in wheat | Different altitude intervals did not show large differences in accuracy in generation of orthomosaics between (30 to 100m). | | ● | ● | | | | |
| (Baluja et al., 2012) | Assessment of water status variability in vineyards | Both multispectral and thermal methods were successful | ● | | | ● | ● | | |
| (Israel, 2011) | Detection of roe fawn deer on meadows | Field campaigns confirmed reliable real-time manual fawn deer detection. | | ● | | ● | | | |

| Reference | Objective | Main conclusion | UAV type | | Used sensors | | | | |
|---|---|---|---|---|---|---|---|---|---|
| | | | **FW** | **RB** | **O** | **T** | **M** | **H** | **L** |
| (Ward et al., 2016) | Detection of animals and displaying their location on a map | Successfully tested and development of a smartphone app integrated with the system. | | ● | | ● | | | |
| (Bendig et al., 2014) | Barley biomass monitoring by combining plant height and vegetation indices | Optical images were highly suitable for deriving barley plant height from CSM for biomass estimation | | ● | ● | | | | |
| (D. Turner et al., 2011) | Vineyard mapping | UAVs provide flexible on-demand multiple sensor data for the whole growing season and especially for the critical times with high spatial resolution. | | ● | ● | ● | ● | | |
| (Candiago et al., 2015) | Evaluation of multiple vegetation indices for precision agriculture applications | The VI were computed based on pixel values and delivered mainly qualitative results. | | ● | | | ● | | |
| (E. Honkavaara et al., 2012) | Combination of hyperspectral imagery and point clouds for biomass estimation | Successful implementation of the use of hyperspectral reflectance mosaics with point clouds for biomass estimation. | | ● | ● | | | ● | |
| (Uto et al., 2013) | Development of a low-cost light hyperspectral sensor for chlorophyll estimation in rice paddies | Experimental results proved that chlorophyll densities can be estimated with high accuracy. | | ● | | | | ● | |
| (Ballesteros et al., 2015) | Leaf area index, green canopy cover and volume characterization of vineyards | The developed work could be useful in decision support to improve crop management, and optimize usage of pesticides and fertilizer. | ● | | ● | | | | |
| (Lukas et al., 2016) | Comparison of basic growth parameters of winter wheat obtained from UAV and satellite | Both methods showed a strong correlation with ground spectrometer measurements but satellite imagery provided a smaller resolution. | ● | | | | ● | | |
| (Comba et al., 2015) | Vineyard row detection | Successful detection of wine rows in grey scale images obtained from a multispectral sensor. | | ● | | | ● | | |
| (Nebiker et al., 2008) | Producing of vigor maps of vineyards | Results highly correlated with ground truth classification. | | ● | ● | | ● | | |
| (Peña et al., 2013) | Weed mapping in maize | The algorithm efficiently identified crop rows, inner row weeds were successfully detected. | | ● | | | ● | | |
| (Caturegli et al., 2016) | Nitrogen status estimation in turfgrass | The knowledge of the nitrogen status can lead to both economic and environmental benefits by a reasonable application of fertilizers. | | ● | ● | | ● | | |
| (Navia et al., 2016) | Multispectral orthomosaic generation and NDVI calculation | Calculated NDVI showed that it can determine weak spots in crop areas and also see change in plant health over time. | | ● | | | ● | | |
| (Rokhmana, 2015) | Teak wood forest stock estimation | Successful wood stock estimation. | ● | | ● | | | | |
| (Pölönen et al., 2013) | Biomass and nitrogen content estimation of wheat and barley | Results showed that the radiometric uniformity amongst individual images forming the image mosaics had impact the biomass estimation quality. | | ● | | | | ● | |
| (Suomalainen et al., 2014) | Development of a hyperspectral sensor and evaluation on various types of | A lightweight hyperspectral mapping system was developed specifically for rotor-based UAV and presented the potential for agricultural mapping and monitoring applications. | | ● | | | | ● | |

| Reference | Objective | Main conclusion | UAV type | | Used sensors | | | | |
|---|---|---|---|---|---|---|---|---|---|
| | | | FW | RB | O | T | M | H | L |
| | crops for orthomosaics and vegetation height maps | | | | | | | | |
| (Chisholm et al., 2013) | Bellow forest canopy mapping | The UAV-measured DBH estimates were strongly correlated with the human-based ones. | | ● | | | | | ● |
| (Luke Wallace et al., 2012) | Development of a low-cost UAV LIDAR sensor applied in forest inventory applications | Comparing with LIDAR sensors used in other remote sensing platforms UAV-borne LiDAR produced point clouds with only slightly worse accuracies but with much higher point densities. | | ● | | | | | ● |
| (Luke Wallace et al., 2016) | Measuring and monitoring structural properties of forests with airborne laser scanner and SfM techniques | Airborne laser scanner got better results in penetrating the upper canopy and vertical distribution of vegetation. SfM lacked the ability to penetrate dense canopy parts, which resulted in a poor definition of the mid and under-store. | | ● | ● | | | | ● |
| (Bendig et al., 2015) | Estimating biomass in barley using vegetation indices and plant height information | Visible band indices showed a better ability to model biomass in early growth stages in comparison to late growth stages. | | ● | | | ● | | |
| (Pablo J. Zarco-Tejada et al., 2012) | Water stress detection in citrus orchards using hyperspectral imager and thermal camera | The experiment enabled water stress detection assessment by using crown temperature, visible and NIR narrow-band indices and chlorophyll fluorescence. | ● | | | ● | | ● | |
| (Bellvert et al., 2013) | Generating maps using CWSI for precision irrigation management in vineyards | Demonstration of the viability of thermal imagery for detecting the level of water stress in vineyards. | ● | | | ● | ● | | |
| (Rocío Calderón et al., 2015) | Automatic methods for early detection of plant diseases | The results demonstrated that the developed methods at orchard scale are validated for flights in large areas consisting of olive orchards with different characteristics. | ● | | | ● | | ● | |
| (A. P. Nolan et al., 2015) | Automated detection and segmentation of vine rows using high resolution UAS imagery in a commercial vineyard | The vine row detection algorithm achieved average precision and sensitivity results. Some sections of vine rows have been falsely classified as being non-vine row pixels, due to overhanging trees, shadows or initial binary segmentation discontinuities. | ● | | ● | | | | |
| (Mathews & Jensen, 2013) | Using SfM to model vine canopy structure | Measured LAI of vine canopy had good results with metrics. | ● | | | | ● | | |
| (Kalisperakis et al., 2015) | Estimating crop LAI using hyperspectral data, 2D RGB mosaic and 3D crop surface models | The lowest correlations against the ground truth data were derived from the calculated greenness levels from the 2D RGB orthomosaics. The highest correlation rates were established for the hyperspectral and the 3D canopy levels. | | ● | ● | | | ● | |
| (Wehrhan et al., 2016) | Quantification of spatial patterns of fresh phytomass and its relation to carbon export of lucerne | Among different tested vegetation indices, the EVI got the highest correlation between ground-based measurements of fresh phytomass of Lucerne. | ● | | | | ● | | |
| (Berni, Zarco-Tejada, Suarez, et al., 2009) | Vegetation monitoring through the use of thermal and multispectral sensors | The obtained results make this platform suitable for a number of applications including precision farming and irrigation scheduling. | | ● | | ● | ● | | |

| Reference | Objective | Main conclusion | UAV type | | Used sensors | | | | |
|---|---|---|---|---|---|---|---|---|---|
| | | | **FW** | **RB** | **O** | **T** | **M** | **H** | **L** |
| (Bellvert & Girona, 2012) | Usage of multispectral and thermal images for irrigation scheduling in vineyards | It was demonstrated the viability of high-resolution thermal imagery for detecting the water stress level in grapevines | ● | | | ● | | | |
| (J. Torres-Sánchez et al., 2014) | Early-season crop monitoring in wheat using vegetation indices | The ExG index is most suitable to calculate early stages crops with accuracy and spatial and temporal consistency. | | ● | ● | | | | |
| (J. Torres-Sánchez et al., 2015) | Detection of vegetation in early-season herbaceous crops (maize, sunflower and wheat) | An automatic thresholding for vegetation classification was achieved based on OBIA algorithm. Demonstrating its ability to automatically select a threshold from gray-level histograms. | | ● | ● | | ● | | |
| (Park et al., 2015) | Estimation of crop water stress in a nectarine orchard | The mapping of spatial variability of nectarine water stress was proved to be effective and an optimal tool to help in irrigation management. | | ● | | ● | | | |
| (L. Wallace, 2013) | Investigating the use of UAV-borne LIDAR systems as a platform to gain knowledge of the canopy structure within forested environments. | UAV-LiDAR data is suitable for use in monitoring changes in the canopy structure. The method based on alpha shapes was the most stable across repeat measures. | | ● | | | | | ● |
| (Gatziolis et al., 2015) | Developing an affordable method for obtaining precise and comprehensive 3D models of trees and small groups of trees | The developed work proved to be capable of handling most conditions encountered in practice to deliver detailed reconstruction of trees. | | ● | ● | | | | ● |
| (Eija Honkavaara et al., 2013) | Investigating the processing and use of UAS image data in precision agriculture | Fundamental need to develop reliable methods for the geometric and radiometric processing of huge numbers of small, overlapping images as well as developing all-weather processing technology in order to take full advantage of this new technology and to make this technology operational in practical applications was identified. | | ● | | | | ● | |
| Díaz-Varela et al. (2015) | Estimating of olive crown parameters | Comparison between reference field measurements and remote sensing estimation of crown parameters confirmed as a good solution in terms of performance and cost-effective alternative for the characterization of the olive tree crown in discontinuous canopy. | ● | | ● | | | | |
| (Mathews, 2015) | The use of compact digital cameras to remotely estimate spectral reflectance based on UAV imagery. | There was found that the red and NIR bands were the most accurate at estimating reflectance. | ● | | | | ● | | |
| (Merino et al., 2011) | Automatic fire detection | A system for fire monitoring was developed, based on several UAVs and a central station. Infrared and visual cameras were the main payload used for the environment perception. | | ● | ● | ● | | | |

FW - Fixed-wing; RB - Rotor-based; O - optical; T - thermal; M - multispectral; H - Hyperspectral; L - LiDAR.

## 2.6. Conclusion

This survey presents a brief comparison of remote sensing platforms, their pros and cons, and how UASs can complement the established manned aircraft and satellite platforms. Most common types of UAVs and sensors are also presented aside with processing methods and applications in agroforestry. This study provides agroforestry professionals with information to assist them in choosing the most suitable UAS for their remote sensing purposes. To achieve this, recent studies were reviewed with the focus on UAV types, sensors, data processing and applications in agroforestry.

Before selecting a proper UAS, the end-user should understand the capabilities and the restrictions of the available systems regarding not only the kind of results that are expected, but also what to do with them since mosaics, digital surface models, vegetation indices, etc., are not the final products but resources for further goals. UAS-based remote sensing in precision farming and forestry aims to provide the adequate decision support, which has a crucial role for the management optimization of farms, woodlands and other similar territorial areas.

Nowadays, farmers and foresters are dependent on companies to perform the processing and presentation of agroforestry-related information, sometimes in a way that will not fulfil the end-user needs. The next step of this ongoing revolution will focus in the development of user-friendly interfaces where just a few parameters are required, releasing the user from a deeper knowledge on data processing, allowing agroforestry professionals to perform interpretation of collected data by UAS in an autonomous and easy way. Our research group is already developing effective solutions allowing the professionals an autonomous analysis.

Better data processing software working with different sources of temporal and spatial data (e.g. meteorological and environmental) for a more effective decision support regarding agroforestry applications will also appear in the near future. Ideally, the future of both precision agriculture and agroforestry remote sensing would be to have the UAVs platforms constantly sensing the environment and sending the resulting data to intelligent entities (centralized or distributed) that control actuators to optimally solve eventual issues such as the lack of water or disease detection in a complete solution of Internet of Things for agroforestry. This kind of proactivity would allow farmers and foresters to be concentrated on the final products and services instead of being concerned with the middle-level processes.

Summing up, UAS platforms with the addressed sensors are going mainstream and its importance for decision support is getting increasingly relevant for researchers, farmers, foresters and related business professionals as innovative techniques are being developed for a sharpen optimization of the agroforestry underlying processes. DroneDeploy (2016) use case statistics confirm that agriculture, including forestry, is the leading application in the UAS market and Simelli and Tsagaris (2015) refer that by 2018, the usage of UAS will continue to grow with increasing affordability and autonomy. In spite of the fact that the UAV can fly autonomously, nowadays it is still required the presence of a pilot. The reasons of this are the lack of device intelligence. Hopefully this issue will be solved in the next years due to the expansion of UAS usage in many sectors and mainly because of the progress of the artificial intelligence, which is capable of providing the autonomous decision support to those devices including law awareness. The optimal scenario of using UAVs is the entire automated process from taking off the vehicle to the processing the data and turning on the pro-active actions. In the agricultural industry, the UAV would do the flights in the area of interest whenever it would be needed, based on previous flights. The collected data would serve as information for another automated machines like irrigation systems or intelligent pesticide sprayers.

## Acknowledgements

This work was financed by the European Regional Development Fund (ERDF) through the Operational Programme for Competitiveness and Internationalisation - COMPETE 2020 under the PORTUGAL 2020 Partnership Agreement, and through the Portuguese National Innovation Agency (ANI) as a part of project “PARRA - Plataforma integrAda de monitoRização e avaliação da doença da flavescência douRada na vinhA” (Nº 3447) and was supported by ERDF and North 2020 -North Regional Operational Program, as part of project “INNOVINE&WINE - Vineyard and Wine Innovation Platform” (NORTE-01-0145-FEDER-000038).

# Chapter 3.

## Multi-Temporal Analysis of Forestry and Coastal Environments Using UASs

*Remote Sensing*, 2017, *10*(1), 24

Journal Impact Factor – 2017: 3.406

5 Year Impact Factor – 2017: 3.952

**Luís Pádua**, Jonáš Hruška, José Bessa, Telmo Adão, Luís M. Martins, José A. Gonçalves, Emanuel Peres, António M. R. Sousa, João P. Castro and Joaquim J. Sousa

Refer to https://doi.org/10.3390/rs10010024 for online published version

## 3.1. Introduction

Unmanned aerial systems (UASs) allow professionals, acting in different areas of society, to capture up-to-date, high resolution, and accurate positional data that may be used for generating advanced data products—such as 3D point clouds, orthomosaics (orthophoto maps), digital surface models (DSMs) and vegetation indices—which are very useful for classification and segmentation. As occurs in many other technological fields, the number of applications is increasing every day, causing a rapid increase in UAS usage around the world, with exponential growth expected in the coming years (Ermacora et al., 2014; Oleire-Oltmanns et al., 2012).

The main factors supporting this growth are related to the: (1) increasing awareness about the benefits that this kind of technology can bring to a wide range of industries and non-commercial sectors; (2) introduction of relatively low-cost systems, and user-friendly controls, as well as general technological advancements and miniaturization of individual components and; (3) the introduction of pragmatic and business-friendly UAS legislation.

According to the Association of Unmanned Vehicle System International (AUVSI), the integration of UASs into the United States national airspace in the decade 2015–2025 is expected to create more than 100,000 jobs and generate an economic impact of $82 billion (Jenkins & Vasigh, 2013).

As a new method of geo-data collection, UASs complement existing techniques, filling the gap between large area imaging (satellites and manned aircrafts) and smaller coverage, time-consuming, but highly accurate terrestrial techniques (Pádua, Vanko, et al., 2017). Compared to high altitude data, UAS data is fairly low cost, with the advantage of allowing frequent and flexible flights (Alessandro Matese et al., 2015). UASs are thus very useful when small and medium-sized land parcels need to be frequently surveyed, allowing a rapid response option for time-sensitive deliverables, disaster situations, or search and rescue operations.

Moreover, the use of UAS brings the benefit of performing inventory analysis based on the collection and archive of aerial imagery, allowing temporal comparison. Recently, multi-temporal analysis has been explored by several authors (Atzberger, 2013; Mirijovský & Langhammer, 2015; Tanteri et al., 2017). In contrast, traditional aerial methods of data acquisition (e.g., satellites and manned aircrafts) may be limited for this type of analysis, due to the high cost involved in obtaining repeated imagery (Jomaa et al., 2008).

Given their very specific characteristics, UASs have been progressively used in several research applications, covering a growing diversity of fields that range from public safety (Niethammer et al., 2012) and infrastructures inspections (Cho et al., 2015), to environmental conservation/preservation (Dooly et al., 2016; Funaki et al., 2014; I. L. Turner et al., 2016), agriculture (Candiago et al., 2015), and forestry (Lisein et al., 2013). It is precisely in the latter for which the greatest economic impacts are expected to occur in the next decade (Jenkins & Vasigh, 2013). A detailed review of the different types of UASs and applications can be found in the work developed by Colomina and Molina (2014).

Considering the mentioned applications there are two fields of particular interest: (1) forestry preservation/conservation; and (2) coastal monitoring for prevention purposes. Regarding the former, diseases and pests cause tremendous economic losses and drastically reduce the quality of many cultivated crops, as well as wild vegetation species, which is of economic relevance for respective exploring communities. Therefore, early detection and assessment of crop symptoms and damage are crucial for plant health (Jia et al., 2016). When in presence of biotic stress, the disease's damage mechanism influences the plants' physiological response, which manifests through certain symptoms (e.g., wilting, stunted growth, reduction in leaf/canopy area, chlorosis or necrosis in some parts, leaf curling), creating some difficulties when trying to obtain an accurate quantification of the affected plants, usually by direct observation in the field. Remote sensing platforms such as the UAS can provide an alternative and cost-effective method, allowing the application of non-destructive and non-invasive methods to obtain accurate spatial data for entire crop fields at frequent intervals (Prabhakar et al., 2012). In the same way, this technology can aid in the prediction and prevention of occurrences related to coastal environments wherein the water progress—for example, caused by coastal perimeter degradation (I. L. Turner et al., 2016), may cause serious problems for local businesses and dwellers as well.

In this paper, two case studies based on the analysis of multi-temporal data acquired using UASs are presented. The first study concerns the monitoring of the health status of chestnut trees in Portugal, particularly in the Padrela region (the north-eastern part of the country). This region generates the highest production of chestnuts in the country (Instituto Nacional de Estatística, I. P., 2016), representing the greatest source of income for the entire region. The second case study is associated to one of the main challenges for the next years: the identification of ways to reduce/reverse the effects of climate change, which are causing alterations to natural resources and ecosystem dynamics. The coastal zones are some of the most affected areas, making sand dune protection an important issue due to their role in coastal defense. In fact, sand dunes play a crucial role in fauna and flora protection and provide sediment supplies to maintain the beaches that, in turn, are responsible for the protection of coastal agriculture systems and inland areas from storms and the rise in sea level (Chen et al., 2004; Mancini et al., 2013). Therefore, the second study presented in this paper focuses on the application of UAS multi-temporal data for monitoring the erosion occurring in coastal zones, particularly in the Cabedelo area where one of the most important and sensitive natural areas of Portugal is located: the Cabedelo sandspit, located in the Douro River estuary (Porto, Portugal). This natural structure is responsible for the preservation of ecosystems and for the protection of the sand area. Thus, these dunes are crucial for preserving the dwellings situated on the coastline as well as those of the local population. In each one of the referred case studies, flights were carried out at different times under similar conditions—light, temperature, etc. to ensure radiometric and geometric consistency.

This paper's main objectives are: (1) to identify the advantages and challenges associated with the use of a reliable, robust and cost-effective solution-using UAS to acquire aerial imagery data in forestry and coastal monitoring contexts; and (2) to demonstrate this remote sensing platform flexibility to cover such distinct environments. Moreover, the benefits of multi-temporal analysis in change detection will also be explored. Five sections comprise this paper: after this introduction, Section 3.2 presents a background on UASs including historical context, supported sensors, achievable products, and several applications towards environmental monitoring. In Section 3.3, the investigation methodology addressing data collection and processing is presented. Case studies are described in Section 3.4. The paper finishes with conclusions and future perspectives in Section 3.5.

## 3.2. Background

In the last 60 years, with developments in electronics, computing, and remote sensing, technological has advanced and platforms suitable for aerial data acquisition have been produced. With respect to this topic, satellites have been the most used system over the past 30 years (Pettorelli et al., 2014). However, its use can represent a high cost when studying small or medium-sized areas (Alessandro Matese et al., 2015), which occurs in many remote sensing applications in the scope of forestry and coastal environments. Ponti (2013) suggests the adoption of an alternative technology, such as UASs. This technology presents itself as a viable alternative to satellites (Zhang & Kovacs, 2012), mostly because of: (1) the higher temporal (up to daily) data acquisition and the higher spatial (up to millimetric) resolution of acquired imagery it typically offers (Lisein et al., 2013; Whitehead & Hugenholtz, 2014); (2) its ease in terms of scheduling and programming image acquisition operations; (3) its flexibility to operate in different environments (often with difficult access); and (4) its versatility, since surveys can be conducted in different contexts and extensions/heights.

Sensors coupled to unmanned aerial vehicles (UAVs) represent the most important system part, as it is through them that data will be acquired and, therefore, valuable data products will be generated(e.g., orthomosaics, DSMs, 3D point clouds, vegetation indices) (Fraser et al., 2016; Gevaert et al., 2017; Suomalainen et al., 2014; Xie et al., 2008). Sensors are classified as active or passive and a large variety can be found. Regarding passive sensors, they are used for detecting natural emissions from both the atmosphere and the Earth's surface (e.g., red-green-blue (RGB), near-infrared (NIR), and thermal emissions), while active sensors transmit their own radiation pulses through their energy sources (e.g., light detection and ranging—LIDAR, radio detection and ranging—RADAR) (Pádua, Vanko, et al., 2017).

The interest in the UAS as a form of remote sensing technology has grown because it allows user-controlled image acquisition and fills the gap—both in scale and resolution—between terrestrial observations and conventional manned aircrafts and satellite sensors. It is a cost-effective solution and enables adapting acquired imagery of the observed objects' real dimensions to the monitored processes and to alteration speed within a given landscape(Laliberte et al., 2011). When compared with traditional remote sensing platforms for imagery acquisition, UASs are considered both more effective and accurate when used in areas up to 10 km$^2$ (Puliti et al., 2015).

Despite the many advantages of remote sensing technologies, it is necessary to consider that there are some factors that may limit their performance, such as (Garcia-Torres et al., 2014): frame mosaicking, band-to-band registration, natural dynamics (such as atmospheric conditions), the Sun's angle, and technical problems (like viewing angle definition or changes in sensor calibration over time). However, if the best usage/operation practices are ensured at the pre-processing stage and during image acquisition, such limitations can be mitigated. In what concerns geographic data acquisition, UAS application is of superlative importance when addressing areas where access is difficult or dangerous by conventional means. UASs can be used for several purposes, such as (Jha, 2016; Watts et al., 2012): spotting, tracking, and fighting fires; support in natural disaster scenarios, timely distribution of medication and aid; air quality monitoring; wildlife surveys (e.g., survey migration flows); crime fighting, surveillance tasks and other protection-related activities; delivering products; monitoring natural phenomena so that preventive actions can be taken; 3D mapping; and search and rescue actions. However, it is worth noting that when measuring and mapping activities are performed, it is imperative to geocode and geometrically correct the acquired images (Aber et al., 2010).

The number of scientifically published case studies involving UAVs as remote sensing platforms is growing, making the application of UASs an interesting subject, especially in the environmental field for tasks such as: weed control monitoring (Gutiérrez et al., 2008); crop pest management (Y. Lan et al., 2009); Artic sea ice and atmosphere monitoring (Fladeland et al., 2011); soil properties monitoring (Oleire-Oltmanns et al., 2012); vineyard vigor mapping (Jacopo Primicerio et al., 2012); water monitoring (Gonzalez-Dugo et al., 2013); habitat mapping (Tamminga et al., 2015); and landslide dynamics (Darren Turner et al., 2015). The diversity of these contributions clearly shows the increasing importance of UASs for remote environmental monitoring.

In addition to these scientific contributions, those which involve protection and preservation of ecosystems' dynamics in coastal zones and vegetation monitoring are considered especially relevant to this paper. During the last years, coastal zones have suffered significant erosion, primarily due to the rising sea action, wind, and storms, mostly triggered by climate change. As such, beaches have experienced rapid morphological changes, which means that it is even more important to preserve natural barriers such as sand dunes (Gonçalves et al., 2011). Topographical changes in beaches and natural barriers need to be monitored and assessed on a regular basis to build models and to simulate scenarios that can help in predicting these natural environments evolution. Nowadays, UASs represent a valuable tool to provide data to compute scenarios and monitor events (Gonçalves & Henriques, 2015). For instance, UASs were applied for quantifying the coastal impact before and after a storm, allowing for the monitoring of the evolution of a rubble-mound breakwater on the mid-New South Wales Australian coast and mapping of the vegetation in a coastal estuary entrance (Drummond et al., 2015). Messinger and Silman (2016) investigated the suitability and application of UASs in environmental emergency response, in the case of coal ash spills. In Portugal, this kind of technology was used for surveillance and control of maritime traffic, fishing surveillance, and the detection/control of coastal hazards (E. Pereira et al., 2009). Hodgson et al. (2013) investigated the conservation and management of marine fauna through the application of UAS, to monitor mammal species population status. Rhee et al. (2017) applied this remote sensing technology on fluvial waters, with the objective of monitoring riparian vegetation, hazardous aquatic algae blooms and submerged morphology, and water-surface slope, among other phenomena.

Regarding vegetation monitoring, protecting and increasing food and water supplies for a global population that is growing quickly and in an exponential manner must be a priority (Abdullahi et al., 2015). Indeed, crop management becomes a critical factor to maximize yield while reducing and environmental risks and impacts where UAS platforms have been playing an important role in this context. Some of applications include tree canopy health mapping in a macadamia orchard for plantation management purposes (Felderhof & Gillieson, 2012), early site-specific weed detection in wheat fields (D. Gómez-Candón et al., 2013), automated crop lodging detection in maize (Chu et al., 2017), and vegetation filtering for river riparian zones (Wei et al., 2017).

UAS flexibility increases its applicability for surveying of the same area over time, especially in very dynamic environments requiring close monitoring, which is not possible—at least, in a cost-effective manner—by means of other remote sensing platforms. This approach has already been applied in some studies, where this remote sensing technology has been used to acquire multi-temporal data with different purposes, in several types of agricultural crops, such as barley (Bendig et al., 2013), sunflowers (Vega et al., 2015), silage maize (Castaldi et al., 2017), rice (Willkomm et al., 2016), wheat (Du & Noguchi, 2017; Holman et al., 2016), and vineyards (Ballesteros et al., 2015). In the aforementioned studies, multi-temporal imagery acquisition gave results that, in some cases, were noticeable only after a certain vegetative cycle stage of the studied crops. Moreover, this approach was already employed in coastal environments (Long et al., 2016), assessment of landslides displacements (Lucieer et al., 2014), and in monitoring of forest growth and biomass estimation (Guerra-Hernández et al., 2017).

Thus, applying UASs can be advantageous for monitoring certain areas, since it allows to assess them and to identify potential problematic zones, and/or to evaluate implemented mitigation/prevention measures in an effective way. The next section will address the methodology used in the two case studies presented in Section 3.4, which benefit from the usage of multi-temporal UAS-based imagery.

# 3.3. Methodology

This section describes the methodology used in the presented case studies. The applied methodology was similar for both studies and consists essentially of two phases: (1) field work-data collection by acquiring high-resolution images using UASs and, when necessary, some ground control points (GCPs); and (2) data processing-manipulation and analysis of the collected data (through specific software) to produce valuable and meaningful information. Since atmospheric influence is of minor impact while using UASs for land surveying (Pádua, Vanko, et al., 2017) and also because conditions—e.g., light and temperature—were consistently ensured between flights, radiometric corrections were considered negligible for both addressed case studies (monitoring of Padrela's chestnut trees and Cabedelo's sandspit) and, thus, they were not performed. These stages are further described in the following subsections.

## 3.3.1. Data collection

The selection of a UAV for data acquisition is influenced by the specificities of each case study. In that selection, some characteristics have to be considered: ground sample distance (GSD); minimum coverage; ability to be deployed in rugged terrain, ability to operate from unprepared surfaces and in constrained conditions; autonomy of at least 30 min; being easy to carry over long distances; ease of simple field maintenance and reparability; reduced environmental emissions and noise signature; and reliable and low cost. The UAVs used in the case studies presented in this paper are described in Section 3.4. All flights were conducted in parallel rows with the minimum longitudinal overlap of 75% and lateral overlap of 60% (Long et al., 2016). The flights were planned by using specific software, wherein the user defines the area of interest, flight direction, longitudinal and lateral overlapping, and pixel-size on the ground (GSD) (Figure 3.1).

The imagery used in this study was collected using the Canon IXUS 127 HS camera (16 mega-pixels) and the Canon PowerShot ELPH 110 HS camera (12 mega-pixels). The former provided the possibility of collecting images in the visible part of the electromagnetic spectrum, i.e., red-green-blue (RGB) bands, while the latter allowed the collection of imagery in RedEdge (RE), green and blue bands. RE is the spectral region where the plant's reflectance changes from low to high (from 680 nm to 730 nm) while RGB acquires data in the visible spectrum (from 380 nm to 700 nm).

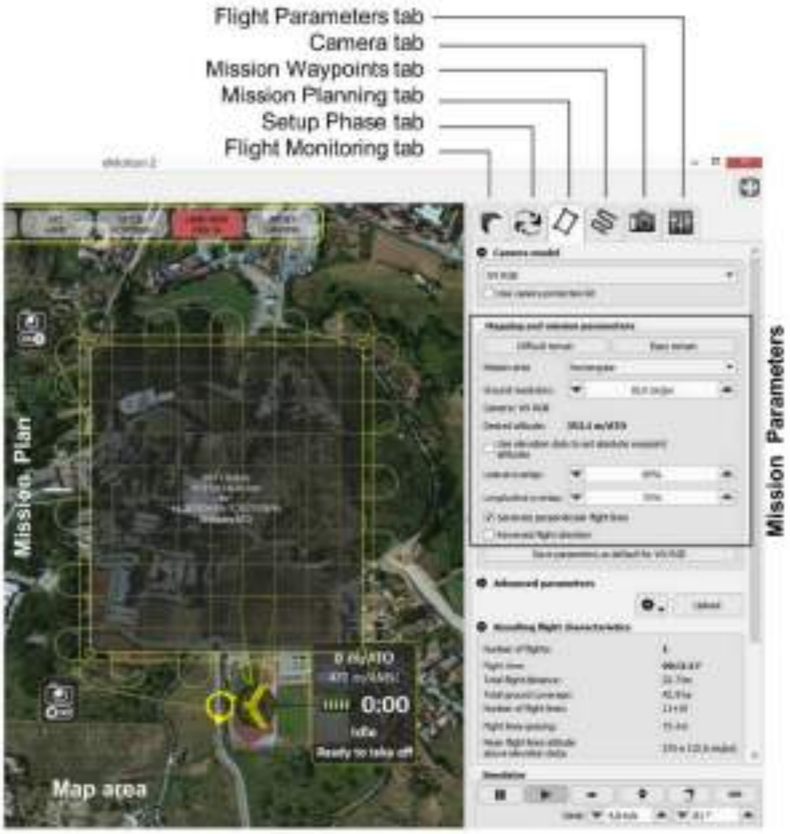


**Figure 3.1.** Planning a mission using eMotion software (senseFly SA, Lausanne, Switzerland) adjusting all the required parameters (e.g., lateral and longitudinal overlap, ground resolution).

The used UAVs' navigation system includes a global navigation satellite system (GNSS) receiver, with a positional accuracy of a few meters. The direct georeferencing achieved by this equipment does not follow the image's pixel resolution, enabling only an approximate location. Therefore, it is necessary to refine the external orientation through the support of tie points included in the automatic aerial triangulation processes. Ideally, these points must be uniformly distributed throughout the surveyed area, because parts that are not properly covered by GCPs are prone to more significant errors (Jianghao Wang et al., 2012), since the determination of an image's exterior orientation will mainly rely on conjugate points between overlapping images. In general, UAV cameras are non-metric (including moving parts), and usually require a self-calibration in the bundle adjustment (Fryskowska et al., 2016). Correlation between exterior and interior orientation parameters (e.g., flying height and focal distance) may lead to model deformations (James & Robson, 2014), which in some cases may not be obviously detected. Not only should there be good GCPs, but independent checkpoints should also be used to verify the quality of the extracted DSM (Martha et al., 2010). If camera pre-calibration (interior orientation parameters) is available, it should be used.

In an urban environment, especially when road markings are present, it is relatively easy to find well-defined points that can be used as GCPs. However, in the case studies presented in this paper, it was not always possible to apply this method. As such, the option was to use panels (approximately with 1 $m^2$ area) with centre-marked crosses, placed before the flight at selected locations and fixed with metal studs. Figure 3.2 provides an example of a target in use, observed from two perspectives: one on the ground (Figure 3.2a) being surveyed by GNSS, and another presenting an UAV aerial image result (Figure 3.2b).

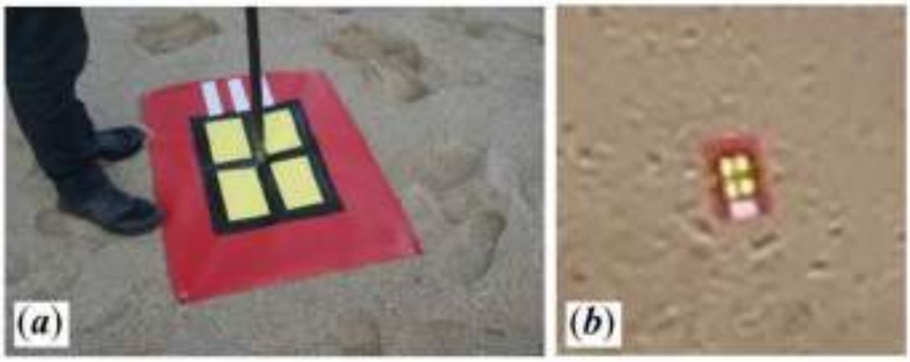


**Figure 3.2.** Example of an artificial ground control point (GCP) measuring 100 × 65 cm: in (a) the ground being surveyed with a global navigation satellite system (GNSS) device placed in the middle of the marker, and in (b) an aerial image taken using an unmanned aerial system (UAS) flying at 175 m.

### 3.3.2. Data processing

Each performed flight generates large amounts of data that need to be contextualized, filtered, and analysed in post-flight operations in order to extract information that will support the creation of knowledge for decision-making processes within forestry/agriculture (e.g., disease treatment) and preservation (e.g., natural protection) contexts.

Specific software for photogrammetric processing is required to extract information from the collected data. This type of processing usually considers the following steps. Firstly, the images are imported and the approximate internal and external orientation parameters (position-based only) provided by the navigation system are identified. Secondly, conjugate points and relative orientation blocks are generated, resulting in a 3D sparse point cloud with the approximate georeferenced location calculated from the projection centres' positions. Points with obvious errors can be eliminated from this 3D sparse point cloud and therefore from the conjugate points list. Thirdly, there is GCP insertion and refinement of the external orientation with self-calibration. Adjustments in focal length (in the principal point position), polynomial coefficients of the radial distortion (K1, K2, K3) and tangential deformation coefficients should also be considered. Moreover, other correction parameters are not especially relevant for cameras with relatively small deformations and they can increase the risks of introducing new ones due to correlations with the external orientation parameters. Fourthly, there is the generation of a dense point cloud, obtaining a dense surface model in a grid. Finally, there is orthorectification ("true ortho" to be used in the DSM) and final mosaic creation.

## 3.4. Case studies

The case studies presented in this paper consist of applying UASs in distinct fields—forestry and coastal environments—that have particular relevance in the development of socio-economic activities and in environmental sustainability. Regarding forestry, the selected UAS was applied to monitor chestnut tree health. Indeed, chestnut fruit is the main income source of the "Castanha da Padrela" region (Portugal). As for conservation and preservation, the selected UAS was applied to monitor and assess topographic changes that occurred in the Cabedelo sandspit, one of the most important and sensitive natural areas in Cabedelo (Porto, Portugal).

### 3.4.1. Chestnut health monitoring

Since the mid-1980s and mainly due to the increase in its economic importance, the area of chestnut (*Castanea sativa* Mill.) cultivation has been growing in Portugal. Currently, chestnut trees occupy around 36,000 hectares, of which 88% is located in northern Portugal (Instituto Nacional de Estatística, I. P., 2016). The growing area of cultivation is clear in the "Castanha da Padrela" region (the north-eastern part of Portugal), where this case study took place. In this region, chestnut fruit is the main source of income for the local population (Instituto Nacional de Estatística, I. P., 2016). However, agricultural practice intensification has favoured the onset of phytosanitary problems, such as ink disease and chestnut blight. Both are considered as the main causes of chestnut tree decline (Gomes-Laranjo et al., 2012).

Chestnut ink disease, caused by the soil-borne *Phytophthora cinnamomi* Rands (Santos et al., 2015) dates back to the end of the 19th century and, since then, it has been recurrently causing chestnut tree death to the present day. With respect to chestnut blight (*Cryphonectria parasitica* (Murr.) Barr.) (Robin et al., 2010), two decades after its first detection in Portugal, hypovirulence began to be observed in some locations. Many of the sub-populations of *C. parasitica* belong to the well characterized and specific vegetative compatibility type EU–11—in spite of having a spectral response that can be similar to other chestnut disorders caused by, for example, abiotic factors, inadequate pruning practice, or insect defoliation—that appears only in some orchards in Italy (Ambrosini et al., 1997). Successful treatment depends on the way the fungus population propagates in the area of interest. In 2014 the oriental chestnut gall wasp was detected for the first time in Portugal, near Barcelos (Braga, Portugal). Scientifically known as *Dryocosmus kuriphilus Yasumatsu* (Hymenoptera: *Cynipidae*), it is considered the world's worst pest for chestnuts, and has become a serious concern for chestnut culture in Portugal due to the potential losses to fruit and timber production (DRAPN, 2014). In three years, has rapidly spread to the most significant chestnut production areas. Many of Europe's southern and western countries have been reporting this phytosanitary issue after its accidental introduction into Piemonte (north-western Italy), where it was found for the first time in 2002 (Sartor et al., 2015).

Remote sensing techniques, such as conventional aerial photography or satellite images, are usually applied for evolution monitoring purposes. However, acquiring those images is costly, especially when the areas to be evaluated are small or there is a need to make several campaigns in relatively short periods of time (Mozas-Calvache et al., 2012).

In this case study, a UAS approach composed of a fixed-wing UAV (senseFly SA, Lausanne, Switzerland) was used to acquire high-resolution aerial data. This type of UAV enables the acquisition of various samples over a significant geographic area (up to 10 km2) in a short amount of time, especially due to the developments in sensors and their spectral and spatial resolutions (Xiang & Tian, 2011). As an example, and when addressing the vegetation monitoring field, this kind of aerial image has been used mainly due to its advantages when compared with ground observations. Temporal and spatial high resolutions, combined with the low complexity and operation costs, make all the difference (Laliberte et al., 2010).

The case study area (438 ha) is located between the villages of "São João da Corveira" and "Padrela e Tazém", in Valpaços (in the north-eastern region of Portugal). For monitoring the chestnut area and recognizing the most disease-affected areas, aero photogrammetric flights were made in three campaigns in 2014, 2015, and 2017 at an average flight altitude of 550 m (GSD ~16 cm), along six flight lines, oriented in the north–south direction. Figure 3.3 shows the evolution of a small part of the case study area, over time. Later on, these aerial images—both in colour (RGB) and near-infrared (NIR)—were used to compare the evolution in consecutive campaigns. RGB images acquired in 2006 by the Portuguese Forest Authority for the National Forest Inventory, with one-meter GSD (ICNF, 2010), were also included in the case study in order to extend the analysed period of time. After the flights, image orthorectification and geocoding were performed based on natural GCPs directly identified in the images.

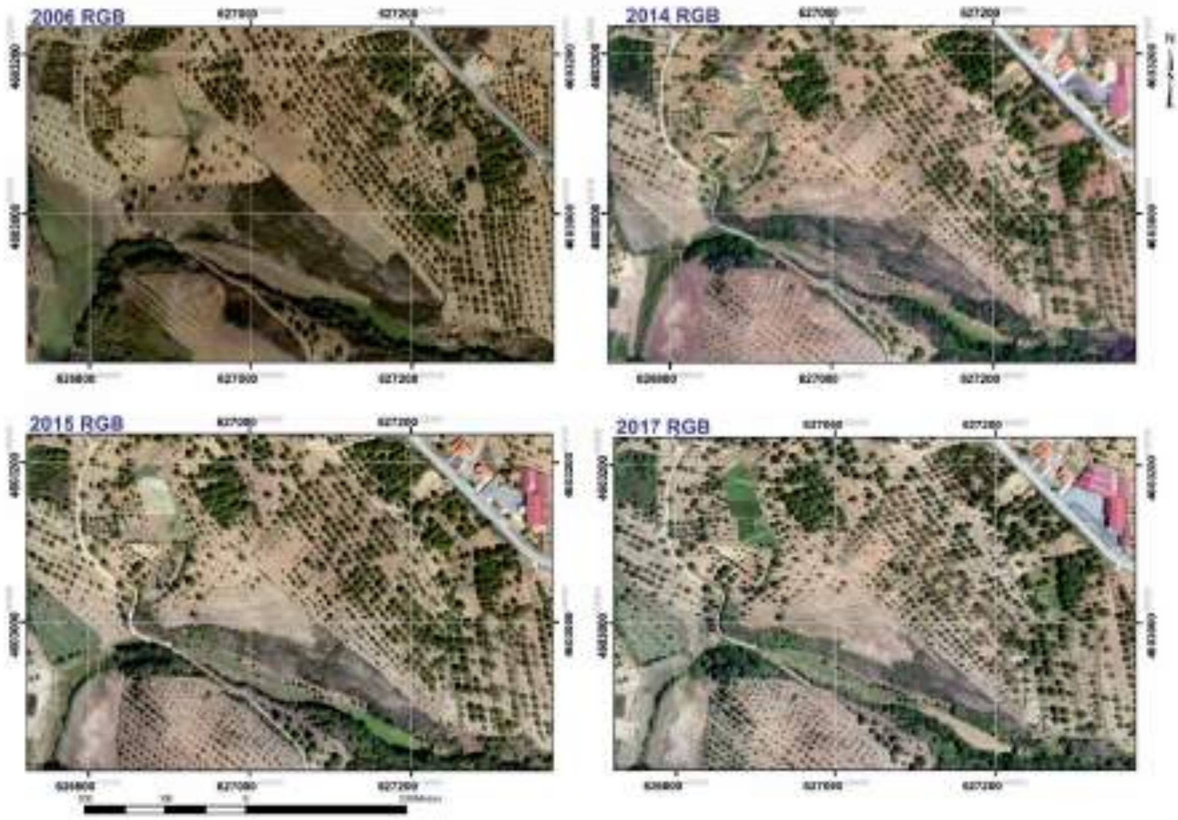


**Figure 3.3.** Temporal evolution of a portion of the study area in each campaign. RGB: red-green-blue.

#### 3.4.1.1. Considerations about surveys of chestnut trees

Photographic keys relating to chestnut trees with different physiological conditions were developed for photo interpretation purposes. Moreover, field data acquired during the campaigns were compared with the acquired aerial images (Figure 3.4), which in turn were processed using Pix4Dmapper software (Pix4D SA, Lausanne, Switzerland).

A geographic information system (GIS) was used for distributing 438 circular plots in the case study area (500 $m^2$ area, each), by using a systematic distribution of 100 × 100 $m^2$, corresponding to a 1-ha grid. Colour and NIR orthorectified aerial photographs obtained in the different campaigns were used in the GIS environment to determine differences in the chestnut canopy between three consecutive campaigns (2006–2014, 2014–2015 and 2015–2017). Canopy cover index (CI) (Equation (1)) considers the ratio between the area covered by the chestnut canopy and each plot's surface (500 $m^2$). This ratio represents ranges from 0 to 100. The same procedure was adopted in all campaigns.

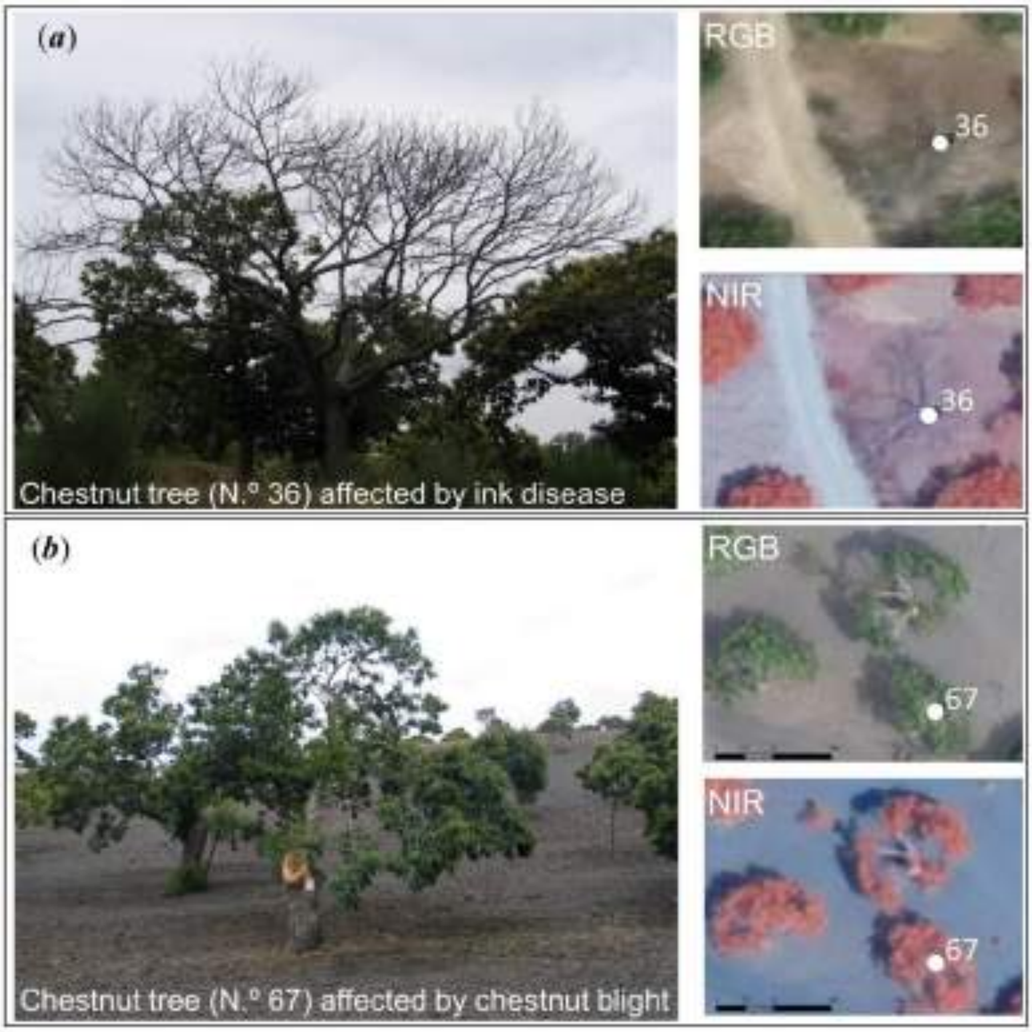


**Figure 3.4.** Chestnut trees affected by (a) ink disease and (b) chestnut blight. The same trees are represented in colour and infrared aerial photographs. NIR: near-infrared.

$$\mathrm{CI} = \frac{CA}{PA} \times 100 \quad (1)$$

In Equation (1), CA represents the plot's canopy area and PA the plot's area (500 $m^2$ in this specific case). To estimate health of the chestnut trees, as well as mortality and new plantation areas, a Student's t-distribution was used. A sampling error with a 95% confidence level was considered. To assess the geographical evolution of vitality, methods to estimate parameters based on attributes observed in neighbour points were used (Soares, 2000). These methods are used to explain the spatial structured phenomena (such as forest diseases) because they do not have a random distribution.

The existence of spatial correlation between georeferenced random variables correlation (that depends on the distance between points, which tends to decrease with distance), can be found using geostatistical methods (Sousa & Muge, 1990). These methods use specific observations for a single regionalized variable of interest, Z(xi), referred to a set of points (Dong et al., 2015) of the study area (univariate methods). Alternatively, auxiliary regionalized variables, whose values can contribute to the improvement of estimates of the main interest variable, can be used to provide the correlation rate.

The behaviour of regional variables in the interpolation, Z(xi), whose spatial continuity could be modelled by a semi variogram represented by Equation (2), was observed. The chestnut growth (CG) for each multi-temporal survey was used as the variable in the geostatistical approach. The model does not use negative or null values. In this sense, the CG was converted into a scale ranging from 1 to 20. The higher the value, the better the tree's health condition.

$$\mathrm{CI} = \frac{1}{2} \times E[Z(x_i + h) - Z(x_i)]^2 \tag{2}$$

The results obtained in two consecutive campaigns were used to evaluate the difference between CIs. For example, the results obtained by using the 2006 and 2014 campaign images were used to estimate CG during that period of time. The CG (Equation (3)) reflects the predictable growth (where CG > 0), but also the chestnut decline (if CG < 0). A 5% chestnut growth rate was admitted for the 8-year period. This is the predictable chestnut trees development considering the soil and climatic conditions of the case study area (Gomes-Laranjo et al., 2012). For the other two periods (2014–2015 and 2015–2017), a 0% minimum growth rate was considered (Gomes-Laranjo et al., 2012).

$$CG(14 - 06) \ = \ CI_{14} - CI_{06} \tag{3}$$

where: CG—Chestnut growth (%); $CI_{06}$—Canopy cover index in 2006; and $CI_{14}$ —Canopy cover index in 2014.

### 3.4.1.2. Results and discussion

Table 3.1 presents the CI results for all the campaigns, with different values for each one. Regarding the 2006–2014 period, CI has significant differences and an important decline can be noticed in 55% of the plots. As for the 2014–2015 period, the decline was even more pronounced, occurring in 60% of the chestnut plots. Between 2015 and 2017, the decline occurred in 35% of the chestnut plots. As it can be observed in Table 2, new plantations were made in forestry areas, abandoned areas, or in soils with less profitable cultures (cereals, pastures, potatoes, etc.). These practices positively influenced the results obtained in the latter analysed period (2015–2017). A significant contribution for this overall result was given by new plantations that increased the total chestnut area by 40%. The 247 ± 10 ha area in 2006 now measures 347 ± 14 ha (Table 3.2). For this reason, the decline can also be related to inadequate soils for such a demanding culture as *Castanea sativa* (Bounous & Conedera, 2014).

**Table 3.1.** CI and chestnut area for the period of the study (2006–2017). The sampling error is according to Student's t-distribution. The average values with (*) are significantly equal.

| Parameter/Year | 2006 | 2014 | 2015 | 2017 |
|---|---|---|---|---|
| **Canopy cover index (CI)** | 21.6 ± 2.5% (*) | 19.5 ± 1.8% | 22.2 ± 2.0% (*) | 25.9 ± 2.1% |
| **CI minimum** | 5 | 5 | 0 | 0 |
| **Canopy cover per hectare (CC/ha)** | 2160 ± 250 $m^2$ (*) | 1950 ± 180 $m^2$ | 2220 ± 200 $m^2$ (*) | 2590 ± 210 $m^2$ |
| **CI maximum** | 100 | 90 | 90 | 90 |
| **Sampling error (SE%) for CC** | 11.7% | 9.2% | 9.2% | 8.2% |
| **Total area (SE% = 4%)** | 438 ± 18 ha | 438 ± 18 ha | 438 ± 18 ha | 438 ± 18 ha |
| **Chestnut area (SE% = 4%)** | 247 ± 10 ha | 303 ± 12 ha | 295 ± 12 ha | 347 ± 14 ha |

**Table 3.2.** Chestnut area and chestnut decline affecting the whole study area (438 ha).

| | 2006 | 2014 | | 2015 | | 2017 | |
|---|---|---|---|---|---|---|---|
| Other cultures | 191 (44%) | 135 (31%) | | 143 (33%) | | 91 (21%) | |
| Chestnut area (ha) | **247** (56%) | **303** (69%) | | **295** (67%) | | **347** (79%) | |
| Chestnut decline | | | 135 (55%) | | 182 (60%) | | 104 (35%) |
| Chestnut growth | | | 112 (45%) | | 121 (40%) | | 191 (65%) |
| Chestnut area variation | | | [303–247] (18%) | | [295–303] (−3%) | | [347–295] (15%) |
| Total (ha) | **438** | **438** | **247** | **438** | **303** | **438** | **295** |

The geostatistical approach allowed for the detection of the three important affected areas (**Figure 3.5**). The decline in foci detected in the 2006–2014 period worsened in the 2014–2015 period. However, an improvement in the health condition of chestnut trees was observed in the 2015–2017 period. These results are in accordance with Table 3.2.

Moreover, these results also demonstrate that RGB and RE/NIR aerial imagery obtained by UAS is a cost-effective alternative to other remote sensing platforms, as they are reliable for monitoring chestnut tree health, allowing mapping affected areas quickly and accurately, namely in:

- detecting chestnut ink disease symptoms (L. Martins et al., 2007);
- monitoring tree canopy cover decline by means of multi-temporal analysis (assess chestnut blight presence);
- providing the means for evaluating gall wasp biological control strategy effectiveness.

Furthermore, this approach also demonstrated to be an effective tool for classifying soil occupation, detecting areas of interest for new cultures and evaluating new plantations.

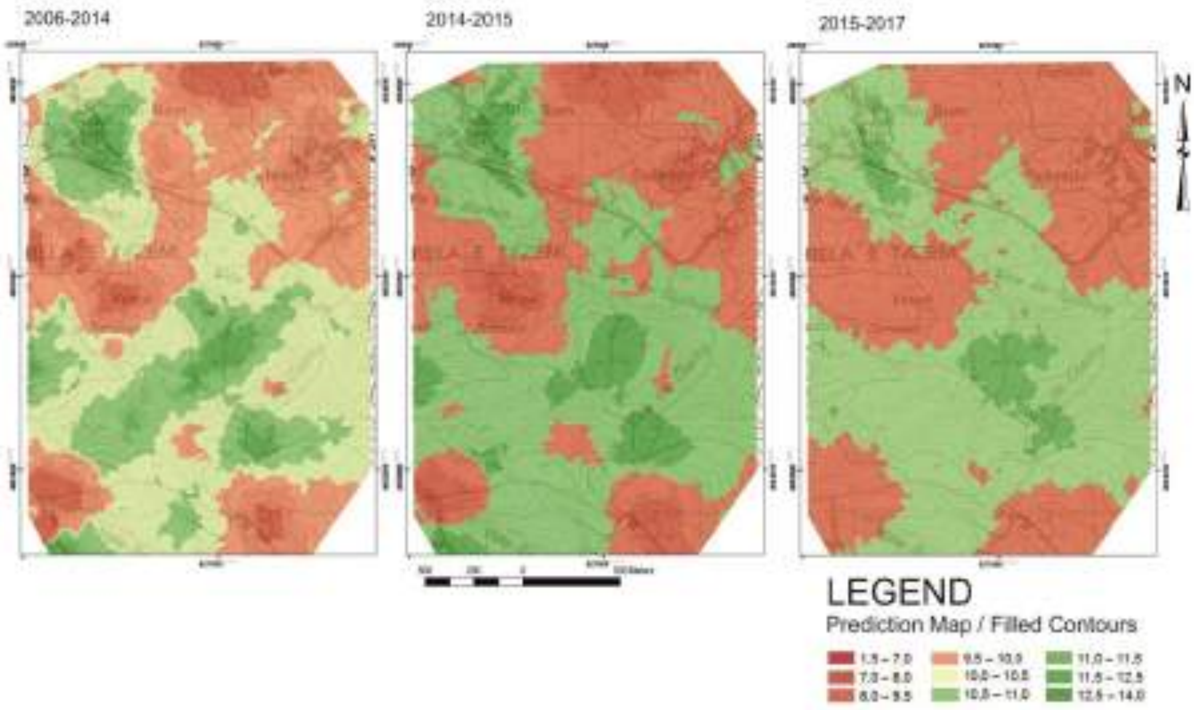


**Figure 3.5.** Chestnut growth (CG) and decline for the 2006–2014, 2014–2015, and 2015–2017 periods. CG was converted into a scale ranging from 1 to 20. The higher the value, the better the tree's health condition.

This study also confirmed interest in chestnut culture, as it showed the new plantations that increased the area of chestnut cultivation from 247 ha in 2006, to 347 ha in 2017 (a 40% greater chestnut area in the case study area in the referred time period). The last period studied (2015–2017) shows a positive value on CG. This growth is related to the new practices used for controlling biotic agents. In fact, the lower soil tillage to reduce chestnut ink disease and the application of hypovirulence strains to control chestnut blight may be directly responsible for this improvement (Gehring et al., 2015).

Lastly, using this approach (when compared with field observations) enables the recognition and quantification of the chestnut tree decline, disease dispersion and the respective most-affected areas. It was also possible to evaluate the decline of the chestnut tree at a substantially lower cost compared to other field surveys or manned aircraft-based images (L. Martins et al., 2001). In Portugal, chestnut is currently facing severe climatic conditions characterized by heat and drought stresses with important consequences for species' health. Thus, it is convenient to model yield forecast and species area redistribution according to climatic constraints.

Due to the similar aerial imagery behaviour presented by other species with high economic impact in Portugal (*Quercus suber* L. and *Olea europea* L.), the obtained results allowed us to conclude that it could be possible to adapt the present methodology to be applied in those species.

### 3.4.2. Cabedelo sandspit variation assessment

The Cabedelo sandspit is responsible for the preservation of ecosystems and for the protection of the sand area. Its dunes are crucial for preserving the dwellings situated on the coastline and those of the local population, as it prevents the Douro River banks being reached by waves. Moreover, there are financial interests in terms local business activities being run in the Douro River estuary navigation channel, and these are highly dependent upon the sandspit conservation (Teodoro et al., 2014).

At present, the Cabedelo sandspit has an approximate size of 800 × 400 m and is well known for its frequent changes in position and shape. Before the construction of a detached jetty, the sandspit morpho dynamics were related to extreme river flow, sea turbulence, and wind. After the construction, the sandspit shape was stabilized and an increase in its area and volume was observed as well (Bio et al., 2015). Figure 3.6 shows orthoimages of different periods that show the large variations in shape and location, as well as the stabilization that occurred after 2006. Through Figure 3.6 it is possible to obtain a multi-temporal view of the morphological dynamics of the case study area.


**Figure 3.6.** Orthoimages of the sandspit in five different periods (images provided by aerial national mapping agency aerial photography archives).

A monitoring program has been developed by the University of Porto, based on GNSS land surveys as well as photogrammetric surveys, using the digital camera ZI–DMC–I (Bio et al., 2015; Gonçalves et al., 2011). Some conventional aerial photography campaigns were carried out, covering a coastline extension of 15 km. Aerial photography would not be affordable just for the Cabedelo sandspit monitoring. The best solution for fast, frequent, and cost-effective monitoring surveys of this area is the use of a UAS. The first survey was carried out in 2013.

In the next few subsections the changes that occurred between the three multi-temporal series are analysed and quantified. Several aspects related to the accuracy of the extracted DSM are also analysed as they may strongly affect the alteration assessment. Although GCPs were not exactly the same in number, eight of them were placed at the same location in all flights, using a global positioning system (GPS) navigation device. Their location was rigorously surveyed using differential GPS, in real-time kinematic (RTK) mode.

### 3.4.2.1. Considerations about surveys in sand areas

The main purpose of UAS surveys in coastal areas is to assess topographic changes in sand volume. For this reason, geometrical accuracy of the resulting surface models and orthoimages are fundamental for the analysis. Sandy areas pose several challenges that must be carefully analysed First, there is the need for accurate GCPs, which must be well defined on both the ground and on the images. Unlike in built-up areas, the natural environments of coastal areas do not provide such points, so artificial marks must be previously placed on the ground (Section 3.3.1).

For this case study, vertical checkpoints are most important since they allow for control of sand volume variation. These are relatively simple to acquire, since surveys of RTK GNSS can be very fast and points do not need to be marked. For a vertical checkpoint of coordinates (E, N, h), residuals (Δh) are calculated by subtracting the height measured by GNSS (hGNSS) and the height interpolated from the DSM, on coordinates (E, N), using bi-linear interpolation (hDSM) (Equation (4)). The overall accuracy is given by the root-mean-square error (RMSE), for n observed checkpoints, as in Equation (5). The mean and the standard deviation can also be determined to assess if some systematic trend may exist in the data.

$$\triangle h_i = h_{i,GNSS} - h_{DSM}(E_i, N_i), i = 1, \ldots, n \tag{4}$$

$$RMS_h \sqrt{\frac{\sum_{i=1}^{n} \triangle h_i^2}{n}} \tag{5}$$

Beside these challenges, others that are typical of sandy areas must be considered to obtain success in applying UAS in this kind of environment. These challenges include, for example, the lack of patterns that sand may have, reducing the quality of the conjugate points obtained by stereo matching. This is especially the case when the sun is high, which may result in too-bright images. It is preferable to perform surveys on cloudy days or in the early morning, when the sun is low (Dandois et al., 2015). Another difficulty, which is combined with sun illumination and the tide, is the requirement of relatively low wind. This is not the regular situation in the Portuguese coastal zone (Troen & Lundtang Petersen, 1989), which makes the availability of adequate moments for the surveys relatively difficult. In this case study, there was also the need to combine the flight time with a low tide. The first flight made in 2013 was performed in the early morning of a cloudy day. In fact, it gave the best vertical accuracy.

Finally, it was possible to verify that waves also pose some difficulties. Although low tides were chosen, with instantaneous sea level height at −1m or below, waves may be present in heights of up to 1 or even 2 m. The extracted DSM has very poor quality in these areas. For that reason, contour comparisons between different campaigns were made for an elevation of 2 m above the sea level.

#### 3.4.2.2. Results and discussion

The first survey was conducted in 2013 with a smaller resolution camera (when compared with the two more recent campaigns) coupled on senseFly Swinglet (senseFly SA, Lausanne, Switzerland) with a GSD of 4.5 cm. The other two surveys were performed in 2015 and 2017, using the UAV SenseFly eBee (senseFly SA, Lausanne, Switzerland) and a GSD of 5.2 cm. This latter GSD meant that for practical purposes the resolution was slightly decreased, while keeping the standards for the monitoring objectives.

The first campaign was performed for experimental reasons and included detailed quality control analysis, which is described in Gonçalves and Henriques (2015). The image orientation process by bundle adjustment was done in Agisoft Photoscan (Agisoft LLC, St. Petersburg, Russia) and provided residuals similar to the GSD, both in planimetry and altimetry. The main concern, especially because the models are intended to rigorously assess height changes, was with vertical accuracy. Although the bundle adjustment may be good in terms of the control points, in areas not so well covered by GCPs the model may have deformations, especially if many adjustment parameters are used. As referred to before, an independent verification with altimetric checkpoints is important to verify that deformations do not occur. Elevation checkpoints were obtained by differential GNSS at the same time as GCP collection, with care taken to choose places where sand had not been moved and without leaving the pole in the sand. At least 100 checkpoints—well distributed throughout the area—were to be acquired, per survey.

The second campaign—done in May 2015—was performed during the breeding season of some birds, such as sand plovers, which limited the access to some areas. Therefore, a smaller number of checkpoints were collected. However, the distribution was reasonably complete. Table 3.3 presents data from the three campaigns, namely their characteristics and the accuracy analysis results.

The vertical errors found on the independent check points (ICP) have positive and negative values, and approximately follow a Gaussian distribution with an average close to zero (Gonçalves & Henriques, 2015). This fact reveals that no systematic trends exist in the surface models. There is an error propagation to the calculated volumes but this is not as significant as if a systematic vertical trend were to exist on the surface.

**Table 3.3.** Cabedelo sandspit campaigns (2013, 2015, 2017) characteristics and analysis results. UAV: unmanned aerial vehicle; GSD: ground sample distance.

| Date and Start Time (h:min) | UAV/Camera Resolution | GSD | # Images Used | GCPs Total/3D RMS | ICPs Total/$RMS_h$ |
|---|---|---|---|---|---|
| 22 July 2013 07:22 | Swinglet/12 Mp | 4.5 cm | 308 | 11/12.8 cm | 114/4.6 cm |
| 06 May 2015 10:55 | eBee/16 Mp | 5.2 cm | 204 | 8/3.0 cm | 34/6.3 cm |
| 29 March 2017 11:15 | eBee/16 Mp | 5.2 cm | 196 | 9/4.2 cm | 146/7.1 cm |

DSMs were generated for the tree campaigns, which enabled the assessment of differences due to the sand movements. Figure 3.7a shows a colour-coded image of the 2017 campaign DSM. Figure 3.7b shows the hill shaded image of the DSM, together with the corresponding contours of height of 2 m. The 2-m contours of the 2013 and 2015 campaigns DSMs are overlaid on top of the 2017 DSM, in different colours to perceive the sand accumulation, profiles were traced in the place of largest separation between the contours, along the steepest slope (A and B). These profiles are represented in Figure 3.8.

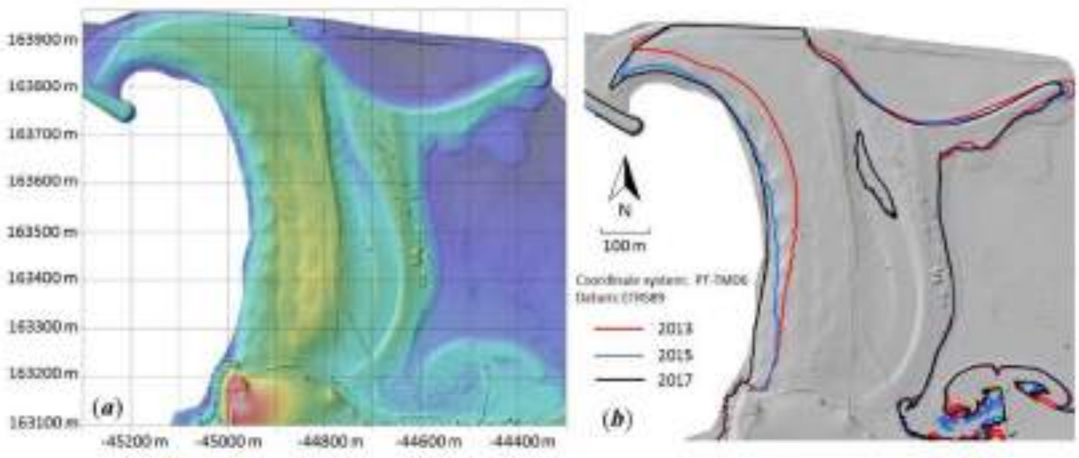


**Figure 3.7.** Differences in Cabedelo sandspit due to the sand movements: (a) colour coded DSM of 2017 and (b) hillshaded DSM with contours of the 2013 and 2015 DSMs overlaid.

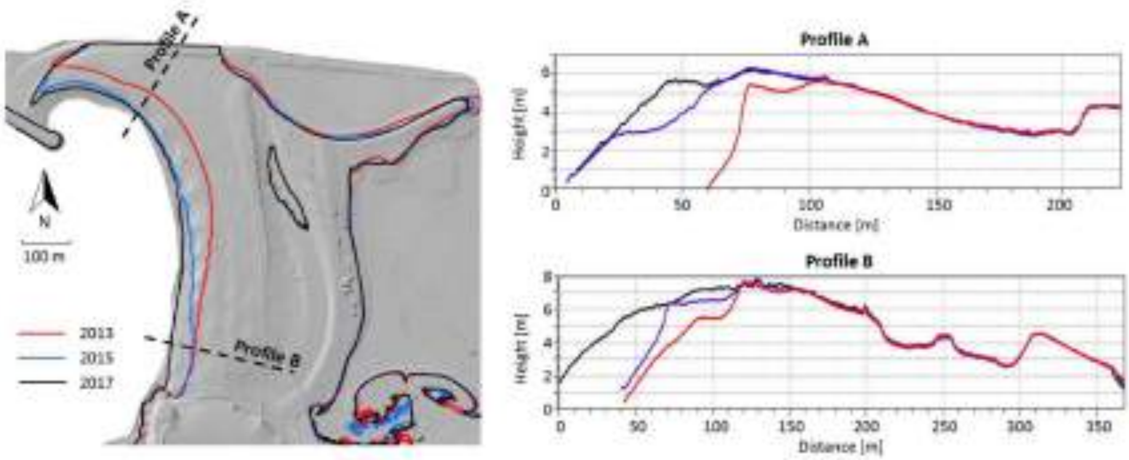


**Figure 3.8.** Profiles along the steepest slope, in the part of largest sand increase for the three epochs: red for 2013, blue for 2015, and black for 2017. Profile A had larger increase from 2013 to 2015, while in profile B the largest increase was from 2015 to 2017.

The main change occurred from 2013 to 2015, with a large accumulation of sand (around 60 m) in the northern and central parts of the sandspit, facing the sea. From 2015 to 2017 there was an accumulation in the southern part of around 40 m. The models were subtracted to calculate the volume difference between consecutive DSMs as the sum of vertical prisms. The largest volume calculated for the increased area facing the sea was of 170,000 cubic meters (volumes above height zero), between 2013 and 2015. The increase from 2015 and 2017 was of approximately 60,000 cubic meters. Sand accumulation that was observed with the DSMs acquired in the successive UAV flights is due to the detached breakwater built in the area. Its aim is to disperse wave energy and fix the sandspit to facilitate boat navigation in the Douro river mouth. As expected, there is an accumulation of sand in the sandspit (Teodoro et al., 2014). Its increase rate (that can be measured from the UAV data) can help in taking measures for the coastal engineering management of the area.

An additional remark on the profile analysis is the noise effect present on the DSMs. The first DSM (2013) was smoother than the other two, especially the one from 2017, which may be explained because it was done on a cloudy day. In the other two, especially that of 2017, there was sun and they were done in the middle of the morning: images were much brighter and with less contrast and patterns for the matching process. This is concordant with the lower vertical accuracy (ICP RMSh in Table 3.3). In any case, detection and quantification of the differences between the three DSMs was possible due to the sand deposition by the sea. This study confirms the feasibility of this methodology for change assessment in sandy beaches. Many studies recently published reveal that it is being regularly used to assess changes in critical areas. From the experience obtained with this study, which involved a relatively sparse dataset along the time with an average revisit period of two years, more frequent surveys would be needed to perceive the continuity of the change process. Some limitations were found due to environmental issues, such as the frequent strong winds in the Portuguese Atlantic coast. Another important constraint was due to logistic effects, because of the need for signalized ground control points. Although flight times were as short as 30 min, several hours were needed to place the signals, survey their coordinates with GNSS, and collect them back. This requirement makes surveys rather time consuming and not so simple to implement with higher frequencies.

A very important improvement can be achieved with UAVs equipped with precise GNSS equipment, working in RTK or post processing kinematic (PPK) mode. Surveys without ground control points, keeping a suitable accuracy (Rehak & Skaloud, 2015; I. L. Turner et al., 2016), can be conducted, allowing for much simpler logistics of data collection. With smaller requirements for field work, a more frequent observation would be possible, allowing not only for change assessment and quantification, but also for a better perception of periodical phenomena, with regular data collection before and after winter seasons.

## 3.5. Conclusions

This work presents two applications of unmanned aerial systems, one of the most recent remote sensing technologies. In the first case study, RGB and NIR high-resolution aerial images were used to monitor the evolution of a chestnut tree area over time. The feasibility of this approach was demonstrated by comparing the results with ground true data. A good agreement was found. Tree canopies, computed in both RGB and NIR high-resolution images, were also used to detect the coverage's evolution. In that way, it was possible to correlate that evolution (growth or decline) with biotic and abiotic factors. Thus, UAS-based methods allow us to detect and fight the major issues affecting chestnut trees.

The second case study presented in this work focuses on the monitoring of the Cabedelo sandspit. In sensitive ecosystems (like this one), the use of UAVs avoids having to walk the terrain, which usually leads to severe damage which, for instance, occurs with ground vehicle tracks. It was possible to detect a significant change between 2013 and 2015, with a large build-up of sand in the northern and central parts of the sandspit. In the study's most recent period (2015–2017), there was an accumulation in the southern part of the sandspit. Within the total period analysed, the sandspit's total volume increased by more than 200,000 cubic meters of sand.

The continuity of both studies will support better knowledge and understanding in assessing the effects of corrective measures that have been applied by chestnut tree producers in the last years, and a better understanding of the dynamics and coastal protection works performed in the Cabedelo sandspit study area.

The UAS may be considered a well-suited configurable tool which is fairly flexible for application in such distinct areas as forest and coastal environments. Moreover, they constitute a cost-effective and non-invasive form of technology capable of covering considerably-sized areas in a single flight, supporting different sensors within their payload. Currently, UASs continue to evolve, offering new opportunities and presenting new challenges.

## Acknowledgements

This work was financed by the European Regional Development Fund (ERDF) through the Operational Programme for Competitiveness and Internationalisation-COMPETE 2020 under the PORTUGAL 2020 Partnership Agreement, and through the Portuguese National Innovation Agency (ANI) as a part of project "PARRA-Plataforma integrAda de monitoRização e avaliação da doença da flavescência douRada na vinhA" (N° 3447), as well as the ERDF and North 2020-North Regional Operational Program, as part of the project "INNOVINE& WINE-Vineyard and Wine Innovation Platform" (NORTE-01-0145-FEDER-000038).

# Chapter 4.

## UAV-Based Automatic Detection and Monitoring of Chestnut Trees

*Remote Sensing*, 2019, *11*(7), 855

Journal Impact Factor – 2019: 4.509

5 Year Impact Factor – 2019: 5.001

Pedro Marques, **Luís Pádua**, Telmo Adão, Jonáš Hruška,
Emanuel Peres, António Sousa and Joaquim J. Sousa

Refer to https://doi.org/10.3390/rs11070855 for online published version

## 4.1. Introduction

In the early 1980′s, the European chestnut tree (*Castanea sativa*, Mill.) assumed an important role in the Portuguese economy (Luís Martins et al., 2015). However, phytosanitary problems, such as: the chestnut ink disease (*Phytophthora cinnamomi*) (Valverde et al., 2017; Vettraino et al., 2005) and the chestnut blight (*Cryphonectria parasitica*) (Rigling & Prospero, 2017; Valverde et al., 2017), along with other threats, e.g. chestnut gall wasp (*Dryocosmus kuriphilus*) (Battisti et al., 2014) and nutritional deficiencies (Portela et al., 2003), are responsible for a significant decline of chestnut trees, with a real impact on production (Luís Martins et al., 2014). Thus, to mitigate the associated risks, it is crucial to establish an effective monitoring process to ensure crop cultivation sustainability. Usually, chestnut trees health condition assessment relies on time-consuming and laborious in-field observation campaigns. Alternatively, the use of remote sensing platforms is becoming attractive in performing dull tasks that are related with land monitoring operations, in which vegetation monitoring can be included (Colomina & Molina, 2014).

Among the different available aerial remote sensing platforms, Unmanned Aerial Vehicles (UAVs) can provide high-resolution imagery, which is acquired using different sensors with a remarkable versatility, ease-of-use, and cost-effectiveness (Pádua, Vanko, et al., 2017). Data resulting from usage of Unmanned Aerial Systems (UAS, composed of UAV, sensor(s), and ground station), along with photogrammetric processing, enable reaching advanced data products, such as orthorectified mosaics (orthophoto mosaics), digital elevation models (DEM), three-dimensional (3D) point clouds, and vegetation indices (VI). Thus, vegetation monitoring is possible, since these types of outcomes enable vegetation detection and features extraction, such as tree height, canopy area and diameter, and individual tree counting. These features help to promote agriculture and forestry sustainability, in both single and multi-temporal perspectives (Pádua, Vanko, et al., 2017).

Järnstedt et al. (2012) used airborne laser scanning (ALS), RGB, and colour infrared (CIR) imagery, to generate 3D point clouds and high-resolution imagery from forests. In that way, it was possible to extract vegetation height and perform vegetation monitoring operations while using high-resolution imagery with cost-effectiveness in comparison to the LIDAR-based approaches. A comparison between point-clouds driven from imagery and ALS was carried out to evaluate different attributes in both models—e.g. tree crown diameter and height, basal area, and volume of growing stock. Zarco-Tejada et al. (2014) used a fixed-wing UAV that was equipped with RGB and NIR sensors to assess olive trees height with discontinuous canopy, through photogrammetric processing. The results highlighted that an approach based on consumer-grade cameras coupled in a hand-launched UAV provide similar accuracies to those of the more complex and costly LIDAR systems, which are commonly used in forestry and environmental applications. Mohan et al. (2017) evaluated the applicability of low-cost consumer grade sensors that were mounted in an UAV for automatic individual tree detection, using a local-maxima based algorithm on Canopy Height Models (CHMs) computed from UAV-based photogrammetric processing. In this way, the resulting model only contains height information from objects above ground.

Regarding the automated Individual Tree Crown Detection and Delineation (ITCD) task, while using remotely sensed data, it plays an increasingly significant role in the efficient, accurate, and complete forests monitoring process (Lindberg & Holmgren, 2017; Zhen et al., 2016). ITCD algorithms have advanced focusing in two main goals: the improvement of traditional algorithms to address specific issues and the development of novel algorithms that take advantage of active data sources or the integration of passive and active data sources. Wallace et al. (2014) used high-resolution LIDAR data acquired from UAS to determine the influence of detection algorithms and the point density on tree detection. The authors implemented five different detection routines to directly delineate trees from the point cloud, the determination of voxel space, and the computation of CHM. The method that used both the CHM and the original point cloud information achieved the best performance. Liu et al. (2015) developed a novel ITCD approach using airborne LIDAR data in natural forests using crown boundary refinement, based on the proposed Fishing Net Dragging (FiND) method and segment merging based on boundary classification. The authors used a machine learning method (random forest) to classify the boundaries between trees and between branches that belong to a single tree. There were some limitations in their approach, since FiND is based on watershed segmentation, and might not work well over areas where the valley shape between trees was not ‘V’ or ‘U’ shaped. Specifically, this limitation becomes serious in cases where a small tree is close to a neighbouring big tree, resulting in a possible merged tree crown. Eysn et al. (2015) benchmarked and investigated eight ALS-based methods for individual tree delineation. The authors claim that, in general, all of the methods achieved comparable results for the matching rates, but they differ in the extraction rates and omission/commission rates.

Ok and Ozdarici-Ok (2017) presented an approach to individually detect and delineate citrus trees based in Digital Surface Models (DSMs) that were computed from the photogrammetric processing of UAV-based imagery. The basis of their approach was the orientation-based radial symmetry transform that was designed for an input as a DSM. The approach was tested in eight different DSMs. However, this approach detects and delineates every circular object above-ground that reduces its precision performance.

Regarding the focus of this study, Martins et al. (2014) carried out a study addressing chestnut trees development, while using high-resolution aerial imagery. UAV-based data that was acquired in July of 2014, at the average height of 550 m (ground sample distance—GSD ~16 cm), was compared with the 2006 imagery, acquired by the Portuguese Forest Authority for the National Forest Inventory, with 1 m GSD. The analysis process used by Martins et al. (2014) was manually performed while using a visual sample-based approach in GIS software, which is a time-consuming procedure. The method that is proposed in this article consists of a fully automatic process to monitor chestnut plantations, allowing for overcoming the major drawbacks that are associated with manual-based methodologies. The area and the data presented in Martins et al. (2014) and Pádua et al. (2017) and representative ground-truth data validate the method. Algorithmic-driven tree identification and counting, individual extraction of tree height, tree crown diameter and area features are at the core of the proposed method, aiming to improve data handling, and processing time, thus ensuring effectiveness towards the outlined goal. Moreover, the proposed method also supports multi-temporal analysis for a decision support system that correlates with features extracted from aerial images of the same area, taken at different epochs.

## 4.2. Materials and Methods

### 4.2.1. Surveyed Area and Data Acquisition

The selection of an UAV for data acquisition is influenced by the specificities of each case study: the size of the area together with UAV's autonomy influence the ground sample distance (GSD), which may make obtaining an acceptable spatial resolution impossible—this considering, of course, the completion of a single flight. In this specific study, while considering the final purpose of the experiment and the UAV characteristics, a fixed-wing UAV, the senseFly's eBee (senseFly SA, Lausanne, Switzerland), was used to collect aerial imagery. The flights were conducted over a chestnut trees area (438 ha), located in the Padrela region

(Valpaços, Vila Real, Portugal: 41º33′51”N, 7º29′40”W), Trás-os-Montes region (Northeast of Portugal). This region concentrates the highest production of chestnuts in Portugal (Instituto Nacional de Estatística, I. P., 2017), representing one of the major agronomical sources of income of the region (Borges et al., 2008). Specific software was used to plan the flights, wherein the user defines the area of interest, flight direction, longitudinal and lateral overlapping, and GSD (Table 4.1). At each epoch, two flights respecting the same flight plan were carried out, each one with a different imagery sensor. A standard RGB sensor and a modified sensor were used to collect colour infrared (CIR) imagery in RedEdge (RE), green, and blue bands (Table 4.1). RE is the spectral region where plant's reflectance changes from low to high (from 680nm to 750nm). These data were acquired on 19 July 2014, 8 September 2015, and 10 July 2017. All of the flights were conducted close to the solar noon time, minimizing shadows, and the same flight plan was used at 550 m height (GSD ~16 cm). Figure 4.1a presents a general overview of the study area. For validation purposes, an extra flight was conducted in June 2017, using the multi-rotor UAV, DJI Phantom 4 (DJI, Shenzhen, China), in two smaller areas within the study area, as presented in Figure 4.1c, at 100 m height (GSD ~ 3 cm). Table 4.1 summarizes the main characteristics of the flight campaigns.

**Table 4.1.** Flight campaigns (2014, 2015, 2017) characteristics and analysis results. UAV: unmanned aerial vehicle; GSD: ground sample distance.

| Date | UAV | Sensor and Resolution | Overlap (%) (front/side) | GSD (cm) | # Images | Area Covered (ha) |
|---|---|---|---|---|---|---|
| 19 June 2014 | Sensefly eBee | RGB: Canon IXUS 12 7 HS (16.1 MP)<br>CIR: Canon PowerShot ELPH 110 HS (16.1 MP) | 75/60 | 16.21 | 85 RGB<br>85 CIR | 490 |
| 08 September 2015 | | | | 14.99 | 92 RGB<br>90 CIR | 436 |
| 10 July 2017 | | | | 16.2 | 86 RGB<br>84 CIR | 517 |

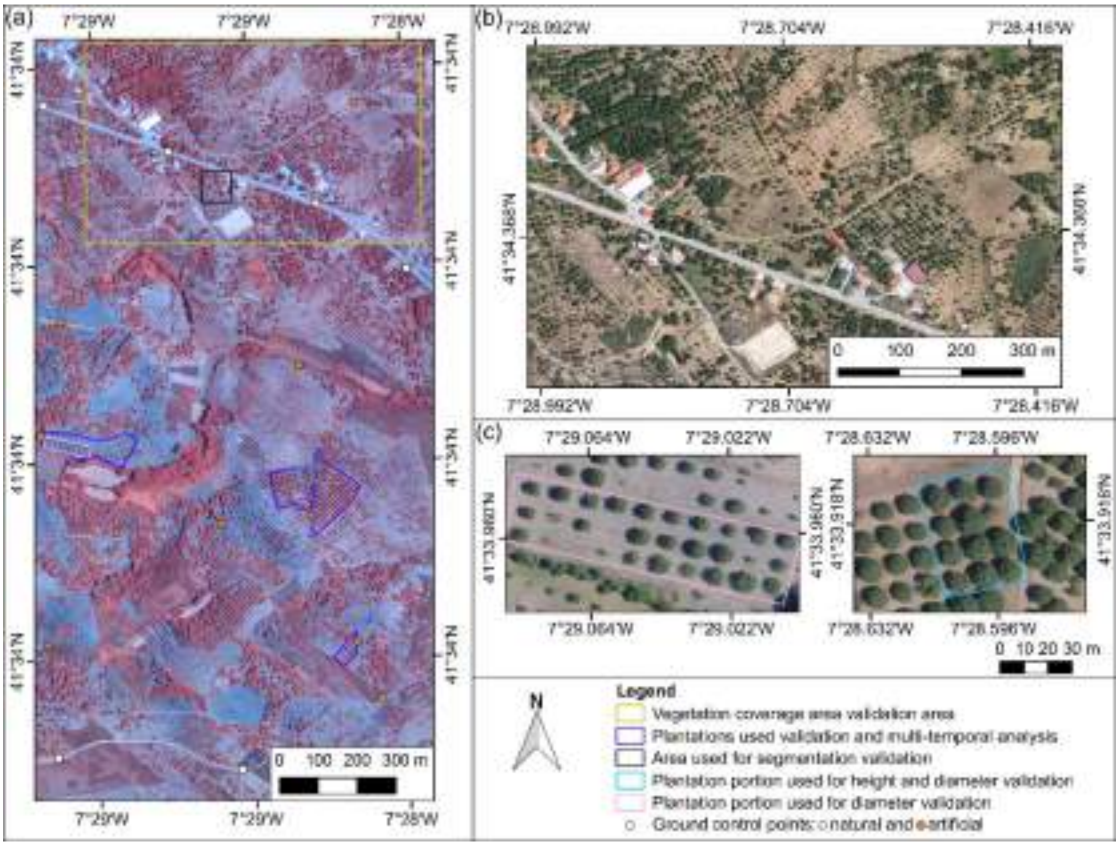


**Figure 4.1.** General overview of the surveyed area: (a) colour infrared (CIR) orthophoto mosaic computed using data from the flight conducted on July 10, 2017; (b) complex area used for vegetation coverage validation; and, (**c**) chestnut plantations used for tree height and tree crown diameter validation. Coordinates in WGS84 (EPSG:4326).

### 4.2.2. UAV Imagery Pre-Processing

Pix4Dmapper Pro software (Pix4D SA, Lausanne, Switzerland) was used for the photogrammetric processing of the UAV-based imagery. The following processing pipeline was applied: (1) imagery coregistration—data corresponding to each sensor was separately processed in different projects and throughout the identification of common point (tie points), allowing for the generation of a sparse point cloud of the surveyed area, for each sensor's imagery; (2) project merging—both blocks were aligned relative to each other by using points that are clearly identifiable in the imagery and then merged and geometric correction was applied using ground control points (GCPs), using both natural features and artificial targets that are deployed in the area (Pádua, Hruška, et al., 2017); (3) dense point clouds computation–two dense point clouds were computed (RGB and RE) using an high point density; (4) point clouds combination—finally, the two sets of point clouds were combined, increasing the total number of points, and ensuring, this way, height information for most of the trees, as shown in Figure 4.2. Orthorectified mosaics, DSM and DTM were the main outcomes that were generated from this pipeline. Data from each flight campaign has resulted in an excess of area surveyed and different GSDs (Table 4.1). As such, a section was chosen and resampled to meet the same area (200 ha), as shown in Figure 4.1a with 16.21 cm GSD.

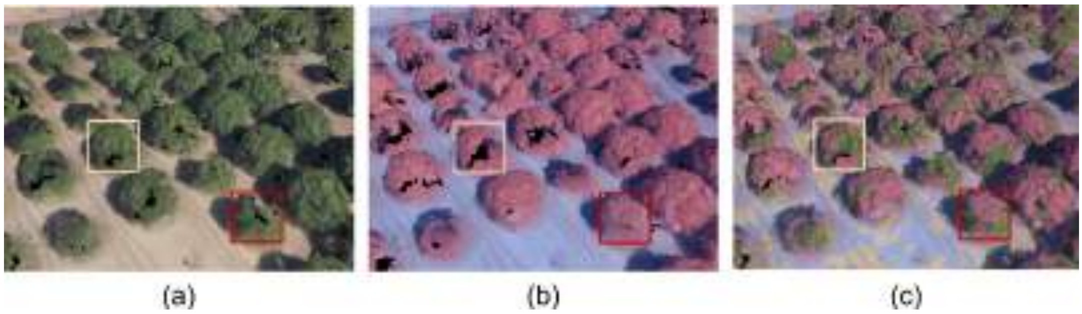


**Figure 4.2.** Differences in the dense point clouds generated from data of each sensor: (a) RGB; (b) colour infrared; and, (c) combination of both. Example of areas that benefited from the merging process are highlighted.

The CHM is computed by subtracting the DTM from the DSM, which makes it almost invariant with respect to terrain's slope, as illustrated in Figure 4.3. The use of CHM is crucial, since it allows for obtaining the height of the objects above ground level, enabling the filtering of undergrowth vegetation, such as grass and shrubs, and only analysing the vegetation of interest—in this specific case, chestnut trees.

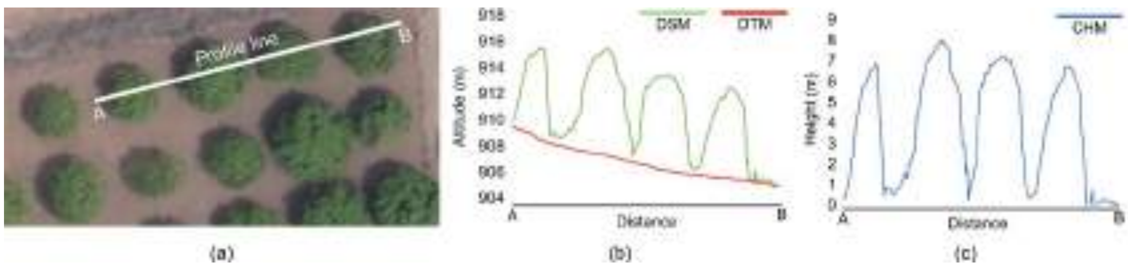


**Figure 4.3.** Computation of the canopy height model (CHM) obtained from the digital terrain model (DTM) and digital surface model (DSM): (a) profile line upon four chestnut trees; (b) DTM and DSM profiles; and, (c) resulting CHM profile line computed from the subtraction between the DTM and the DSM.

Regarding the geometric correction of the obtained photogrammetric processed data, and from a multi-temporal analysis perspective, it is mandatory to assure a subpixel alignment of all the epochs, otherwise the results may be biased. The used UAVs' navigation system includes a Global Navigation Satellite System (GNSS) receiver, with a positional accuracy of a few meters. Thus, the georeferencing that is achieved by this equipment does not follow the image's pixel resolution, only enabling an approximate location. Therefore, it is necessary to use tie points to refine the external camera orientation. Ground Control Points (GCPs) must be distributed throughout the surveyed area in order to avoid significant errors (Jianghao Wang et al., 2012). However, not only should good GCP coverage be done, but also independent check points should be used to verify the quality of the extracted products. In an urban environment, especially when road markings are present, it is relatively easy to find well-defined points that can be used as GCP. However, in the specific case of this study, it was not always possible to apply this method. In fact, only a few areas that were occupied by man-made objects allowed for the identification of such points. As such, the option was to use targets (approximately with 1 $m^2$ area (Pádua, Hruška, et al., 2017)) with centre-marked crosses, placed before the flight at selected locations, and fixed with metal studs (see Figure 4.4). In total, 16 (6 natural + 10 artificial) GCPs and 20 natural check points were used in every flight.


**Figure 4.4.** Example of an artificial ground control point (GCP) measuring 100 x 100 cm:(a) being surveyed with a global navigation satellite system (GNSS) receiver placed in the middle of the marker, (b) aerial image taken by the unmanned aerial vehicle. In the left, RGB representation, and in the right, colour infrared representation.

The imagery geocoding was performed while using the 16 GCPs and the alignment quality assessment was carried out using the 20 check points. For this case study, horizontal check points are the most important, since they allow for controlling the geometric alignment of the different outcomes, which crucial in implementing the multi-temporal analysis. These points are relatively simple to acquire, since surveys of real time kinematic (RTK) GNSS can be quickly acquired in the marked points. A GNSS receiver, in RTK mode, with an accuracy of approximately 2 cm, was used. For a check point of coordinates (E, N), the residuals are calculated by subtracting the coordinates that were measured by GNSS $(E_{GNSS}, N_{GNSS})$ and the corresponding point on the corresponding point interpolated over the reference (ref) orthophoto mosaic. The overall accuracy is given by the root mean square error (RMSE), for the n observed check points, as in equation (1). The mean and the standard deviation can also be determined to assess whether some systematic trends may exist in the data. However, the final results will not be influenced, since the orthophoto mosaics were independently geocoded and the distribution and geometry of the GCPs remained (Agüera-Vega et al., 2017).

$$RMSE_{E,N} = \sqrt{\sum_{i=1}^{n} \frac{\left(E_{i,ref} - E_{i,GNSS}\right)^2 + \left(N_{i,ref} - N_{i,GNSS}\right)^2}{n}} \tag{1}$$

Depending on the combinations of campaigns, the reference orthophoto mosaics may vary. The oldest orthophoto mosaics was used as reference and then the differences between the coordinates of the remaining two epochs were computed to assess the geometric quality of the alignment.

### 4.2.3. Proposed method

The outputs that are described in Section 4.2.2 were processed to extract the chestnut trees features. Figure 4.5 shows the main steps of the method that was developed in this research. The different steps are described in detail in the next sub-sections. Two imagery data sets (RGB and CIR orthophoto mosaics) and the CHM are loaded as inputs to fully exploit the proposed method. It should be noted that the method remains functional, even if RGB or CIR images are individually used as input. This way, the proposed method still fully operational, even in the cases where only imagery resulting from cost-effective platforms, which normally only supports RGB sensors, is available.

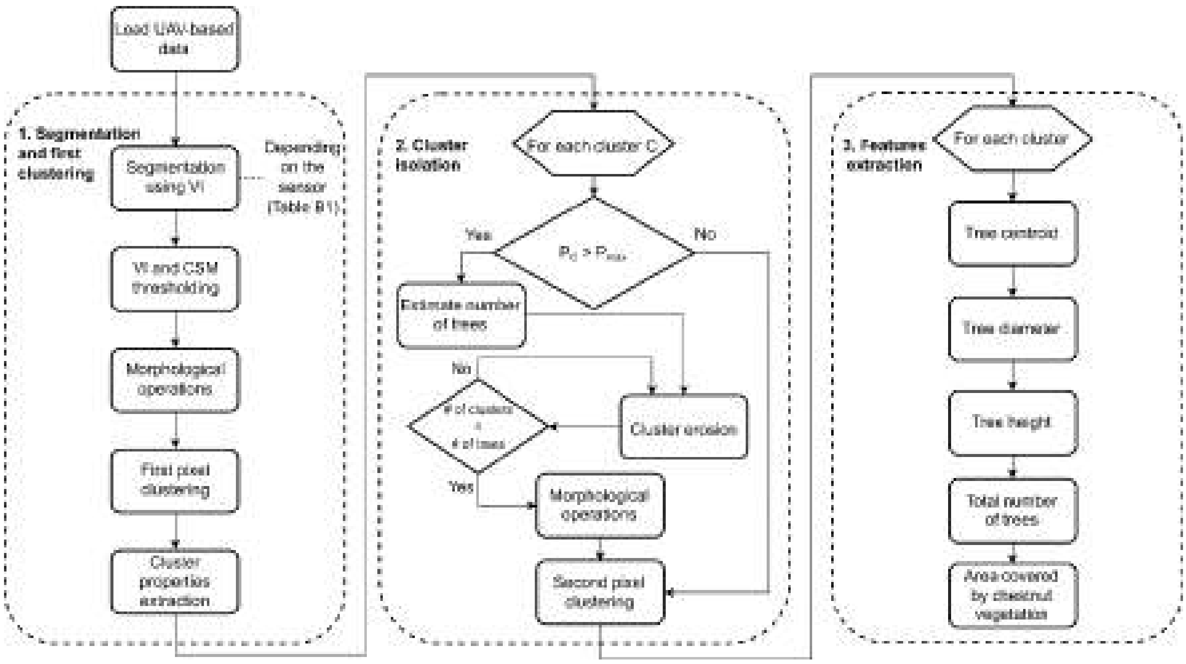


**Figure 4.5.** Proposed method general flow chart.

In addition, the proposed method also supports multi-temporal analysis, enabling the temporal vegetative evolution monitoring of chestnut plantations.

#### 4.2.3.1. Segmentation and First Clustering

The first step relies on the preliminary selection of pixels that represent all of the vegetation, mainly associated to chestnut trees. To achieve this, common segmentation thresholding techniques are not appropriate, since those techniques will not distinguish between vegetation and non-vegetation areas, resulting in an image with other objects besides vegetation (e.g. infrastructures, bare soil, roads, and the possible shadowing effects from the chestnut trees canopy). To overcome this issue, the use of broadband spectral VIs was considered. A comparison of different segmentation techniques and vegetation indices was conducted to select the most performant. Appendix A presents the results of this study.

The image resulting from the application of VI-based segmentation (Figure 4.6b) enables the creation of a vegetation mask by applying the Otsu's method (Otsu, 1979) (Figure 4.6c). From this selection, a binary image is created that contains all of the pixels that potentially correspond to vegetation. The same approach is applied to the CHM being binarized using a height threshold, then both binary images are joined with a logical AND operation. Next, a set of morphological operations is applied to the thresholding operation result. A 3×3 morphological structuring element is used for the open operation (to remove small objects from the foreground), and to the close operation (to remove small holes in the foreground, changing small islands of background into foreground). Thus, the implemented morphological operations allow for simplifying the resultant binary image by improving the detection of sets of interconnected pixels C (i.e. clusters of pixels), forming a set of all clusters $\mathcal{C}$, where $C \in \mathcal{C}$, which enables the individual analysis of the regions. When located close to each other, the larger trees may be represented as being connected in the binary image (overlapped trees) and, consequently, grouped into the same cluster (Figure 4.6d).

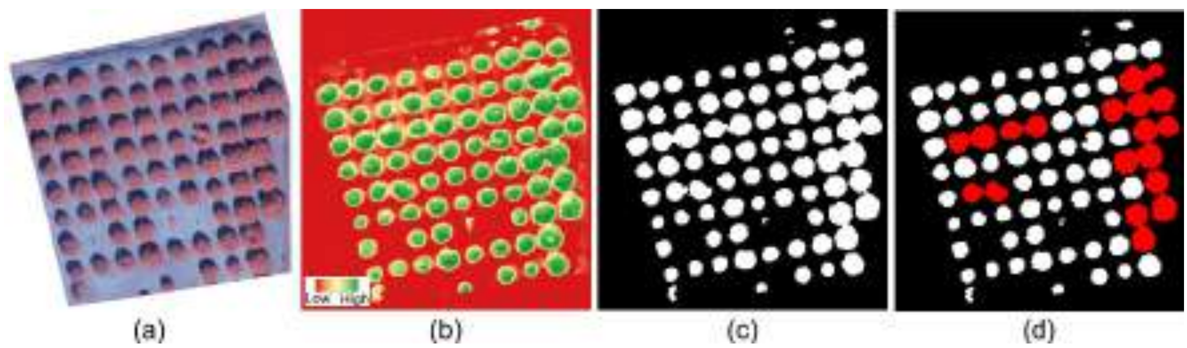


**Figure 4.6.** Segmentation and first clustering: (a) the original colour infrared image; (b) colour-coded image resulting from the application of ExRE vegetation index; (c) binary image resulting from both the threshold and morphological operations; and, (d) clusters including connected trees highlighted in red.

To prepare the proposed method's step 2—cluster isolation—a data structure is created with individual cluster parameters. Those parameters are retrieved from the binary image and they are composed of the clusters' area and centroid. The cluster's centroid is crucial in associating an identification (ID). At this stage, the cluster's area value will be used to find clusters that represent inter-connected trees.

### 4.2.3.2. Cluster Isolation

The approach that is applied in the first step of the method can correctly remove most of the non-vegetative areas, allowing for the detection of large vegetation areas. However, even though chestnut trees plantations for chestnut production are usually evenly distributed across the field, their canopy can grow considerably in height and width, forming connected tree crowns, resulting in clusters with interconnected pixels that may include several trees, in the segmented images. Due to this fact, it is necessary to individually distinguish each tree for precise chestnut trees' monitoring. To achieve this, an individual analysis per cluster C, detected in the first step, needs to be performed. Chestnut plantations generally have a group of trees that typically depict the tree canopy coverage area. As such, the presence of interconnected trees can introduce significant differences on clusters' area, which can result in a skewed distribution. Therefore, the statistical mode of this set of values—that represents the value appearing most often, i.e. the value that is most likely to be sampled—is determined and a 10% threshold is applied to this value. Clusters' area mode is used to define the reference area ($A_{Mo}$), which will then be compared—in an iterative process—with the area of each detected cluster $A_C$. Areas higher than $A_{Mo}$ are divided by it, to estimate the number of trees ($\hat{T}$) present in each cluster, as shown in equation (2). Figure 4.7a presents an example of clusters meeting this condition.

$$\hat{T} = \left\lfloor \frac{A_C}{A_{Mo}} \right\rfloor \tag{2}$$

Afterwards, a morphological operation of erosion (see the example of Figure 4.8) is performed. It consists in interactively removing a line with a pixel thick from the borders, until a new cluster is formed. This new cluster is removed from the selection and the process continues until $\hat{T}$ is achieved (Figure 4.8b). Finally, the application of the thickening morphological operation to properly separate the clusters by using a one pixel-thick line reverses the process (Figure 4.8c). This process is achieved by adding pixels to the boundaries of the unconnected clusters (as shown in Figure 4.7b), nevertheless preserving the total number of clusters, without connecting them. The resulting image is also known as skeleton by zone of influence (SKIZ). Figure 4.7c presents an example of this operation, being highlighted in red. The SKIZ mask is then used to separate the initially connected clusters by performing per-pixel binary AND operation, resulting in the disconnection of the previously connected clusters. The newly created clusters will be submitted to a second pixel clustering to update the original set, created in step 1. Figure 4.7d presents the result of this operation, highlighting the separated clusters.

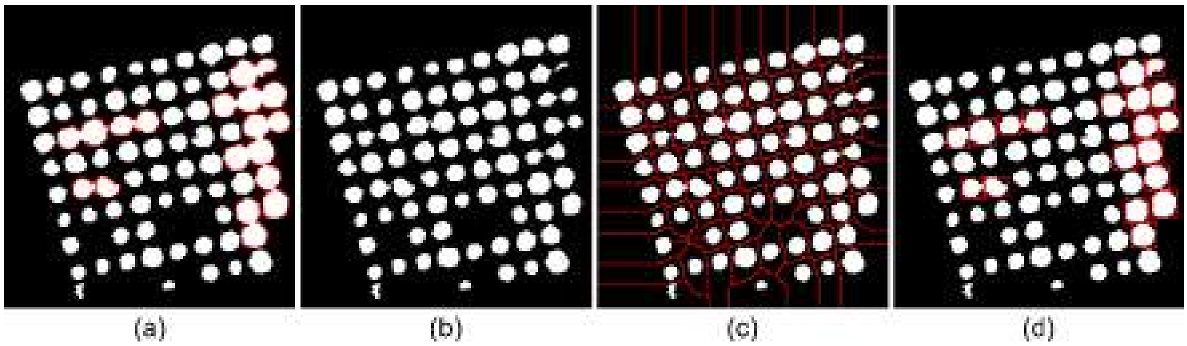


**Figure 4.7.** Cluster isolation operation applied to an entire chestnut plantation: (a) clusters with area higher than the reference area value, highlighted in red; (b) eroded image; (c) skeleton by zone of influence boundaries, in red, on top of the eroded image; and, (d) image with the separated clusters highlighted in red.

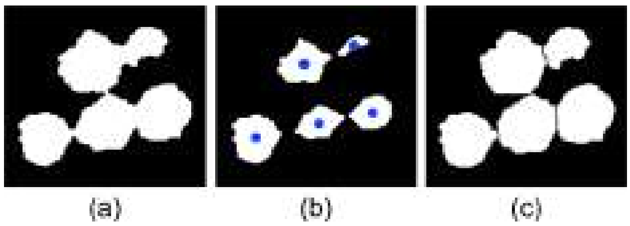


**Figure 4.8.** Cluster isolation process: (a) original cluster composed by five connected chestnut trees; (b) clusters resulting from the morphological erosion operation represented with their centroids; and, (c) effect of the thickening morphological operation, resulting in five unconnected clusters.

### 4.2.3.3. Parameters Extraction

At this point, each cluster corresponds to a single tree and their centroids are used to extract the tree crown diameter, canopy area, and height. Combining the masks that were obtained from the previous pixel clustering process, it is possible to extract the correct parameters from each chestnut tree. Regarding the diameter extraction, the centroids are overlapped to the binary image that was obtained in the method's second step. The diameter is extracted by measuring each cluster's Euclidean distances. Thus, the maximum distance is selected and transposed to estimate each tree's crown diameter. The same approach is applied to obtain the tree's height. However, the height value is directly extracted from the CHM, by matching the cluster's centroids with the corresponding CHM and retrieving the maximum value, which is then assumed to be the tree crown's top. The mean vegetation index value per cluster can also be computed. This value can be interesting to assess chestnut trees vigour and the potential presence of phytosanitary problems.

Furthermore, it is also possible to calculate parameters of the whole plantation, such as the total number of trees and total canopy coverage area and its percentage, by summing out all of the individual areas.

#### 4.2.3.4. Multi-Temporal Analysis

Data acquired in different epochs can be used to create time series, allowing for the comparison between different periods. It is an excellent tool for the management of chestnut plantations, enabling the evaluation of their evolution over time both at the plantation scale and at the individual tree scale. In addition to parameters extraction, it is also possible to detect missing trees and new plantations over the years, through a multi-temporal analysis. This achieved by applying the proposed method to different epochs. By overlapping the detected clusters, missing and new trees can be detected. The implemented multi-temporal analysis can also be performed at the tree crown level. Performing a pixel-wise comparison between the evaluated epochs achieved the chestnut tree canopy growth/decline. The following scenarios may occur: (1) common vegetation in both epochs—vegetation is present in both epochs in the same pixel ($i$, $j$) coordinates; (2) vegetation growth—vegetation is not detected in the first epoch, but it is detected in the second epoch, meaning a chestnut tree growth; and, (3) vegetation decline—pixels considered as vegetation in the first epoch that were not represented in the second epoch. Chestnut trees with a decline percentage greater than 15% are signalled as potentially having phytosanitary problems, meaning that they need to be inspected in the field, reducing time-consuming and laborious field inspections. Therefore, these results can be analysed both at a plantation level and at the individual tree level.

### 4.2.4. Validation

To validate the proposed method and the feasibility of the data that was obtained from photogrammetric processing of the UAV-based imagery, different tests were conducted for different parameters, namely: VI selection; vegetation coverage area assessment; number of detected trees; and, tree crown diameter and tree height estimation. This way, five test areas were selected for this purpose. All of the chestnut trees present within each area were manually segmented for validation purposes. The first test area represents about 23% of the whole surveyed area (46.89 ha), as presented in Figure 4.1b. The area was selected, since it includes several types of elements/objects. Beyond recently planted chestnut trees, non-controlled chestnut plantations, several vegetation outliers (e.g. lawns), and infrastructures, such as buildings and roads cover the area. It was considered to analyse the general behaviour of the method when facing outliers and it was only tested in vegetation coverage area. Apart from this area and since the proposed method focus is the monitoring of chestnut plantations, four other chestnut plantations were selected and analysed as the test areas (Figure 4.9). Plantation #1 (Figure 4.9a) has approximately 1.45 ha, Plantation #2 (Figure 4.9b) has 1 ha, Plantation #3 (Figure 4.9c) has an area of 0.26 ha, and the area of Plantation #4 (Figure 4.9d) is about 1.3 ha. While Plantations #1 and #2 are composed of fully developed chestnut trees, Plantation #3 has chestnut trees at different development stages and Plantation #4 is mainly composed of more recent chestnut trees. These four areas were used for determining the area coverage, assessing the number of trees detected, and for selecting the optimal vegetation indices (Appendix B). Reference masks of these areas were manually created for the three available flight campaigns.

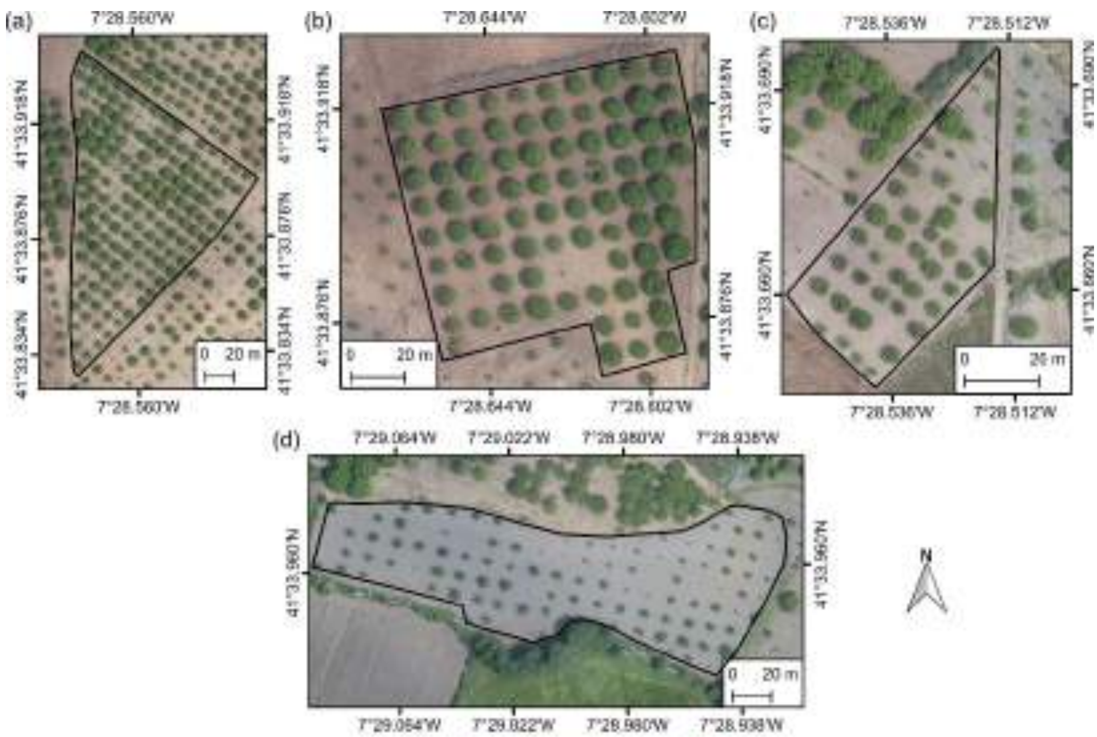


**Figure 4.9.** Chestnut plantations used for validation: (a) Plantation #1; (b) Plantation #2; (c) Plantation #3; and, (d) Plantation #4. Black lines represent the boarder of the plantation. Coordinates in WGS84 (EPSG:4326).

### 4.2.4.1. Vegetation Coverage Area

The purpose of this validation is to evaluate the behaviour of the proposed method in the detection of chestnut trees vegetation. The method was applied in a large and heterogeneous area (Figure 4.1b) with different vegetation covers, in an uncontrolled environment, and to four different plantations (Figure 4.9). The computational time of the algorithm to perform in the complex area was measured to be compared with the time that is required to manually create the reference mask of the same area. Validation was conducted comparing the method’s obtained results with the binary images that were created from the manual segmentation. This way, each pixel ($i$, $j$) was analysed, and it is classified as being true and false positive (TP/FP, exact/over detection), which refer to the number of correct/incorrect pixels that are classified as chestnut vegetation and similarly true and false negatives (TN/FN, exact/under detection) for non-chestnut trees vegetation. For this purpose, different parameters were evaluated, namely: producer's accuracy, user's accuracy, and the overall accuracy. Producer's accuracy is obtained by the percentage of how many pixels on the map are correctly labelled as corresponding to chestnut and to non-chestnut vegetation, encompassing errors of omission. User's accuracy is obtained by the percentage of all pixels that were identified as a chestnut and non-chestnut vegetation that were correctly identified, encompassing errors of commission.

#### 4.2.4.2. Number of Detected Trees

This validation consisted in the comparison of the number of trees that were detected by the proposed method with the real number existing into a specific plantation at a specific epoch. Since the area that is used for vegetation detection validation contains thousands of trees, which makes the segmentation difficult, it was decided to use a controlled environment consisting of the four different plantations (Figure 4.9). The selection was done assuring the representativeness of most real cases present in the study area.

In what regards this validation, different parameters were evaluated: (1) good detection—the three was correctly detected when compared with the reference mask; (2) missed detection—the tree was not detected; (3) extra detection—corresponding to a wrongly detected chestnut tree; (4) over detection—a single chestnut tree being classified in multiple clusters; (5) under-detection—multiple trees classified in a single cluster; (6) larger detection—tree is larger than its actual size; and, (7) smaller detection—chestnut tree is smaller than its actual size.

#### 4.2.4.3. Tree Height and Crow Diameter Estimation

To validate trees height estimation, 12 chestnut trees, as presented in the right side of Figure 4.1c, were measured in the terrain using a laser rangefinder with a precision of ± 20 cm (TruPulse 200, Laser Technology, Inc., Colorado, United States of America). Chestnut experts from University of Trás-os-Montes e Alto Douro have consistently monitored Padrela's region regarding chestnut trees cultural practices, environmental context, phytosanitary conditions, and an evolution, in recent decades. This monitoring activity resulted in several publications (J. Castro et al., 2010; L. Martins et al., 2007, 2009; L. M. Martins et al., 2001, 2015; Luís Martins et al., 2005, 2014, 2015; Pádua, Hruška, et al., 2017), which conclude that both cultural practices and environmental context are identical throughout the region. Therefore, the 12 trees selected from plantation #2—the selection was made based on the main characteristics of an adult chestnut tree, well represented in this Plantation—can be considered representative for the entire area under study. Regarding tree crown diameter estimation validation, two groups of trees were selected: the 12 trees that were used for the tree height estimation validation composed the first group and 28 chestnut trees composed the second group (both areas presented in Figure 4.1c). These measurements were obtained in the 2017 flight campaign day. Tree crown diameter were obtained by tape measuring. Two measurements were considered that corresponded to the four quadrants and the mean value was used as ground-truth. These values were compared with those that were estimated from the proposed method. Finally, a comparison was performed and the overall agreement between the observed in-field measurements (o) and the root mean square error (RMSE) verified the estimated values (e), as in equation (3), where n represents the total number of analysed trees. In general, RMSE is a good metric to evaluate (punctually) the quality of the method's measurements.

$$\mathrm{RMSE} = \sqrt{\frac{\sum_{i=1}^{n}(e_i - o_i)^2}{n}} \tag{3}$$

The coefficient of determination ($R^2$), which consists in a statistical measure of how close the data is to the fitted regression line, was also calculated.

## 4.3. Results

This section presents the results of accomplishing the validation procedures that are described in Section 4.2.4, concerning the proposed method's validation and extracted features reliability. Moreover, a multi-temporal analysis, by applying the proposed method to four chestnut plantations in three different epochs, is also presented.

### 4.3.1. Data alignment

Table 4.2 presents data from the three campaigns combinations, namely the results from their accuracy analysis. Analysing the values that were obtained for the residuals mean and standard deviation—the mean value is close to zero meters and standard deviation is lower than RMSE—means that there are no systematic errors. The results presented in Table 4.2 also allows to conclude that the geometric adjustment between epochs is very similar in less than one pixel. These results validate the multi-temporal analysis that is performed by applying the proposed method.

**Table 4.2.** Geometric quality of the orthophoto mosaics used in the multi-temporal analysis.

| Orthophoto Mosaics Compared | N. Checkpoints | RMSE (px) | RMSE (cm) | Standard Deviation (px) | Mean of Residuals (px) | Min/max Residuals (px) |
|---|---|---|---|---|---|---|
| 2014 – 2015 | | 0.61 | 9.94 | 0.25 | 0.06 | -0.93/1.28 |
| 2014 – 2017 | 20 | 0.90 | 14.44 | 0.38 | 0.10 | -1.12/1.82 |
| 2015 – 2017 | | 0.71 | 11.38 | 0.32 | -0.04 | -1.36/1.03 |

## 4.3.2. Vegetation Coverage Area

Figure 4.10 illustrates the result of the proposed method, when compared with the manual segmented image, in an uncontrolled environment (RGB representation presented in Figure 4.1b). The proposed method obtained 94.31% of exact detection and an error rate of 5.69%, from which 3.05% is of under detection (FN) and 2.63% over detection (FP).

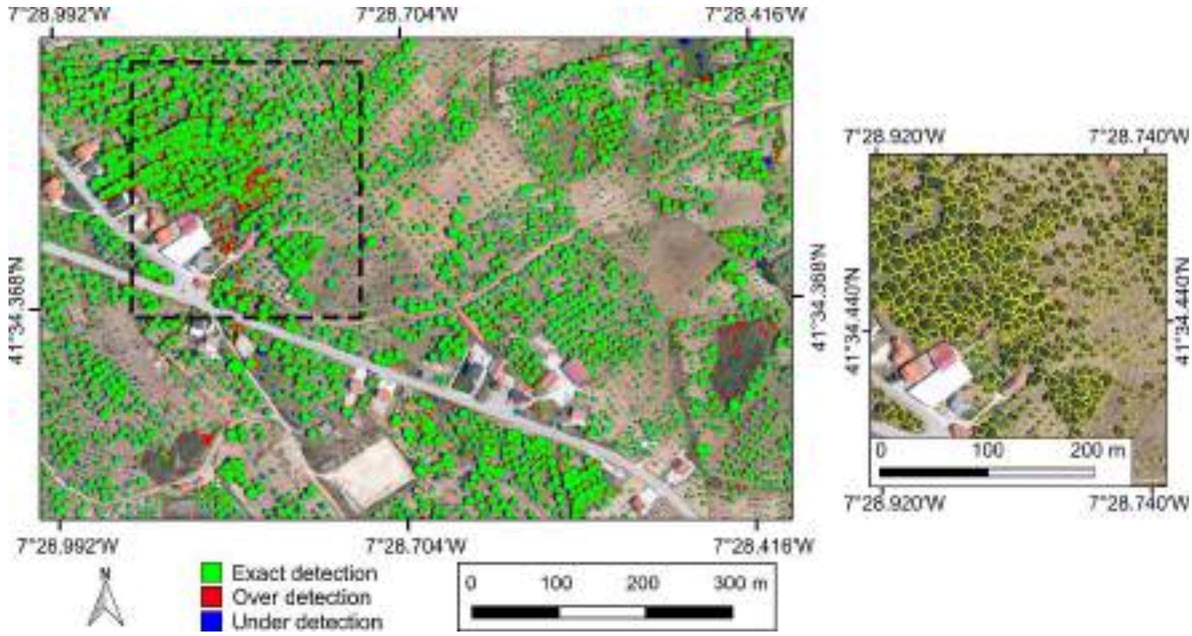


**Figure 4.10.** Validation of the vegetation coverage area by comparing the automatic binary mask, in an uncontrolled environment, produced by the proposed method, with the reference mask, represented in three colours, overlaid in the orthophoto mosaic, in the left. In the right, contours of the detected trees of the area marked in the dashed polygon. Coordinates in WGS84 (EPSG:4326).

According to the manual binary mask, in a total area of 48.2 ha, only 12 ha contains chestnut trees, corresponding to 25% of the total area. From this area, the proposed method identified 12.2 ha of chestnuts trees, which corresponded to an over estimation of 1.6%. Producer's accuracy was around 88% and user's accuracy is 89.5% (see Table 4.3 for further results).

For reference, the manual mask was created in eight hours, while the method was performed in approximately 10 minutes using a laptop computer with an Intel core I7-4720HQ CPU @ 2.6 GHz, 8 GB of RAM, a NVIDIA GeForce GTX 950 GPU with 2 GB of dedicated memory, and a 700 GB HDD. For a more realistic study, four chestnut plantations, as presented in Figure

4.9, were selected for evaluation. Figure 4.11 shows a visual interpretation of the results. Table 4.3 provides the results per plantation, in each epoch, for the parameters that were considered in this evaluation. Producer's and user's accuracy were only evaluated for chestnut vegetation class. Regarding, the non-chestnut vegetation class was not deeply analysed, but it was higher than 95% in most of cases, with a mean of 97% for producer's accuracy and 96% for User's accuracy.

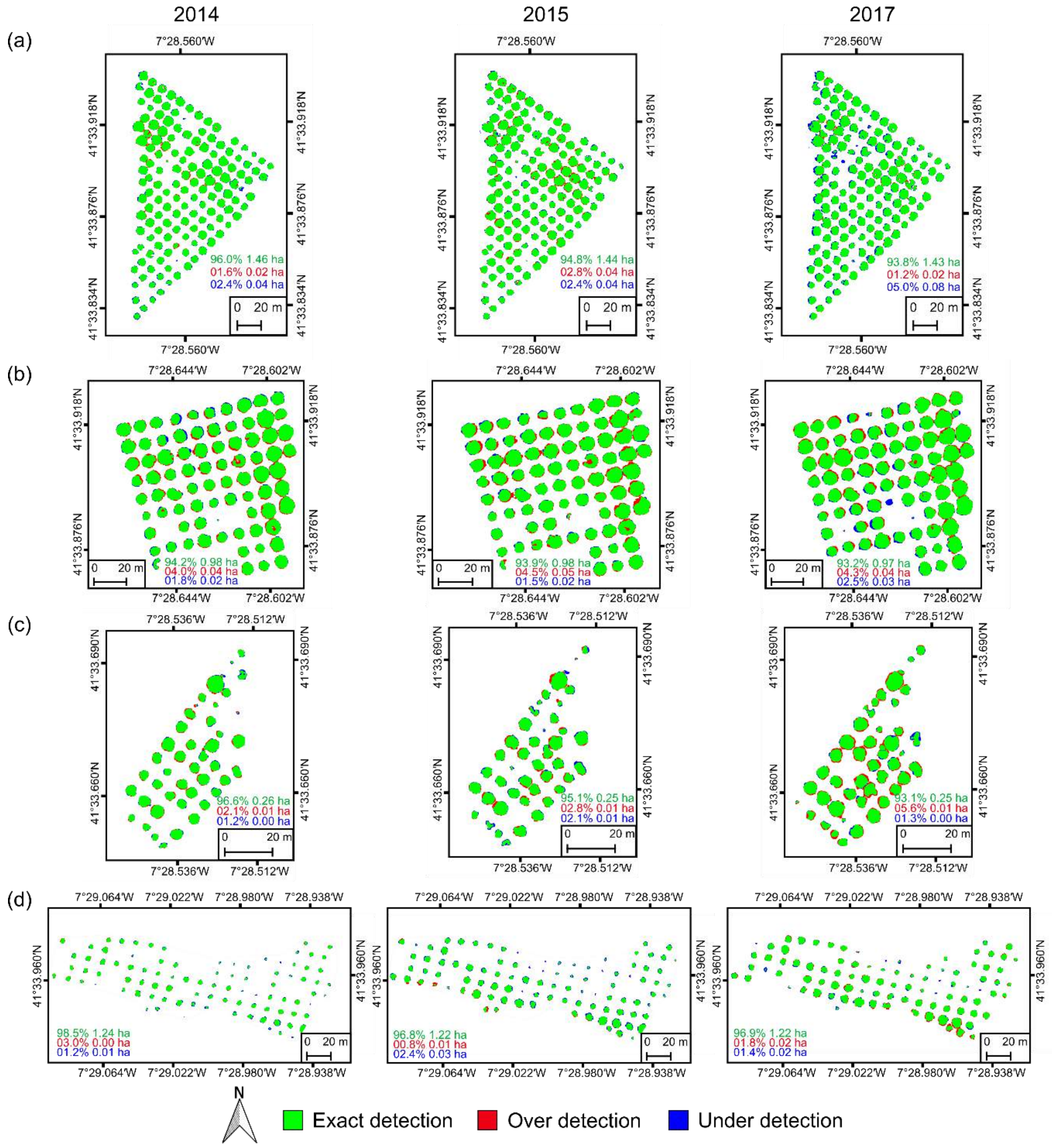


**Figure 4.11.** Validation of the vegetation coverage area by comparison of the automatic binary mask, produced by the proposed method, in four chestnut plantations, with the reference mask, represented in three colours: (a) Plantation 1; (b) Plantation 2; (c) Plantation 3; and, (d) Plantation 4. Left represents 2014; centre 2015, and in the right 2017. Percentage and area of exact, over and under detection are also presented. Coordinates in WGS84 (EPSG:4326).

When analysing the four chestnut plantations in the three epochs, the mean overall detection reaches 95%. Evaluating these results in a plantation basis, higher detection values were observed in plantation #4 (97.4%) and lower in plantation #2, with 93.8%. The remaining plantations reached accuracies of around 95%. When observing results by epoch, the highest detection rates were obtained in 2014 (96.3%), whereas 2017 reached the lower mean values (94.2%). As for the 2015 flight campaign, its mean accuracy value was of 95.2%. The higher values were obtained for plantation #4, in 2014, and the lowest was 93.1%, for plantation #3. As such, it can be stated that the method is suitable for chestnut detection, with accuracy greater than 93% and varying up to approximately 99%, depending on the plantation characteristics.

**Table 4.3.** Chestnut trees vegetation coverage results for the bigger and complex area in 2017 epoch and in four plantations ($P\#_{epoch}$) for the three epochs (2014, 2015, and 2017). Area of true and false positives (TP/FP) and true and false negatives (TN/FN), in $m^2$ along with producer's accuracy (PA) and user's accuracy (UA) for chestnut vegetation, and overall accuracy (OA) percentage values. Mean values for the plantation in all parameters are also presented.

| Area / Plantation | TP ($m^2$) | FP ($m^2$) | FN ($m^2$) | TN ($m^2$) | UA (%) | PA (%) | OA (%) |
|---|---|---|---|---|---|---|---|
| Complex area | 107610 | 14698 | 12687 | 346582 | 89.45 | 87.98 | 94.31 |
| $P1_{14}$ | 4951 | 246 | 365 | 9630 | 93.13 | 95.27 | 95.97 |
| $P1_{15}$ | 5096 | 425 | 366 | 9305 | 93.30 | 92.30 | 94.79 |
| $P1_{17}$ | 5248 | 187 | 752 | 9004 | 87.47 | 96.55 | 93.82 |
| $P2_{14}$ | 3460 | 415 | 186 | 6355 | 94.91 | 89.28 | 94.23 |
| $P2_{15}$ | 3632 | 471 | 161 | 6152 | 95.77 | 88.51 | 93.93 |
| $P2_{17}$ | 3929 | 446 | 262 | 5780 | 93.75 | 89.80 | 93.20 |
| $P3_{14}$ | 554 | 57 | 33 | 2033 | 94.42 | 90.62 | 96.64 |
| $P3_{15}$ | 569 | 75 | 55 | 1977 | 91.20 | 88.31 | 95.13 |
| $P3_{17}$ | 719 | 149 | 36 | 1773 | 95.25 | 82.84 | 93.09 |
| $P4_{14}$ | 780 | 44 | 147 | 11645 | 84.15 | 94.66 | 98.49 |
| $P4_{15}$ | 1216 | 99 | 299 | 11002 | 80.28 | 92.45 | 96.85 |
| $P4_{17}$ | 1648 | 223 | 174 | 10572 | 90.46 | 88.09 | 96.86 |
| Mean of P | 2650 | 236 | 236 | 7102 | 91.17 | 90.72 | 95.25 |

### 4.3.3. Number of Detected Trees

To evaluate the number of trees detected by the proposed method, the same test plantations that are presented in Figure 4.9 (see Figure 4.1 for location) were used. The results were compared with the manual counting of the number of trees present in the plantations and the three epochs (2014, 2015, and 2017) were evaluated. Table 4.4 presents the obtained results, per plantation in each epoch.

**Table 4.4.** Chestnut trees detection accuracy in four plantations (P#epoch) for the three epochs with number of estimated trees and its detection type.

| Plantation | Number of Trees | Estimated Trees (Variation) | Detection Type (%) | | | | | | |
|---|---|---|---|---|---|---|---|---|---|
| | | | Good | Missed | Extra | Over | Under | Larger | Smaller |
| $P1_{14}$ | 146 | 145 (-1) | 97.93 | 0.69 | - | - | - | 0.69 | 1.38 |
| $P1_{15}$ | 146 | 147 (+1) | 98.64 | 0.68 | - | 0.68 | - | 0.68 | - |
| $P1_{17}$ | 148 | 147 (-1) | 97.96 | 1.36 | - | 0.68 | - | - | 1.36 |
| $P2_{14}$ | 80 | 80 (0) | 100.00 | - | - | - | - | - | - |
| $P2_{15}$ | 80 | 80 (0) | 97.50 | - | - | - | - | 2.50 | - |
| $P2_{17}$ | 80 | 79 (-1) | 93.67 | 1.27 | - | - | - | 1.27 | 5.06 |
| $P3_{14}$ | 44 | 43 (-1) | 93.02 | - | - | - | 2.33 | - | 4.65 |
| $P3_{15}$ | 43 | 42 (-1) | 85.71 | - | - | - | 2.38 | 4.76 | 7.14 |
| $P3_{17}$ | 44 | 44 (0) | 86.36 | - | - | 2.27 | 2.27 | 6.82 | 2.27 |
| $P4_{14}$ | 91 | 88 (-3) | 89.77 | 3.41 | - | - | - | - | 10.23 |
| $P4_{15}$ | 97 | 89 (-8) | 91.01 | 8.99 | - | - | - | 3.37 | 5.62 |
| $P4_{17}$ | 93 | 90 (-3) | 92.22 | 3.33 | - | - | - | 2.22 | 5.56 |
| Mean detection (%) | | | 93.65 | 1.64 | - | 0.30 | 0.58 | 1.86 | 3.61 |

In total, 1092 chestnut trees were included in the analysis. The proposed method was able to detect 1074 chestnut trees. However, six of those corresponded to wrongly estimated trees (approximately 0.5%), i.e. trees classified as extra, over or under detections. Globally, 1068 trees were correctly classified, representing an accuracy rate of about 98%. This way, exclusively concerning the detection of chestnut trees (i.e. good, larger, and smaller detections), the method has a mean classification of 99%, per flight campaign. Regarding this detection in a plantation basis, the mean accuracy of all flight campaigns is also of about 99%, being the lower value corresponding to plantation #3 (approximately 97%). Moreover, no cases of wrongly estimated trees (extra detections) were observed. In total, 19 chestnut trees were not detected (1.7%).

## 4.3.4. Tree Height and Crow Diameter Estimation

Figure 4.12 presents the results that show the relationship agreement between in-field measurements (ground-truth data) and the measurements that were estimated by applying the proposed method. The height values ranged from 7.6 m to 10.2 m, with a mean value of 8.8 m. For the model with 16 cm GSD (Figure 4.12a), the linear regression presents a $R^2$ = 0.79 and a RMSE of 0.69 m, and the estimated maximum, minimum, and mean values were 10 m, 6.4 m, and 8.2 m, respectively. Using data resulting from a flight at lower height, there was a significant increase in this parameter accuracy. Indeed, to test the influence of the flight height in tree's height estimation, a 100 m height (GSD ~ 3 cm) flight was carried out with DJI Phantom 4, in the same area. In this case, the accuracy significantly improved, $R^2$ = 0.86 with a RMSE of 0.33 m (Figure 4.12b), the maximum, minimum, and mean height values were also closer to the measured values, being, respectively, 10.2 m, 7.3 m, and 8.8 m.

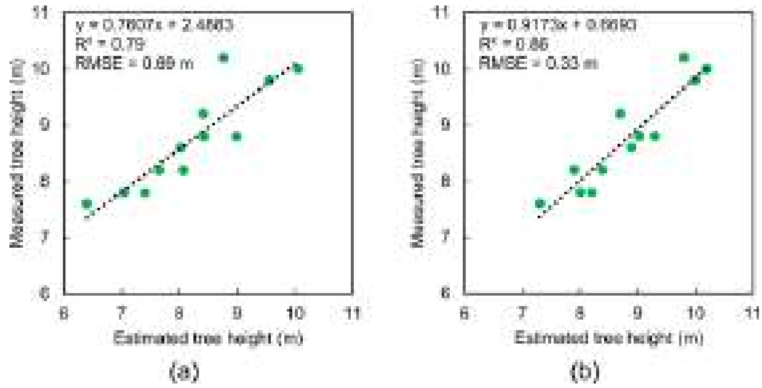


**Figure 4.12.** Trees' height estimation validation: comparison between the trees' height retrieved by the proposed method and those measured in-field using a: (a) 16 cm GSD data and (b) 3 cm GSD data.

Concerning tree diameter validation, analogously to tree height validation, the estimated diameter values that were obtained from the proposed method were compared with ground-truth data, where the 40 chestnut trees' diameter ranged from 2.45 m to 12.23 m, with a mean value of 6.71 m. Figure 4.13 presents the relationship between in-field measurements and those that were estimated by the proposed method. From the data acquired at 550 m (GSD ~ 16 cm), the linear regression presents a $R^2$ = 0.92 (Figure 4.13a), which indicates that the estimated tree crown diameter fits the real data in an 92% accuracy rate. As for the RMSE value, an error of 0.44 m was obtained. Regarding the minimum, maximum, and mean values that were estimated from the 16 cm GSD data were 2.1 m, 10.66 m, and 6.73 m, respectively. Concerning tree's crown diameter estimation that was obtained when using the flight conducted at 100 m height (GSD ~ 3 cm), similarly to tree height estimation, there was an improvement in this parameter (see Figure 4.13b). The linear regression presents a $R^2$ = 0.96 and the RMSE shows a value of 0.44 m, minimum, maximum, and the mean estimated values were, respectively, 2.92 m, 11.55 m, and 6.67 m.

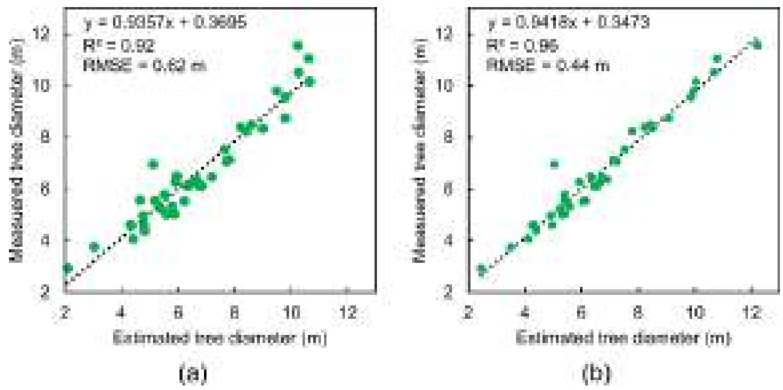


**Figure 4.13.** Trees' diameter validation: comparison between the in-field measurements by the diameter values estimated by the proposed method: (a) 16 cm GSD data and (b) 3 cm GSD data.

## 4.3.5. Multi-Temporal Analysis

One of the major advantages of the proposed method, compared to the actual state of the art, consists of its capacity to perform multi-temporal analysis, both at the tree and plantation levels.

### 4.3.5.1. Plantation-Level Analysis

The data available from the 2014, 2015, and 2017 campaigns was used to perform a multi-temporal analysis. The number of chestnut trees in the plantation and their respective coverage areas were compared. The same plantations that are presented in Figure 4.9 (see Figure 4.1 for location) were used. Table 4.5 shows the occupation area of the chestnut trees in the four plantations for each flight campaign, along with the mean values of tree height, canopy diameter, and area. Figure 4.14 shows the evolution over time of the four chestnut plantations, representing the differences between 2014–2015, 2015–2017, and 2014–2017 campaigns.

**Table 4.5.** Multi-temporal analysis at the plantation level for: total chestnut area, chestnut coverage area (CA), and mean values of chestnut trees present at the plantation (height, canopy diameter, and area). Values retrieved from four chestnut plantations in each epoch ($P\#_{epoch}$).

| **Plantation** | **Chestnut Area ($m^2$)** | **Chestnut CA (%)** | **Mean Tree Height (m)** | **Mean Tree Diameter (m)** | **Mean Tree Area ($m^2$)** |
|---|---|---|---|---|---|
| $P1_{14}$ | 5197 | 34.2 | 6.2 | 7.0 | 36 |
| $P1_{15}$ | 5521 | 36.3 | 6.0 | 7.2 | 38 |
| $P1_{17}$ | 5436 | 35.8 | 6.7 | 7.4 | 37 |
| $P2_{14}$ | 3876 | 37.2 | 6.6 | 8.1 | 48 |
| $P2_{15}$ | 4104 | 39.4 | 6.7 | 8.5 | 51 |
| $P2_{17}$ | 4375 | 42.0 | 7.1 | 8.6 | 55 |
| $P3_{14}$ | 611 | 22.8 | 3.2 | 4.4 | 14 |
| $P3_{15}$ | 645 | 24.1 | 3.9 | 4.7 | 15 |
| $P3_{17}$ | 868 | 32.4 | 4.2 | 5.3 | 20 |
| $P4_{14}$ | 824 | 6.5 | 4.1 | 3.6 | 9 |
| $P4_{15}$ | 1315 | 10.4 | 4.6 | 4.5 | 15 |
| $P4_{17}$ | 1870 | 14.8 | 5.2 | 5.3 | 21 |

Regarding the number of trees (Figure 4.15), plantation #4 presented more changes during the analysed period, constituting a total of 20 new or missing chestnut trees (10 new trees and 10 missing trees). Plantation #1 presented a total of four changes: a missing tree and a new tree were detected in the 2017 period; two new trees were also detected in the 2015 period. Five changes were observed in plantation #2: two new trees were detected in 2015; and, three were considered as missing in 2017. When considering plantation #3, four chestnut trees were considered missing, two in each period (2015 and 2017), and four new trees were detected, one in 2015 and three in 2017, performing a total of eight changes. Potential phytosanitary problems were also detected in all of the analysed plantations.

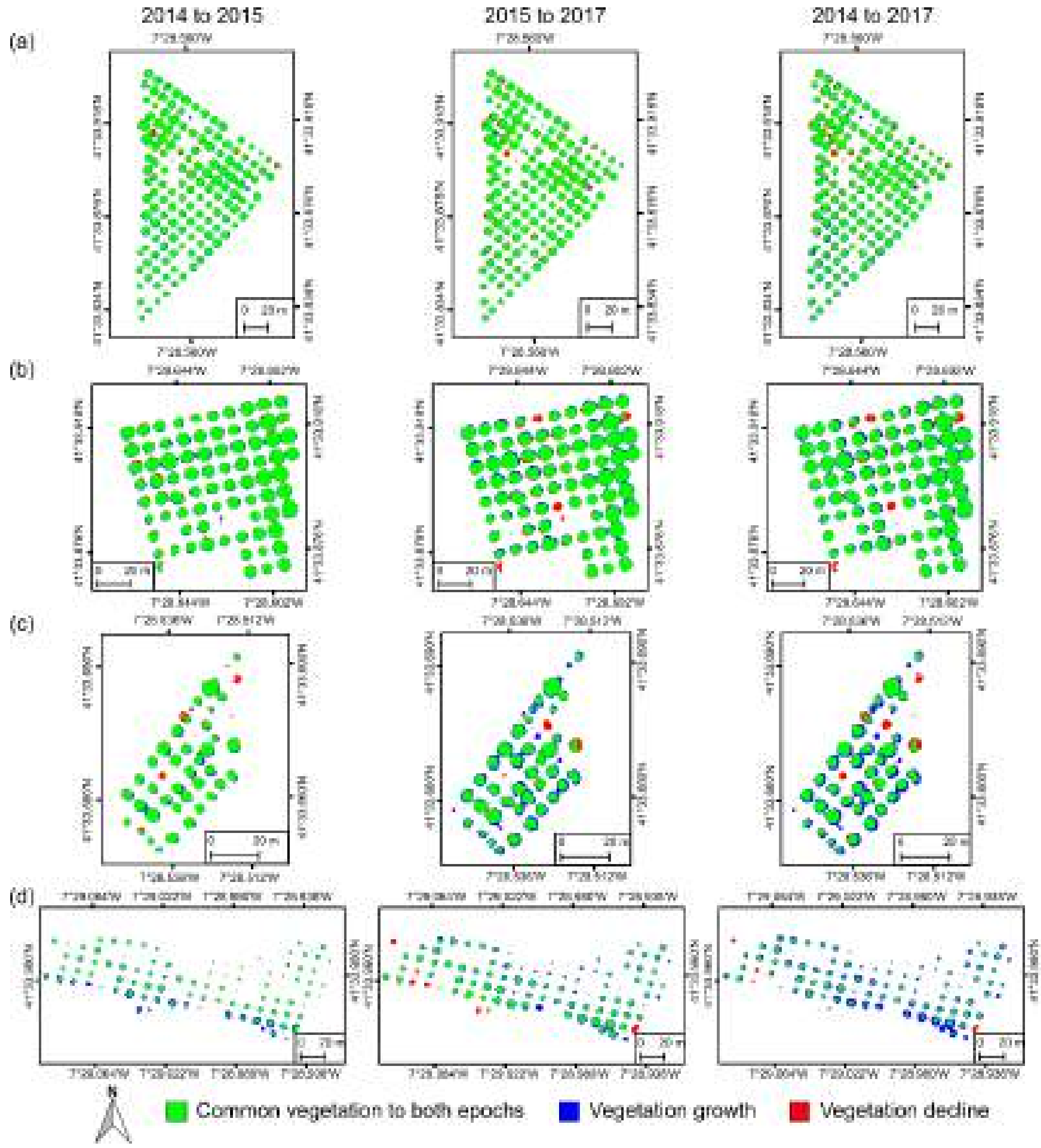


**Figure 4.14.** Multi-temporal analysis between three different periods: (a) Plantation 1; (b) Plantation 2; (c) Plantation 3; and, (d) Plantation 4. Left represents 2014 to 2015; centre 2015 to 2017; and, in the right 2014 to 2017.

### 4.3.5.2. Tree-Level Analysis

The proposed method is also able to perform a multi-temporal analysis at the tree-level. This is only possible due to method's step 3—cluster isolation—where the trees are properly separated. To illustrate the method's performance, Figure 4.16 highlighted the results of ten trees. Those trees refer to the line of trees that is present in the top of plantation #2 (Figure 4.9b) and it is used to illustrate the behaviour of the proposed method.

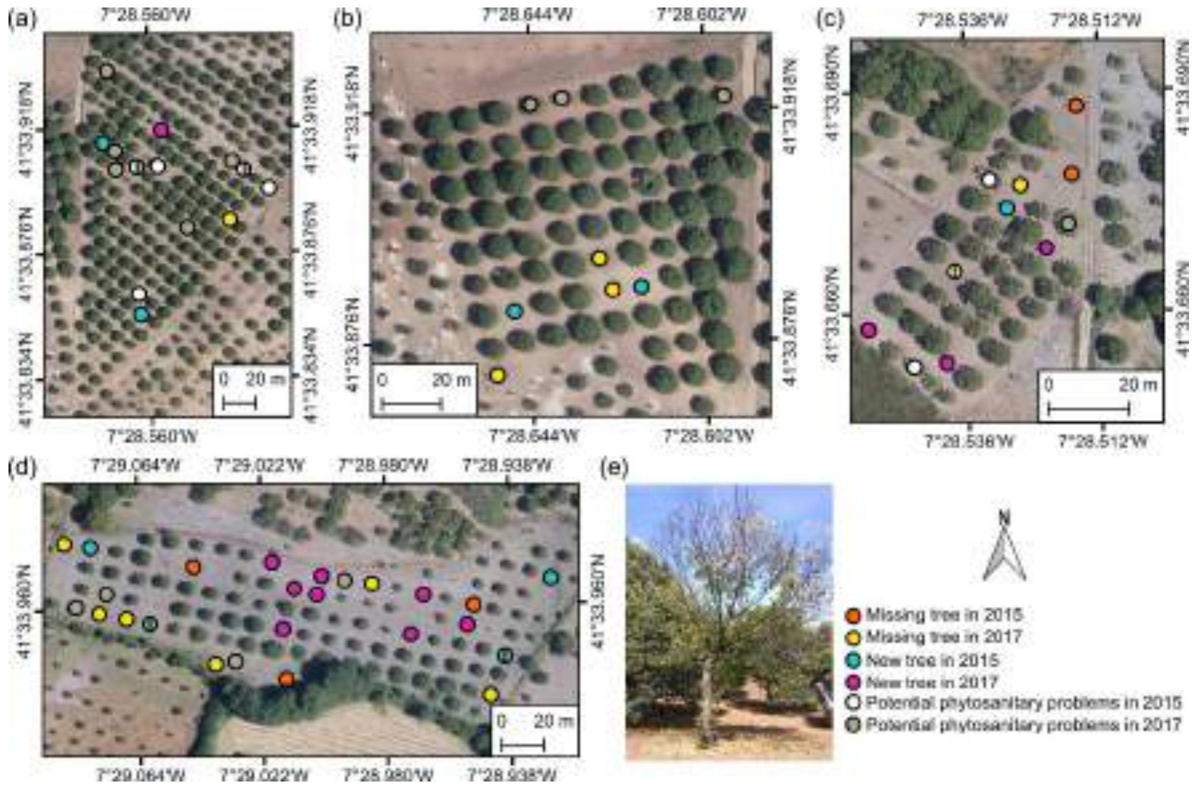


**Figure 4.15.** Missing trees, new trees and trees with potential phytosanitary problems detected in the multi-temporal analysis of the chestnut plantations and the period when the detection occurred: (a) Plantation 1; (b) Plantation 2; (c) Plantation 3; and (d) Plantation 4; and, (e) example of a tree affected by ink disease from plantation 2.

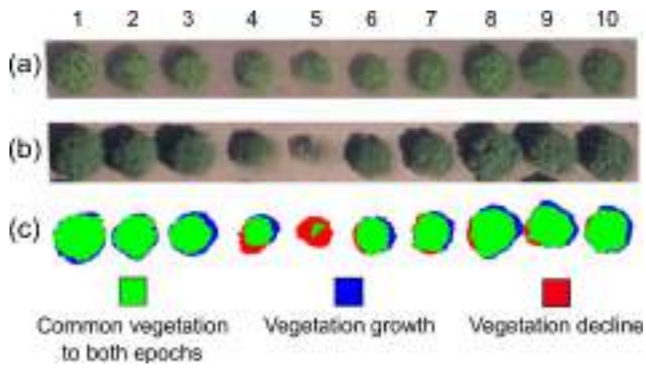


**Figure 4.16.** Multi-temporal analysis at the individual tree-level: (a) RGB image from 2014 campaign; (b) RGB image from 2017; and, (c) difference mask retrieved by the application of the proposed method.

Table 4.6 presents the quantitative results obtained from applying the proposed method to the ten trees selected.

**Table 4.6.** Multi-temporal analysis at the individual tree-level: canopy coverage area (CA), canopy diameter (D), and trees' height (H) estimation for each tree presented in the studied plantation.

| ID | 2014 | | | 2015 | | | 2017 | | |
|---|---|---|---|---|---|---|---|---|---|
| | CA ($m^2$) | D (m) | H (m) | CA ($m^2$) | D (m) | H (m) | CA ($m^2$) | D (m) | H (m) |
| 1 | 65.7 | 10.1 | 7.2 | 63.9 | 9.5 | 7.4 | 73.1 | 10.2 | 8.1 |
| 2 | 51.8 | 8.9 | 7.2 | 47.1 | 8.2 | 6.6 | 55.4 | 9.1 | 6.4 |
| 3 | 45.4 | 8.4 | 6.4 | 43.3 | 8.1 | 6.8 | 59.1 | 9.3 | 7.1 |
| 4 | 35.2 | 7.7 | 5.6 | 34.7 | 7.2 | 5.5 | 33.7 | 7.1 | 4.0 |
| 5 | 33.7 | 7.4 | 5.6 | 24.7 | 6.4 | 5.5 | 9.2 | 4.8 | 4.8 |
| 6 | 39.2 | 7.3 | 6.3 | 37.2 | 7.2 | 6.0 | 45.5 | 7.9 | 6.8 |
| 7 | 44.3 | 7.8 | 7.0 | 43.0 | 7.9 | 6.8 | 48.7 | 8.2 | 7.2 |
| 8 | 61.9 | 9.5 | 8.2 | 64.5 | 9.8 | 8.4 | 72.1 | 10.1 | 8.4 |
| 9 | 54.9 | 9.2 | 7.4 | 55.4 | 9.5 | 7.5 | 63.7 | 9.5 | 8.1 |
| 10 | 52.1 | 8.3 | 6.7 | 54.1 | 8.9 | 6.9 | 62.5 | 9.2 | 7.7 |

# 4.4. Discussion

## 4.4.1. Vegetation Coverage Area

The method achieved good overall results, even in the presence of a complex and larger scenario (Figure 4.11), which constitutes an extreme limit situation. For the complex area (Figure 4.1b), there was a slight tendency for the method to overestimate chestnut vegetation rather than underestimate it. Still, both of the values are around 11%. Concerning these errors, it was observed that a large part of the over detection is related to the difficulty of discriminating some lawns—since there were trees within the lawns—and due to some undergrowth, which have a considerable height in the CHM, making it difficult to discriminate. This was also reported in (Yin & Wang, 2019). Regarding under detection, some errors were observed on the VI in trees that had few leaves and from the CHM in some recent chestnut trees where the height information was not representative, causing misclassifications from the method. These problems persist, even when considering higher resolution UAV-based imagery (Pádua, Marques, Adáo, et al., 2018; Surový et al., 2018). Probably, those trees may be misclassified due to the absence of leaves, while considering the imagery resolution. At the same time, this fact may be used in a multi-temporal approach to highlight the trees that are potentially affected by phytosanitary problems. An important aspect is that non-vegetation features present in this area were correctly classified as being so, which includes most of undergrowth vegetation and infrastructures as buildings, which have height values that are similar to some chestnut trees.

It is worth noting that this large area (Figure 4.1b) is not representative of a chestnut plantation used for economic purposes. Indeed, most chestnut plantations, namely the more recent ones, follow a well-defined alignment. In these cases, the method's performance reaches higher overall accuracies (93 to 99%). However, when excluding non-chestnut vegetation (true negatives: soil and undergrowth vegetation), the results differ from the overall accuracy. When considering the producer's accuracy, its mean value is 90.7%, being that the higher and lower values were reached in the 2017 campaign, for plantations #1 (96.6%) and #4 (88.1%), respectively. When analysing the results in a plantation-basis, plantation #1 obtained the higher values in this parameter (94.7%), while plantation #3 obtained the lowest producer's accuracy (87.3%). When considering the producer's accuracy per epoch, this value is closer, with lower precision in 2017 (89.3%), while the higher values were obtained in 2014 (92.5%). In 2015, this value was of 90.4%. As for user's accuracy, which encompasses all chestnut vegetation present in the image (i.e. also considers chestnut vegetation classified as being not), plantation #4 is the most influenced by these errors (mean of 85.0%). This fact can be related with the type of trees present in this plantation—more recent than other plantations—and due to the lack of pixels that represent each tree at this GSD, which caused the method to not detect part of the canopies. On the other hand, plantation #2 provided higher rates in all of the seasons, with a mean value of 94.8%. The epoch with lower user's accuracy was 2015 (90.1%), followed by 2014 (91.65%) and 2017 (91.7%).

Despite the mean user's and producer's accuracy values being similar (~91%), it can be sated that the method tends to overestimate chestnut vegetation (FP), rather than underestimate it (FN). Plantation #1 was the less influenced by FP and FN, while plantation #4 was the most influenced, especially by FN. These results clearly contrast with the ones that were obtained in the overall accuracy, where plantation #4 obtained higher overall accuracy (97.4%) the remaining with accuracy around 94% to 95%. If only accuracy was analysed, the results could be wrongly interpreted, since the non-chestnut part in some plantations is considerably higher than other plantations. Indeed, the area of FN and FP is not so different and is, in most of the cases, mainly located in the borders of canopies. This way, when considering the obtained results, it can be pointed out that plantation #1 was the area with the best results, while plantation #4 was the less performant in chestnut vegetation detection. Nevertheless, another aspect is that reference masks were manually created, which means that small errors can be present.

The proposed methodology was developed with the underlying premise that it was to be used to detect and monitor chestnut trees plantations whose own characteristics and those of the trees that constitute them lead to few crown overlaps. Nevertheless, regular development of trees may bring—even when regarding with ordered plantations—canopy overlaps. These are well resolved by applying the proposed method (Figure 4.8). The study area also has some older (and therefore disordered) chestnut plantations, where the proposed method presented high precision results (Figure 4.10 right). As such, the proposed method may be potentially adapted to other plantation types. Nevertheless, further studies are needed to evaluate this issue.

### 4.4.2. Number of Detected Trees

Despite the high accuracy in the results that was obtained in the evaluation of this parameter (presented in Table 4.3), some trees were not detected, mostly in cases where trees crown was too small. This is the case of plantation #4, where the missing detection reached a mean value of 5%, when considering the three epochs. Being this mainly related to the used data, since flights were performed at 550 m height, making these small trees almost imperceptible in the image. Moreover, detection also fails when the trees present few or no foliage due to phytosanitary problems, making it almost impracticable to detect canopy vegetation through VIs. This is the case of a tree with considerable size (approximately 50 $m^2$), which was not detected in plantation #2 on the flight campaign of 2017 (see Figure 4.11b right). However, this apparent limitation constitutes a strong point of the method, since when applied in a temporal perspective, it allows for the detection of trees that are potentially affected by phytosanitary phenomena. As for over detection cases, these are related to the method's cluster separation in chestnut trees that had an irregular canopy shape, causing it to be divided into multiple clusters. However, the number of cases is relatively small (mean of 0.3%). In regards to under detection, it was only verified in plantation #3, being caused by a small tree adjacent to a considerably larger tree. Larger detections mainly occurred in chestnut trees with a considerable canopy area (see Figure 4.11b), in the other hand, smaller detections cases were observed in smaller chestnut trees (see Figure 4.11d). The proposed method accuracy is above or in line with the existing similar methods for tree detection. In Mohan et al. (2017), an open canopy mixed conifer forest was surveyed and a total of 312 trees were detected by their method, from a total of 367 reference trees with an accuracy of 85%, missing 55 trees. However, 46 trees were over detected, performing a total of 358 trees. Ok and Ozdarici-Ok (2017) evaluated individual citrus trees delineation from UAV-based DSMs, and an overall precision of 91.1% in a pixel-based analysis and 97.5% in the object-based analysis was obtained by the method. The results from the proposed method are also greater or in line with the ones that were obtained from the application of complex and expansive LIDAR data (Liu et al., 2015; Luke Wallace et al., 2014).

### 4.4.3. Tree Height and Crow Diameter Estimation

The results that were obtained for tree height and crown diameter estimation are in line or even better than the ones from another studies. Tree height estimation was the less accurate when comparing both parameters. However, when considering that the instrument used in the measurements has an intrinsic error of about 20 cm, this accuracy is perfectly acceptable (Mohan et al., 2017). Moreover, some errors can be related to the used digital elevation models, since the flight was performed at 550 m height (GSD ~16 cm). When considering the differences for the flight performed at 100 m height (GSD ~3 cm), as expected, there is a direct correlation between height accuracy and image resolution: the better the spatial resolution the better the reached accuracy. It is worth noticing that, in most cases, the flight height will be lower than 120 m (UAV regulations (Regulamento nº 1093/2016, 2016)), which assures the method's effectiveness, even in the estimation of trees' height. The results prove the effectiveness of the proposed method in the estimation of structural properties (tree height and canopy diameter) of chestnut trees, with a good hit rate and with a relatively low error. Zarco-Tejada et al. (2014) conducted a tree height assessment of 152 olive trees, with heights that range between 1.16 and 4.38 m, a $R^2$ = 0.83 and a RMSE of 35 cm was obtained. Similarly, to this study, the results tended to be less precise in lower spatial resolutions. Panagiotidis et al. (2017) obtained a $R^2$ = 0.72 to 0.75 and RMSEs of 3 m in two plots (48 and 39 trees, ranging from 15 to 35 m). As for tree crown diameter a RMSE of 0.82 and 1.04 m and $R^2$ = 0.63 and 0.85, for plot 1 and 2, respectively, with a diameter varying from 11 to 19 m. Díaz-Varela et al. (2015) acquired UAV-based imagery to estimate parameters from olives (150 trees, heights ranging between 1 and 3 m) with 7 cm GSD, obtaining a RMSE of 0.45 ($R^2$ = 0.07) for tree height and for tree crown diameter obtained an RMSE of 0.32 ($R^2$ = 0.58), with values that range from 1 to 2.5 m. Lim et al. (2015) evaluated tree detection using DSM from photogrammetric processing of UAV-based imagery, and obtained a RMSE of 0.84 m for tree height coniferous trees and 2.45 m for deciduous coniferous trees, tree crown width of crown an RMSE varying from 1.51 m to 1.53 m was obtained for each area. Iizuka et al. (2018) obtained a RMSE of 1.7m from heights that ranged from 16 to 24 m. Guerra-Hernández et al. (2018) compared the accuracy in tree detection using ALS and UAV-based imagery in eucalyptus trees with heights that ranged from 10 to ~20m. The authors obtained RMSE values from 1.83 to 2.84 and correlation coefficient (r) 0.61 to 0.69. Moreover, it was reported that ALS performed better in steep slope areas. Guerra-Hernández (2016) extracted properties from 52 *Pinus pinea* L. trees also evaluating crown diameter and tree height using UAV-based imagery (GSD of 6.23 cm). Obtaining $R^2$ = 0.81 and RMSE of 0.45m for tree height (7 to 12 m), as for tree crown diameter, the authors found an RMSE of 0.63 m and $R^2$ = 0.95 for tree diameter (6 to 14 m). Pádua et al. (2018) obtained $R^2$ values that ranged from 0.91 to 0.96 from an area that was composed mostly by chestnut trees, in flights ranging from 30 to 120 m and RMSEs from 0.6 to 0.33 m. Despite the overall good results, the flights at lower heights had lower accuracies than flights that were performed higher, it was also reported that double-grid flights had an increase in accuracy. Popescu et al. (2003) obtained $R^2$ from 0.62 to 0.63 for tree crown diameter estimation and a RMSE 1.36 to 1.41 m using LIDAR data for pines and deciduous trees. Despite both parameters showing a good regression agreement, further studies must be done, especially by evaluating recent chestnut plantations composed of trees with lower heights and, therefore, irregular canopy shapes (Surový et al., 2018). Different spatial resolutions can also be evaluated.

### 4.4.4. Multi-Temporal Analysis

UAV-based multi-temporal analysis remains a topic not broader explored, and some studies have focused on this topic. Guerra-Hernández et al. (2017) proposed a method for multi-temporal analysis to monitor the growth of *Pinus pinea* L. with different treatments. Michez et al. (2016) employed a multi-temporal analysist for riparian forests monitoring. UAVs can carry different sensors, providing more properties to be evaluated for chestnut trees monitoring, as, for instance, UAV-based thermal infrared imagery can provide insights on water status level of trees (David Gómez-Candón et al., 2016; Park et al., 2015), or vegetation indices, from multispectral imagery, to provide plant vigour and disease detection (Gago et al., 2015).

Concerning the multi-temporal analysis that was conducted in Section 4.3.5, the four plantations had a growth in its chestnut canopy area, for the spanned period addressed in this study. The higher development was observed in plantation #4, with a growth of more than 1000 $m^2$ (126%). A similar behaviour is also noticeable in the mean tree development values, with +1.1 m in height, +1.6 m in canopy diameter, and 11.5 $m^2$ in canopy area. This plantation was mostly composed by younger chestnut trees when compared to the other plantations, then with a greater margin of development. The plantation with the lowest development was plantation #1, which had a growth of around 240 $m^2$ (4.6%) in the period of 2014 to 2017. However, a case of chestnut decline was verified in this plantation from 2015 to 2017 period with -85 $m^2$ (-1.5%). As for the remaining two plantations, plantation #2 had an overall growth of 499 $m^2$ (12.9%) and plantation 3 growth was 257 $m^2$ (42.1%). By analysing the obtained results, it can be stated that plantations that contained more recent chestnut trees had the higher growth rates (plantations #3 and #4), whereas plantations with adult chestnut trees presented lower growth rates (plantations #1 and #2), which was expected. When observing the mean chestnut tree parameters per plantation, the higher values were verified in plantation #4, as previously mentioned, followed by plantation #3, with a mean growth of approximately 1 m for tree height and canopy diameter, and finally by plantations #1 and #2, which presented 0.5m growth for tree height, as tree diameter plantation #2 presented a mean growth of 0.5 m and plantation #1 showed the lower value of 0.3 m. Regarding the mean canopy area, plantation #2 presented 6.9 $m^2$ growth, while plantation #3 presented 5.5 $m^2$ growth. Again, plantation #1 showed the lower growth value, being 1.1 $m^2$.

As for the number of trees in the plantations (Figure 4.15), it was observed that more changes were verified in more recent plantations (plantations #3 and #4), with this being mainly related to some chestnut trees that were cut off from the plantation as well with the detection of smaller trees, whereas the older chestnut plantations presented less changes. Concerning the detection of potential phytosanitary problems, for plantations #2 and #4, these cases were only verified in data from 2017 campaign. There was one case in plantation #3 of a chestnut tree with potential phytosanitary problems detected in 2015, which lead to the tree to be removed and become missing in 2017 campaign. Consecutive decline was verified in two trees from plantation #1. Two trees that were detected in plantation #4, in 2015, where signalled as potentially affected by phytosanitary problems in 2017. Thus, the method showed its effectiveness in the multi-temporal analysis of chestnut plantations. Figure 4.15e presents a chestnut tree that was infected by ink disease, as observed in the 2017 campaign at plantation #2. This represents that, despite some problems in the development of young trees and the presence of phytosanitary problems, there is still an interest in the this crop, as reported in Martins et al. (2015) and Pádua et al. (2017).

Regarding the results from the multi-temporal analysis of individual trees, as presented in Section 4.3.5.2, a growth in the canopy coverage and diameter of the analysed chestnut trees was verified (Figure 4.16 and Table 4.6). However, trees #4 and #5 showed a regression in those parameters. Particularly, chestnut tree #5 had a coverage area regression of 25.3 $m^2$ (-78%) and a decrease of 3.6 m in its diameter (-53%). A field campaign confirmed that this decline was due to the chestnut ink disease (Figure 4.15e). Apart from these two cases, the chestnut trees that are represented in Figure 4.16 had an average growth of 7.5 $m^2$ (+15%) in their canopy coverage area and 0.6 m (+7%) in their diameter. Regarding trees' height, it was referred before that the model quality influences the measurement quality. However, chestnuts trees #2, #4, and #5 showed a regression in height well beyond the expected error. Despite these regressions in the trees' height, the remaining chestnut trees showed an average growth of 0.4 m (+5%).

This way, the method that is proposed in this study as the ability to individually detect chestnut trees and to extract dendrometric parameters in chestnut plantations with the ability to perform multi-temporal analysis and to detect trees with potential phytosanitary problems. When considering other remote sensing platforms, this approach makes use of the flexibility that is provided by UASs to acquire data on-demand with higher spatial resolution that other platforms, which cloud coverage (Pádua, Vanko, et al., 2017) and lower operational costs can also affect, when compared to manned aircrafts (Alessandro Matese et al., 2015). When comparing the UAV-based approach against field surveys, the method can quickly cover larger areas in a lower temporal window and directing management operations to trees with potential phytosanitary problems

## 4.5. Conclusions and future work

An automatic method was developed to assist chestnut tree management operations from aerial images. The presented research used several types of chestnut plantations with mixed tree density, size, and background covers, covering most of the real-world scenarios to develop and validate the proposed method, which includes image segmentation, based on CHM and VIs, and the extraction of chestnut tree parameters.

For image segmentation, different VIs that are based on NIR and RGB bands combinations were evaluated on a complex area composed of thousands of trees in a mixed environment. Moreover, a novel VI was proposed for vegetation segmentation in CIR imagery, ExRE. The segmentation accuracy on a pixel-based level was evaluated and a rate that is greater than 95% was reached. VIs using NIR band on its computation allowed for obtaining slightly better results, however the overall RGB-based VIs performance allows for the proposed method to be applied to aerial images that were acquired from low-cost consumer-grade cameras, commonly used in UAS.

Experiments were conducted to evaluate the behaviour of the proposed method estimating the global parameters of chestnut plantations, such as the total vegetation cover area, the total number of trees, and the trees' height and crown diameter. The values that were estimated for the proposed method were compared with ground-truth data obtained in-field measurements. In the case of vegetation coverage and trees counting, the accuracy was greater than 90%, respectively, 91% and 97%. Regarding parameters that can be adjusted by a linear regression, as the case of tree heights and crown diameter, two sets of images, obtained at 550 m and 100 m height were used, and the proposed method fits the model with an accuracy of 86%, with a RMSE of 0.33 m, for the tree heights, and with an accuracy of 96% with RMSE of 0.44 m for the crown diameters. In the determination of these parameters, a correlation with the accuracy and the flight height was found. Indeed, the accuracy increases with image resolution. Thus, at the maximum legal flight height (120 m), the proposed method performs very well.

In summary, this research has proven that UAV-based imagery is a fast and stable method in chestnut tree parcel management. The overall results suggest that the proposed method can be used as an effective alternative to the manual method for monitoring chestnut plantations.

The experiments that were made in the different study plantations allow for us to conclude that the method is generally used for chestnut trees monitoring. Of course, it is more effective if applied to parcels that were created for sustainable production. Usually, in this type of plantations, the trees are distributed in a grid-shape. Moreover, the method would be performant in other plantation sites (e.g. olives, orchards) so long as they are planted in a grid-shape and the shape of those specific trees, in an aerial image, is very similar. Research towards chestnut plantations that were affected by different phytosanitary problems (chestnut ink disease, chestnut gall wasp and nutritional deficiencies) and how chestnut trees in-season growth is affected is being conducted.

Furthermore, the method allows a multi-temporal analysis, which constitutes a useful and powerful tool in chestnut plantation management. Therefore, by enabling the substitution of time-consuming and costly field campaigns, this automatic method represents a good contribution for managing chestnut plantations, providing equivalent results when applied at the tree-level and plantation-level studies, both for static and multi-temporal analysis. Thus, the proposed approach exposed the future potential of UAV-based analysis for plantation monitoring. Future research should focus on forest monitoring and management, but also in the estimation of individual tree attributes, such as tree height, crown size, and diameter, and thereby develop predictive models for estimating biomass and stem volume from UAV-imagery as to discriminate/detect chestnut trees that are affected by biotic or abiotic problems.

# Acknowledgements

Funding: This work was financed by the European Regional Development Fund (ERDF) through the Operational Programme for Competitiveness and Internationalisation - COMPETE 2020 under the PORTUGAL 2020 Partnership Agreement, and through the Portuguese National Innovation Agency (ANI) as a part of project “PARRA - Plataforma integrAda de monitoRização e avaliação da doença da flavescência douRada na vinhA” (Nº 3447).

This work supported by the North 2020 - North Regional Operational Program, as part of project “INNOVINEandWINE - Vineyard and Wine Innovation Platform” (NORTE–01–0145–FEDER–000038).

# Chapter 5.

## Monitoring of Chestnut Trees Using Machine Learning Techniques Applied to UAV-Based Multispectral Data

*Remote Sensing*, 2020, *12*(18), 3032

Journal Impact Factor – 2019: 4.509

5 Year Impact Factor – 2019: 5.001

**Luís Pádua**, Pedro Marques, Luís Martins, António Sousa,
Emanuel Peres and Joaquim J. Sousa

Refer to https://doi.org/10.3390/rs12183032 for online published version

## 5.1. Introduction

Chestnut trees (*Castanea sativa* Mill.) are one of the most important species in Portugal for both forestry and agricultural purposes. In an agricultural context, in 2018, this species represented a surface of 38,728 ha with 33,929 tons of chestnuts produced. It is especially relevant in the northern region of the country, where it represents 89% of planted surface (34,504 ha) and 88% of yield (29,908 tons) (Instituto Nacional de Estatística, I. P., 2019). Chestnut trees can be affected by several phytosanitary issues due to both biotic or abiotic factors. These issues can significantly impact the chestnut development and yield (Luís Martins et al., 2014). Chestnut ink disease (*Phytophthora cinnamomi* Rands) (Valverde et al., 2017), chestnut blight (*Cryphonectria parasitica* (Murr.) Barr.) (Rigling & Prospero, 2017), nutritional deficiencies (Portela et al., 2003) and, more recently (June 2014), the chestnut gall wasp (*Dryocosmus kuriphilus* Yasumatsu) (Aebi et al., 2006), are among the most meaningful biotic and abiotic factors that can affect chestnut trees. The phytosanitary condition of chestnut stands is usually evaluated by in-field observations, which are time-consuming, laborious, demand specialized human resources, and are based on small samples. Using currently available methods and tools, all based on manual and laborious measurements, phytosanitary conditions monitoring over a longer period of time is even more challenging.

Remote sensing can be considered as a viable approach to help in monitoring and managing chestnut stands regarding phytosanitary issues caused by either biotic or abiotic factors. There are several studies published using remote sensing platforms coupled with different sensors that have chestnut trees as their research subject. Small format aerial photography via manned aircrafts was used to assess chestnut ink disease (Ambrosini et al., 1997; L. M. Martins et al., 2001; Vannini et al., 2005) and chestnut blight (Ambrosini et al., 1997). The same aerial imagery format was also used to assess chestnut ink disease and blight spread through the use of geostatistical methods (J. Castro et al., 2010; L. Martins et al., 2007) and to discriminate different phytosanitary statuses (Luís Martins et al., 2005). Airborne low-density LiDAR (Light Detection and Ranging) data were also used for biomass estimation (Montagnoli et al., 2015). However, these initial attempts to use aerial images to assess chestnut trees' health status revealed low correlation. More recently, Marchetti et al. (2019) proposed an approach for mapping chestnut stands using WorldView satellite multispectral imagery, enabling the classification of chestnut stands within a heterogeneous landscape.

Meanwhile, unmanned aerial vehicles (UAVs) have been established as a versatile remote sensing platform capable of being coupled to an array of different sensors and to operate under diverse flight and terrain conditions. Furthermore, they are also able to adapt to specific requirements for monitoring different crops (both temporal and spatial). Precision agriculture and forestry have greatly benefited from this remote sensing platform in the last few years, with many advances being published and already in use. As for studies related to chestnut trees, orthophoto mosaics obtained through photogrammetric processing of high-resolution imagery acquired from UAVs were used by Martins et al. (2015) to monitor 231 ha of chestnut trees. By comparing these data with aerial imagery acquired almost ten years earlier, it was possible to measure areas of new plantations and to assess the decline of chestnut trees. The main conclusion drawn by this study was that the decline was very significant along that time period. The study was extended to subsequent years, and the results are presented in Pádua el al. (2017), where a decline from 2014 to 2015 was confirmed. A novel method based on image processing was proposed in Marques et al. (2019), enabling the automatic monitoring of chestnut trees through estimation of some of the main parameters, such as tree height and crown diameter and area. By applying this methodology, multi-temporal analysis was possible both at the tree and plantation level. Di Gennaro et al. (2020) used a similar method to estimate the pruning wood biomass of chestnut trees. Finally, in Pádua et al. (2018), the impact of different flight heights in the estimation of tree height and crown diameter was evaluated using UAV-based RGB imagery. It was concluded that flight altitudes of 60 and 120 m (corresponding to a spatial resolution of 2.65 and 5.25 cm, respectively) presented the best overall results.

Nonetheless, despite the numerous advances in monitoring chestnut trees provided by the use of UAV-based high-resolution aerial imagery, little progress has been made in both automatic detection and classification of the biotic or abiotic factors that can affect them. The ability to act (or react) in the timely detection of factors that can negatively affect the phytosanitary condition of a chestnut stand will be essential to improve management practices and, therefore, have a significant social and economic impact. In this study, we explore UAV-based multispectral imagery with high spatial and temporal resolutions (Pádua, Vanko, et al., 2017) of chestnut stands to detect potential phytosanitary problems.

There are studies with comparable objectives for vineyards (Albetis et al., 2017) to detect Flavescence dorée, for olive groves (P. J. Zarco-Tejada et al., 2018) to detect symptoms of Xylella fastidiosa, and for oil palm plantations (Shamshiri et al., 2018) to assess health status and disease detection. Balasundram et al. (2020) provided insights into the deployment of site- and time-specific approaches to manage plant disease problems. However, and according to the authors' best knowledge, there are no similar studies or approaches applied to chestnut trees. Indeed, the challenge is even greater when dealing with chestnut trees as there are several biotic and abiotic factors that can cause similar symptoms, with very different mitigation treatments or methods.

As such, seeking to determine precisely which factors are affecting a given tree, the proposed methodology also includes an incremental approach based on machine learning methods. Several flight campaigns were accomplished to acquire multispectral imagery over a chestnut stand located in north-eastern Portugal. Furthermore, field surveys were also conducted, by an expert, to obtain the phytosanitary characterization of every individual chestnut tree within the monitored area. The proposed methodology begins by applying photogrammetric processing to the acquired high-resolution aerial imagery. Then, tree crowns are detected using the outcomes of the first step. A random forest (RF) classifier is then applied to distinguish healthy trees from those affected by any biotic or abiotic factor. This process is repeated to determine which phytosanitary problem is affecting each tree. Multi-temporal analysis comes into play by applying the proposed methodology to data acquired in different flight campaigns that occur in the same growing season. It is a contributing factor to improve this methodology' precision as some chestnut trees were asymptomatic or showed a low incidence of phytosanitary issues early in the growing season. The proposed methodology is able to distinguish healthy chestnut trees, and it can also identify which is the specific limiting factor affecting the development of each tree.

## 5.2. Materials and Methods

### 5.2.1. Study Area Characterization

Research involving trees, in general, and chestnut trees, in particular, requires keen knowledge of the area under study. The studied chestnut stand is a laboratory area located in north-eastern Portugal (Figure 5.1a, 41°22–42.8N, 7°35–01.4W, altitude 760 m) within one of the main chestnut production regions in Portugal (M. Pereira et al., 2011). It has an area of approximately 0.4 ha and is composed of 52 trees from which 46 are chestnut trees (marked in Figure 5.1b). This area was rigorously characterized by experts from the University of Trás-os-Montes e Alto

Douro (Vila Real, Portugal), and to ensure the representativeness of this area, the most common cultural practices were also used (Marques et al., 2019).

In-field observations were carried out during the 2018 growing season, on the same dates as the flight campaigns, to assess the phytosanitary condition of the chestnut stand. Issues such as chestnut ink disease and potential nutritional deficiencies were evaluated using a discrete scale ranging from zero (absence) to four (strong incidence). Furthermore, the condition of each chestnut tree was evaluated using a five-level scale ranging from 1 = very bad condition to 5 = excellent condition, considering the severity of the phytosanitary issues along with the overall tree status. This qualitative classification was performed by an expert and based on the severity of visible symptoms (L. M. Martins et al., 2015). Dendrometric measurements of each tree were also acquired. Soil analyses were also conducted to assess the nutrient levels.

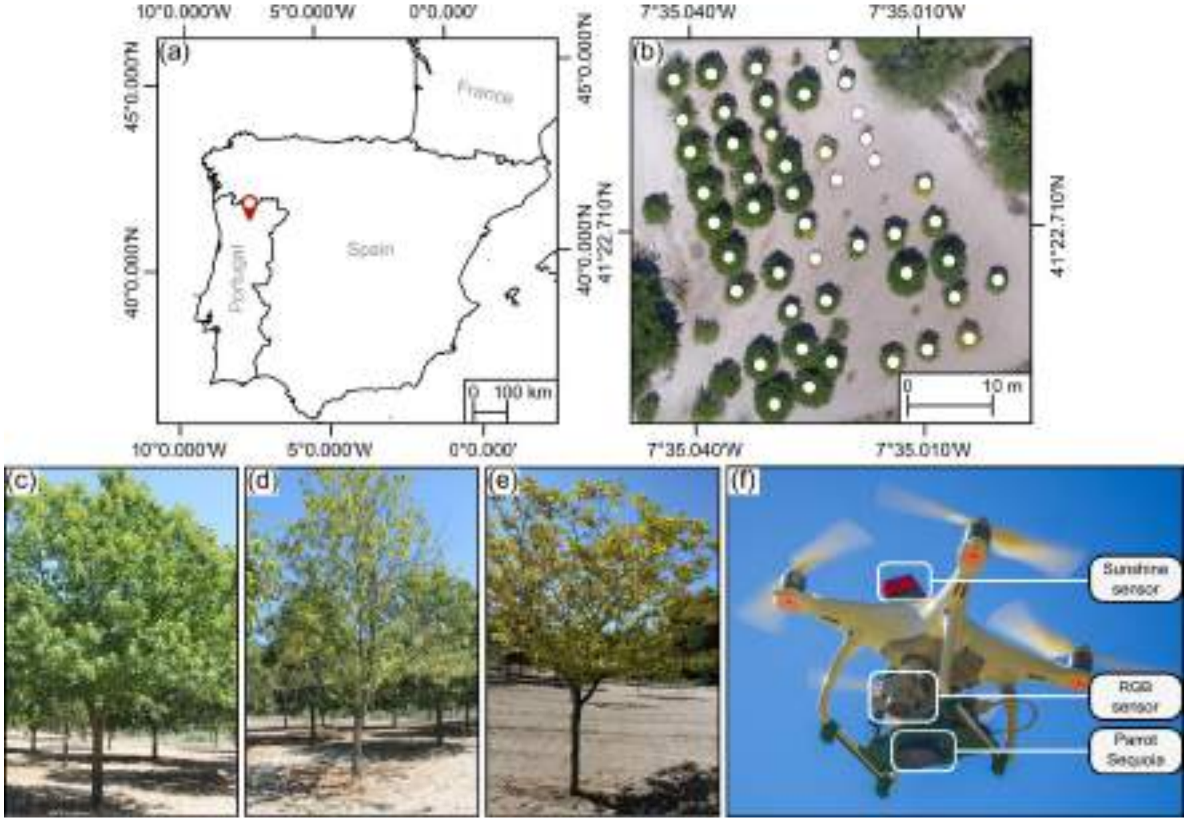


**Figure 5.1.** Study area overview: (a) geographic location in Portugal's mainland; (b) aerial overview of the chestnut stand, where chestnut trees are marked (WGS84, coordinate system, EPSG:4326). Ground perspective of some of the monitored trees, showing (c) absence of visual symptoms, (d) chestnut ink disease, and (e) nutrient deficiency. Unmanned aerial vehicle during take-off (d), used sensors are highlighted.

### 5.2.2. UAV-Based Data Acquisition

A DJI Phantom 4 (DJI, Shenzhen, China) was used to acquire the aerial imagery used in this study. This multi-rotor UAV comes equipped out-of-the-box with a complementary metal oxide semiconductor (CMOS) sensor—mounted in a 3-axis gimbal—capable of acquiring georeferenced RGB imagery with 12.4 MP resolution (details about UAV and sensor specifications can be found at (DJI Official, n.d.)). The UAV was modified to support multispectral imagery acquisition (Figure 5.1f) using the Parrot Sequoia (Parrot SA, Paris, France). This sensor is composed of a camera array responsible for acquiring green, red, red-edge (RE), and near-infrared (NIR) single-band images. Each band has a 1.2 MP resolution. For radiometric calibration of the multispectral imagery, irradiance data are acquired during flight (from a sensor positioned at the top of the UAV—see Figure 5.1f) and, prior to each flight, reflectance data are acquired using a calibration target.

Flight campaigns were carried out throughout the growing season of 2018 to acquire multispectral aerial imagery. A flight mission was planned to provide a complete overview of the area, in a double-grid pattern, with 80% overlap between images and 70% overlap between flight lines. Flight height from the take-off point was set to 60 m, and the total area covered by flights was approximately 2 ha. Considering the planned imagery overlap and the flight height, the sensor was set up to acquire images at each 11 m travelled. The same flight plan was used for all flight campaigns.

The selected dates—27 May, 24 June, 8 July, 8 August, 25 September, and 16 October—allowed spanning across the most important stages of chestnut tree development: sprouting, flowering, fruiting, and defoliation. The vegetative dormancy of chestnut trees usually spans from November to March (Bergonoux et al., 1978).

### 5.2.3. Data Processing

Figure 5.2 presents the main steps of the proposed methodology as applied to each flight campaign's data. Outcomes generated from the initial photogrammetric processing enable output of a crop height model (CHM) and several vegetation indices. The latter are computed from different combinations of the four acquired bands and can be used for different purposes: (1) individual tree crown detection; (2) object-based image analysis (OBIA); and (3) dataset features. Training and prediction processes are the same to (1) classify the presence of phytosanitary issues, and (2) to identify the specific phytosanitary issue (if any). Only the number of classes varies. The proposed methodology remains functional, regardless of the sensor used.

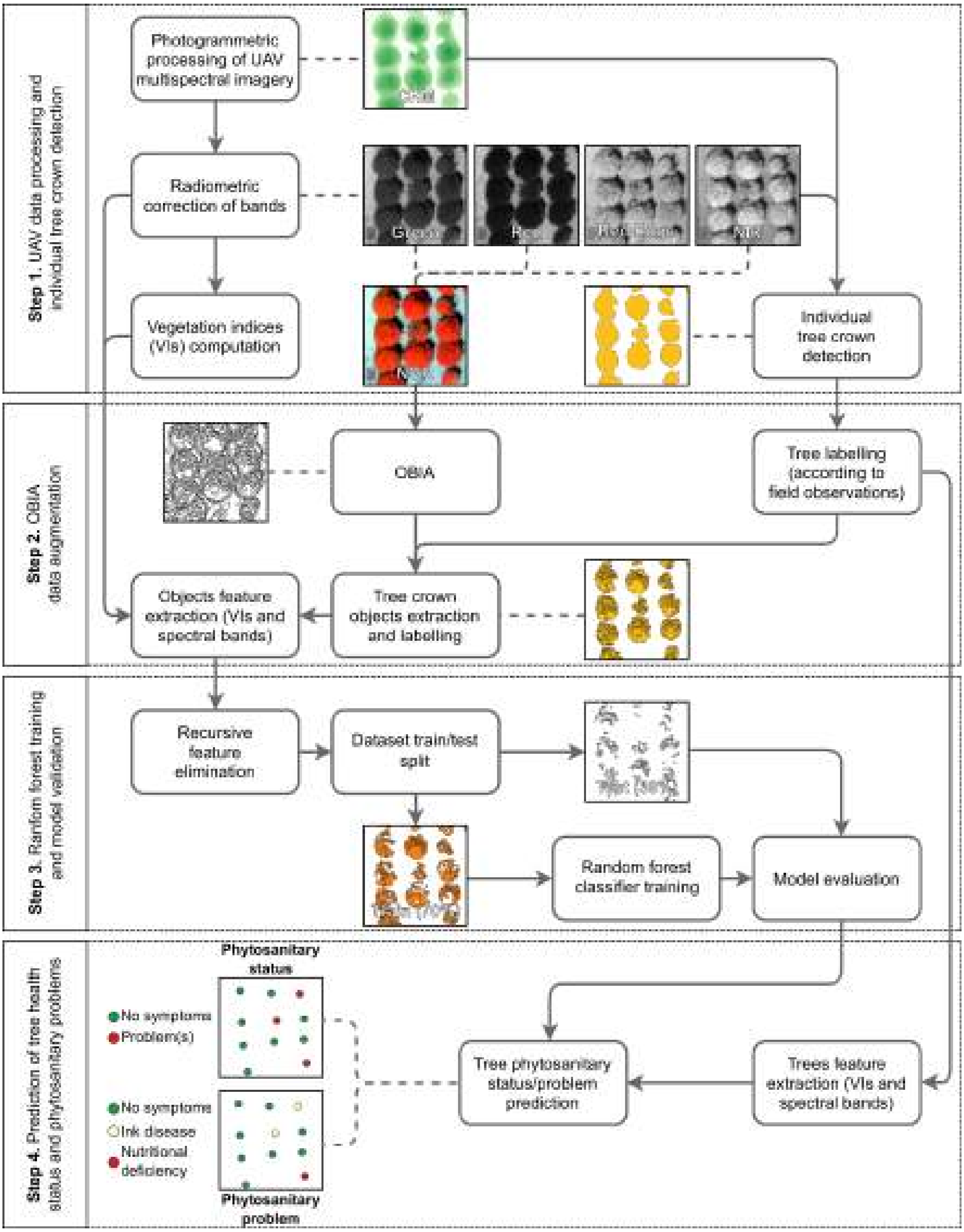


**Figure 5.2.** Main steps of the proposed methodology for data of a single flight campaign.

### 5.2.3.1. Photogrammetric Processing and Vegetation Indices Computation

Pix4DMapper Pro (Pix4D SA, Lausanne, Switzerland) was used to achieve the photogrammetric processing of the acquired aerial imagery. It provides a complete processing pipeline dealing with imagery correction, alignment, and radiometric calibration, producing dense point clouds.

Within this study, RGB orthophoto mosaics were computed for visualization purposes only. Despite the flight campaigns being carried out at the same height with both sensors, their spatial resolution differs. Indeed, due to different sensor resolutions, the ground sample distance (GSD) of the RGB imagery is approximately double that of the multispectral imagery (2.6 and 6 cm, respectively). Point cloud density, per $m^3$, was, respectively, ~500 and ~40 points. Data from both sensors were aligned relative to each other by using points that are clearly identifiable in the imagery and then merged, and geometric correction was applied using ground control points (GCPs) using both natural features and artificial targets.

In projects using multispectral imagery, a radiometric calibration is performed. Reflectance maps are generated for each band, and the most relevant vegetation indices—suggested in the literature—to monitor spatiotemporal variations in biomass and yield and to estimate leaf pigments (Albetis et al., 2017) are computed (Table 5.1). A digital surface model (DSM) and a digital terrain model (DTM) are also generated, and a CHM is computed. This process was accomplished in QGIS software by subtracting the DTM to the DSM.

**Table 5.1.** Computed vegetation indices found in the literature and their respective equations.

| Name | Equation | Ref. |
|---|---|---|
| Normalized Difference Vegetation Index | $\mathrm{NDVI} = \frac{\mathrm{N} - \mathrm{R}}{\mathrm{N} + \mathrm{R}}$ | (Rouse et al., 1974) |
| Green Normalized Difference Vegetation Index | $\mathrm{GNDVI} = \frac{\mathrm{N} - \mathrm{G}}{\mathrm{N} + \mathrm{G}}$ | (Gitelson et al., 1996) |
| Green Red Vegetation Index | $\mathrm{GRVI} = \frac{\mathrm{G} - \mathrm{R}}{\mathrm{G} + \mathrm{R}}$ | (Tucker, 1979) |
| Normalized Difference Red Edge | $\mathrm{NDRE} = \frac{\mathrm{N} - \mathrm{RE}}{\mathrm{N} + \mathrm{RE}}$ | (Barnes et al., 2000) |
| Soil Adjusted Vegetation Index | $\mathrm{SAVI} = \frac{\mathrm{N} - \mathrm{R}}{\mathrm{N} + \mathrm{R} + \mathrm{L}} \times 1 + \mathrm{L}$ | (Huete, 1988) |
| Renormalized Difference Vegetation Index | $\mathrm{RDVI} = \frac{\mathrm{N} - \mathrm{R}}{\sqrt{\mathrm{N} + \mathrm{R}}}$ | (Roujean & Breon, 1995) |
| Simple Ratio | $\mathrm{SR} = \frac{\mathrm{N}}{\mathrm{R}}$ | (Birth & McVey, 1968) |
| Transformed Chlorophyll Absorption Reflectance Index | $\mathrm{TCARI} = 3\left[(\mathrm{RE} - \mathrm{R}) - 0.2(\mathrm{RE} - \mathrm{G}) \times \frac{\mathrm{RE}}{\mathrm{R}}\right]$ | (Haboudane et al., 2004) |

G: Green; R: Red; N: NIR; RE: Red edge; L = 0.5.

In addition to the vegetation indices shown in Table 5.1, new ones are proposed in this study. In fact, knowledge about the typical spectral signature of symptomatic and asymptomatic chestnut trees, allowed to conclude the relevance of the red-edge (RE) and near-infrared (NIR) regions. Figure 5.3 presents the spectral signatures for the main issues identified in the chestnut stand (chestnut ink disease and nutritional deficiencies) and for chestnut trees with no visible symptoms obtained from UAV-based hyperspectral data using the Nano-Hyperspec® VNIR (400–1000nm) imaging sensor (Headwall Photonics, Inc., Massachusetts, USA). Significant differences among them are observed along spectrum; in the visible part (400–690 nm), a higher reflectance is achieved in trees with nutritional deficiencies, followed by trees with no visible symptoms, while in the RE and NIR parts (690–900 nm), the opposite is verified. Trees affected by the ink disease always presented the lowest reflectance.

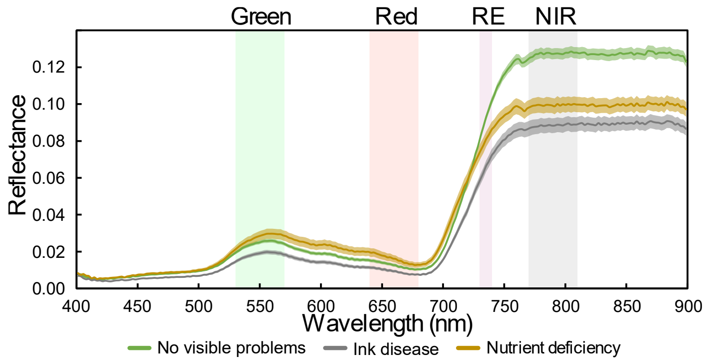


**Figure 5.3.** Typical spectral signatures and standard error, computed using the average of 100 points, in chestnut trees with no symptoms and from trees with chestnut ink disease and nutrient deficiency. Spectral band width of the four Parrot Sequoia bands is highlighted.

Therefore, customized vegetation indices were developed considering the strong influence of the RE and NIR bands. These vegetation indices are inspired by the Excess Green Index (ExG) (D. M. Woebbecke et al., 1995) that showed effectiveness in weed discrimination (D. M. Woebbecke et al., 1995), crop identification (Kiani & Jafari, 2012; G. E. Meyer & Neto, 2008) and quantification (Kim et al., 2018), early-season crop monitoring (Marcial-Pablo et al., 2019), and multi-temporal mapping of vegetation fractions (J. Torres-Sánchez et al., 2014) using both close-range and UAV-based imagery. Thus, the assumption that added weight of both RE and NIR bands would improve the detection of phytosanitary problems was made (Figure 5.3). Two new vegetation indices are proposed and were named Excess NIR (ExNIR) and Excess RE (ExRE) and are represented by the following equations:

$$\mathrm{ExNIR} = 2 \times \mathrm{N_n} - \mathrm{G_n} - \mathrm{R_n} - \mathrm{RE_n}, \quad (1)$$

$$\mathrm{ExRE} = 2 \times \mathrm{RE_n} - \mathrm{G_n} - \mathrm{R_n} - \mathrm{N_n}, \quad (2)$$

where $G_n$, $R_n$, $NIR_n$ and $RE_n$ corresponds to the division of, respectively, green, red, NIR and RE bands by the sum of the four bands. Normalized difference versions of the two proposed indices, the Normalized Difference Excess NIR (NDExNIR) and the Normalized Difference Excess RE (NDExRE), were also computed as follows:

$$\mathrm{NDExNIR} = \frac{2 \times \mathrm{N_n} - \mathrm{G_n} - \mathrm{R_n} - \mathrm{RE_n}}{2 \times \mathrm{N_n} + \mathrm{G_n} + \mathrm{R_n} + \mathrm{RE_n}} \tag{3}$$

$$\mathrm{NDExRE} = \frac{2 \times \mathrm{RE_n} - \mathrm{G_n} - \mathrm{R_n} - \mathrm{N_n}}{2 \times \mathrm{RE_n} + \mathrm{G_n} + \mathrm{R_n} + \mathrm{N_n}} \tag{4}$$

#### 5.2.3.2. Individual Tree Crown Detection and Multi-Temporal Analysis

For extraction of individual tree parameters (Step 1 from Figure 5.2), each tree must be isolated from its surrounding environment (soil, vegetation, and other trees). However, given its planting distance and crown size, chestnut trees tend to be too close from each other, giving rise to the need for their segmentation and isolation. In this way, the orthorectified outcomes can be used as input in an image processing method for individual tree crown detection. For this purpose, the principles enunciated in Marques et al. (2019) were used with slight modifications to encompass multispectral imagery. The method was developed for chestnut plantation monitoring with the scope of performing multi-temporal analysis. It relies on the combination of photogrammetric outcomes in a raster format which, in turn, is automatically binarized. Some changes were implemented to ensure that all monitored chestnut trees within the study area were included for analysis. Taking both the NIR band and the CHM as inputs, a locally adaptive threshold (Bradley & Roth, 2007) is used in the binarization of the stand. A visual analysis allowed us to conclude that apart from trees of significant size (chestnuts and other trees) the amount of green vegetation in the study area was low or almost absent (depending on the flight campaign). For that reason, a value of 0.20 m was selected for CHM thresholding. Both binary images were then concatenated.

In the output, most of the pixels in the binary image (Figure 5.4b) belong to the crowns of chestnut trees. Still, some clusters of pixels can eventually represent more than one tree, leading to the need for a cluster isolation step (see Figure 5.4). The inverse of the binary imagery is used to compute a distance transform (Figure 5.4c) based on the Euclidean distance transform (Maurer & Raghavan, 2003), where a value is assigned for each pixel corresponding to the distance to the nearest pixel with a zero value. In turn, the complement image is used in the watershed transform (F. Meyer, 1994). This way, in an ideal scenario, clusters representing multiple trees are separated into individual clusters representing a single tree (Figure 5.4d). However, given the high spatial resolution, there can be cases where small parts can be erroneously separated. The process is reversed by analysing the bounding boxes overlap ratio, namely, if it is higher than 90% relative to another. Binary images as presented in Figure 5.5b,d were used to mask the colour–infrared image.

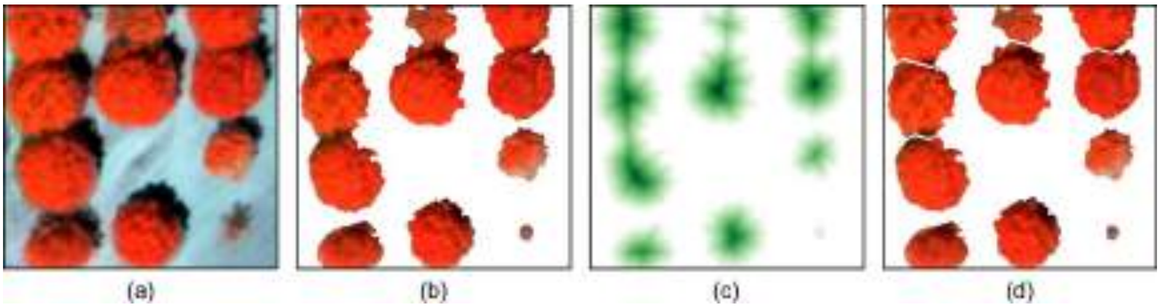


**Figure 5.4.** Individual tree crown isolation process: (a) colour–infrared image; (b) detected vegetation; (c) color-coded representation of the complement distance transform result; and (d) unconnected clusters from the watershed transform.

After cluster isolation, it is possible to obtain individual tree parameters. Several parameters can be driven by the analysis of each cluster, such as the crown diameter, perimeter, and area. Moreover, values retrieved from remotely sensed data, such as the CHM (tree height), vegetation indices, or spectral bands, can be obtained by matching each cluster to the raster data. This information can be presented as geospatial data in vector format (shapefile) to be analysed in a geographic information system (GIS) or in a table format.

Finally, multi-temporal analysis can be carried out using the values extracted for each flight campaign by comparison with the subsequent campaign. This way, the extracted parameters can be used for individual tree monitoring or to obtain an overview of the chestnut stand at the time of each flight campaign. In this study, the tree crown area and the mean NDVI value are analysed in a multi-temporal perspective, focusing on the overall stand development and on trees affected/non-affected by phytosanitary issues.

### 5.2.4. Detection of Phytosanitary Issues Using a Random Forest Classifier

Apart from the possibility of doing multi-temporal analysis using the extracted parameters, they can be used in a machine learning (ML) approach to distinguish chestnut trees in different phytosanitary conditions. Then, it is possible to (1) classify healthy chestnut trees and chestnut trees with phytosanitary issues and (2) distinguish among phytosanitary issues. The clusters resulting from the automatic individual tree detection were labelled in two ways according to their phytosanitary status: in two classes—with or without phytosanitary issues; and in three classes—to distinguish the different major phytosanitary problems (no visible symptoms, ink disease, and nutritional deficiencies).

An RF algorithm was used to carry out these classifications. It is a type of ensemble classifier that generates several decision trees using a random subset of training samples capable of handling high data dimensionality and multicollinearity and is insensitive to overfitting (Belgiu

& Drăguţ, 2016). This method is widely used in remote sensing applications (Ö Akar, 2016; Feng et al., 2015; Ma et al., 2017), including tree species classification (Goodbody et al., 2018; Michez et al., 2016; Nevalainen et al., 2017).

#### 5.2.4.1. Data Augmentation from Object-Based Image Analysis

As mentioned in Section 5.2.1, the use of a well-characterized area with well-known behavior is essential for validation of results. However, the fact that the stand used in the study is composed of a relatively small number of samples is a challenge for ML techniques. In fact, the essence of ML is based on using a high number of observations/samples. To overcome this limitation, the number of available samples was substantially increased using an OBIA approach (Step 2 from Figure 5.2). This was done using large-scale segmentation based on the mean shift algorithm (Michel et al., 2014) from the Orfeo ToolBox (OTB) (Inglada & Christophe, 2009). It requires a raster as input and results in a set of objects in vector format with a similar spectral similarity. To better discriminate tree crowns, the NIR, green, and red bands (NGR, example in Figure 5.4a) were concatenated and rasterized to produce a three-band false-colour image. This combination of bands was revealed to be the best compromise for this specific task. To increase the number of objects produced in this procedure, its sensitivity was augmented. Therefore, the spectral radius was set to 10 while the spatial radius and minimum segment size were kept at five and 50, respectively. The originated objects which intercept the detected tree crowns inherit the same classification as their correspondent tree, being classified according to its predominant phytosanitary issue that was observed in the field. Figure 5.5a presents part of the output obtained from the OBIA step; the objects matching tree crowns (Figure 5.5b) are then used for further model training and testing (Figure 5.5c).

#### 5.2.4.2. Feature Selection, Training, Validation, and Prediction

The created dataset is composed of the mean values of 16 features: the eight vegetation indices presented in Table 5.1; the green, red, RE and NIR bands; and the last four corresponding to the vegetation indices proposed in this study (see Section 5.2.3.1). As such, the database connected to the objects representing the tree crowns include a column with the mean value of these features. However, given the number of features to discriminate, those may behave differently by class. Hence, to decrease the number of features, an intermediate step was introduced. For this purpose, recursive feature elimination (RFE) (Guyon et al., 2002) was used (Step 3, from Figure 5.2). This method ranks features recursively based on their respective importance (Granitto et al., 2006).

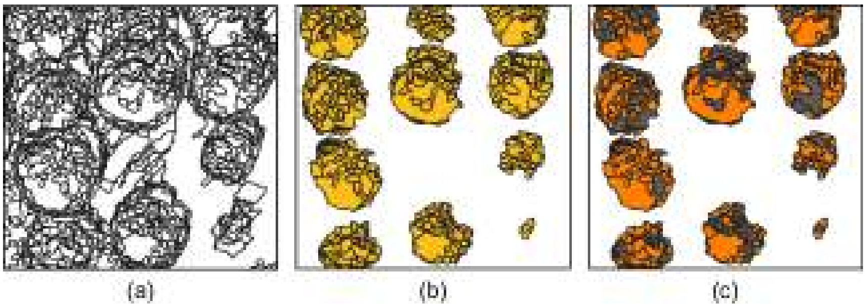

**Figure 5.5.** Data augmentation procedure: (a) objects from the mean-shift algorithm; (b) objects intersecting the detected tree crowns; (c) train-test split of the objects used for training (orange for training an and grey for testing).

For training and evaluation of the RF models (Step 3, from Figure 5.2), a hold-out strategy was used by randomly performing train-test splits (70% to train and 30% to test). To avoid possible discrepancies in the solution, an average of 10 repetitions was used. The data split operation is made by considering the area of each object within each tree and using 70% of the tree crown area for training and the remaining 30% for testing. This step is applied to the datasets from each flight campaign.

To evaluate the classification procedure in the different flight campaigns, the resultant confusion matrices were analysed. For this purpose, the following metrics were used: precision—the number of objects correctly classified for a given class divided by its total number of samples; recall—the number of correct classifications for a given class divided by its row total; and F1score—the harmonic mean of precision and recall measures. The overall accuracy and the Cohen's kappa coefficient (K) (McHugh, 2012)—a statistic used to measure inter- or intra-rater reliability for qualitative items—were also analysed for a general perspective of the models' behaviour. While the overall accuracy indicates the proportion of correct classifications in the total number of samples, the kappa coefficient evaluates the performed classification while considering the possibility of the agreement occurring by chance.

To predict potential phytosanitary issues in the analysed stand (Step 4, from Figure 5.2), the mean value of each tree is used. The mean feature value differs from the training values since the mean value of the whole tree crown is different from the mean value of their objects (used from training and testing). To evaluate the performance, the overall accuracy and the classification errors for each class were assessed. The predictions were made for two classes (with or without phytosanitary problems) and categorized according to the detected issue (no visible symptoms, ink disease, and nutritional deficiencies).

# 5.3. Results

## 5.3.1. Phytosanitary Characterization of the Study Area

The phytosanitary issues detected in affected trees were mostly ink disease and nutritional deficiencies. Both show symptoms on tree crown and foliage: while for chestnut ink disease, the dieback can be observed by low-density foliage or even its absence in some parts of the canopy (Figure 5.1d), nutritional deficits are noticeable by leaf discoloration and stress symptoms (Figure 5.1e). From the 46 chestnut trees assessed, 16 presented nutritional deficiencies (Figure 5.6a), eight had a higher predominance of ink disease symptoms (Figure 5.6b), and the remaining 22 were considered to be without symptoms. The latter had 6.5 m mean height and a mean crown diameter of 6.5 m. Those presenting ink disease symptoms had 6.2 m mean height and 6.1 m mean crown diameter. Chestnut trees with symptoms of nutritional deficiencies had a mean height of 4.5 m and a mean crown diameter of 4.0 m. The overall mean chestnut tree height was 5.8 m, and the overall mean crown diameter was 5.6 m. The global condition of each evaluated chestnut tree is presented in Figure 5.6c.

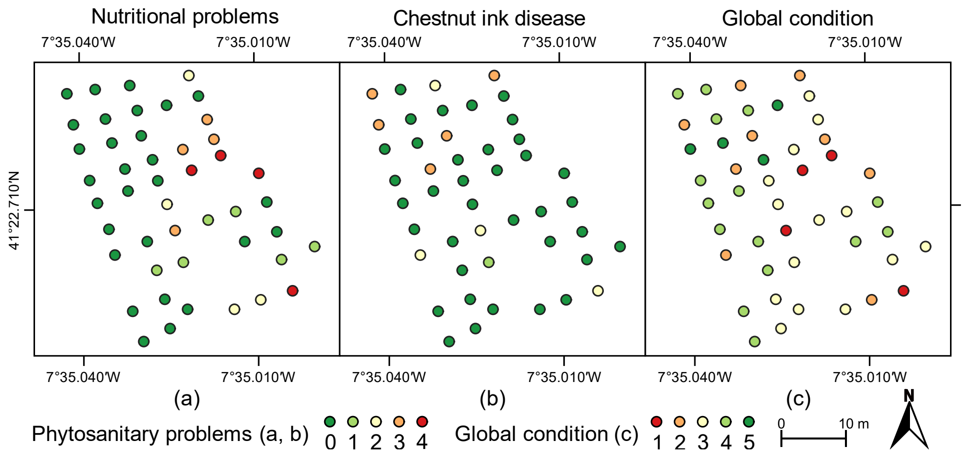


**Figure 5.6.** Phytosanitary assessment of chestnut trees for (a) nutrient deficiency; (b) chestnut ink disease; and (c) global condition.

## 5.3.2. Multi-Temporal Analysis

The estimated individual parameters of the chestnut trees from the different flight campaigns allowed for an understanding of the overall evolution of the stand. From these, the crown area and vegetation indices are the foremost parameters that can support multi-temporal analysis. Figure 5.7a presents the overall area occupied by chestnut trees, while Figure 5.8 depicts the individual crown area for each chestnut tree. A growth trend from the first (late May) to the fourth flight campaign (August) can be observed. From the fourth up to the last flight campaign, an overall decline occurred. The first three flight campaigns (May to June and June to July) presented a growth in area of 9% and 5%, respectively (from 767 to 877 $m^2$), while from the third to the fourth flight campaign, a growth of 13% was verified (991 $m^2$). In the last two flight campaigns, a decline was registered (16% and 6%, respectively), resulting in a final chestnut tree crown area of 783 $m^2$.

Considering trees with no visible symptoms (22 trees, ~48% of the total number of trees) and trees otherwise affected by phytosanitary issues (24 trees affected by ink disease or/and nutritional deficiencies), the former represents between 63% to 67% of the crown area along the flight campaigns. Figure 5.7a presents the crown area of the chestnut trees (i) that had no visible phytosanitary issues detected in the in-field characterization; (ii) with phytosanitary issues, regardless of which (24 trees); (iii) affected by ink disease (8 trees); and (iv) with nutritional deficiencies (16 trees). In general, the various curves fit well in their behaviour, presenting an almost linear increase in crown area until the third flight. Maximum crown area was reached in the fourth flight. Crown area decline for trees affected by phytosanitary issues was 29% (–98 $m^2$, from 341 to 244 $m^2$), with data acquired in the two last flight campaigns. As for chestnut trees with no visible symptoms, the area decline was 17% (–108 $m^2$, from 626 to 519 $m^2$). Crown areas of chestnut trees affected by ink disease or/and with nutritional deficiencies have a 30 $m^2$ mean difference, representing 14% and 18% of the overall crown area, respectively.

The distribution of tree crown area is presented in Figure 5.7b–d. While some trees present a tree crown area higher than 40 $m^2$, others present an area lower than 1 $m^2$ (Figure 5.7b). Such discrepancies can be justified by the fact that the trees of smaller area represent recent plantations, carried out to replace dead trees. Considering all flight campaigns, the mean chestnut tree crown area is 18 $m^2$. Whereas chestnut trees with no visible phytosanitary issues had a higher mean crown area (26 $m^2$), trees affected by ink disease had 15 $m^2$, and trees with nutritional deficiencies presented a mean crown area value of 10 $m^2$.

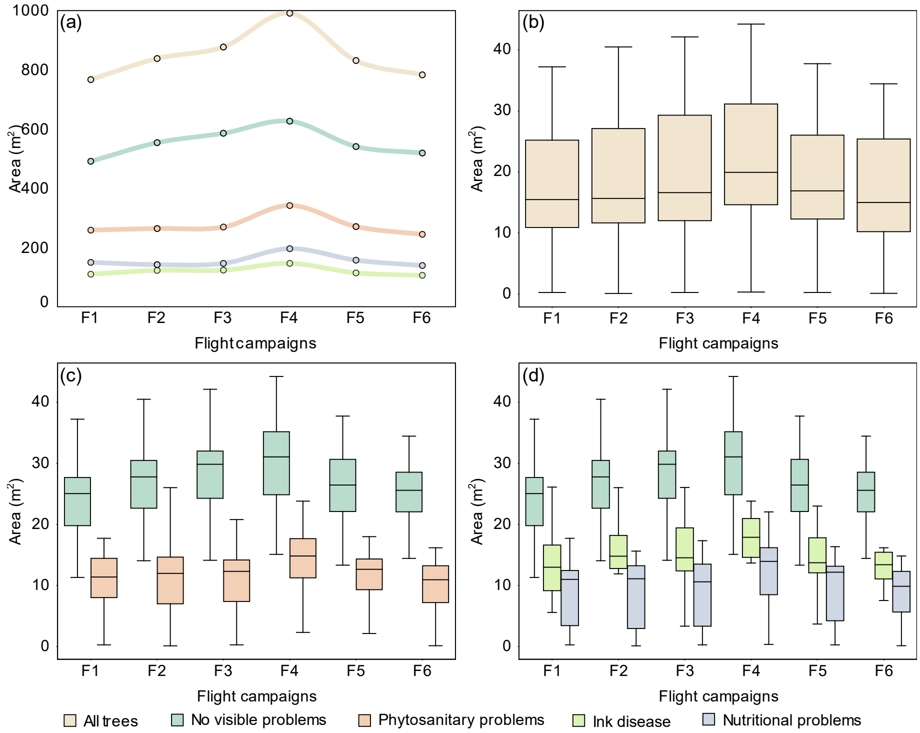


**Figure 5.7.** Overall chestnut tree crown area (a), its distribution per flight campaign (b) and per class (c, d).

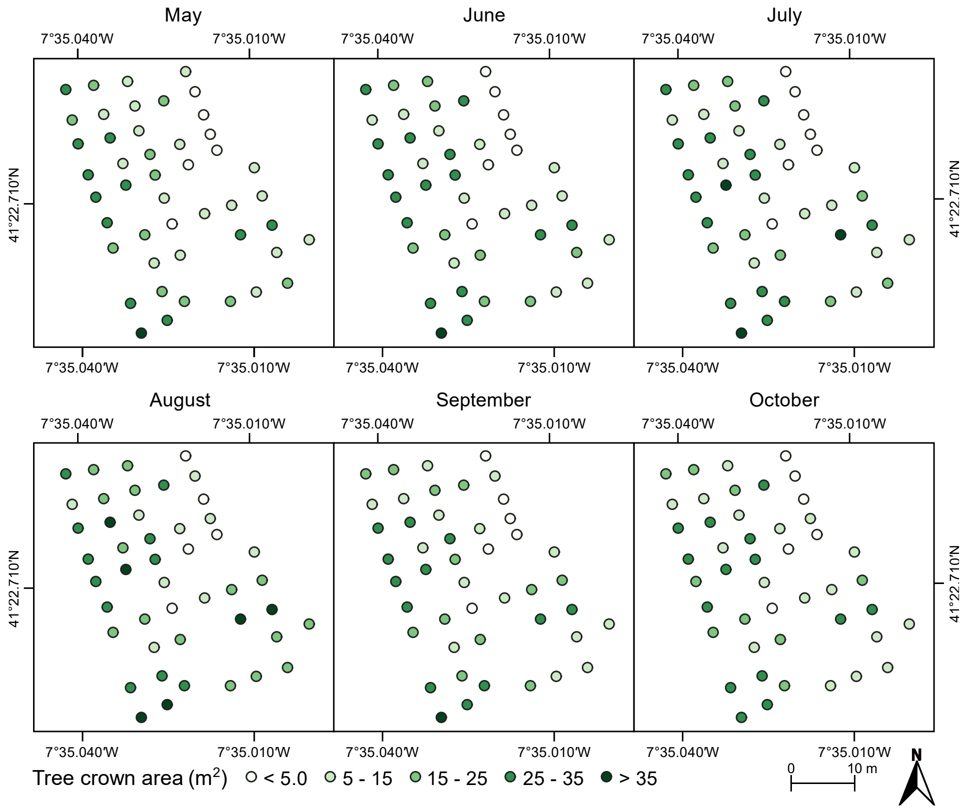


**Figure 5.8.** Crown area of each analysed chestnut tree per flight campaign, from 27 May to 16 October 2018.

The mean NDVI value of each chestnut tree is presented in Figure 5.9. Slight variations can be detected in the first two flight campaigns. However, a constant decline was verified in the remaining campaigns. Chestnut trees with symptoms of phytosanitary issues presented a lower

NDVI value in all flight campaigns when compared to healthy trees. Indeed, the lowest mean values were presented by trees with nutritional deficiencies. This difference increased throughout the flight campaigns. While for the first four campaigns, the mean difference—tree crown growth—was –0.06 for trees affected by ink disease and –0.17 for those that showed nutritional deficiencies, for the last two flight campaigns—tree crown decline—these were –0.09 and –0.32, respectively.

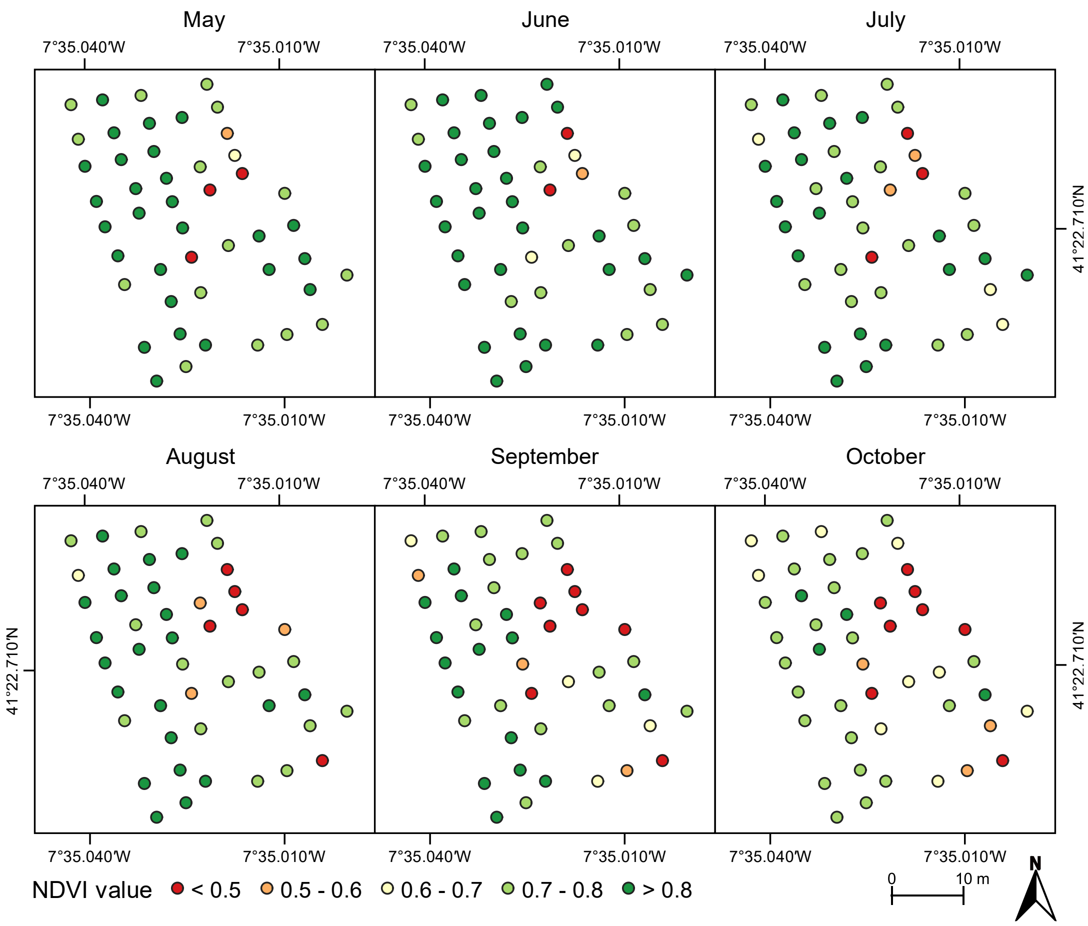


**Figure 5.9.** Mean NDVI values for the chestnut trees analysed throughout the flight campaigns (27 May to 16 October 2018).

### 5.3.3. Detection of Trees with Phytosanitary Symptoms

The individual tree crown projections obtained with each flight campaign were subjected to an OBIA procedure to output a set of objects (step 2, in Figure 5.2). Naturally, each set has a different number of objects due to canopy area evolution and appearance over time. An average of 1650 objects was obtained throughout all flight campaigns. While 1527 objects were identified in May, that number grew in the following two flight campaigns—1668 in June and 1720 objects identified in July—and decreased in August (1389 objects). Then, it grew again in the last two flight campaigns, with 1452 objects identified in September and 2165 in October.

These variations can be explained by changes in the canopy appearance over time, which result in reflectance alteration. The latter can be justified either by the dieback observed in the overall leaf discoloration and/or by the presence of some chestnut fruits, which results in higher spectral differences among each tree crown. As for the distribution of objects per class (considering the average of all epochs), the class of healthy trees has a higher number (67%), while the class with phytosanitary issues is left with the remainder (33%). Ink disease represents 15% and nutritional deficiencies 19% of the latter class.

#### 5.3.3.1. Dataset Description and Feature Selection

Figure 5.10 presents the trends for vegetation indices throughout the flight campaigns. Excluding RVI—for the first campaign—the majority of the vegetation indices present values disposed in a shorter interval. However, in the last flight campaigns, values are spanned on a larger interval. An example is NDVI: it tends to decrease in value but presents an increased value span in the last two flight campaigns. GNDVI shows a different trend, increasing in the first four flight campaigns and decreasing in the last ones. As for GRVI, it presents an overall decline along the flight campaigns. ExNIR, NDExNIR, NDRE, ExRE, and NDExRE present a similar behavior, increasing in value from the first to the second flight campaigns, followed by a small decrease in the third flight campaign. Hereinafter, values increase again in the fourth campaign and decrease in the last two flight campaigns. Lastly, RVI presents values spread over a larger interval in almost all flight campaigns, being lower in the last two.

When analysing the values of the vegetation indices automatically extracted from the detected tree crowns—considering trees with or without phytosanitary symptoms (Figure C.1)—both classes are distinguishable by their interquartile range (IQR). Trees presenting ink disease and/or nutritional deficiencies can be clearly distinguished from those that are healthy in all flight campaigns and by vegetation indices, with the exception of ExRE (see distribution in Figure C.2). Moreover, ExRE is again the exception when comparing values between healthy trees and those affected by chestnut ink: in the remaining vegetation indices, the latter presented lower values. As for nutritional deficiencies, only the third flight campaign of ExRE presents a higher value when compared to healthy trees. It should also be noted that trees affected by chestnut ink disease had higher values in comparison with those affected by nutritional deficiencies.

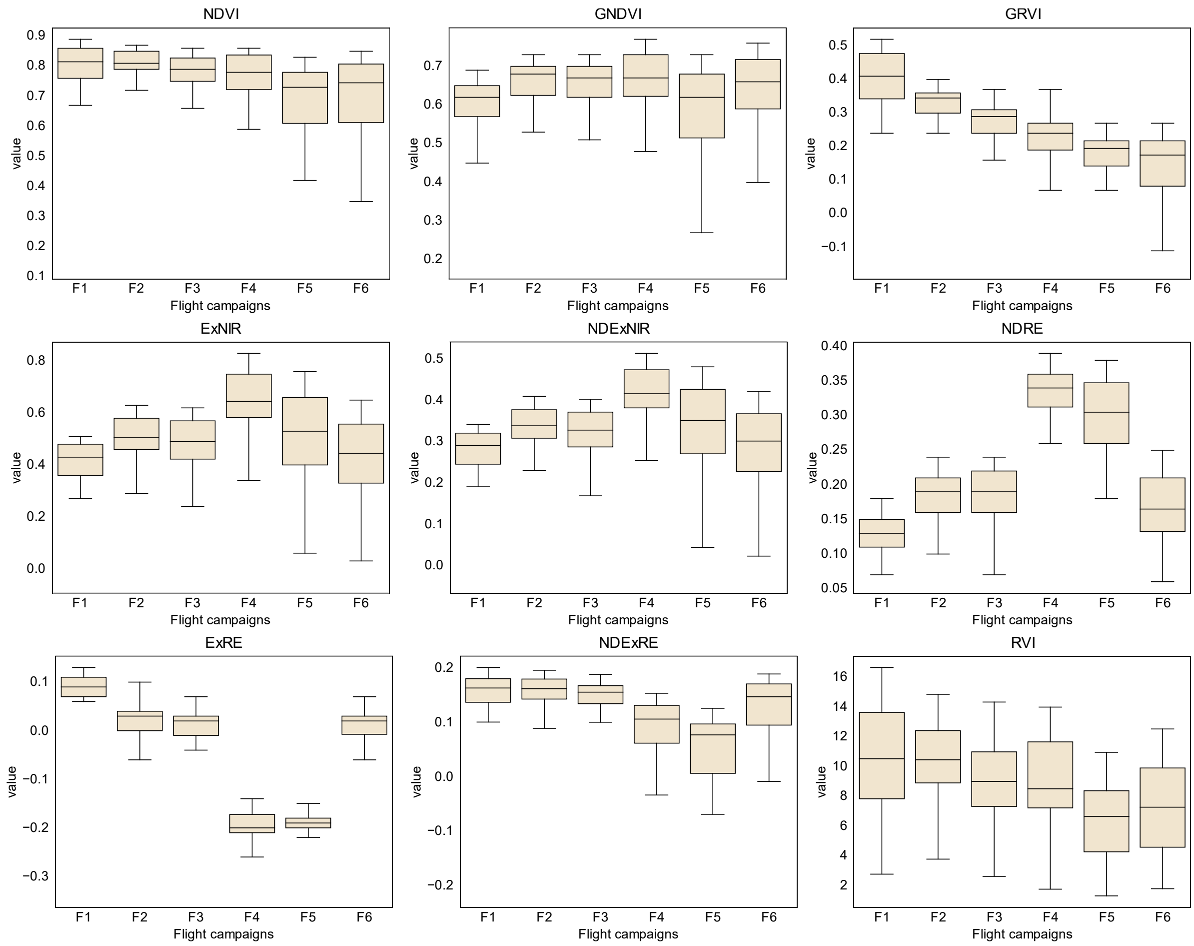


**Figure 5.10.**Tree crown area and mean NDVI values of the chestnut trees analysed throughout the flight campaigns.

Feature selection based on RFE allowed for understanding the influence of features extracted from each object on the RF classifier. These results are presented in Table C.1. By analysing the overall results—achieved by adding all ranks and sorting the features by their lower value—when considering two and three classes, the top ten features are the same in both situations (highlighted in bold in Table C.1). As such, those features were selected to be used in the subsequent analysis.

## 5.3.3.2. Random Forest Classifier and Dataset Performance Evaluation

The model was trained by using ten random selections of 70% of each tree crown area per epoch. It was then tested using the remaining 30%. The mean accuracy of the ten random splits and their standard deviations were used to evaluate the model performance.

Table 5.2 presents the results when considering only two classes: absence or presence of phytosanitary issues. Datasets acquired from all flight campaigns obtained an overall accuracy equal or higher than 85%. The highest value (91%) was achieved in September's flight campaign. As for accuracy statistics (kappa index), a substantial agreement (kappa > 0.65) was obtained in all flight campaigns. From July onward, kappa was always equal or higher than 0.71. Regarding metrics, when each class is analysed individually—precision, recall, and F1score—the healthy tree class achieved better results. When comparing each flight campaign, June and May showed similar results. However, a higher standard deviation was observed in May. Similarly, July, August, and October presented similar results. Still, results from August are slightly lower.

**Table 5.2.** Performance evaluation results (and its standard deviation) of OBIA objects considering two classes (1: no visual symptoms; 2: phytosanitary issues) for each flight campaign.

| Month | Class | Precision | Recall | F1-score | Kappa index | Overall accuracy |
|---|---|---|---|---|---|---|
| May | 1 | 0.89 (0.02) | 0.92 (0.01) | 0.90 (0.01) | 0.65 (0.04) | 0.86 (0.01) |
| | 2 | 0.79 (0.04) | 0.72 (0.04) | 0.75 (0.03) | | |
| Jun. | 1 | 0.88 (0.01) | 0.90 (0.01) | 0.89 (0.01) | 0.66 (0.02) | 0.85 (0.01) |
| | 2 | 0.79 (0.02) | 0.75 (0.02) | 0.77 (0.02) | | |
| Jul. | 1 | 0.90 (0.01) | 0.92 (0.01) | 0.91 (0.01) | 0.72 (0.02) | 0.88 (0.01) |
| | 2 | 0.83 (0.02) | 0.80 (0.02) | 0.81 (0.02) | | |
| Aug. | 1 | 0.91 (0.02) | 0.89 (0.01) | 0.90 (0.01) | 0.71 (0.02) | 0.87 (0.01) |
| | 2 | 0.79 (0.02) | 0.83 (0.02) | 0.81 (0.02) | | |
| Sep. | 1 | 0.93 (0.01) | 0.94 (0.02) | 0.94 (0.01) | 0.80 (0.02) | 0.91 (0.01) |
| | 2 | 0.88 (0.03) | 0.85 (0.03) | 0.86 (0.02) | | |
| Oct. | 1 | 0.91 (0.01) | 0.92 (0.01) | 0.91 (0.01) | 0.72 (0.03) | 0.88 (0.01) |
| | 2 | 0.82 (0.02) | 0.81 (0.02) | 0.81 (0.02) | | |

Table 5.3 presents the results obtained when distinguishing between specific phytosanitary issues of ink disease and/or nutritional deficiencies. The minimum overall accuracy is 80% (May and August flight campaigns) and the highest (85%) was achieved in the September and October flight campaigns. However, the statistical significance of the results differs: a moderate agreement (kappa > 0.55) was registered in May, while in the remaining epochs, the value increased. Indeed, the highest value was in September (0.69). July and October also registered a kappa value of at least 0.65. Regarding each class classification, F1-score was always higher than 0.90 for trees without phytosanitary problems. As for the other two classes—affected by ink disease and/or by nutritional deficiencies—the F1-score was lower. Nonetheless, the class containing trees affected by nutritional deficiencies had better results.

**Table 5.3.** Performance evaluation results (and its standard deviation) from OBIA objects considering three classes (1: no visual symptoms; 2: ink disease; 3: nutritional deficiencies) for each flight campaign.

| Month | Class | Precision | Recall | F1-score | Kappa index (STD) | Overall accuracy (STD) |
|---|---|---|---|---|---|---|
| May | 1 | 0.88 (0.01) | 0.93 (0.01) | 0.91 (0.01) | 0.55 (0.01) | 0.80 (0.01) |
| | 2 | 0.58 (0.08) | 0.53 (0.04) | 0.55 (0.04) | | |
| | 3 | 0.58 (0.04) | 0.49 (0.03) | 0.53 (0.02) | | |
| Jun. | 1 | 0.88 (0.01) | 0.92 (0.02) | 0.90 (0.01) | 0.60 (0.02) | 0.81 (0.01) |
| | 2 | 0.64 (0.04) | 0.55 (0.06) | 0.59 (0.03) | | |
| | 3 | 0.66 (0.03) | 0.61 (0.04) | 0.64 (0.03) | | |
| Jul. | 1 | 0.89 (0.01) | 0.94 (0.01) | 0.91 (0.01) | 0.65 (0.03) | 0.83 (0.02) |
| | 2 | 0.66 (0.04) | 0.63 (0.07) | 0.64 (0.05) | | |
| | 3 | 0.74 (0.06) | 0.62 (0.04) | 0.67 (0.03) | | |
| Aug. | 1 | 0.89 (0.02) | 0.91 (0.01) | 0.90 (0.01) | 0.60 (0.03) | 0.80 (0.01) |
| | 2 | 0.58 (0.06) | 0.58 (0.07) | 0.58 (0.05) | | |
| | 3 | 0.64 (0.06) | 0.60 (0.05) | 0.62 (0.02) | | |
| Sep. | 1 | 0.92 (0.02) | 0.94 (0.01) | 0.93 (0.01) | 0.69 (0.02) | 0.85 (0.01) |
| | 2 | 0.60 (0.03) | 0.57 (0.05) | 0.58 (0.03) | | |
| | 3 | 0.77 (0.05) | 0.73 (0.05) | 0.75 (0.03) | | |
| Oct. | 1 | 0.90 (0.01) | 0.94 (0.01) | 0.92 (0.01) | 0.67 (0.03) | 0.85 (0.01) |
| | 2 | 0.62 (0.04) | 0.60 (0.04) | 0.61 (0.03) | | |
| | 3 | 0.83 (0.04) | 0.71 (0.04) | 0.76 (0.03) | | |

#### 5.3.3.3. Detection of Chestnut Trees Affected by Phytosanitary Issues

The mean value of each tree crown feature was used to assess whether it was affected by phytosanitary issues. Results are presented in Figure 5.11 and Figure C.3a. The overall accuracy is equal to or higher than 85%. The lowest value was achieved in May (85%) and the highest in the last two flight campaigns (96%). In the remaining flight campaigns, the overall accuracy is 91% in both June and August, and 94% in July. Indeed, the earliest flight campaign in the season (May) had the most misclassifications—seven chestnut trees, representing about 15% of the total number of chestnut trees monitored (46): two healthy trees were classified as being affected by phytosanitary issues and five the exact opposite. The number of misclassified chestnut trees without visible symptoms was consistently low in the remaining flight campaigns: one in June, and two in both July and August. As for misclassified chestnut trees with phytosanitary issues, there were three in June, one in July, and two in the remaining flight campaigns.

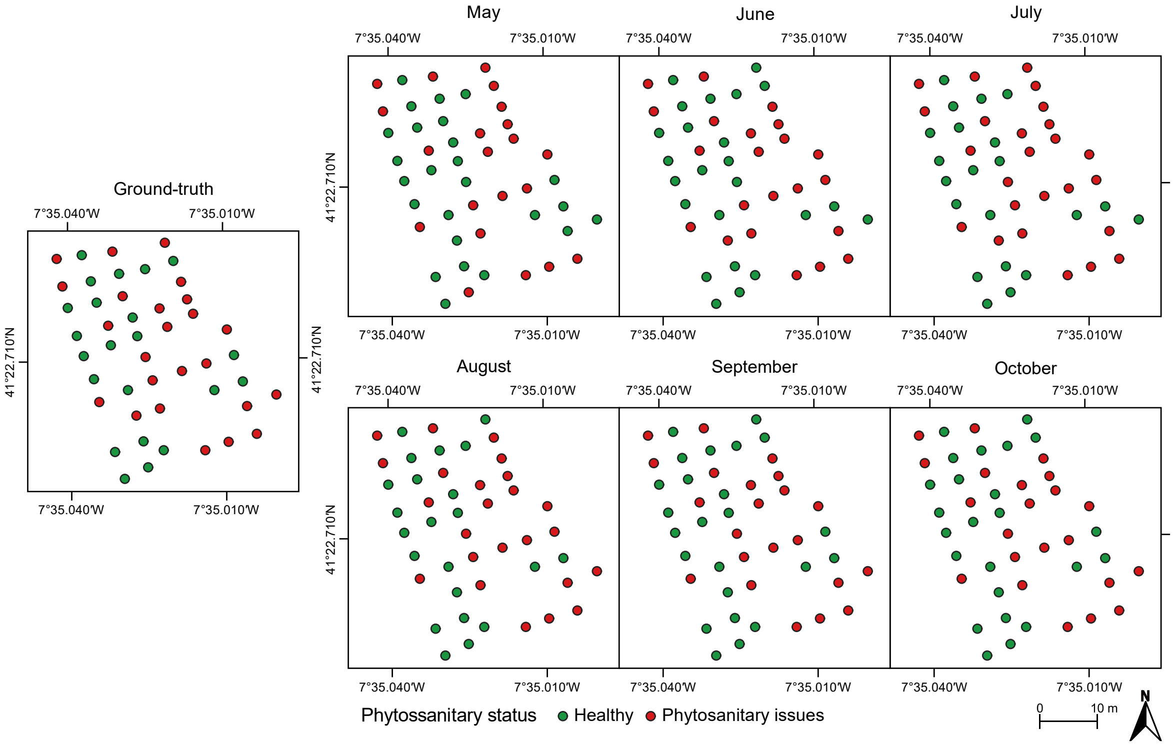


**Figure 5.11.** Detection of phytosanitary issues in chestnut trees throughout the flight campaigns.

Figure 5.12 presents the assessment results when using three classes (no visual symptoms, ink disease, and/or nutritional deficiencies). The higher overall accuracy value is achieved in September (91%) and the lowest in May (78%); see Figure C.3b. The remaining flight campaigns present a relatively stable overall accuracy value, ranging between 83% and 87%. Chestnut trees without visible symptoms present the lowest misclassification values (5% overall). No misclassifications were observed in both September and October. Moreover, in July, there were no misclassifications in chestnut trees affected by ink disease. Affected trees were mainly misclassified as having no phytosanitary issues: there were two misclassifications on average (August and October had three). Regarding chestnut trees affected by nutritional deficiencies—an average of four misclassified trees considering all flight campaigns— they were misclassified in both of the other two classes: 10 in healthy trees and 12 in trees affected by ink disease.

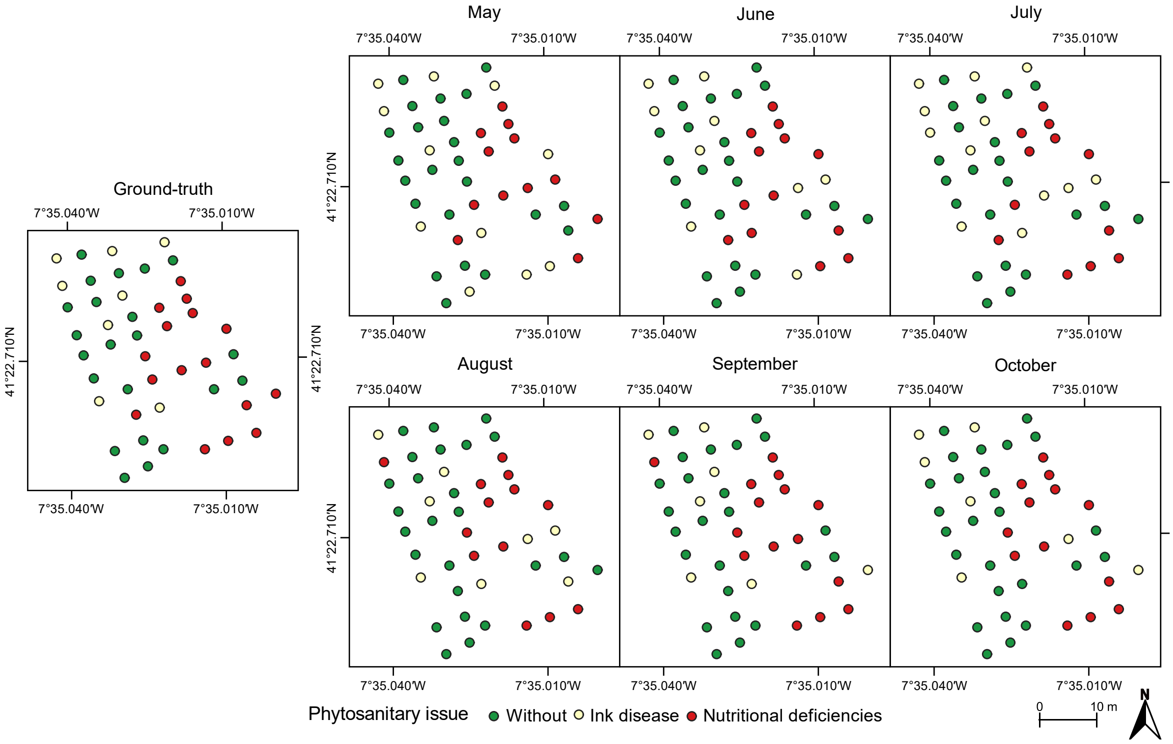


**Figure 5.12.** Detection of ink disease and nutritional deficiencies in chestnut trees throughout the flight campaigns.

## 5.4. Discussion

The multi-temporal data analysis enabled characterization of both spatial and temporal variability of the studied chestnut stand. Studies on chestnut trees management rely only on yearly flight campaigns (Pádua, Hruška, et al., 2017) to monitor the overall condition and to study vegetation decline (L. M. Martins et al., 2015), limiting the intra-seasonal monitoring of potential issues. Indeed, no intra-seasonal multi-temporal studies were found for chestnut trees, and these can be fundamental for detecting potential phytosanitary issues earlier on, which will enable timely mitigation actions. Furthermore, each tree can automatically be classified regarding its phytosanitary status as affected, ink disease or nutritional deficiencies, or healthy.

Regarding the crown area for the monitored chestnut trees throughout the season, it is of note that it increased from May to August and decreased hereinafter. This trend is verified more often in healthy chestnut trees (see Figures 5.7 and 5.8). Those affected by phytosanitary issues presented a smaller crown area growth in the first three flight campaigns. The west side area of the stand had higher NDVI values throughout the analysed period (Figure 5.9) while the opposite was verified in the east. Whereas the size of the chestnut trees—smaller precisely in the east area (Figure 5.8)—can explain this because it usually means lower foliage density, trees affected by phytosanitary issues are mostly located in that area (see Figure 5.6). A clear distinction between trees with and without phytosanitary problems (Figure 5.7c), and between phytosanitary problems can be observed.

The crown area of chestnut trees affected by ink disease are usually larger when compared to the ones from trees affected by nutritional deficiencies (Figure 5.7d). The latter present a small increase in crown area in August. As for NDVI, while chestnut trees affected by phytosanitary issues presented decreasing values throughout the season, this trend is less clear-cut in chestnut trees affected by ink disease. With reference to the feature selection procedure, the proposed vegetation indices were among the ones with best discrimination performance. This can be explained by the fact that spectral differences are more significant when addressing symptoms caused by the studied phytosanitary issues (Figure 5.3). Spectral bands can also be considered less relevant features than vegetation indices. Indeed, green, NIR, and RE bands did not perform well when compared to the VIs, which was not verified in studies using RGB-based vegetation indices (Pádua, Guimarães, et al., 2019).

The employed methodology can be regarded as accurate not only when classifying chestnut trees as affected (or not) by phytosanitary issues (Figure 5.7c), but also (when affected) in distinguishing which phytosanitary issue is present in each case. The crowns detection for individual trees employed in this study allow for discarding most outliers unrelated to chestnut trees, such as soil and low-height vegetation, while other studies relied on OBIA with more steps (Jorge Torres-Sánchez et al., 2015). As such, an ML classification step to detect trees is not a requirement.

When considering the possibility of having a chestnut tree affected by a phytosanitary issue (Table 5.2, Figures 5.11 and C.3a), the obtained results show that, both in testing and detection, September’s flight campaign data had the best accuracy rates. While similar results were achieved in October, the kappa value was slightly lower. Remaining campaigns also achieved good accuracy values. May corresponds to an early phase of the chestnut’s phenological cycle, when most symptoms caused by phytosanitary issues are not yet clearly noticeable. This justifies the higher standard deviation observed in May. However, when three classes are considered—healthy, ink disease, and nutritional deficiencies—the overall accuracy generally decreases (Table 5.3, Figures 5.12 and C.3b). Again, September’s data outperform those of the remaining flight campaigns. Whilst the October flight campaign presented better results when distinguishing ink disease, this can be explained by environmental factors: chestnut trees were exposed to longer periods of low/no precipitation (causing low soil moisture) and higher temperatures than those registered in the summer, which result in trees having more stress and, therefore, to manifest a higher incidence of phytosanitary symptoms (Camisón et al., 2019). On the other hand, this decrease in classification can also be related to the chestnut harvesting season (and, therefore, trees start their senescence). Currently, to mitigate the occurrence of chestnut ink disease, hybrid chestnut trees are being used with good results (Brito et al., 2012).

It should be noted that some chestnut trees did not present symptoms uniformly. Indeed, some parts had similar spectral responses than healthy trees. Despite values in Figures C.1 and C.2 having a different separation between classes in the training phase, objects formed from the OBIA procedure have similar objects in the classes, since the whole tree was considered as being affected by only one issue. In other works, different types of classes were classified as different tree species (Hill et al., 2010; Lisein et al., 2015; Melville et al., 2019; Michez et al., 2016) or distinguished completely different types of classes (Özlem Akar, 2018; Akcay et al., 2019; Guerrero et al., 2012; Pádua, Guimarães, et al., 2019). Moreover, in Gini et al. (2018), multispectral imagery was combined with texture features for tree species classification, increasing the overall accuracy. In this study, only *Castanea sativa* Mill. trees were evaluated using UAV-based multispectral data to automatically distinguish the presence (or absence) of phytosanitary issues. Therefore, it was more challenging when considering data classification into three classes since there were more spectral similarities.

When compared to traditional in-field approaches that require several days of field surveys/measurements, the whole pipeline proposed in this study can deliver the final results in a single day. Future developments would rely on data processing and results being delivered on the fly, similar to what was demonstrated from tree counting (Salamí et al., 2019). Data from sensing payloads other than multispectral imagery can help improve the differentiation between the phytosanitary issues analysed in this study. Indeed, thermal infrared, hyperspectral, and fluorescence data (R. Calderón et al., 2013; López-López et al., 2016; P. J. Zarco-Tejada et al., 2018) are options to be considered (e.g. allowing the creation of narrow-band vegetation indices). However, hyperspectral data require more complex data processing and with higher computational and financial costs compared to multispectral data. The proposed method can also be explored in other contexts such as arid and semi-arid land vegetation monitoring (T. T. Sankey et al., 2018).

## 5.5. Conclusions

This study shows the suitability of image analysis and processing to automatically detect phytosanitary issues in individual chestnut trees within a chestnut stand using UAV-based multispectral data. The results demonstrate the effectiveness of the RF classifier in discriminating trees with and without phytosanitary issues and to classify according to the issue affecting the trees (ink disease and nutrient deficiency). In addition, new vegetation indices were proposed, which helped to improve the results. The obtained results also allowed us to conclude that the latter stages of the season are the optimal time (less misclassifications) for the application of the proposed methodology. This way, the dormancy period can be used to apply corrective treatments on the trees identified as having phytosanitary issues (e.g., soil nutrient corrections, biomass pruning tree optimization, tree replacement). However, the results from early and mid-season (May to June) are also promising—phytosanitary issues can be detected even in cases when symptoms are not significant—and can be used to optimize field inspections, reducing the amount of work/time needed compared to manual/visual inspections. Some treatments can be directed to those trees to prevent the further development of issues. Moreover, the usage of multi-temporal data enabled the monitoring of the chestnut stand along the season.

In the near future, the proposed methodology can be applied to monitor chestnut trees at a larger scale, providing a cost-effective and less laborious alternative to field surveys to assess overall phytosanitary condition. Moreover, it can also be used in the long-term monitoring of damage caused by the chestnut gall wasp in both phytosanitary and development status of individual chestnut trees. Lastly, the greater spatial resolution provided by UAV-based data when compared to other remote sensing platforms can allow for yield estimation by automatically detecting chestnut clusters, since they tend to grow in tree branch tips and are therefore visible from an aerial perspective. Other types of sensors should also be evaluated, such as thermal and hyperspectral, increasing the variety of features that can be used for analysis and in promoting efficient and sustainable management practices.

## Acknowledgements

The authors would like to thank to the owner of the chestnut stand for conceiving the authorization to conduct this study.

## Funding

This work is financed by National Funds through the Portuguese funding agency, FCT - Fundação para a Ciência e a Tecnologia within project UIDB/50014/2020. Financial support provided by the FCT (PD/BD/150260/2019) to Pedro Marques, under the Doctoral Programme "Agricultural Production Chains – from fork to farm" (PD/00122/2012) and to Luís Pádua (SFRH/BD/139702/2018).

# Chapter 6.

## Vineyard properties extraction combining UAS-based RGB imagery with elevation data

*International Journal of Remote Sensing*, 2018, *39*(15-16), 5377-5401

Journal Impact Factor – 2018: 2.493

5 Year Impact Factor – 2018: 2.456

**Luís Pádua**, Pedro Marques, Jonáš Hruška, Telmo Adão, José Bessa, António Sousa, Emanuel Peres, Raul Morais and Joaquim J. Sousa

Refer to https://doi.org/10.1080/01431161.2018.1471548 for online published version

## 6.1. Introduction and background

Requirements to optimize vineyards' (*Vitis Vinifera* L.) performance in a Precision Viticulture (PV) context are high because both yield and quality should be maximized, while environmental risks and impacts should be reduced (A. P. B. Proffitt et al., 2006). Therefore, farmers achieve the utmost control over vineyard management by considering its variability. Grapevine quality and development directly relate with the vineyards' spatial heterogeneity, which depends on several factors associated to the vineyard itself—soil, crop management, irrigation, nutritional status, pest and disease control and external variables, as the climate—to determine the inter-annual and intra-vineyard variability of both yield and quality (Alessandro Matese et al., 2015). These factors can lead to the occurrence of biotic and abiotic issues. Depending on their severity, they can result in a significant production decrease and consequently in significant economic losses (Baofeng et al., 2016). Recent technological development opened the possibility of implementing both Precision Agriculture (PA) and PV, along with the combination of certain procedures, to improve the decision making process in several field-related tasks (Zarco-Tejada et al. 2014). Hence, remote sensing data can provide a better understanding of a terrain's variability and can be applied in the context of PV management (Bobillet et al., 2003). Indeed, sensors used in remote sensing platforms provide an effective way to extract spatial information about crops' state in a non-destructive manner (Weiss & Baret, 2017).

Regarding vineyards, the usage of remote sensing platforms is usually related to: grape varieties mapping (Lacar et al., 2001); vineyard Leaf Area Index (LAI) estimation (L. Johnson et al., 2003; Kalisperakis et al., 2015; Mathews & Jensen, 2013); irrigation scheduling and water stress variability (Baluja et al., 2012; Bellvert et al., 2013; Bellvert & Girona, 2012; P. Zarco-Tejada et al., 2004); grapevine phenology monitoring (Helder Fraga, Amraoui, et al., 2014; Lamb et al., 2004); disease detection and mapping (Albetis et al., 2017; A. Matese et al., 2013); grape quality mapping in vineyards affected by nutrients deficiency (Martín et al., 2015); and chlorophyll estimation (P. J. Zarco-Tejada, Berjón, et al., 2005), among others. However, the use of remote sensing techniques is challenging due to the alternation of vines' canopies—which form a set of parallel rows—along with the presence of bare soil or vegetation cover, within the vineyard plot (Burgos et al., 2015; Alessandro Matese et al., 2015). By considering the whole vineyard terrain, the presence of information other than vines' canopy is added, i.e., the inter-row vegetation cover and shadows produced by vines' canopy and its surroundings.

To detect vine's canopy, several authors and research teams proposed approaches based on the use of vegetation indices (VIs) applied to the imagery data provided by remote sensing platforms (Albetis et al., 2017; Bellvert & Girona, 2012; Helder Fraga, Amraoui, et al., 2014; L. Johnson et al., 2003; Alessandro Matese et al., 2015; Naidu et al., 2009; Smit et al., 2010). VIs are simple arithmetic operations applied to the spectral narrow-band or broad-band imagery, with information from different parts of the electromagnetic spectrum (Pádua, Vanko, et al., 2017). However, VIs are often computed over the whole vineyard or at the plot level. Thus, information not related with vines is present. To produce correct vineyard maps, a separation of vine pixels from non-vine pixels in the remote sensing data is required. Although feasible manually, it is a laborious, error-prone and time-consuming task. Still, it is crucial since it heavily contributes to the obtained results' global accuracy, which, in turn, increases vineyards' management efficiency by providing information about crops' variability. This enables the application of more efficient treatments to the plants and autonomous guidance for unmanned ground vehicles.

Considering the previously presented requirements, satellite imagery is not suitable for vineyards management tasks. The spatial resolution provided is, in general, too sparse (Alessandro Matese et al., 2015) and the data acquisition frequency too low. Manned aircrafts and Unmanned Aerial Systems (UAS) provide more timely and flexible data acquisition solutions (Weiss & Baret, 2017). While manned aircrafts can cover larger areas with high resolution, they can be expensive for small sized-projects (Pádua, Vanko, et al., 2017). On the other hand, the ability of UAS (Unnamed Aerial Vehicle [UAV] + sensors and ground control station) to perform low-altitude flights—enabling the acquisition of very high-resolution data—makes them an ideal tool to use when versatility, cost-effectiveness and temporal data are needed.

To overcome the vine's vegetation identification issue, different studies proposed (semi)automatic methods, using image-processing techniques on a single-band image, VIs or Digital Elevation Models (DEMs). Bobillet et al. (2003) proposed a method to classify vine rows based on a vineyard' active contours. This method's main issue was the requirement of manual adjustments in pre- and post-processing stages to achieve valid results. Furthermore, problems identifying vine rows with grass in-between them were also reported. Chanussot et al. (2005) studied the identification of missing vines and proposed a method that uses the Radon transform of the Fourier spectrum over a vineyards' image. This image is computed by subtracting the red band from the green band of the RGB image. The process allowed finding both the inter-row spacing and row orientation. Next, a set of morphological operations and a median filter over a binary image generate an image that signals missing vines. However, this method reportedly fails when dealing with irregularly spaced, too sparse or curved plantations. Comba et al. (2015) proposed a method that benefits from vegetation's high reflectance in Near Infrared (NIR) imagery to apply the Hough space clustering over an image. This image is a result of local histogram equalisation thresholding to estimate vine's canopy vegetation and Total Least Squares technique to estimate vine rows. The method uses techniques that require a large amount of processing time in big areas or images with lower Ground Sample Distance (GSD) values. The method developed by Comba et al. (2015) was also applied in other studies to produce vigour maps (J. Primicerio et al., 2015) and to estimate vines positions in a vineyard (Primicerio et al. 2017). In the latter, the trunk's position was estimated along with the canopy shape of each individual plant. It was assumed that the plants are equally spaced along each vine row, which enabled the application of a machine learning procedure to discriminate between the presence or the absence of a plant along a row. Nolan et al. (2015) used skeletonization techniques to accurately segment vineyard rows for vineyard mapping. The proposed method used single-band images from distinct types of sensors as inputs, with the only requirement of having a high spatial resolution to distinguish vine rows from soil. The reported failure rate was related with the presence of trees obscuring vine rows, shadows, and segmentation discontinuities. To detect vine rows, Puletti et al. (2014) proposed a method that considers the lower reflectance values from the vineyard canopy red channel and the soil's high reflectance. An image obtained by a high-pass filter is then processed and passed to a modified version of Ward's technique (Ward Jr, 1963), which provides an unsupervised hierarchical cluster analysis. There were problems reported in areas with low contrast between vineyard canopy and soil. Poblete-Echeverría et al. (2017) studied different approaches to perform vineyard vegetation detection, using VIs and both supervised (artificial neural networks and random forests) and unsupervised (k-means clustering) classification methods in three classes: plant, shadow and soil. The obtained results showed that the combination of VIs with artificial neural networks provided good results. Poblete-Echeverría et al. (2017) stated that supervised classification methods needed human intervention for model calibration with a training dataset. On the other hand, VIs complemented with the Otsu's method (Otsu, 1979) for thresholding, had a higher overall accuracy and performed very well in the detection of vineyards' canopy.

This resulted in an easy and automatic method for vine vegetation extraction, even though VIs can also classify vegetation with the same reflectance in between vine rows.

The problem of inter-row vegetation classification can be surmounted with a more straightforward method: using DEMs computed from the photogrammetric processing of UAV-based imagery and by considering the vineyard plot structure's height. DEMs are an accurate representation of the surface elevation. They can provide terrain's surface elevation data – Digital Terrain Model (DTM) – and contain elevation data from features present in the ground surface – Digital Surface Model (DSM). Using this type of data, Kalisperakis et al. (2015) were able to estimate vineyards' LAI, achieving good correlation rates when compared with ground-truth measurements, whereas hyperspectral and RGB imagery obtained lower correlation rates. Burgos et al., (2015) used this type of data to separate non-vine pixels from vine pixels, by producing a Digital Differential Model (DDM) —that results from subtracting the DTM from the DSM—also known as Canopy Height Model (CHM) or Crop Surface Model (CSM), CSM will be the terminology used in this study. To assess CSM obtained from photogrammetric processing of UAS-based multispectral data in a vineyard plot (Alessandro Matese et al., 2016) found a relationship between vines' heights—obtained from CSM—and Normalized Difference Vegetation Index (NDVI) values: higher vegetation heights coincided with higher NDVI values. Moreover, the authors also shown that UAS are suitable for vineyard's biomass estimation. However, flight altitude allied with the sensor's resolution caused a smoothness on the DSM, which lead the authors to consider only a vegetation's height above 0.5 m. Both in Burgos et al. (2015), Kalisperakis et al. (2015) and Matese et al. (2016), elevation data obtained from the UAS proved to be an effective technique to estimate vineyard's vegetation, regardless of the terrain slope or outliers. Baofeng et al. (2016) proposed a method that used the DSM to estimate missing plants and plants potentially affected from biotic and abiotic problems. The method relied on the DSM's local normalization with a sliding window to remove the terrain slope effect, transforming it in a binary image that differentiates vine from non-vine pixels. This approach requires the image to be both inverted and rotated to get a vertical row alignment and divided into a grid. If the non-vine pixels percentage is greater than 90%, it is considered as missing vine, whereas if it is between 20% and 90%, it is deemed to be affected vine. Weiss and Baret (2017) processed UAV-based RGB imagery to extract the vineyard's macro structure, vine row orientation, cover fraction, row width, row spacing, percentage of vegetation and missing vegetation. The method analyses the percentage of points in the processed dense-point cloud, where a threshold was used to separate vine row pixels from background pixels. This method also requires vertical vine rows alignment, obtained by estimating the row orientation using the Hough transform. Thus, row spacing results from using row peaks' average value from a horizontal profile line. Moreover, a cover fraction estimation results from dividing the estimated row width by the row spacing or by computing the ratio between the number of pixels estimated as vineyard vegetation and the total number of pixels in the image. Missing plants calculation was done by individual analysis of each row based on the percentage of non-vegetation pixels. This procedure, as stated by the authors, is not very sensitive to large variations of row width and height. However, depending on the flight characteristics (image overlapping, altitude, sensor, data processing software) and of the vineyard management practices or its phenological cycle, produced elevation models can be imprecise, rendering them unable to differentiate accurately between vines and soil.

The aforementioned studies show the diversity of methodologies found in literature concerning the segmentation of vine rows and vineyard vegetation. Each has their own strengths and weaknesses and this work uses them in a complementary way, especially UAS-based methodologies. Indeed, photogrammetric processing of imagery—acquired during an aerial survey, as point cloud(s)—along with individual UAV imagery, can be used to compute orthophoto mosaics, DTMs and 3D models of the surveyed area (Pádua, Vanko, et al., 2017). By combining the very high-resolution outcomes produced from UAVs imagery, the proposed method's main goals are to: (1) identify and extract vineyard's vegetation by distinguishing it from soil, canopy shadow and eventual inter-row vegetation; (2) detect vine rows for a given vineyard plot; and (3) estimate possible missing vine plants.

The proposed method works independently from the type of broadband imagery sensor coupled to the UAV, the vineyard plot orientation and terrain slope. In addition, it uses as few parameters as possible to be robust enough to achieve the defined goals. Finally, the proposed method also considers the potential of imagery data to estimate vineyard parameters. Thus, combining VIs with elevation data to provide accurate vineyard maps may be used to extract vineyard-related parameters in the scope of PV, helping in both the management and decision-making tasks. The proposed method proved to be effective when applied with low-cost consumer-grade sensors carried by UAVs.

This paper is structured in 6 sections. In this section, the motivation and main goals were described, along with some related works and applications of remote sensing in PV, which enabled to assess the actual state-of-the-art. Section 6.2 describes the data acquisition process, the used UAV platforms and the vineyard data used in the study. Section 6.3 presents an evaluation of the different VIs' suitability to detect vineyard vegetation. Then, the proposed method is described in Section 6.4. Section 6.5 presents the results, validation and discussion of the proposed method, when applied to different vineyard plots. Finally, Section 6.6 points out the main conclusions and future directions towards new developments and the method's applicability.

## 6.2. Data description

Data used in this study came from vineyards located in Portugal's north-eastern, which has some unique features concerning the size, terrain slope and management practices.

Aerial surveys were performed using the low-cost and light-weight (1380 g) rotary-wing UAV DJI Phantom 4 (DJI, Shenzhen, China), which has a maximum flight time of approximately 28 minutes per battery, vertical take-off and landing (VTOL) capabilities. It is equipped with a remote controller, a Global Navigation Satellite System (GNSS) receiver, a camera and a frontal collision avoidance system. Regarding the camera—attached to a 3-axis gimbal that provides stabilization—it has a 12.4-megapixel sensor, which allows acquiring RGB images with a maximum resolution of 4000 × 3000 pixels. Autonomous flights were carried out using the Pix4Dcapture app (Pix4D SA, Lausanne, Switzerland) on an Android smartphone.

This study's flights took place during June and July 2017, using a double-grid configuration, at 60 to 80 metres height, from the UAV take-off position and with an image overlap between 70% and 80%. Acquired data was processed using Pix4Dmapper Pro (Pix4D SA, Lausanne, Switzerland), which can compute orthophoto mosaics, DSM and DTM from a dense point cloud. This type of very high-resolution data provides a general overview of the whole vineyard. Furthermore, it enables to associate operations—such as VIs—that allow the enhancement of certain vegetation features by using combinations from multiple bands and CSM, which can be computed to obtain surface's objects' heights. The computation of both the photogrammetric and the proposed method were performed by using a laptop equipped with a 2.6 GHz Intel i7-4720HQ CPU, 16GB RAM (DDR3, 1600 MHz) and a NVidia GeForce GTX 970m (3GB GDDR5 5000 MHz) GPU.

Aerial surveys included three different vineyards, from which 16 plots were used for further evaluation. Figure 6.1 shows the orthophoto mosaics of the three vineyards used in this study and presents details about the flight characteristics for each vineyard, along with the boundaries of each analysed plot and the areas used for VIs and method's validation. Vineyards B and C are used for commercial purposes, while vineyard A is not. When compared in-field, plots belonging to vineyard B show better management practices or are less affected by biotic issues than vineyards A and C. The latter has more missing vine plants along the plots. Vineyard C plots have larger areas and are surrounded by trees—that cover part of the rows—at their outer limits. Regarding the analysed plots, 11 plots were from vineyard A, 2 from vineyard B and 3 from vineyard C, as presented in Figure 6.1.

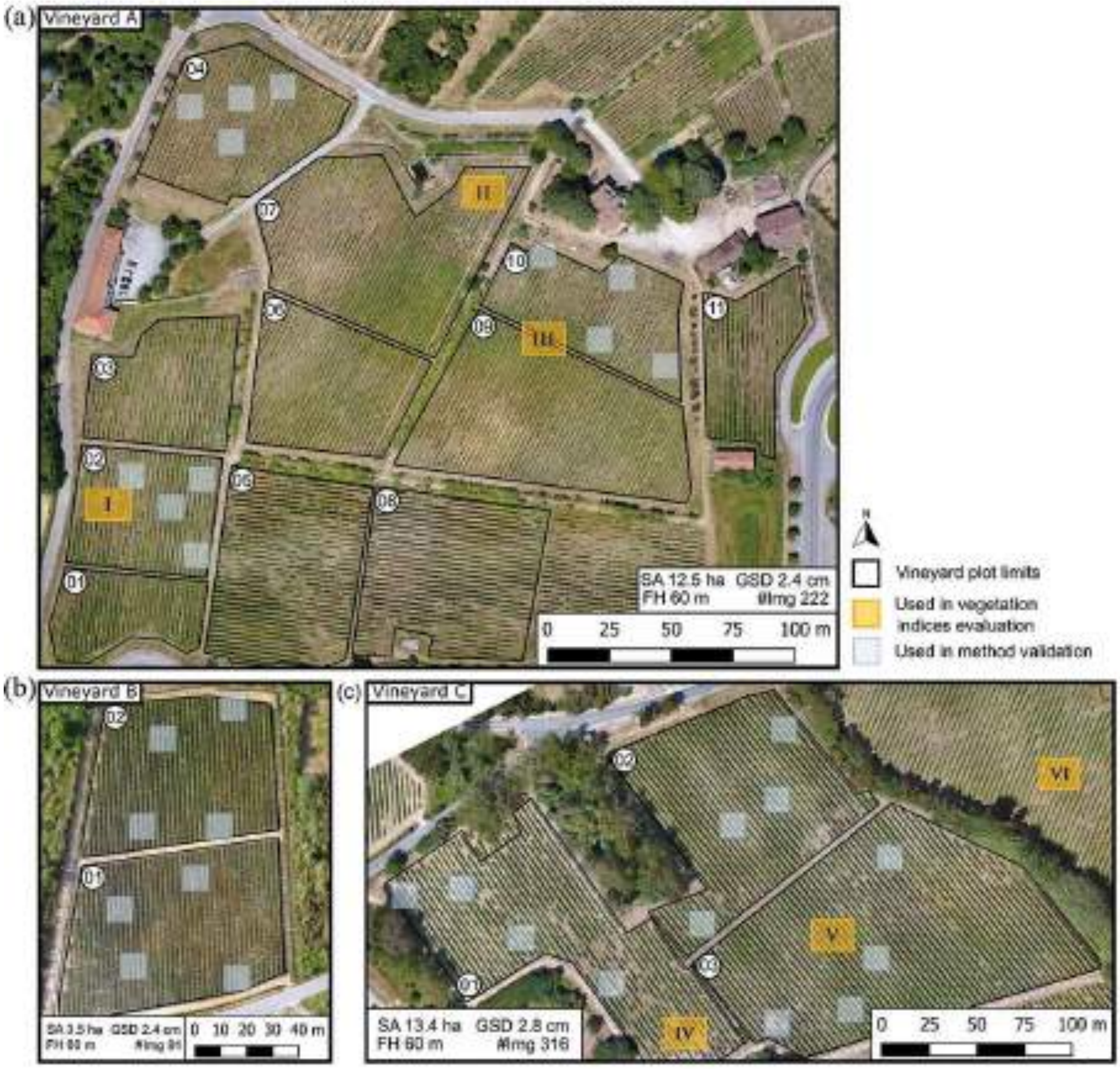


**Figure 6.1.** Resulting orthophoto mosaics from the three surveyed vineyard plots used to evaluate the proposed method along with their flight characteristics, surveyed area (SA), flight height (FH), ground sample distance (GSD), and number of acquired images (#Img). Vineyard A is located at 41°17'08.0"N, 7°44'12.0"W; vineyard B at 41°17'41.5"N, 7°29'51.3"W; and Vineyard C at 41°15'51.5"N, 8°14'12.1"W. The analysed plots are delimited by black lines and areas extracted from the orthophoto mosaics being polygons delimited in yellow (used in vegetation indices) and blue (used in the method's validation).

## 6.3. Vineyard vegetation detection using vegetation indices

VIs behaviour with different vineyard images, vine rows orientation, shadow presence, inter-row vegetation and missing vine plants, was observed and compared. Six different areas within the studied vineyard plots were analysed, as presented in Figure 6.2.

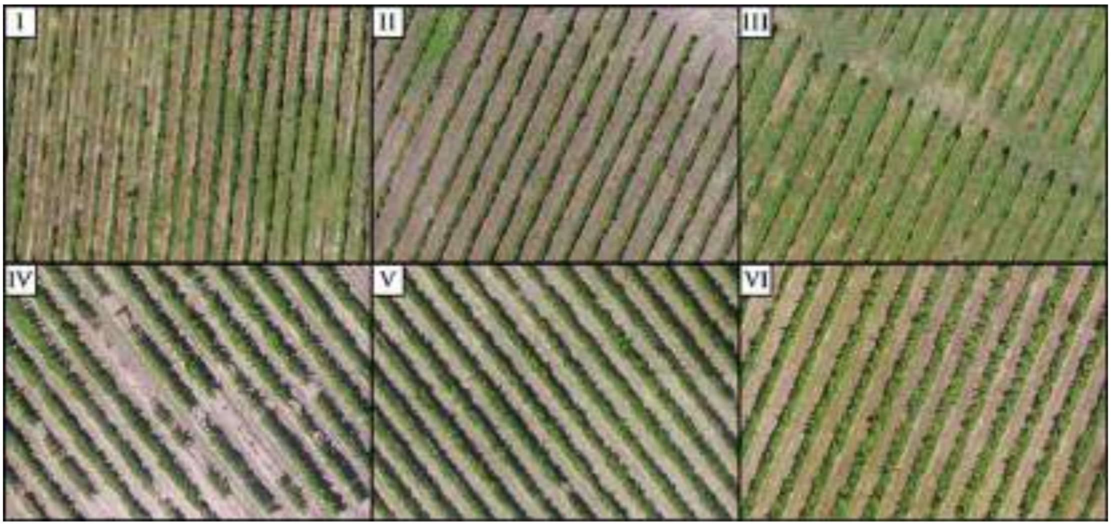


**Figure 6.2.** RGB images of the areas used to evaluate VI behaviour (row orientation, shadow presence, inter-row vegetation, and missed plants were considered).

The evaluation process is composed of the following steps: (1) VIs are computed in each area, producing a greyscale image from the arithmetic operations done on different bands; (2) then, a global threshold is applied on the resulting images to create a binary image, based on Otsu's method (Otsu, 1979). This method is capable of automatically threshold a single-band image by dividing its histogram in foreground and background pixels; (3) morphological operations (open and close) are carried out to filter the binary images (small clusters of pixels are removed), thus improving the results obtained from VIs; and (4) lastly, the resulting binary image is compared with a manually segmented image that is used as reference.

Accuracy is computed by comparing the resulting image obtained for each VI by applying the aforementioned steps with its reference image. Results are calculated by analysing the value of each pixel, from which one of three conditions can be observed: (1) same pixel value in both images (0 or 1), which is classified as 'exact detection'; (2) a false detection, if the pixel value of the manually segmented image is one and in the resulting image is zero, being classified as 'under detection'; and (3) classified as 'over detection' if the situation is opposite to the one described in (2). Based on the bibliographic review, 13 VIs were selected, which are presented in Table 6.1, and evaluated in this process. From these, only some were directly applied to vineyards.

**Table 6.1.** RGB vegetation indices evaluated in the estimation of vineyard vegetation.

| Index | Formula | References |
|---|---|---|
| Normalized Green red difference index | $\mathrm{NGRDI} = \frac{\mathrm{Green} - \mathrm{Red}}{\mathrm{Green} + \mathrm{Red}}$ | (Falkowski et al., 2005; Gitelson et al., 2002; Kawashima & Nakatani, 1998; Tucker, 1979) |
| Normalized Green Blue Difference Index | $\mathrm{NGBDI} = \frac{\mathrm{Green} - \mathrm{Blue}}{\mathrm{Green} + \mathrm{Blue}}$ | (Kawashima & Nakatani, 1998) |
| Modified Normalized Green red difference index | $\mathrm{MNGRDI} = \frac{\mathrm{Green}^2 - \mathrm{Red}^2}{\mathrm{Green}^2 + \mathrm{Red}^2}$ | (Bendig et al., 2015) |
| Red Green Blue Vegetation Index | $\mathrm{RGBVI} = \frac{\mathrm{Green}^2 - (\mathrm{Blue} \times \mathrm{Red})}{\mathrm{Green}^2 + (\mathrm{Blue} \times \mathrm{Red})}$ | (Bendig et al., 2015) |
| Blue/Green Pigment Index | $\mathrm{BGVI} = \frac{\mathrm{Blue}}{\mathrm{Green}}$ | (P. J. Zarco-Tejada, Berjón, et al., 2005) |
| Blue/Red Pigment Index | $\mathrm{BRVI} = \frac{\mathrm{Blue}}{\mathrm{Red}}$ | (P. J. Zarco-Tejada, Berjón, et al., 2005) |
| Excess Green | $\mathrm{ExG} = 2\mathrm{g_n} - \mathrm{r_n} - \mathrm{b_n}$ | (Woebbecke et al., 1995) |
| Woebbecke Index | $\mathrm{WI} = \frac{\mathrm{g_n} - \mathrm{b_n}}{\mathrm{r_n} - \mathrm{g_n}}$ | (Woebbecke et al., 1995) |
| Vegetation Index Green | $\mathrm{VARIg} = \frac{\mathrm{Green} - \mathrm{Red}}{\mathrm{Green} + \mathrm{Red} - \mathrm{Blue}}$ | (Gitelson et al., 2002) |
| Green Leaf Index | $\mathrm{GLI} = \frac{2\mathrm{Green} - \mathrm{Red} - \mathrm{Blue}}{2\mathrm{Green} + \mathrm{Red} - \mathrm{Blue}}$ | (Gobron et al., 2000; Hunt et al., 2013) |
| Triangular Greenness Index | $\mathrm{TGI} = \mathrm{Green} - 0.39 \times \mathrm{Red} - 0.61 \times \mathrm{Blue}$ | (Hunt et al., 2013) |
| 2G_RGi | $\mathrm{2G\_RGi} = 2\mathrm{Green} - (\mathrm{Red} + \mathrm{Blue})$ | (Richardson et al., 2007) |
| Green Percentage Index | $\mathrm{G\%} = \frac{\mathrm{Green}}{(\mathrm{Red} + \mathrm{Green} + \mathrm{Blue})}$ | (Richardson et al., 2007) |

where, $\mathrm{r_n} = \frac{\mathrm{Red}}{(\mathrm{Red+Green+Blue})}$; $\mathrm{g_n} = \frac{\mathrm{Green}}{(\mathrm{Red+Green+Blue})}$; $\mathrm{b_n} = \frac{\mathrm{Blue}}{(\mathrm{Red+Green+Blue})}$ and Green, Red and Blue are the reflectance values of each band.

An overall average result of 87% of vineyard vegetation exact detection was reached. The only exception was the WI VI that was very inconsistent amongst the tested areas (from 49% to 89% exact detection), as presented in Table 6.2. It is worth to note that many VIs had over 90% accuracy when applied to the different areas.

**Table 6.2.** Vegetation indices performance evaluation when detecting vineyard vegetation: exact detection (=), over detection (+), under detection (-) and estimated threshold value (*T*) from Otsu's Method. The cells in bold correspond to vegetation indices with higher mean accuracy in vine vegetation detection, the vegetation index with lower performance is marked in purple.

| Index | Area I | | | | Area II | | | | Area III | | | | Area IV | | | | Area V | | | | Area VI | | | |
|---|---|---|---|---|---|---|---|---|---|---|---|---|---|---|---|---|---|---|---|---|---|---|---|---|
| | = (%) | *T* | + (%) | - (%) | = (%) | *T* | + (%) | - (%) | = (%) | *T* | + (%) | - (%) | = (%) | *T* | + (%) | - (%) | = (%) | *T* | + (%) | - (%) | = (%) | *T* | + (%) | - (%) |
| NGRVI | 88.07 | 0.04 | 0.46 | 11.46 | 87.38 | 0.05 | 4.31 | 8.31 | 83.9 | 0.05 | 6.93 | 9.17 | 90.47 | 0.06 | 2.23 | 7.3 | 91.64 | 0.04 | 2.52 | 5.84 | 89.08 | 0.06 | 8.53 | 2.39 |
| MGRVI | 87.75 | 0.08 | 0.43 | 11.82 | 87.2 | 0.1 | 4.07 | 8.74 | 83.98 | 0.11 | 7.17 | 8.84 | 90.44 | 0.13 | 2.22 | 7.33 | 91.39 | 0.09 | 2.42 | 6.19 | 89.12 | 0.12 | 8.48 | 2.4 |
| BGVI | 91.06 | 0.59 | 3.81 | 5.13 | 91.8 | 0.74 | 2.49 | 5.71 | 92.95 | 0.67 | 2.43 | 4.62 | 88.63 | 0.59 | 7.54 | 3.83 | 93.65 | 0.68 | 4.06 | 2.29 | 90.11 | 0.53 | 7.1 | 2.79 |
| BRVI | 86.69 | 0.53 | 3.68 | 9.62 | 88.65 | 0.73 | 2.1 | 9.25 | 91.23 | 0.67 | 1.86 | 6.91 | 83.42 | 0.58 | 8.97 | 7.61 | 91.9 | 0.64 | 2.9 | 5.2 | 87.63 | 0.55 | 6.88 | 5.49 |
| **ExG** | **89.87** | **0.19** | **0.92** | **9.21** | **90.54** | **0.15** | **1.29** | **8.16** | **90.61** | **0.19** | **1.19** | **8.2** | **91.35** | **0.21** | **2.6** | **6.06** | **93.58** | **0.16** | **2.11** | **4.3** | **92.45** | **0.25** | **3.93** | **3.62** |
| WI | 87.98 | 0.48 | 6.90 | 5.12 | 49.43 | 0.46 | 48.51 | 2.06 | 83.38 | 0.47 | 15.02 | 1.6 | 86.35 | 0.49 | 11.68 | 1.97 | 62.54 | 0.48 | 36.04 | 1.42 | 60.78 | 0.49 | 38.95 | 0.27 |
| VARIg | 88.25 | 0.05 | 0.50 | 11.26 | 86.1 | 0.07 | 5.94 | 7.96 | 80.77 | 0.08 | 10.03 | 9.2 | 90.33 | 0.09 | 2.46 | 7.21 | 91.46 | 0.06 | 2.92 | 5.62 | 86.75 | 0.07 | 11.23 | 2.02 |
| **GBVI** | **85.17** | **0.31** | **0.86** | **13.97** | **89.8** | **0.18** | **1.1** | **9.1** | **90.36** | **0.24** | **0.86** | **8.78** | **88.98** | **0.29** | **1.97** | **9.05** | **92.65** | **0.23** | **1.82** | **5.54** | **91.27** | **0.35** | **2.08** | **6.65** |
| **RGBVI** | **90.14** | **0.28** | **1.24** | **8.62** | **91.01** | **0.2** | **1.47** | **7.51** | **91.32** | **0.26** | **1.36** | **7.32** | **91.09** | **0.29** | **3.59** | **5.33** | **93.82** | **0.24** | **2.4** | **3.79** | **92.27** | **0.36** | **4.19** | **3.54** |
| **GLI** | **90.71** | **0.13** | **1.14** | **8.14** | **91.06** | **0.1** | **1.51** | **7.43** | **91.25** | **0.13** | **1.45** | **7.3** | **91.38** | **0.14** | **3.14** | **5.48** | **93.88** | **0.11** | **2.44** | **3.68** | **92.26** | **0.17** | **4.45** | **3.29** |
| TGI | 86.65 | 0.12 | 2.35 | 11 | 90.78 | 0.09 | 1.72 | 7.5 | 91.57 | 0.1 | 1.42 | 7.01 | 82.9 | 0.11 | 10.42 | 6.68 | 91.46 | 0.09 | 2.79 | 5.75 | 89.52 | 0.15 | 6.5 | 3.98 |
| 2GRGi | 87.47 | 0.2 | 1.95 | 10.58 | 90.91 | 0.15 | 1.56 | 7.53 | 91.76 | 0.18 | 1.33 | 6.92 | 84.41 | 0.18 | 9.46 | 6.13 | 91.71 | 0.16 | 2.56 | 5.73 | 88.78 | 0.26 | 8.03 | 3.19 |
| **G%** | **90.6** | **0.39** | **1.10** | **8.3** | **91.86** | **0.37** | **1.94** | **6.21** | **91.17** | **0.39** | **1.41** | **7.42** | **91.38** | **0.4** | **2.95** | **5.67** | **94.05** | **0.38** | **2.78** | **3.17** | **92.38** | **0.42** | **4.2** | **3.42** |

G%, with 91.9%, GLI with 91.8%, RGBVI with 91.6%, ExG and NGBDI, both with 91.4%, are the VIs with the highest average accuracy. Moreover, while NGBDI reached 4.6% of over detection, the remaining had lower values, around 2%. These five VIs were compared to select the most suitable for vineyard's vegetation detection. Figure 6.3 presents the evaluation regarding the areas where VIs presented the same value. As depicted, the five VIs have an overlap of 94% for the six tested areas, which makes their performance very similar. However, G% has a slightly higher performance and was therefore selected for this study.

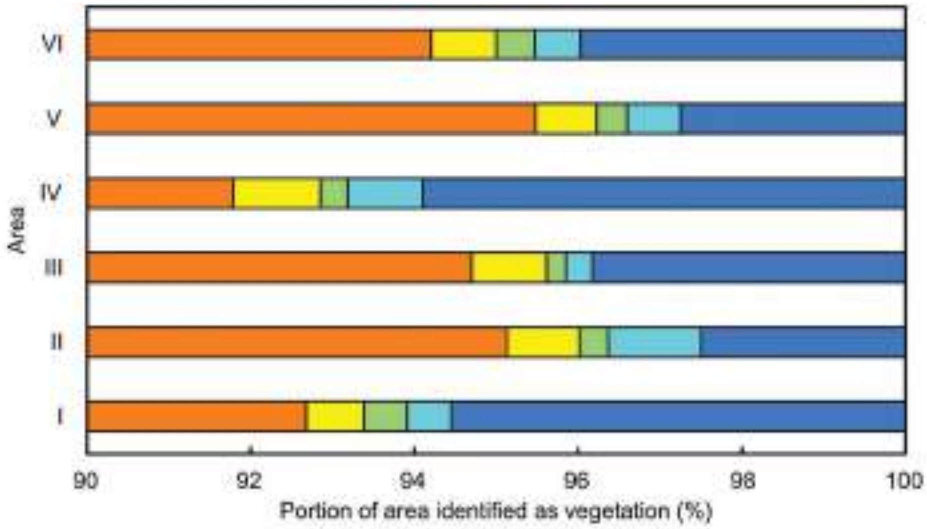


| Identified vegetation (%) | Area I | Area II | Area III | Area IV | Area V | Area VI |
|---|---|---|---|---|---|---|
| In 5 indices | 92.68 | 95.13 | 94.70 | 91.79 | 95.48 | 94.21 |
| In 4 indices | 0.70 | 0.89 | 0.91 | 1.06 | 0.75 | 0.79 |
| In 3 indices | 0.53 | 0.35 | 0.24 | 0.34 | 0.37 | 0.46 |
| In 2 indices | 0.54 | 1.13 | 0.32 | 0.91 | 0.65 | 0.57 |
| In 1 index | 5.56 | 2.50 | 3.82 | 5.90 | 2.75 | 3.97 |

**Figure 6.3.** Percentage of common pixels to the five-selected VIs in the test areas.

**Figure 6.4** shows the agreement between the automatic threshold value obtained from the Otsu's method and a selected fixed threshold value. The obtained results are in line with the mean values given from the Otsu's method in the six evaluated areas and the overall detection percentage assumes only one maximum value, proving the suitability of the Otsu's method to automatically estimate a threshold value.

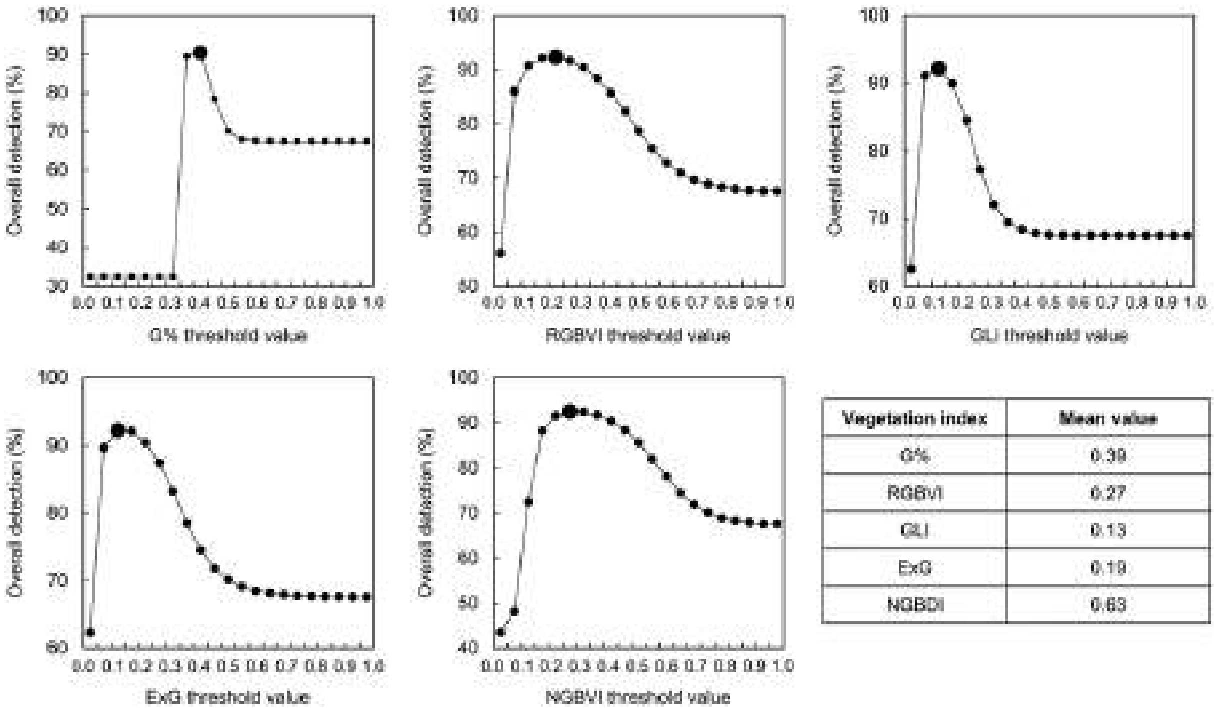


| Vegetation index | Mean value |
|---|---|
| G% | 0.39 |
| RGBVI | 0.27 |
| GLI | 0.13 |
| ExG | 0.19 |
| NGBDI | 0.63 |

**Figure 6.4.** Vine vegetation detection accuracy based on the threshold values for the top five vegetation indices in area III. It is also presented a table with the averaged results.

# 6.4. Proposed method for vineyard analysis

This section presents the proposed method to identify vineyard vegetation, distinguishing it from non-vineyard features that can be present in a vineyard plot. The main challenge when regarding vineyard vegetation monitoring is related with the similar reflectance that other types of vegetation can present, which is especially noticeable in common RGB imagery and less noticeable in NIR or hyperspectral imagery. Therefore, by considering the usual vineyards' row structure and its regularity, the method explores the usage of the different outcomes provided by photogrammetric processing of UAS imagery in combination with image processing techniques, that namely use elevation data and orthophoto mosaic. This enables the classification of vine vegetation within a given vineyard plot and distinguish it from vegetation cover, shadows, and bare soil. Moreover, the proposed method is also capable to estimate potential missing vine plants. As inputs, the UAS-based photogrammetric outcomes are used. Features extraction from a given vineyard plot is achieved by masking non-vine vegetation.

Figure 6.5 presents the proposed method's operations sequences. There are three distinct steps composing it: (1) vegetation extraction and pixel clustering; (2) vine rows reconstruction, by means of analysing each formed pixel cluster retrieved in step 1; and (3) vineyard parameters extraction—vine rows, vineyard vegetation and potential missing vines. Each step plays an essential role in the process of vineyard vegetation extraction. All are further detailed in the next subsections. The notation used in this section is explained in Table 6.3.

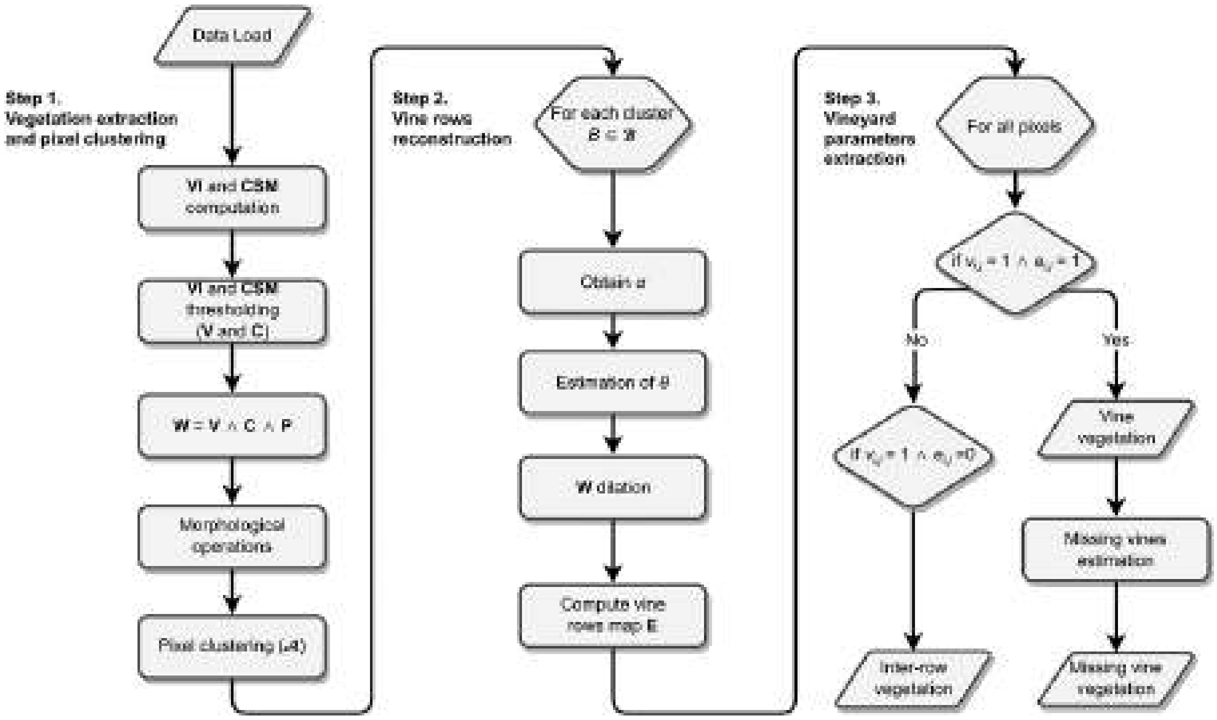


**Figure 6.5.** Proposed method's operation general flow chart.

### 6.4.1. Step 1: Vegetation extraction and pixel clustering

Method's step 1 aims to extract vine-related pixels from the aerial high-resolution images of a given vineyard plot, which defines the polygon P (Figure 6.6f). As such, data that does not represent vine vegetation, such as soil, grass and possible shadowing effects caused by vine canopies, trees, and buildings, is discarded. To accurately complete this step, both orthophoto mosaic (Figure 6.6a), and elevation data (Figure 6.6b and c), are used. The former is used to compute the VI (Figure 6.6d). Assuming that in the produced orthophoto mosaic, vegetation presents higher reflectance values than non-vegetation areas, a threshold operation can be applied to separate both. The computed VI, is used to create a binary image produced using Otsu's method (Otsu, 1979), as presented in equation (1), where **V** (Figure 6.6g), represents the computed binary image resulting from the Otsu's method application, VI represents the image produced by the vegetation index computation and T represents the defined threshold from Otsu's method. For each $(i, j)$ pixel position in the image, i represents the line number and j the column number. In this way, $v_{i,j}$ represents the matrix V entry for the position (i, j). The same notation is used in the remaining equations.

**Table 6.3.** Notation table.

| Notation | Meaning |
|---|---|
| **P** | Binary image of the polygon of the plot to be analysed |
| **VI** | Single band image obtained from vegetation index computation |
| $T$ | Threshold value obtained from Otsu's method application |
| **V** | Binary image resultant from **VI** thresholding step |
| **CSM** | Single band image obtained from subtraction of the DTM to the DSM computation |
| $h_{\text{max}}$ | Maximum height range used for CSM thresholding |
| $h_{\text{min}}$ | Minimum height range used for CSM thresholding |
| **C** | Binary image resultant from CSM thresholding according to $h_{min}$ and $h_{max}$ |
| **W** | Binary image resultant from the conjunction of **V**, **C** and **P** |
| $B$ | Group of interconnected pixels forming a cluster resultant from pixel clustering |
| $\mathcal{B}$ | Set of all detected clusters B in **W** |
| $\alpha$ | Orientation angle of the cluster B |
| $\theta$ | Mean orientation all $\alpha$ values from the set of clusters $\mathcal{B}$ |
| $\mathbf{F}_{\theta}$ | Structuring element used to dilate **W**, forming **E**. It is constituted by a line with orientation $\theta$ |
| **E** | Binary image resultant after dilation of **W** |
| $D$ | Group of interconnected pixels forming a clusters resultant from the pixel clustering of **E** |
| $\mathcal{D}$ | Set of all detected clusters in **E** |
| **U** | Binary image containing estimated inter-row vegetation |
| **L** | Binary image with all pixels detected in **V** present in **E** |
| $\overline{\mathbf{L}}$ | Complement of **L** |
| $S_{\text{centre}}$ | Line segment that intersects each cluster's ($D$) centroid, ends in its extremities and has its orientation |
| **S** | Binary image contained all detected $S_{centre}$ elements |
| $\mathbf{F}_r$ | Structuring element used to dilate **G**, forming **Q**. It has a disk shape element with radius $r$ |
| **G** | Binary image produced after intersection of all $s_{i,j}$ pixels with $\overline{l}_{i,j}$, representing vine row areas with potential missing vines |
| **Q** | Binary image produced after **G** dilation, representing vine rows areas with potential missing vines |
| **K** | Property intended be used to calculate its area, which can assume the value of the binary images **E**, **L**, **Q** |
| $A$ | Area of a given property to calculate **K**, which is the sum of all pixel values (0 or 1) of a binary image with $m \times n$ size |

$$\mathrm{v_{i,j}} = \begin{cases} 1, \mathrm{vi_{i,j}} \geq T \\ 0, \mathrm{vi_{i,j}} < T \end{cases} \qquad (1)$$

Next, CSM (Figure 6.6e) is computed using elevation data, as shown in equation (2) (Holman et al., 2016; Alessandro Matese et al., 2016). Each pixel contains a value h that corresponds to the height of objects above ground: values close to zero represent the ground. This operation removes the field's topography.

$$\mathrm{CSM} = \mathrm{DSM} - \mathrm{DTM} \qquad (2)$$

In the same way as V, the computed CSM has a thresholding operation, as represented in equation (3), where each height value (h) is analysed according to a height range (from $h_{min}$ to $h_{max}$), producing a binary image **C** (Figure 6.6h), only containing pixels within the values defined for the height range. This process enables a CSM's pixel-wise filtering to discard pixels other than vineyard's vegetation. Knowledge of the analysed areas allowed the selection of h values ranging from 0.5 to 2 metres, thus removing possible data other than vineyard's vegetation. However, height range may depend on both the vineyard's architecture and the management practices used.

$$c_{i,j} = \begin{cases} 1, h_{min} \leq csm_{i,j} \leq h_{max} \\ 0, \quad \text{otherwise} \end{cases} \tag{3}$$

As shown in the RGB image presented in Figure 6.7a and in the false colour image, that results from applying G% vegetation index (Figure 6.7b), part of the inter-row vegetation has almost the same reflectance value of some vine canopies, which is not verified in the CSM computation, presented in Figure 6.7c.

The method's main steps are summarized in Figure 6.6, were plot 02 from vineyard A is used to illustrate its application, from the input data to the final extracted parameters.

Figure 6.8 presents a fraction of a vineyard plot where the superimposed lines are related to the thresholded G%—in yellow—(V) and CSM above 0.5 m and below 2 m—in red (C). The detection of inter-row vegetation is noticeable in V. However, it is accurate in the row's vegetation. On the other hand, shadows detection is also considered in the C threshold but not in V.

By merging both types of data, it is possible to obtain areas where only pixels considered as vegetation and with a certain height are present, thus removing vegetation cover that could also be identified as vine vegetation, which would lead to erroneous classification of vine rows. In this way, the conjunction of the binary images produced after thresholding (V and C) are used to create a new binary mask image ($\mathbf{W}$) (Figure 6.6k), according to equation (4), where P is also considered to discard pixels outside the area under analysis.

$$w_{i,j} = \begin{cases} 1, \text{if } v_{i,j} = 1 \wedge c_{i,j} = 1 \wedge p_{i,j} = 1 \\ 0, \text{otherwise} \end{cases} \tag{4}$$

The resulting binary image ($\mathbf{W}$) is submitted to a sequence of morphological operations (open, close and removal of small objects) to remove outliers and improve the detection accuracy. This step can evaluate different properties from each generated group of interconnected pixels $B \in \mathcal{B}$, where $\mathcal{B}$ represents all the detected clusters at the plot level. Resulting clusters are areas where vine canopies are present. At this stage, each vine row is not connected and therefore a reconstructive process takes place to join the unconnected clusters into row shapes.

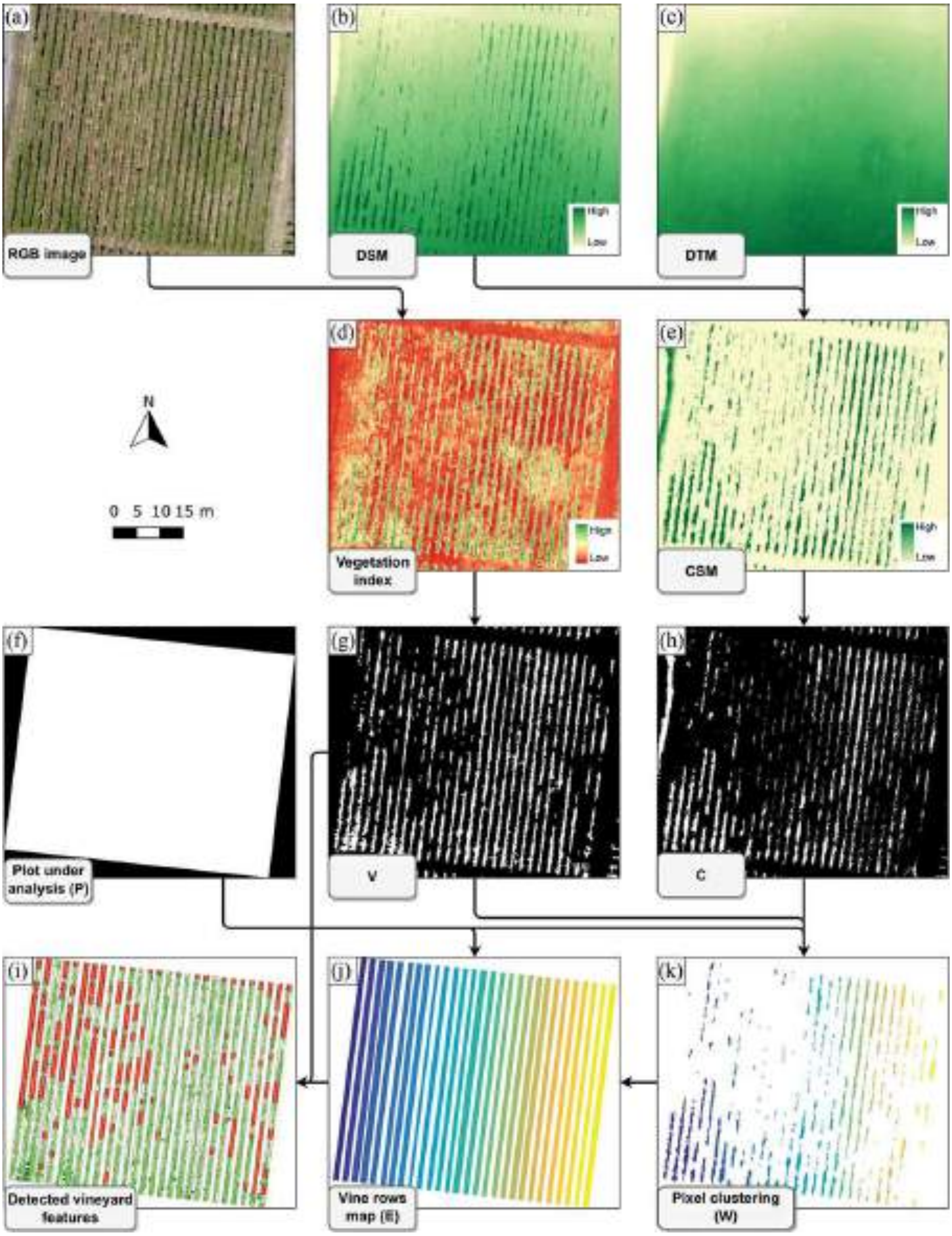


**Figure 6.6.** Extracted parameters resulting from the proposed method's step 3. Green colours represent detected vegetation – light green corresponds to vine row vegetation and dark green to inter-row vegetation; red represents the estimated missing vegetation; yellow represents the row centre; and grey the estimated vine rows boundaries.

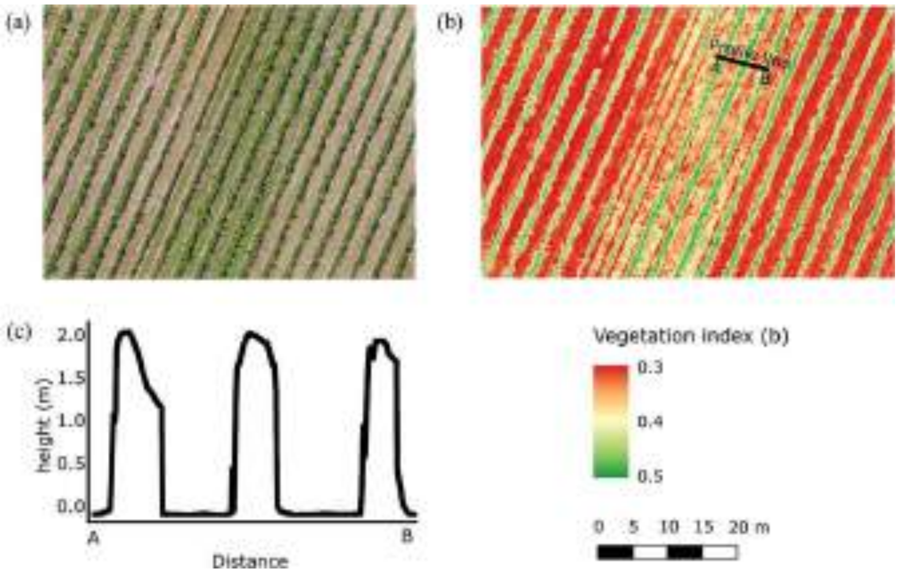


**Figure 6.7.** Different UAS-based outcomes from part of a vineyard plot: (a) RGB image; (b) corresponding false colour image from the green percentage index computation; and (c) CSM line profile from the line traced upon three vine rows.

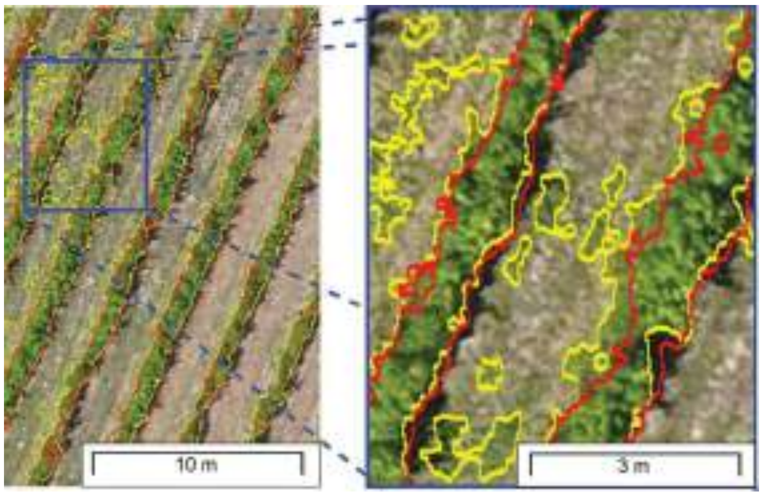


**Figure 6.8.** Method processing steps applied to the plot 02 from vineyard A, some images are in a false colour representation for better interpretation.

## 6.4.2. Step 2: Vine rows reconstruction

Depending on the vineyards' management practices and on the acquired data resolution, clusters of pixels obtained in the proposed method's step 1 do not represent complete vine rows, requiring a reconstruction process. Therefore, the mean plot orientation $\theta$ is estimated based on the dominant angle of all detected clusters from the set of clusters $\mathcal{B}$. This angle ($\theta$) is obtained by the orientation $\alpha$ of each detected cluster, which is computed based on the angle between the x-axis and the major axis of the ellipse containing the same second-moments as B. $\theta$ assumes the mean value of all $\alpha \in \mathcal{B}$. Then, clusters are submitted to a dilation process, $\phi$, using a linear structuring element $\mathbf{SE}_\theta$ with one-pixel width and orientation $\theta$, obtaining E, which depicts the vine rows map of the plot under analysis, as represented in equation (5) (**Figure 6.6**j). This forms a new set of clusters $\mathcal{D}$, where D represents a single vine row.

$$\mathrm{e_{i,j}} = \phi\mathbf{SE}_\theta(\mathrm{w_{i,j}}), \text{where } \mathrm{e_{i,j}} \wedge \mathrm{p_{i,j}} = 1 \tag{5}$$

By applying this procedure, previously unconnected clusters begin to form a set of clusters representing the connection of clusters in each row, therefore enabling vine rows reconstruction.

### 6.4.3. Step 3: Vineyard parameters extraction

Method's step 3 relies on the final extraction of vineyard-related information, namely by estimating vine rows, vineyard vegetation and areas with missing vine plants (Figure 6.6i). The resulting vine rows estimation image ($\mathbf{W}$)—obtained after the proposed method's step 2—enables to estimate the number of rows and their occupation area present in P. After estimating rows, the mask with vegetation ($\mathbf{V}$) is used to detect vine's vegetation, where all pixels present in $\mathcal{B}$ and contained in $\mathcal{D}$ form L, which represents the vine vegetation.

Vegetation that lies outside vine rows area and that is considered in $\mathcal{B}$, is classified as inter-row vegetation (U). Areas with potential missing vine plants are predicted by matching the estimated vine rows mask central lines S with the complement of the estimated vine vegetation $\bar{\mathbf{L}}$, forming a new binary image G. S is constituted by, $S_{centre}$ which is a line segment that intersects each cluster's (D) centroid and ends at its extremities and has its orientation. However, detecting possible missing vine plants is typically a more complex problem, since, in many cases, adjacent vines tend to cover the empty space of the missing vine canopy, making the estimation more complicate. Next, the clusters pass through a process of image dilation, represented in equation (6), to compute a representative map of the detected areas, Q. However, this time, SE is a disk-shaped structuring element whose radius r is half of the mean value of all cluster's width ($\mathcal{D}$).

$$\mathrm{q_{i,j}} = \phi\mathbf{SE}_r(\mathrm{g_{i,j}}) \tag{6}$$

The area $A$ of each estimated output can be calculated by equation (7), which represents the sum of all pixels contained (matrix with m lines and n columns) in the property to calculate K (vine rows area, vine vegetation, potential missing vine plants and inter-row vegetation), multiplied by the squared GSD value.

$$A = \left( \sum_{i=1}^{m} \sum_{j=1}^{n} \mathrm{k_{i,j}} \right) GSD^2 \quad (7)$$

Figure 6.9 presents the detected vegetation, potential missing vine plants and the estimated vine rows area. The method's outputs are an accurate and quick way to provide vineyard status information in a PV context, to help viticulturists in their vineyard management activities.

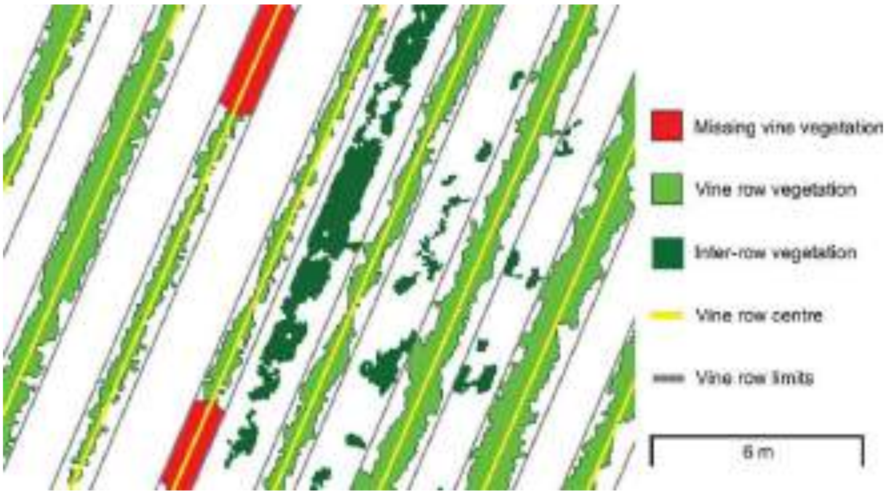


**Figure 6.9.** Visual interpretation of both the thresholding and the masking processes: vegetation index represented in yellow and the canopy height model in red.

## 6.5. Results and discussion

For validation purposes, the proposed method was applied to 16 plots from three different vineyards presented in Section 6.2, Figure 6.1. As an accurate manual segmentation of the vineyard vegetation present in all the selected plots is a highly laborious and time-consuming task, small fractions of eight plots—A.02, A.04, A.10, B.01, B.02, C.01, C.02 and C.03—were extracted. This allowed a more precise and quicker process to create precise manual segmented images. The aforementioned fractions—four per plot, each with an approximated area of 100 $m^2$ (10 m × 10 m)—were selected assuring diversity in terms of rates of missing vine plants, rows orientation and inter-row vegetation.

### 6.5.1. Proposed method validation

Regarding vine rows estimation, different parameters were evaluated: (1) good detection—the row was detected with a high overlap when compared with its real position; (2) missed detection—the row was not detected; (3) extra detection—wrongly detected vine row; (4) over detection—the row was classified in multiple vine rows; (5) under detection—multiple vine rows classified as one row; (6) larger detection—row is larger than its actual size; and (7) smaller detection—vine row is smaller than its actual size. The proposed method validation occurred by using the extracted vineyards fractions and comparing the obtained results with the manual segmentation.

As presented in Table 6.4, the proposed method achieved a good accuracy in vine rows estimation. Correct row detection was always greater than 90%, with 93.4% mean value. Moreover, the method could detect successfully all the vine rows, of 353 analysed. On the analysed fractions, missed, extra, over or under detection cases were not found. Regarding the detected vine rows, 19 were not correctly estimated and from those, 2.67% were classified as 'larger detection' and 2.88% as 'smaller detection'. Moreover, the percentage of real vineyard vegetation contained in the estimated vine rows area was calculated to further validate vine rows estimation achieving a mean value of 99.7%. This was achieved by intercepting the manual segmented vineyard fractions with the estimated vine rows.

**Table 6.4.** Vine row detection accuracy in 8 different vineyard plots, with the number of rows analysed per plot and percentage of detected vineyard vegetation contained in the plot's estimated vine rows.

| Plot no. | Number of rows | Detected vegetation portion (%) | Type of vine rows detection (%) | | | | | | |
|---|---|---|---|---|---|---|---|---|---|
| | | | 1. Good | 2. Missed | 3. Extra | 4. Over | 5. Under | 6. Larger | 7. Smaller |
| A.02 | 28 | 99.78 | 92.86 | - | - | - | - | 3.57 | 3.57 |
| A.04 | 34 | 99.97 | 91.18 | - | - | - | - | 5.88 | 2.94 |
| A.10 | 45 | 99.40 | 95.56 | - | - | - | - | - | 4.44 |
| B.01 | 43 | 99.50 | 97.50 | - | - | - | - | 2.50 | - |
| B.02 | 37 | 99.78 | 91.89 | - | - | - | - | 2.70 | 5.41 |
| C.01 | 75 | 99.55 | 97.30 | - | - | - | - | 1.35 | 1.35 |
| C.02 | 53 | 99.87 | 92.59 | - | - | - | - | 3.70 | 3.70 |
| C.03 | 60 | 99.93 | 96.72 | - | - | - | - | 1.64 | 1.64 |
| Mead detection (%) | | 99.72 | 94.45 | - | - | - | - | 2.67 | 2.88 |

Finally, vine vegetation extracted by applying the proposed method also underwent a validation process that consisted in comparing it with the manual segmented images. Figure 6.10a presents these results. The method achieved a 94.10% mean percentage of exact vegetation detection, a mean value of 2.93% regarding over classification and 2.97% of under classification. Differences between plots' fractions were not meaningful. Indeed, even those with a higher rate of missing vines did not influence the vegetation extraction process. In what regards the validation of missing vegetation estimation, the process was the same as that applied to vegetation estimation. However, only the fractions that have missing vegetation were evaluated. Thus, all plot fractions from vineyard B, as well as those from plot 02 from vineyard C were discarded, as they have low rates of missing vegetation. Results achieved a mean value of 97.04% in exact classification of missing vegetation, as shown in Figure 6.10b.

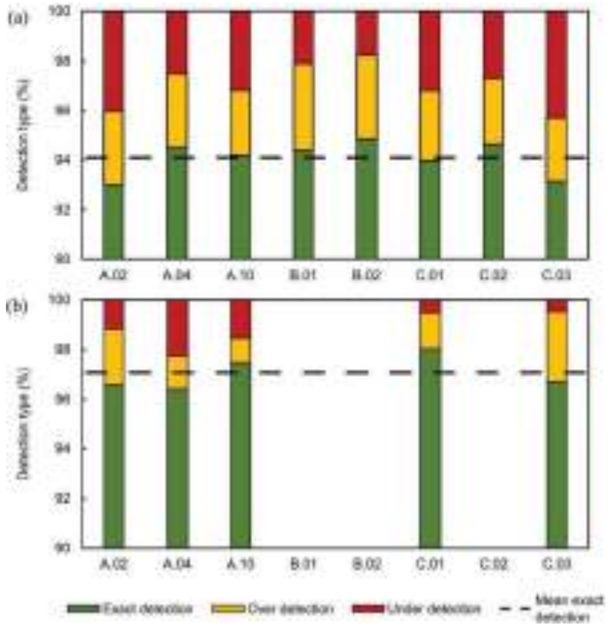


**Figure 6.10.** Results from validation of the vine vegetation extraction process (a) and potential missing vine vegetation process (b).

Figure 6.11 shows only a fraction of the detected vine vegetation, its manual segmented image and the comparison between both. Most of the non-detected vegetation lies in the vine plants' borders. In vineyard B plots' fractions, variations are less noticeable than in the other vineyards' fractions. This is due to fewer regions with missing vine vegetation in this vineyard. In vineyards A and C there are cases were the presence of shadows and grass in the row is also considered in the estimation of vine vegetation.

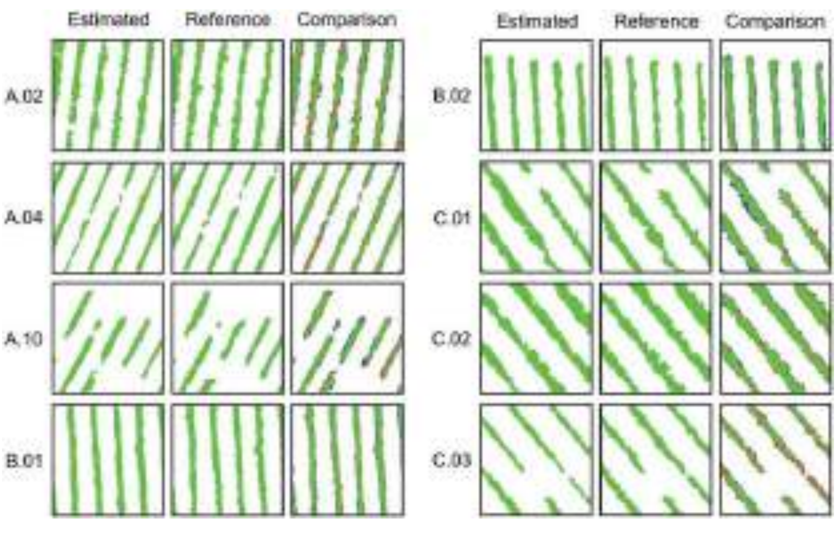


**Figure 6.11.** Comparison between the estimated vine vegetation with manually segmented plot fractions. Represented in green are exact classifications, in blue over classifications, and in red under classifications.

These results are satisfactory, since the method proved to be able to accurately detect vine rows with vegetation in almost all scenarios: present inside the estimated vine rows (99.72%); to exactly estimate the actual vine vegetation (94.10%); with a low percentage of under detection of vegetation (2.97%); missing vine vegetation also achieved a good accuracy (97.04%). The various parameters automatically extracted by applying the proposed method support the generation of accurate vineyard maps and vine rows-related properties, such as: percentage of vineyard vegetation, missing vines and inter-row vegetation. This proves that the proposed method is useful in PV management and in its decision-making tasks. Furthermore, obtained results are in line with those of previous works (Comba et al., 2015; A. Nolan et al., 2015), which made use of different image acquisition sensors (NIR)—more expensive when compared with the sensors used in this study—to obtain imagery data.

### 6.5.2. Proposed method application

The proposed method was applied to 16 plots from vineyards A, B and C. In all plots, the following parameters were extracted: vine rows estimation, vine vegetation and missing vines plants estimation. Figure 6.12 presents an overall view of the evaluated plots. In vineyard A, vine rows occupation area ranged from 40% to 55%; in vineyard B from 37% to 49%; and in vineyard C, from 53% to 61%. As expected, a higher percentage of missing vine vegetation was found in vineyard A (plot A.01 to A.11), with an average of 28% of missing vineyard vegetation. On the other hand, vineyard B presented only 1% of missing vegetation, while vineyard C presented approximately 7%.

Figure 6.13 presents a visual interpretation, based on the results obtained by applying the proposed method to plots A.04, A.06, A.07, B.02 and C.03. These plots differ in size and in vine rows coverage area. Some of the noticed limitations are related with the absence of vegetation or highly affected vines that did not developed properly. These issues resulted in lower heights that correspond to low vine rows formed. For example, in plot A.06 that was not classified, as can be seen in Figure 6.13b. Green vegetation cover was considered as vegetation in plot A.07 (shown in Figure 6.13c). In plot B.02, vegetation absence in the estimated row centre caused an over estimation of missing vine vegetation (shown in Figure 6.13d).

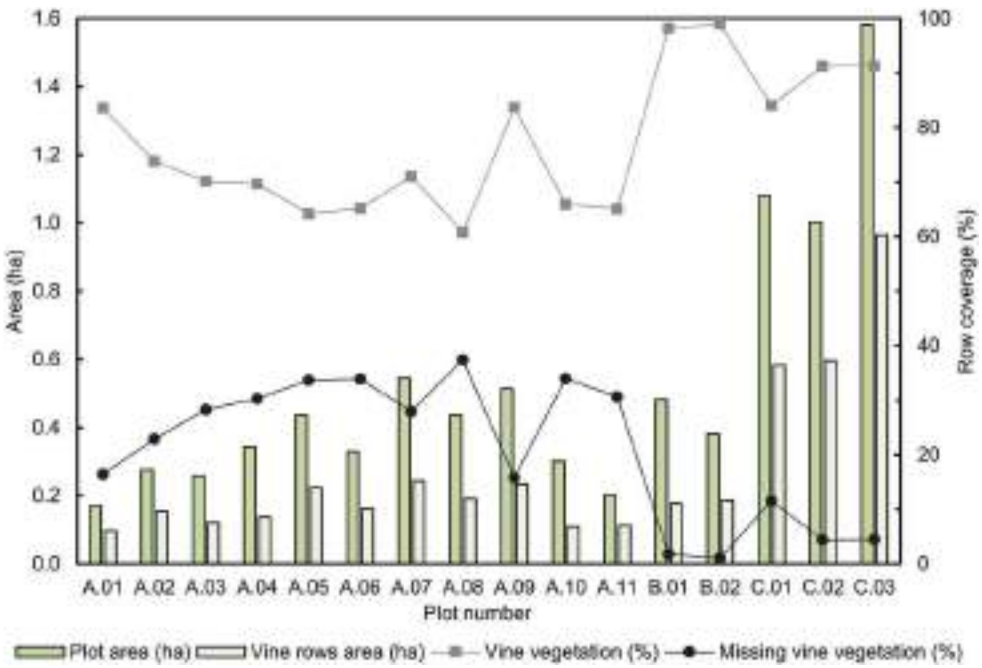


**Figure 6.12.** Area of the evaluated vineyard plots, along with vine rows occupation area, vines, and potential missing vines percentage.

The processing time spent in each vineyard was 8 minutes and 45 seconds for vineyard C and 5 minutes and 32 seconds for vineyard A. Noticeably in vineyard B, the method took about 47 seconds to complete the analysis due to the lower number of plots and the lesser amount of images' detail – lower number of pixels due to the higher flight altitude that results in a lower GSD. Processing time is not related with the number of plots under analysis but with the areas' characteristics. This can be observed in the time spent during the vineyard C processing (only 3 plots were analysed) in comparison with vineyard A (11 plots analysed): vineyard C took 3 min more to be completed. The average plot processing time was 30 seconds for vineyard A, 23 for vineyard B and almost 3 minutes for vineyard C.

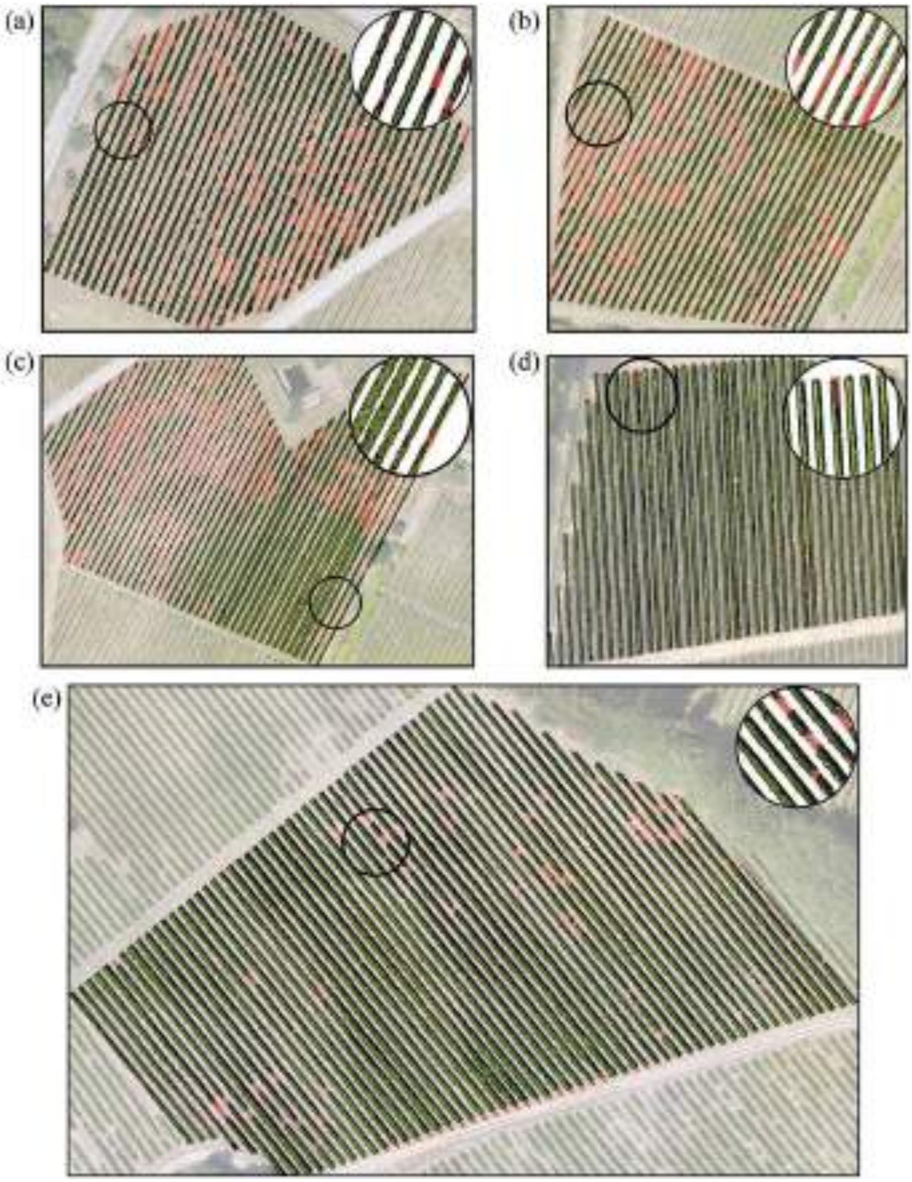


**Figure 6.13.** Results obtained by applying the proposed method to plots 4, 6, and 7 from vineyard A, plot 2 from vineyard B, and plot 3 from vineyard C. Faded RGB images are used as background; detected vegetation is represented in black and highlighted rows areas; and detected missing vegetation areas are represented in light red.

## 6.6. Conclusions and future work

In this paper, a method to extract vineyard vegetation from high-resolution aerial imaginary is presented. It combines the benefits of VIs and CSM along with image processing techniques to automatically extract vine plot related parameters, overcoming the presence of inter-row vegetation and canopies shadowing effects. The method is able to estimate missing vegetation and its correspondent overall percentage. It provides useful information about the current vineyard state, which can be used as a tool to be effectively applied in the management process within PV scope. The usage of relatively low-cost UAV with an RGB sensor proved to have enough accuracy to detect vineyard vegetation, being a cost-effective alternative to more expensive UAS and sensors used in PA surveys. The results obtained by applying the proposed method in RGB orthophoto mosaics and DTMs with very-high resolution (GSD from 2.4 to 3.8 cm) demonstrated its efficiency in the estimation of vine rows (94.45%), vine vegetation (94.10%) and missing vines plants (97.04%). These results are in line with other methods that use imagery data from more expensive sensors types, such as NIR. Misclassifications were noticeable in areas where vine vegetation suffered from neighbouring trees shadows and in vine rows constituted only by dead vine plants. Small variations in vegetation detection were noticeable in vine rows' edges.

As future work, the proposed method will be applied at a multi-temporal level to detect possible biotic and abiotic problems in the vineyard and to study its in-season and inter-season evolution dynamics. Even though the used data was RGB, the method is also suitable to be applied alongside with multi-spectral or thermal UAS-based data. More parameters can be accurately estimated, such as vine vegetation vigour and water status, crucial to assist in the application of crop-variable treatments and irrigation scheduling. The presented method has also potential to be applied in different crops with the same row-oriented plantation structure, as fruit orchards and vegetable crops. The usage of UAVs can be useful to automate vineyard management using unmanned ground vehicles and/or ground sensors, from soil and meteorological data. It is also intended to provide the ability to automatically detect vine plots and to interpret its plantation shape type, so that correct methodologies can be applied in vine vegetation detection and analysis. Data acquisition parameters must be studied (altitude, image overlap, UAV speed, camera angle or resolution) to evaluate its influence in the photogrammetric processing to ensure maximum data quality.

## Acknowledgements

This work was financed by the European Regional Development Fund (ERDF) through the Operational Programme for Competitiveness and Internationalisation - COMPETE 2020 under the PORTUGAL 2020 Partnership Agreement, and through the Portuguese National Innovation Agency (ANI) as a part of project "PARRA - Plataforma integrAda de monitoRização e avaliação da doença da flavescência douRada na vinhA" (Nº 3447) and ERDF and North 2020 - North Regional Operational Program, as part of project "INNOVINEandWINE - Vineyard and Wine Innovation Platform" (NORTE–01–0145–FEDER–000038).

# Chapter 7.

## Multi-Temporal Vineyard Monitoring through UAV-Based RGB Imagery

*Remote Sensing*, 2018, *10*(12), 1907

Journal Impact Factor – 2018: 4.118

5 Year Impact Factor – 2018: 4.740

**Luís Pádua**, Pedro Marques, Jonáš Hruška, Telmo Adão,
Emanuel Peres, Raul Morais and Joaquim J. Sousa

Refer to https://doi.org/10.3390/rs10121907 for online published version

# 7.1. Introduction

As with precision agriculture (PA), precision viticulture (PV) depends on the adoption of emerging technologies to acquire data that allow the assessment of field variability to support the PV decision making process (Ozdemir et al., 2017; Pablo J Zarco-Tejada et al., 2014). Grapevine (*Vitis vinifera* L.) yield has both spatial and temporal variability (R. Bramley & Hamilton, 2004) and several field- and crop-related factors can influence yield, such as the soil, terrain topography, and microclimate conditions. Therefore, it is important to have information allowing specific and proper operations for each identified management zone within vineyards (R. Bramley, 2005; R. G. V. Bramley, 2001; R. Bramley & Hamilton, 2004; Ozdemir et al., 2017).

Canopy management is critical for improving grapevine yield and wine quality (Smart et al., 2017) by influencing canopy size and vigour and reducing phytosanitary problems (Vance et al., 2013). As such, it is important to estimate above-ground biomass (AGB), which helps with the monitoring of plant status and can potentially provide a yield forecast (Bendig et al., 2014). Grapevine biomass can be estimated through crop models (CeSIA et al., 1997) by using leaf area, global solar radiation, and air temperatures (Duchêne & Schneider, 2005), and based on vegetation indices, which correlate several grapevine biophysical parameters (Dobrowski et al., n.d.). More direct methods to estimate biomass require accurate field measurements and involve destructive processes (Kankare et al., 2013; Yu et al., 2013).

Remote sensing is an effective solution, allowing the acquisition of several types of data with various spatial and temporal resolutions. Specifically, unmanned aerial systems (UAS) are considered to be cost-effective, able to acquire the needed data at the needed time and place, and able to provide greater spatial resolution compared with other remote sensing platforms, such as satellites and manned aircrafts (Alessandro Matese et al., 2015; Pádua, Vanko, et al., 2017). Several research studies successfully applied UAS-based remote sensing in distinct vineyard monitoring contexts by coupling different sensors—such as red/green/blue (RGB), multispectral, thermal, hyperspectral sensors, and Light Detection And Ranging (LIDAR)—to unmanned aerial vehicles (UAVs), for the estimation of potential phytosanitary problems (Baofeng et al., 2016), water status assessment (Baluja et al., 2012; Romero et al., 2018; Santesteban et al., 2017), leaf area index (LAI) calculation (Kalisperakis et al., 2015), and grapevine biophysical parameters (Alessandro Matese et al., 2016).

Several studies explored UAV-based plant monitoring using hyperspectral sensors, namely for biomass and nitrogen estimation in wheat (Pölönen et al., 2013; Yue et al., 2017), in grassland with different treatments (Capolupo et al., 2015), for rice paddies characterization (Uto et al., 2013), using UAV-based RGB photogrammetry for tree identification, and to estimate phytosanitary damages mapping (Näsi et al., 2015; Nevalainen et al., 2017). In Kalisperakis et al. (2015), a high correlation was found in a vineyard's canopy greenness map, computed from hyperspectral data, compared with the three-dimensional (3D) canopy model. However, some current hyperspectral sensor data acquisition technology (e.g., push-broom sensors) does not support structure from motion (SfM). As such, geometric parameters' estimation is difficult (Adão et al., 2017). These sensors are also highly dependent on cloud coverage (Pölönen et al., 2013), leading to over- or under-exposure, which affects data reliability. LIDAR sensors have proven their usefulness and precision when applied to forestry inventory (Luke Wallace et al., 2012), individual tree detection (L. Wallace et al., 2014), and forest understory studies (Chisholm et al., 2013). Despite providing high accuracy, they are costly (P. J. Zarco-Tejada et al., 2014).

UAV-based RGB imagery stands out as a cost-effective solution, providing reasonable precision compared to LIDAR (Madec et al., 2017). Sensor fusion was a focus of other studies, such as Sankey et al. (2017), where hyperspectral and LIDAR sensors were both used for forest and vegetation monitoring (T. T. Sankey et al., 2018). Cost-effective sensors (RGB and multispectral) have been used for biomass estimation and parameters extraction in different contexts, such as in pasture lands (Von Bueren & Yule, 2013), near-infrared (NIR), sunflower crops (Vega et al., 2015) (NIR), maize (Castaldi et al., 2017; Li et al., 2016), winter wheat (Schirrmann et al., 2016), barley (Bendig et al., 2014, 2015), and vegetable crops (Kim et al., 2018; Moeckel et al., 2018). These sensors were proven to be suitable for tree detection and height estimation (Karpina et al., 2016; P. J. Zarco-Tejada et al., 2014), and diameter at breast height estimation (Carr & Slyder, 2018).

Regarding vineyard AGB estimation, Mathews and Jensen (2013) used UAV-based imagery with SfM algorithms to compute a vineyard's point cloud to generate the canopy structure model. The authors stated that SfM-based point clouds can be used to estimate volumetric variables, such as AGB. Thus, providing this type of data throughout the different grapevine phenological stages would benefit winegrowers in assessing a grapevine's canopy spatial variation (Mathews, 2014; Mathews & Jensen, 2013). Weiss and Baret (2017) used dense point clouds, generated through photogrammetric processing of UAV-based RGB imagery, to characterize a vineyard's properties, such as grapevine row height, width, spacing, and cover fraction. Matese et al. (2016) used a multispectral sensor mounted on a UAV to assess the photogrammetric processing of multispectral imagery. The authors concluded that greater normalized difference vegetation index (NDVI) (Rouse et al., 1974) value matched areas where grapevines were located were higher, proving the effectiveness of UAV-based data for vineyard mapping. Grapevine volume was estimated by considering three classes of grapevine height, width, and length. However, the low-resolution of the multispectral sensor caused a smoothing effect in the evaluated vineyard plot's digital surface model (DSM). Caruso et al. (2017) used an UAV equipped with RGB and NIR sensors to obtain biophysical and geometrical parameters relationships among grapevines, using high, medium, and low vigour zones of a vineyard, determined from the NDVI. The volume was calculated for grapevines' lower, middle, and upper parts. UAV-based data were acquired in four different periods: May, June, July, and August. De Castro et al. (2018) proposed an approach where a DSM computed from photogrammetric processing of UAV-based RGB imagery was used in object-based image analysis (OBIA) software to compute individual vineyard parameters. Unlike in Matese et al. (2016), the smoothing effect was less significant. The authors stated that multi-temporal monitoring of grapevine biophysical parameters using UAV-based data can be both efficient and accurate, constituting a viable alternative to time-consuming, laborious, and inconsistent manual in-field measurements.

This article supports the findings of De Castro et al. (2018) about the relevance of using multi-temporal data acquired from remote-sensing platforms in PV, to monitor the size, shape, and vigour of grapevines canopies. This study aimed to characterize vineyard vegetation evolution through multi-temporal analysis using a commercial low-cost rotary-wing UAV equipped with an RGB sensor, enabling the acquisition of very high-resolution imagery up to few millimetres of ground sample distance (GSD). The multi-temporal data acquired over the area of interest (AOI) were automatically analysed and grapevine vegetation was non-evasively estimated using vegetation area and volume, as well as identifying vineyard areas that need canopy management operations, by extracting several of the vineyard's parameters.

This article is structured as follows: the next section describes the study area and the methods used for data acquisition and processing. Section 7.3 presents the results of multi-temporal analysis and Section 7.4 provides a discussion. Finally, Section 7.5 presents our most significant conclusions.

## 7.2. Materials and Methods

The study area characterization; the description of the used UAS; and the methods applied to acquire, process, and interpret the UAV-based imagery are presented in this section. The methodology followed in this study was proposed by Pádua et al. (2017) and was intended for multi-temporal crop analysis of UAV-based data. The method is based on three main stages: vegetation segmentation, parameters extraction, and multi-temporal analysis.

### 7.2.1. Study Area Context and Description

Typical *Vitis vinifera* L. phenological stages are well defined, occurring within known time periods depending on geographical context. In Portugal, budburst occurs from March to April, followed by flowering and an intensive vegetative growth in the period between May and June. Then, veraison occurs. During this stage, usually between July and August, grapevine ripening starts. Fruit maturity and harvesting typically happens between September and October. In the remaining months, grapevines are in a dormancy stage (Magalhães, 2008). However, these stages might vary slightly in time, depending on environmental conditions and grapevine variety (Costa et al., 2015). The warm and dry Portuguese summers can limit crop growth due to limited water availability during summertime (Helder Fraga, Malheiro, et al., 2014). To improve both fruit quality and yield, vineyard canopy management methods are performed, which involve different operations throughout the year. They include pruning, shoot thinning, leaf removal, cover crop cultivation, irrigation scheduling, and application of soil and crop amendments (L. Johnson et al., 2003). Regarding UAV-based aerial survey in vineyards, data should be acquired after the budburst stage, when grapevine leaves begin to be noticeable. These data can be used to monitor vineyard vegetation growth.

Two experimental vineyard plots were selected as the AOI for this work. Figure 7.1 presents an overview of both plots, located at the University of Trás-os-Montes e Alto Douro campus in Vila Real, Portugal (41°17′09.7″ N, 7°44′12.9″ W). Plot 1 (P1) had an area of 0.33 ha and was composed of red grapevine varieties. Plot 2 (P2) had an area of about 0.55 ha and contained white grapevine varieties. The grapevine varieties planted in both plots are recommended in the Douro Demarcated Region (DDR), where this study occurred. Grapevines were planted in 1995 in parallel rows, separated by 2 m, and with 1.2 m space between plants within a row. They were trained in a vertical shoot positioning (VSP) system, with a double Guyot training system—one of the most commonly used training systems in DDR (H. Fraga & Santos, 2017).

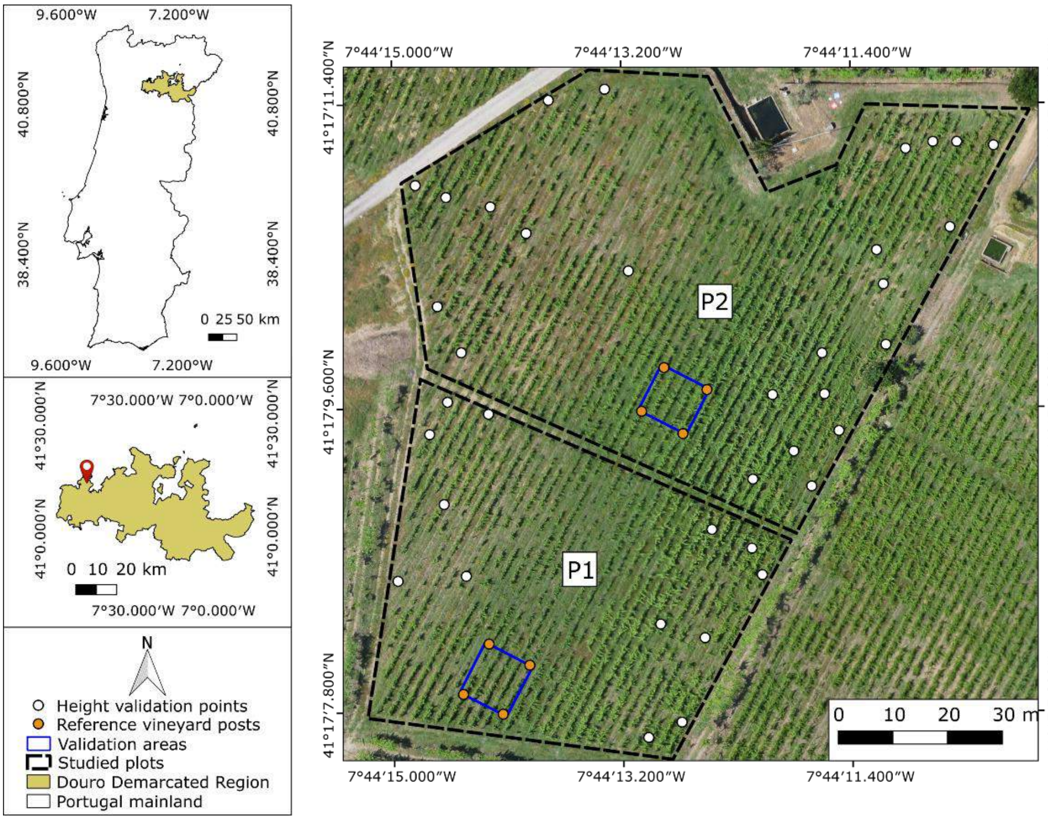


**Figure 7.1.** Area of interest (AOI) general overview: analysed vineyard plots, validation areas, height validation points, and their location in the Douro Demarcated Region, coordinates in WGS84 (EPSG:4326).

For a better understanding of the results obtained in this study, weather contextualization is necessary. Therefore, parameters such as monthly precipitation, potential evapotranspiration (PET) and mean, minimum, and maximum air temperatures were acquired from an automatic weather station (iMETOS 1, Pessl Instruments GmbH, Weiz, Austria), located 300 m from the AOI. Figure 7.2 represents daily mean air temperature parameters for each month and the monthly accumulated precipitation and PET for the period of September 2016 to September 2017.

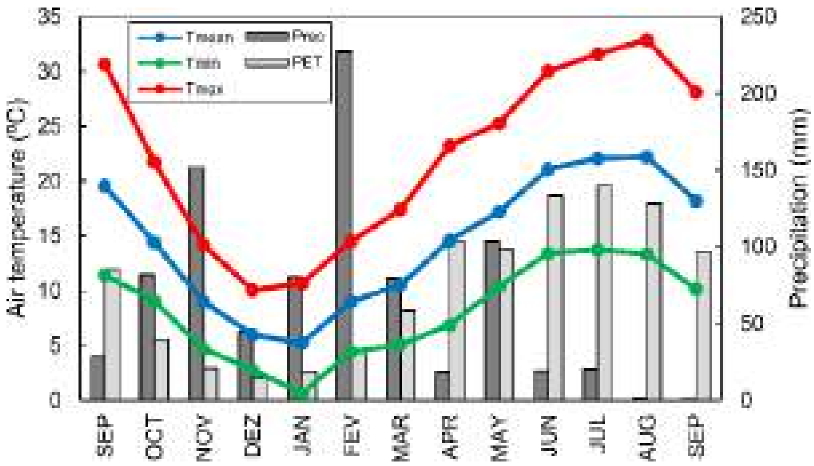


**Figure 7.2.** Monthly mean weather variables for the study areas in the period between September 2016 and September 2017: mean (Tmean), minimum (Tmin) and maximum (Tmax) air temperatures, and precipitation (Prec) and potential evapotranspiration (PET) values.

The high air temperature during summer 2017, together with low precipitation in spring 2017 and winter 2016 caused a drought period in Portugal and earlier grape maturation in the DDR region. As such, harvesting was anticipated in late August to mid-September: about two or three weeks earlier than usual. In the AOI, harvesting occurred in mid-September. This can be explained by comparing the weather data against the climatological normal of Vila Real (retrieved from the Instituto Português do Mar e da Atmosfera, IPMA, Lisbon, Portugal) for the period of 1981 to 2010. Comparing the one-year period with the climatological normal, we noticed a difference of +3.2 °C in the maximum air temperature (+4.1 °C for the period of the flight surveys), +0.6 °C in the mean air temperature (+1.1 °C for the period of the flight surveys), –0.7 °C in the minimum air temperature (−0.6 °C for the period of the flight surveys), and approximately 220 mm less accumulated precipitation.

## 7.2.2. Flight Campaigns

A commercial UAV, the DJI Phantom 4 (DJI, Shenzhen, China), was used in this study for data acquisition. It is a flexible and cost-effective off-the-shelf solution, able to perform manual or fully automatic flights in different configurations through a set of user-defined waypoints. The UAS consists of this multi-rotor UAV equipped with a rolling-shutter 1/2.3″ CMOS sensor attached to a 3-axis electronic gimbal, which acquires 12.4 MP resolution RGB imagery.

Nine aerial campaigns were completed in the selected plots, covering the time span from 2 May to 15 September, 2017. Details about these flight campaigns are presented in Figure 7.3. The flight strategy enabled the inclusion of most of the plants' phenological development until harvesting season. The performed canopy management operations in the studied vineyard plots were performed by the farmers and the aerial surveys were conducted within one week of its ending. All flights were conducted between 1:00 p.m. and 2:00 p.m. to minimize the sun angle influences and shadows. A double-grid configuration was used when planning each flight campaign to ensure a high overlap of 75% between images. Flight height relative to the UAV take-off position was set to 60 m.

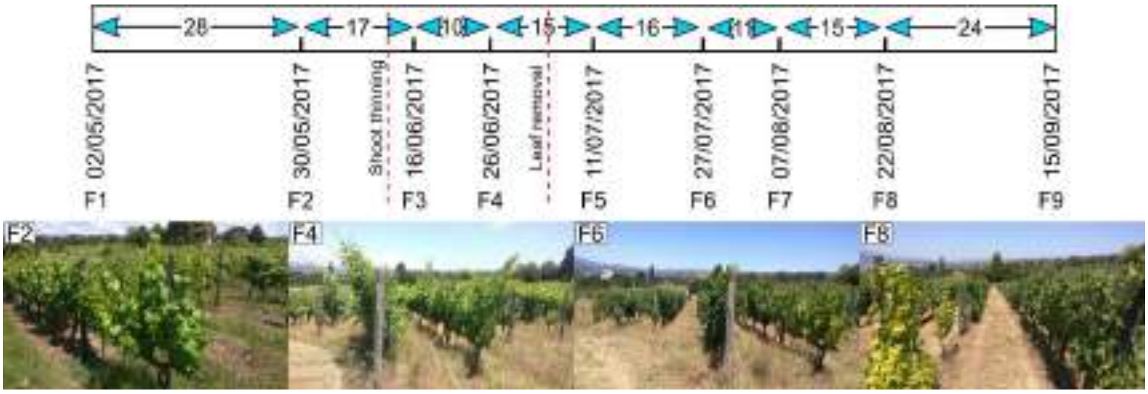


**Figure 7.3.** Flight campaign details. Flight number (F#), date, and the temporal difference in days between flights and the performed vineyard canopy management operations in dashed lines. Plot 2 images in different flight campaigns are also provided.

## 7.2.3. Data processing

The imagery acquired in each flight was subjected to a photogrammetric processing using SfM algorithms to compute different orthorectified outcomes, which were used to segment vineyards and extract their features. This enabled a multi-temporal analysis of the AOI, along with the estimation of areas that potentially need canopy management operations.

### 7.2.3.1. Photogrammetric Processing

Photogrammetric processing was applied to the high-resolution aerial imagery using Pix4Dmapper Pro software (Pix4D SA, Lausanne, Switzerland). This software allows the generation of different orthorectified outputs, such as orthophoto mosaics, DSMs, and DTMs.

The processing involved three main stages: (1) generation of a sparse point cloud by using SfM algorithms to establish relationships between the geo-tagged RGB imagery through matching corresponding points (tie points) in multiple images, thus estimating its three-dimensional (3D) position. In this study, the computed outputs were aligned by setting manual tie points in areas that were clearly identifiable in the imagery of all flight campaigns: five points were used. This ensured that all generated outputs shared the same relative latitude, longitude, and altitude coordinates, differing only on the surface’s changes as vegetation develops. (2) The next step was the generation of a dense point cloud by considering the computed tie points and enlarging the number of candidate points (in this case point density was set to high); and (3) then computation of orthorectified outcomes, namely orthophoto mosaics, DSM, and DTM, which was achieved by submitting the dense point cloud to a noise filtering process, and by interpolating it using a triangulation algorithm. Since the mission plan was the same in all flights, the photogrammetric processing allowed the generation of orthophoto mosaics, DSMs, and DTMs with a GSD of 3 cm.

#### 7.2.3.2. Vineyard Properties Extraction

Besides grapevine vegetation, inter-row vegetation and shadows cast by grapevines canopies are two examples of elements usually present in vineyard aerial imagery (Burgos et al., 2015). To automatically separate grapevine vegetation in aerial high-resolution imagery acquired by UAVs, different approaches have been proposed in the literature: digital image processing-based techniques (Comba et al., 2015; A. Nolan et al., 2015), supervised and unsupervised machine learning classification techniques (Poblete-Echeverría et al., 2017), point clouds (obtained from SfM methods) filtering (Weiss & Baret, 2017); and the use of DEMs (Burgos et al., 2015; Kalisperakis et al., 2015).

Pádua et al. (2018) proposed a method for segmenting vineyards. The method uses UAV-based RGB imagery—commonly available in most UAS— assumes that vineyards are organized in rows, and that grapevine heights are greater than inter-row vegetation. Grapevine canopy is often constrained to a certain area using a wire-based training system along the rows. This confines grapevines to both a given width and height. By complementarily using the different outcomes from photogrammetric processing of very high-resolution UAV-based imagery and resorting to vegetation indices, the method is able to filter vegetation within a certain height range in a given vineyard plot. Therefore, the method can extract parameters, such as grapevine vegetation, and estimate the number of vine rows, the inter-row vegetation, and potentially missing grapevines. Vegetation indices proved to be an accurate and quick mean to extract vineyard vegetation, compared to more complex supervised and unsupervised machine learning methods which, respectively, require datasets for both training and validation purposes or that provide lower accuracy rates (Poblete-Echeverría et al., 2017). Table 7.1 explains the notation used in this section.

**Table 7.1.** Notation table.

| Notation | Meaning |
|---|---|
| $\mathbf{S}$ | Binary image containing the central lines of the grapevine rows |
| $h_{\max}$ | Maximum height range used for crop surface model (CSM) thresholding |
| $h_{\min}$ | Minimum height range used for CSM thresholding |
| $\mathbf{D}$ | Binary image resultant from CSM and G% thresholding |
| $\mathbf{F}$ | Binary image resultant from the intersection of clusters of pixels in **D** with **S** |
| $\mathcal{C}$ | Set of all detected clusters in **F** |
| $\bar{\mathbf{F}}$ | Complement of **F** |
| $\mathbf{L}$ | Binary image created from the intersection of $\bar{\mathbf{F}}$ with the thresholded G% binary image |
| $A$ | Area of a given property to calculate (**F** or **L**), which is the sum of all pixel values (0 or 1) of a binary image with $m \times n$ size, multiplied by the squared GSD value |
| $H_{\mathcal{C}_i}$ | Mean height of a given cluster $\mathcal{C}_i$, obtained from the CSM |
| $V$ | Grapevines' vegetation volume, given by the area of clusters $\mathcal{C}_i$, multiplied by its mean height |
| $k$ | Flight campaign number |
| $\mathbf{X}$ | Single-band image resultant from pixel-wise comparison of two consecutive flight campaigns ($k$ and $k$ + 1) |
| $w$ | Maximum width that grapevines can assume |

This work proposes a modified and enhanced version of the method introduced by Pádua et al. (2018). The original method was applied to the AOI's two plots, resulting in a mask (S) with the central lines of grapevine rows. Figure 7.4 illustrates the method's main steps and the different outputs obtained from its application.

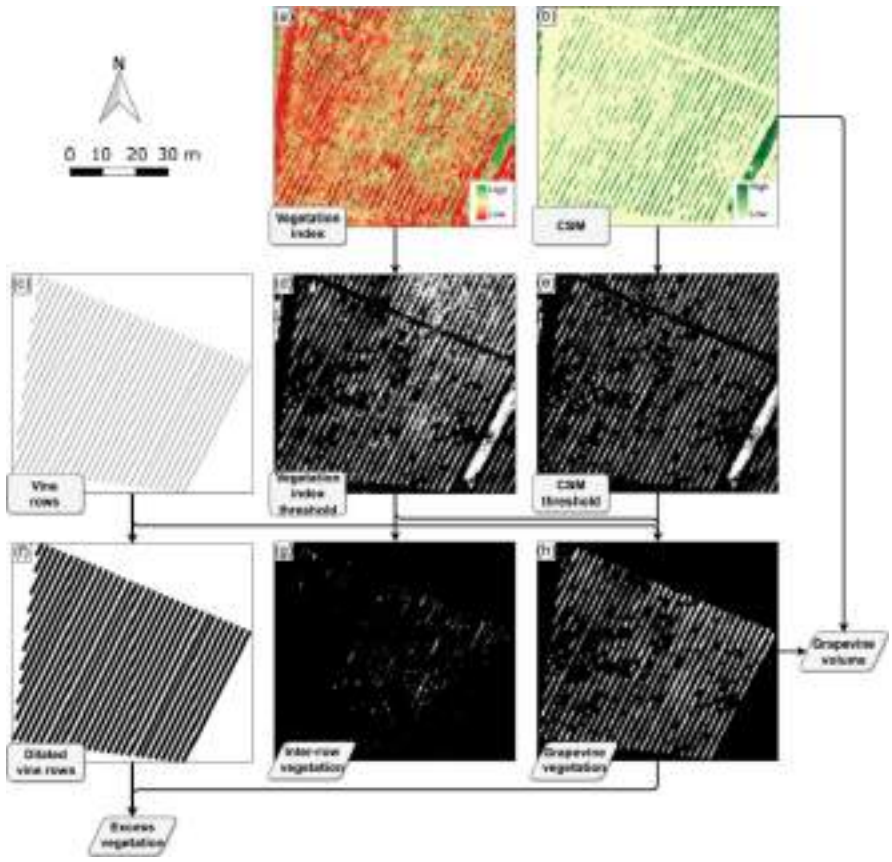


**Figure 7.4.** General workflow of the proposed method and main outputs, illustrated with data acquired on 11 July 2017 (F5) from plot 1 (P1).

The orthophoto mosaics obtained from photogrammetric processing of each flight campaign data were used to compute the green percentage index (G%) (Richardson et al., 2007) (Figure 7.4a), as presented in Equation (1), where the green band was normalized by the sum of all RGB bands, allowing the extraction of the green vegetation cover.

$$\mathrm{G\%} = \mathrm{Green}/(\mathrm{Red} + \mathrm{Green} + \mathrm{Blue}) \tag{1}$$

Next, an automatic threshold value based in Otsu's method (Otsu, 1979) was applied to G% (Figure 7.4d), generating a binary image. From the difference between the DTM and DSM, the crop surface model (CSM) was generated, as shown in Equation (2) (Figure 7.4b). CSM values represent the height of objects above the terrain that, upon further processing, allows obtaining grapevine vegetation height.

$$\mathrm{CSM} = \mathrm{DSM} - \mathrm{DTM} \tag{2}$$

The CSM was filtered by height (h), ranging from $h_{\mathrm{min}}$ to $h_{\mathrm{max}}$. The outcome was a new binary image (Figure 7.4e), in which each pixel $(i, j)$ assumes the value "1" or "0", based upon whether the matching pixel in the CSM has a height value within the defined range. A new binary image D, containing all the vegetation within the defined height range, was obtained by combining the binary images resulting from the threshold of G% and the CSM. Then, a set of morphological operations (e.g., open, close, or remove small objects) was applied to D to delete potential outliers that did not represent grapevines. This also contributed to reducing the proposed method's computational burden.

Each cluster of D was individually analysed and discarded if it did not intercept S (Figure 7.4c) at least once. The result was a set of clusters $C$, which constitute a new binary image F that contains only vegetation within a certain height range (Figure 7.4h). Hence, inter-row vegetation was estimated by the interception between F's complement $\bar{\mathbf{F}}$ and the binary image resultant from G% thresholding (Figure 7.4g). The resulting binary image, L, was composed of vegetation that did not belong to grapevines.

Thus, a vineyard's plot parameters can be estimated. Equation (3) presents the method of calculating grapevine vegetation area A: the sum of each pixel $(i, j)$ from F multiplied by the squared GSD value, where m and n represent the image's number of rows and columns, respectively. The same approach can be used to determine inter-row vegetation area using L instead of F.

$$A = \left( \sum_{i=1}^{m} \sum_{j=1}^{n} f_{i,j} \right) \mathrm{GSD}^2 \tag{3}$$

In terms of grapevine volume V, expressed in m$^3$, the estimation is performed by adding the individual volumes of F's clusters of pixels ($\mathcal{C}$), which in turn are obtained by multiplying each cluster's area by its mean height, as presented in Equation (4), where a cluster $\mathcal{C}_i$ area is represented by $A_{\mathcal{C}_i}$, and $H_{\mathcal{C}_i}$ represents the mean height of a given cluster $\mathcal{C}_i$ and its value is obtained from the CSM.

$$V = \sum_{i=1}^{n} A_{\mathcal{C}_i} \times H_{\mathcal{C}_i} \tag{4}$$

#### 7.2.3.3. Multi-Temporal Analysis Procedure

Although significant, parameters computed from individual flight campaigns are only capable of offering a snapshot about a crop's developmental stage and its contextual environmental conditions. A multi-temporal approach allows analysis changes over time and to create data series that may prove valuable for extracting patterns about crops and environmental conditions, which can further improve PV management tools.

As this study aimed to characterize vineyard vegetation evolution throughout the most significant grapevine vegetative growing cycles and given the importance of managing biomass for both fruit and yield optimization, a multi-temporal analysis was conducted. The process used grapevine vegetation detected in consecutive flight campaigns (k and k + 1) to perform a pixel-wise estimation of grapevine vegetation development. This produced one of the following three possible outcomes per pixel: (1) considered as grapevine vegetation in both flights and remains as such; (2) not considered as grapevine vegetation in k but considered in k + 1, representing grapevine vegetation growth; or (3) considered as grapevine vegetation in k but not in k + 1, representing a grapevine vegetation decline.

A new image X with grapevine vegetative growth values was created by applying Equation (5) to both F images from k and k + 1 flight campaigns. Values 1, 0, and −1 represent grapevine vegetation growth, maintenance, and decline, respectively. No value (NaN) was attributed to areas with no grapevine vegetation detected in consecutive flight campaigns.

$$x_{i,j} = \begin{cases} 1, f(k)_{i,j} = 0 \wedge f(k+1)_{i,j} = 1 \\ 0, f(k)_{i,j} = 1 \wedge f(k+1)_{i,j} = 1 \\ -1, f(k)_{i,j} = 1 \wedge f(k+1)_{i,j} = 0 \\ \mathrm{NaN}, \text{otherwise} \end{cases} \quad k = 1, \dots, n \tag{5}$$

#### 7.2.3.4. Canopy Management

Given the diversity and sheer number of field operations performed throughout a year to maintain and extend grapevine life and increase their productivity, the ability to identify vineyard areas in need of canopy management actions can significantly contribute to PV sustainable practices. This process can help evaluate, hierarchize, and schedule field operations based on the operation's potential benefit evaluation in the identified vineyard area, while considering cost and environmental impact.

Grapevine vegetation outside a defined area is considered as excess. To identify excess, S is dilated according to a given width (w) (Figure 7.4f), which represents the maximum width of grapevine vegetation in a row, according to its spacing. Afterward, the resulting binary image is combined with F. Grapevine vegetation pixels belonging to F outside the dilated S mask are estimated as excess vegetation.

#### 7.2.3.5. Validation Procedure

To monitor the selected vineyards temporally, a total of nine aerial campaigns were carried out, covering the grapevines' most significant life cycle. The first flight, performed on 2 May, 2017, corresponding to the beginning of the grapevine vegetative cycle; and the last flight was carried out on 15 September, 2017, corresponding to the grapes' final maturation stage (i.e., harvesting season). Field data acquisition consisted of collecting vine row height and width measurements at marked positions to estimate the vine row area and volume to compare the estimated parameters by the proposed method and the one calculated with ground-truth data. Vine row height was obtained by taking measurements using a surveyor's levelling rod (Figure 7.5a), and width by using a measuring tape and two surveyor's levelling rods, used as presented in Figure 7.5b. These validation points were selected from two 10 × 10 m areas (blue polygons in Figure 7.1). They are limited by characteristic features present in all vineyards and easily recognised both in aerial images and in the field: posts equally spaced along the rows (every 5 m in our AOI). This way it was possible to identify the same area over the flight epochs and to compare ground measurements with those provided by the proposed method. In total, 50 measurement points were selected, 25 located in each validation area, to allow correct representation of the vine row. If the vine row presents a regular shape, five points were selected per row, with 2 m average separation. These areas were selected due to the presence of different vigour levels and missing grapevine plants. Moreover, 37 other points (see Figure 7.1 for location) outside the 10 × 10 m areas were used as verification points (24 in P1 and 13 in P2). These points were selected to ensure sample representativeness in different contexts (dense and sparse grapevine vegetation, different height values, etc.). In this case, only vine row heights were measured and compared with heights estimated by the CSM.

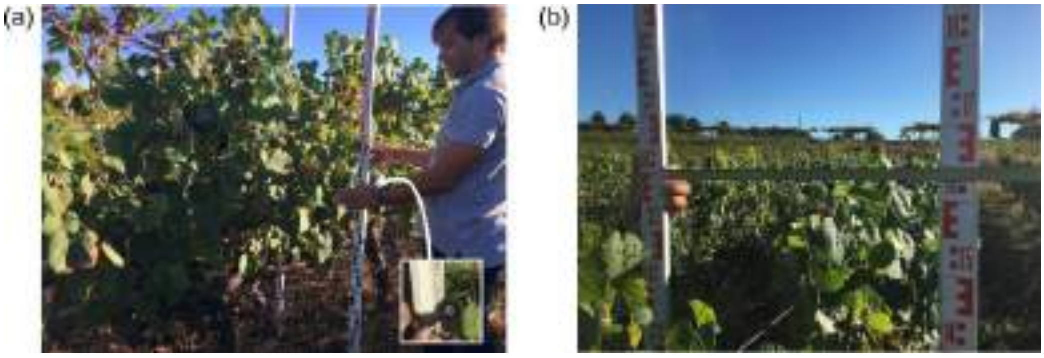

**Figure 7.5.** In-field measurements at specific points: (a) row height measurements; and (b) row width measurements.

Grapevine height and area of the two 10 × 10 m validation areas was estimated using three different approaches: (1) ground-truth data; (2) a mask produced by manual segmentation of the computed orthophoto mosaics for the computation of grapevine vegetation area, which was then multiplied by the vine row's average height, computed using the results of the CSM; and (3) applying the proposed method to UAV-acquired data and extracting both row area and height in a fully automatic process.

The accuracy of the method was assessed using vine rows heights and widths measured in-field as reference. Then, those values were compared with those obtained using the proposed method. The overall agreement between the observed in-field measurements **o** and the estimated values **e** were verified through the root mean square error (RMSE), as shown in Equation (6).

$$\mathrm{RMSE} = \sqrt{\frac{\sum_{i=1}^{n}(e_i - o_i)^2}{n}} \quad (6)$$

## 7.3. Results

As stated in Section 7.2.3., this modified and enhanced version of Pádua et al. (2018) method enabled the estimation of grapevine area and volume, as well as vineyard areas that can potentially benefit from canopy management operations. By using multi-temporal data analysis, this method enables monitoring grapevine vegetation evolution.

### 7.3.1. Study Area Characterization

Both vineyard plots analysed—one composed of red wine varieties (P1) and another by white wine varieties (P2)—were characterized by orthophoto mosaics, DSMs and DTMs with 3 cm GSD, resulting from photogrammetric processing of UAV-based RGB imagery, acquired during each flight campaign. Table 7.2 presents the mean error and RMSE values for each direction (X: easting, Y: northing, Z: height), obtained during photogrammetric processing, using five ground control points extracted from F1 coordinates, as reference. Higher deviations were found in Z, while the error rate is lower in both X and Y.

**Table 7.2.** Mean error and root mean square error (RMSE) in each direction (X, Y, Z) on the five tie points for each flight and its global values, considering the deviations from all tie points. F1 coordinates were used as reference.

| **Flight Campaign (F#)** | **Mean Error (cm)** | | | **RMSE (cm)** | | |
|---|---|---|---|---|---|---|
| | **X** | **Y** | **Z** | **X** | **Y** | **Z** |
| F2 | 0.39 | 0.67 | −2.62 | 2.10 | 2.72 | 9.51 |
| F3 | −0.31 | −0.64 | 1.28 | 4.21 | 3.16 | 3.90 |
| F4 | −0.67 | 0.26 | −2.57 | 3.38 | 2.79 | 10.48 |
| F5 | 0.03 | 0.07 | −0.01 | 2.29 | 0.74 | 3.87 |
| F6 | −0.35 | −0.13 | −2.00 | 1.65 | 0.61 | 4.81 |
| F7 | −0.20 | −0.17 | −0.04 | 1.66 | 0.90 | 2.84 |
| F8 | −0.08 | −0.56 | −0.44 | 1.75 | 1.29 | 2.37 |
| F9 | −0.08 | −0.02 | −0.16 | 2.09 | 1.24 | 0.33 |
| Global | −0.16 | −0.06 | −0.82 | 2.54 | 1.93 | 5.78 |

Figure 7.6 presents the generated orthophoto mosaics along with the percentages of both grapevine vegetation and inter-row vegetation. Grapevine vegetation was denser in the right side of both studied vineyard plots, particularly in P2's lower-right side and P1's upper right side. Conversely, there was a greater incidence of missing grapevines in the studied vineyard plots' left sides. Canopy management operations that occurred were also perceivable between flight campaigns when considering multi-temporal analysis, as observed in the flights of 16 June (F3) and 11 July (F5).

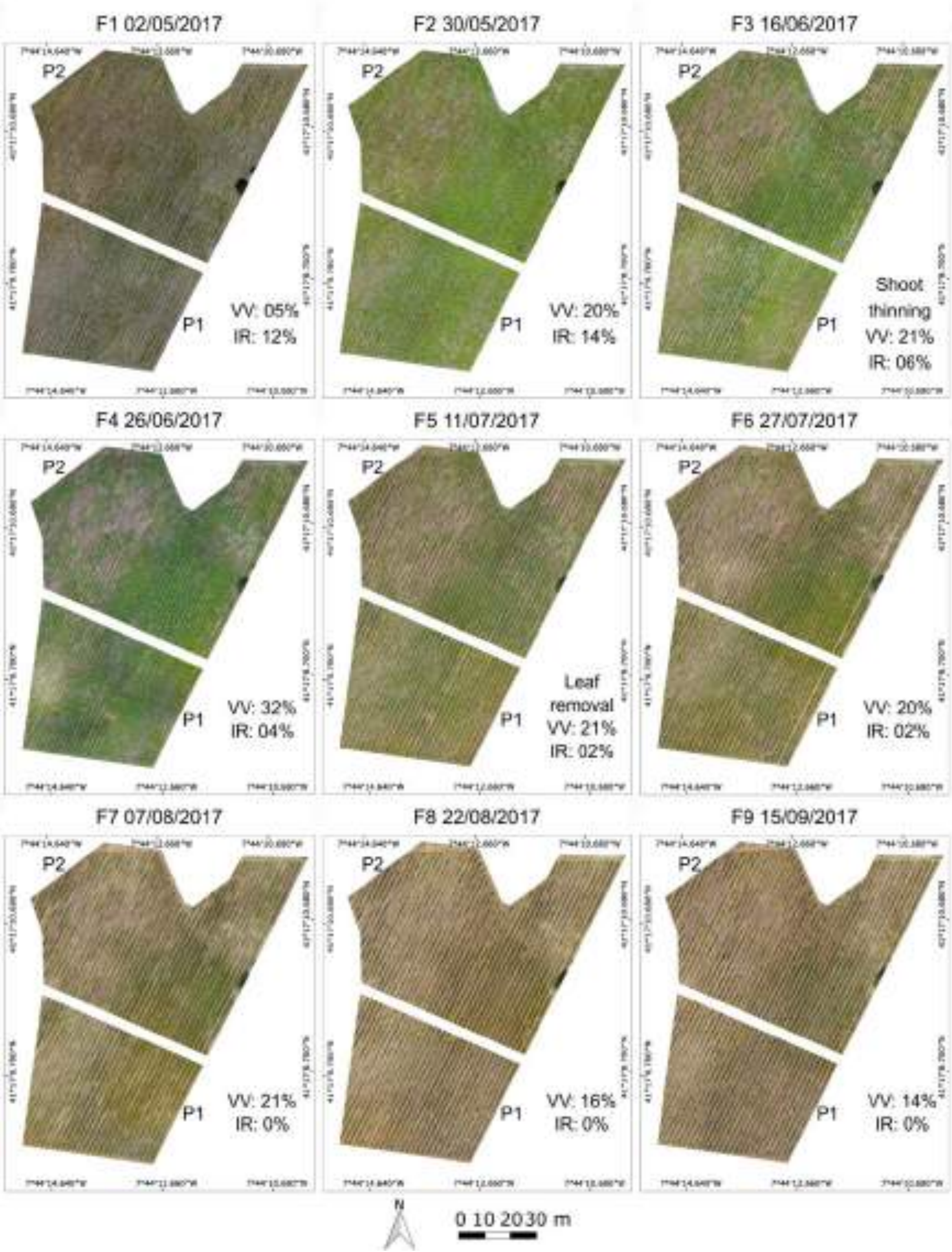


**Figure 7.6.** Generated orthophoto mosaics for each flight campaign carried out in both vineyard plots (P1 and P2), along with grapevine vegetation (VV) and inter-row vegetation (IR) percentages. The result of canopy management operations, such as shoot thinning and leaf removal, is noticeable by comparing the orthophoto mosaics. Coordinates in WGS84 (EPSG:4326).

Regarding the other orthorectified outcomes, the DSM and DTM enabled obtaining the CSM, and G% was computed from the orthophoto mosaics. Figure 7.7 presents a color-coded representation from these results from data acquired on the 27 July, 2017 flight campaign. Regarding CSM height range in this study, $h_{\mathrm{min}}$ and $h_{\mathrm{max}}$ were set to 0.2 and 2 m, respectively. Those values were selected according to the known characteristics of the study vineyards.

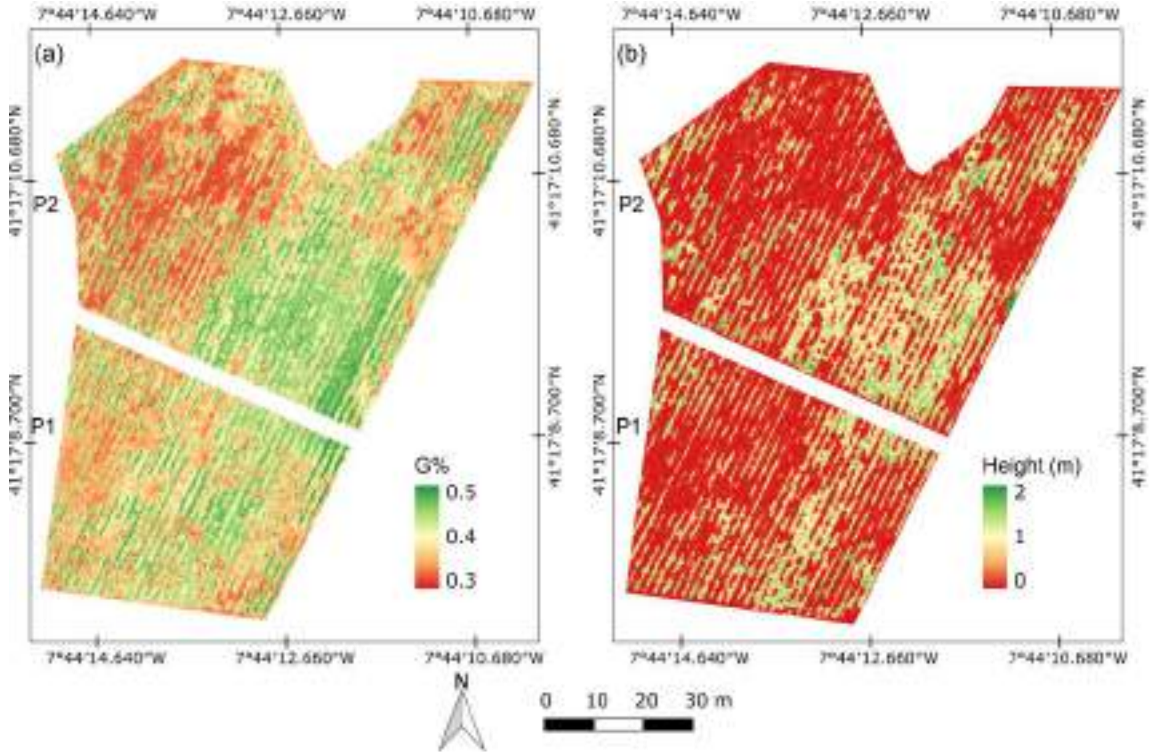


**Figure 7.7.** Examples of inputs used in this study, computed from the photogrammetric processing of imagery acquired on the 27 July, 2017 flight campaign: (a) green percentage index; and (b) crop surface model. Coordinates in WGS84 (EPSG:4326).

## 7.3.2. Vineyard Vegetation Change Monitoring

By applying the proposed method to the orthorectified products from the photogrammetric processing of data acquired in each flight campaign, it was possible to (1) identify vine rows, (2) determine individual vine row's central line, (3) estimate grapevines' vegetation, and (4) distinguish grapevines from other types of vegetation (e.g., inter-row vegetation). Two relevant canopy management operations took place during this study (marked both in figures and tables): one in the first half of June 2017 (shoot thinning between the second and the third flight campaigns) and another one in the first week of July 2017 (leaf removal between the fourth and fifth flight campaigns).

Figure 7.8 shows an estimation of grapevine vegetation area and volume per flight campaign, as well inter-row vegetation area. As expected, P1 and P2 begin by having the smallest estimated grapevine vegetation area (F1, 2 May, 2017) with 172 $m^2$ and 257 $m^2$, respectively, representing 5% of the total plot occupation area. An intensive vegetative growth was expected between May and June, together with some relevant canopy management operations. These results coincide with the expected vegetative evolution of grapevines in DDR. Moreover, they allow not only identification but also estimation of the impact on grapevine vegetative area of two relevant canopy management operations.

In terms of grapevine vegetation volume, the behaviour was similar to grapevines' vegetation area: it increased from the first to the fourth flight campaigns and decreases thereafter, as presented in Figure 7.8. Whereas the first canopy management operation—shoot thinning—that occurred a few days before the third flight campaign did not decrease the volume's growth, the second canopy management operation—leaf removal—verifiable in the fifth flight campaign, clearly did.

In general, no significant differences amongst red and white grapevine varieties in regards to either area or volume were detected. Both parameters presented a similar behaviour per flight campaign.

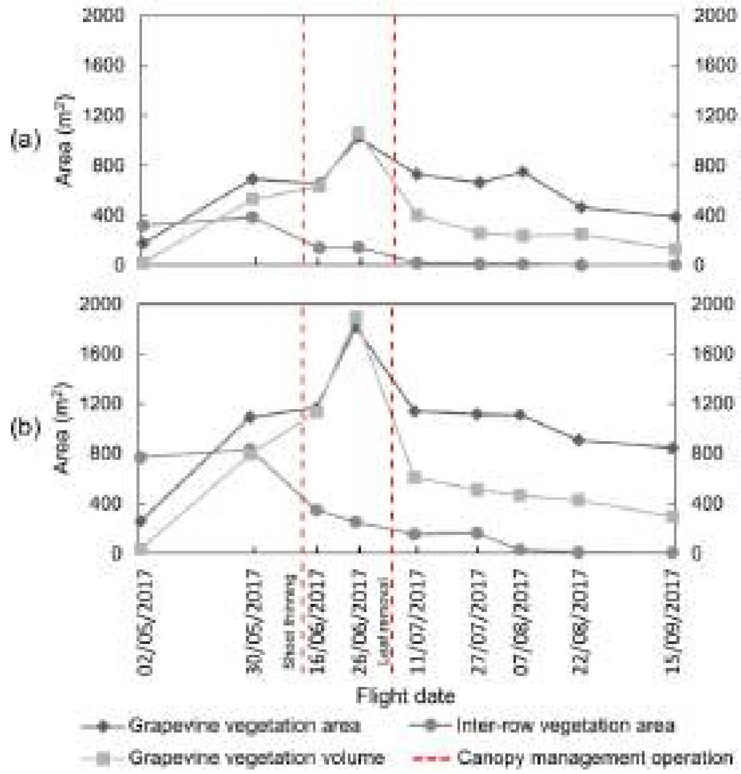


**Figure 7.8.** Estimated outcomes from applying the proposed method to data acquired in all aerial campaigns, from (a) P1 and (b) P2: grapevines' vegetation area, inter-row vegetation area, and grapevine vegetation volume.

In this study, we also estimated the area of non-grapevine vegetation (e.g., inter-row vegetation) in the same plots, P1 and P2 (Figure 7.8). After the winter and spring months, the first flight campaign data—about 300 $m^2$ in P1 (6% of occupation area) and approximately 800 $m^2$ in P2 (14% of occupation area)—and the second flight campaign data revealed a slight increase in both plots. Data acquired in the following flight campaigns showed a decrease in inter-row vegetation area.

### 7.3.3. Multi-Temporal Analysis

By applying the proposed method to consecutive flight campaigns' data, a multi-temporal analysis of the study area was performed, as described in Section 7.2.3.4. This enabled the observation of canopy management operations that occurred during grapevines growing season. Figure 7.9 presents a visual representation of the multi-temporal analysis of grapevine vegetation area variation between flight campaigns.

The main vegetative development occurred between the first and the second flight campaigns, with an estimated grapevine area increase of about 300% for P1 (~540 $m^2$) and 320% for P2 (~870 $m^2$) and the lowest decline (nearly 26 $m^2$ for P1 and 38 $m^2$ for P2, corresponding to 4% and 3% of grapevine vegetation area in the fight campaigns) registered during this study. This result further supports those presented for grapevine' vegetation area and volume (Section 7.3.2).

### 7.3.4. Estimation of Vineyard Areas for Potential Canopy Management Operations

By obtaining continuous information about grapevine vegetation evolution, it is possible to estimate which areas (if any) within a given vineyard plot that could potentially benefit from canopy management operations at any given time. This can be useful as a decision-support system for canopy management operations scheduling, enabling the optimizing of physical means, managing biomass, and further improving vineyards' overall performance.

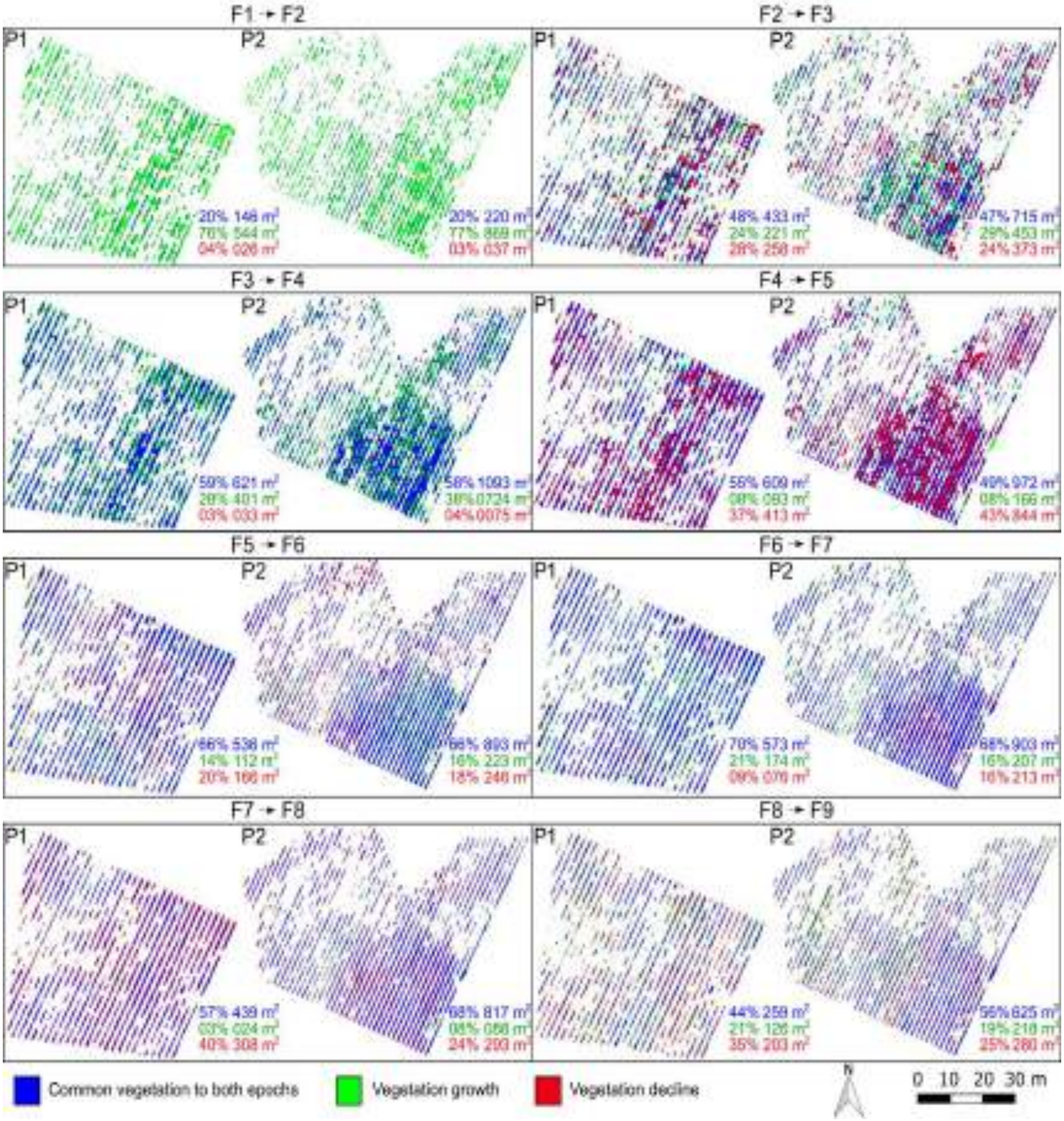


**Figure 7.9.** Multi-temporal analysis of grapevine vegetation: blue stands for vegetation present in both consecutive flight campaigns; green means vegetation growth; and red represents vegetation decline. Percentage and area ($m^2$) values are also presented for each class.

Both P1 and P2 were analysed to estimate areas that potentially needed canopy management operations. Grapevine vegetation is considered excessive when outside a defined area. To identify it, the binary image S was dilated according to a given width w, representing the maximum width of grapevine vegetation in a row. Several tests were performed in this analysis to determine the best value for w. Accordingly, for the canopy management operations performed in the field, a value of 0.6 m was considered optimal for the estimation of potential excess vegetation. This procedure was applied for all flight campaigns' data. Figure 7.10 presents the outcomes obtained for data from the second, third, fourth, and fifth flight campaigns. Those flights were the ones that revealed excess vegetation, except for F5, which was included in Figure 7.10 to show an example where no excess vegetation was detected. F5 occurred after the second management operation. After that, vegetation was contained in the range of w = 0.6 m until harvesting season.

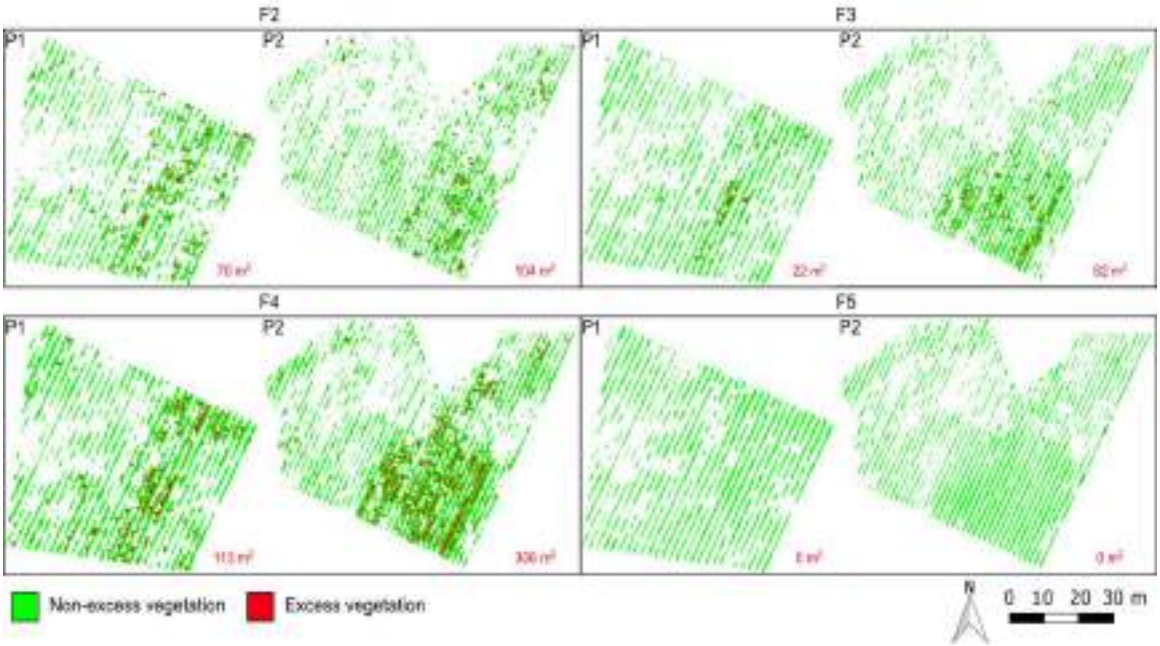


**Figure 7.10.** Estimated grapevines' vegetation both in P1 and P2. Green identifies grapevines' vegetation, red signals areas of excess grapevines' vegetation and therefore that potentially could benefit from canopy management operations along with its area in $m^2$.

### 7.3.5. Accuracy Assessment

The results presented in the last subsections were obtained by automatically applying the proposed method. However, to assess the method's accuracy and effectiveness, a validation procedure was used, as described in Section 7.2.3.5. Figure 7.11 presents the boxplots of the differences in height per flight campaign between the measurements taken in the field and the heights generated by the proposed method at the 50 points belonging to the validation areas. The influence of field management operations and the vegetative vigour of the plants are clearly detectable in the method's height estimation accuracy. The dispersion of values increased with plant vigour and decreased after each field management operation, remaining stable after the last field operation, because after that time, the vegetative expansion was no longer so prominent.

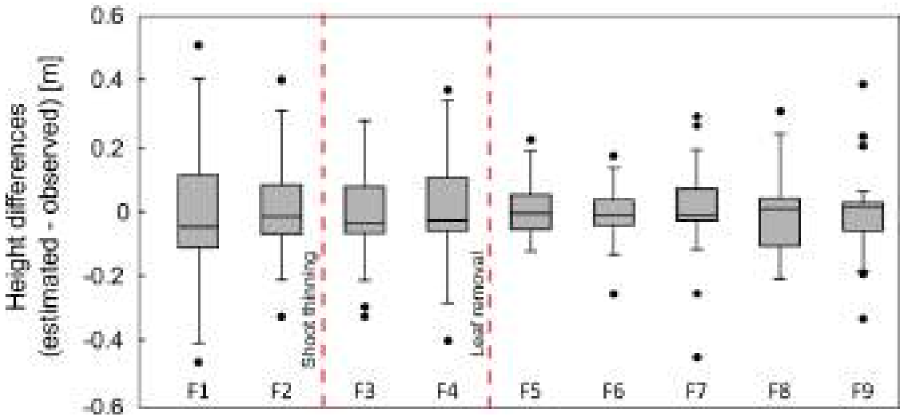


**Figure 7.11.** Boxplots of the height differences per flight campaign.

Table 7.3 presents the results of the comparison between heights estimated by the proposed method and measured in the field per flight campaign. In general, the RMSE indicates the expected difference between heights per campaign. As can be concluded from Table 7.3, Figure 7.11, and demonstrated in the next section, the RMSE varied significantly and a direct correlation was obtained with canopy management operations and the grapevine vegetative cycle.

**Table 7.3.** Accuracy assessment per flight campaign (F#) using the 50 points in the two validation areas and the 37 sparse points used for control. RMSE: root-mean-square error, $R^2$: coefficient of determination. Red dashed lines represent canopy management operations.

| | F#—Date (dd/mm/yyyy) | RMSE (m) | | Overall | |
|---|---|---|---|---|---|
| | | $n$ = 50 | $n$ = 37 | RMSE (m) | $R^2$ |
| | F1—02/05/2017 | 0.20 | 0.19 | | |
| Shoot thinning | F2—30/05/2017 | 0.15 | 0.14 | | |
| | F3—16/06/2017 | 0.13 | 0.12 | | |
| Leaf removal | F4—26/06/2017 | 0.14 | 0.13 | | |
| | F5—11/07/2017 | 0.10 | 0.11 | 0.13 | 0.78 |
| | F6—27/07/2017 | 0.10 | 0.10 | | |
| | F7—07/08/2017 | 0.12 | 0.11 | | |
| | F8—22/08/2017 | 0.12 | 0.12 | | |
| | F9—15/09/2017 | 0.13 | 0.12 | | |

Regarding grapevine area estimation, three different approaches were used, as explained in Section 7.2.3.3. The method was validated by comparing manual segmentation of two different areas, each one located in a different vineyard plot where the following three conditions could be observed: (1) the pixel-value is the same and is classified as exact detection; (2) over detection, if grapevine vegetation estimated in the method's application result is not classified as grapevine vegetation in the reference mask; and (3) under detection, corresponding to areas of grapevine vegetation that were not accurately estimated from the obtained results. The results from this evaluation are presented in Figure 7.12. Overall, the proposed method provided a mean accuracy of 94.40% in the exact detection of grapevine vegetation, similar to Pádua et al.

(2018). However, the mean exact detection percentage in P1 area was greater than the area located in P2, at 95.01% and 93.79%, respectively.

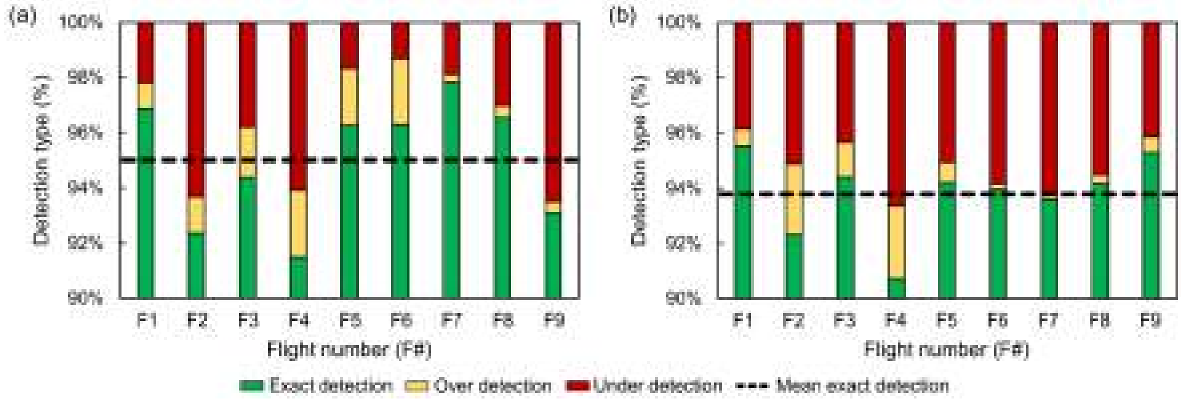


**Figure 7.12.** Results from occupation row area validation from data from each flight in an area of 10 × 10 m from both studied vineyard plots (a) P1 and (b) P2.

# 7.4. Discussion

A relationship was clearly established between grapevine vegetative cycle, field canopy management operations, and the different parameters obtained using the proposed method based on the results presented in Section 7.3. This section presents a discussion regarding vineyard vegetation evolution, determination of vine row height, and the impact that the proposed method can have in canopy management operations scheduling.

## 7.4.1. Vegetation Evolution

AOI vegetation evolution over time can be observed in Figures 7.6 and 7.8. As expected, the grapevine vegetative cycle was verified. P1 and P2 begin by having the smallest estimated grapevine vegetation area (F1, 2 May 2017), at 172 $m^2$ and 257 $m^2$, respectively. This represents 5% of the total vineyard area. An intensive vegetative growth follows, between the months of May and June. From the fifth flight campaign onward, grapevine vegetation area remained relatively stable, with only some minor variations. Some vegetation growth still occurred within the AOI, but grapevine vegetation steadily declined until the harvesting season, with a greater emphasis to the last two flight campaigns.

The impact of the first canopy management operation (shoot thinning, which took place in mid-June) is distinctly noticeable when comparing the second and third flight campaigns. Whereas vineyard vegetation area variation was not meaningful for both P1 and P2 (approximately −5% and 7%, respectively), the decline area was about 258 $m^2$ for P1 and 373 $m^2$ for P2, which are among the highest values registered in this study. As mentioned when presenting the grapevine vegetation volume, the type of canopy management operation can be directly correlated to grapevine canopy. This can be further established by analysing vineyard vegetation evolution from the fourth to the fifth flight campaigns, in between which another canopy management operation, leaf removal, took place (Figure 7.9, F4→F5). Grapevine vegetation area variation was higher than when the first canopy management operation occurred. Larger vegetation decline values were registered, about −29% (413 $m^2$) for P1 and −37% for P2 (843 $m^2$), when considering that the more intensive grapevines vegetative growth period ended in late June.

When comparing consecutive flights (Figure 7.9), the slight differences in the results concerning temporal evolution may be explained by the proposed method's implementation. However, grapevine leaves can (and do) change colour either when entering in their later phonological stages or as a manifestation of potential phytosanitary problems. As an example, in P1, some misdetections occurred mostly in the last two flight campaigns, because grapevine leaves were turning red.

Regarding grapevine canopy area, and when analysing each flight campaign individually (Figure 7.12), data from the flight prior to leaf removal (F4) showed the lowest accuracy in both analysed areas—91.50% and 90.73%, respectively—which can be explained by the existence of some grapevine branches that were not correctly detected in the CSM. This means F4 was the flight with the greatest overall under detection rate. The highest accuracy was achieved in F7 for P2 with 97.83% and F1 for P2 with a detection accuracy of 95.50%. Regarding misclassifications, under detection was verified in the boarders of grapevine plants and in the few thinner parts, whereas over detection was observed in shadowed areas and when there was more abundant vegetation, resulting in connected rows. Some inter-row vegetation was also classified. However, these misclassifications did not significantly influence the proposed method's overall performance in terms of grapevine canopy area evaluation.

With respect to grapevine vegetation volume, the behaviour was similar to grapevine vegetation area: it increased from the first to the fourth flight campaign and decreased thereafter, as presented in Figure 7.8. The first canopy management operation—shoot thinning—that took place a few days before the third flight campaign, did not decrease the volume's growth. The second canopy management operation—leaf removal—verifiable in the fifth flight campaign, clearly did decrease the volume: P1 decreased by about 62% in its 1000 $m^3$ and P2 grapevines' vegetation volume decreased about 68%, from 1900 $m^3$. This can be explained by the applied canopy management operations.

When assessing both grapevine area and volume from aerial imagery, management operations such as shoot thinning, which helps to focus grapevine development to have the best possible yield by removing secondary shoots and uncrowning areas to open up the canopy and help avoid diseases and improve air flow, may have no significant visual impact in grapevines' canopy. This happens because much of this operation is performed in the grapevines' canopy understory, and uncrowning does not completely remove surrounding vegetation—it only reduces it. Leaf removal effectively and unequivocally removes a significant amount of grapevine vegetation, with a visible impact on grapevine canopy level. In the sixth, seventh, and eighth flight campaigns, grapevine vegetation volume was about 240 $m^3$ in P1, having decreased to 125 $m^3$ (−53%) in the ninth (and final) flight campaign. P2 grapevine vegetation volume progressively decreased about 15% per flight campaign, until approximately 295 $m^3$ in the ninth flight campaign.

No significant differences amongst red and white grapevine varieties in regards to either area or volume were detected. Both parameters presented a similar behaviour per flight campaign.

Inter-row vegetation (Figure 7.8) in P1 and P2 was practically non-existent after the fourth and seventh flight campaigns, respectively. By cross-referencing estimated non-grapevine vegetation area with environmental data (Figure 7.2), the evolution was as expected. Whereas some precipitation during May 2017 can account for the slight increase in area between the first and the second flight campaigns, the lack of precipitation, the non-existent irrigation system, along with the high air temperature, and some inter-row management operations justify a reduced or even non-existent inter-row vegetation until the harvesting season.

### 7.4.2. Grapevine Row Height

The determination of grapevine row height is critical since it is used to compute vegetation volume, which was one of this study's goals. As such, a thorough validation was carried out, following the procedure presented in Section 7.2.3.3. A total of 87 measurements were recorded both in P1 and P2 per flight campaign, separated in two groups: 50 points were used for the proposed method's validation and the remaining 37 were used as control points. Field measurements were recorded simultaneously with flight campaigns and provided heights ranging from 1.01 m to 1.95 m. By analysing the results presented in Figure 7.11 and Table 7.3, an overall RMSE of 0.13 m was attained. These results are in line with other studies that used this type of validation: in De Castro et al. (2018) a $R^2$ of 0.78 and a RMSE of 0.19 m were observed in measurements ranging from 1 m to 2.5 m, from three different vineyards, at two different epochs. In Caruso et al. (2017), a $R^2$ of 0.75 and a RMSE of 0.15 m were obtained, with heights ranging from 1.4 m to approximately 2 m. Again, grapevines' vegetative cycle, together with the canopy management operations, influenced the quality of row height estimation. Leaves scarcity made it difficult to estimate heights using the proposed method in the first flight campaign; as a result, the highest RMSE (~0.2 m) was obtained. Then, vegetation development facilitated the use of photogrammetric tools, and the RMSE decreased in a consistent manner until ~0.13 m, just before the leaf removal canopy management operation. After that, RMSE drastically reduced (~0.10 m), influenced by the rows' regularity after the canopy management operation and the density of leaves. In the last stage of the grapevine vegetative cycle, RMSE moderately increased, since some grapevine branches influenced the photogrammetric estimation. From this point onward, both phenological and environmental contexts contributed so that no further excess grapevine vegetation was detected until the harvesting season.

### 7.4.3. Field Management Operations

Whereas the analysis of the data acquired in the second flight campaign identified some excess grapevine vegetation both in P1 and P2, a canopy management operation—shoot thinning—conducted before the third flight campaign reduced it significantly (P1 had about 22 $m^2$ and P2 had 82 $m^2$, representing 3% and 7% of the detected grapevine vegetation, respectively). However, given the intense grapevine vegetative growth until the end of June—the time when the fourth flight campaign took place—more excess grapevine vegetation was detected on both plots (P1 had about 113 $m^2$, representing 11% of the grapevine vegetation, and P2 had 306 $m^2$, representing 17% of the estimated grapevine vegetation). Another canopy management operation—leaf removal—which occurred before the fifth flight campaign, meant none excess grapevines vegetation in P1 and P2.

Besides being a potentially useful tool to identify vineyard areas that can benefit from canopy management operations, the analysis in Figure 7.10 shows the estimation of excess vegetation is possible at any given point in time. Therefore, grapevine biomass management can be optimized accordingly. Together with multi-temporal analysis, this approach enables a more complete characterization of vineyard's parameters' evolution, as well as the construction of historical series to further define intra-seasons crops' profiles.

## 7.5. Conclusions

Canopy management is critical to improving grapevine yield and wine quality by influencing canopy size and vigour and by reducing phytosanitary problems. As such, finding an operational method to estimate vineyards' geometric and volumetric parameters via remote sensing would improve the efficiency of vineyard management. In this context, we introduced the potential of applying low-cost and commercially off-the-shelf UAS equipped with an RGB sensor in the PV context. The acquired high-resolution aerial imagery proved to be effective for vineyard area, and volume estimation and multi-temporal analysis. The image-processing techniques we used enabled the extraction of different vineyard characteristics and the estimation of its area and canopy volume. Our method provides a quick and transparent way to assist winegrowers in managing grapevine canopy.

RGB orthophoto mosaics provide a context of the whole vineyard for visual interpretation of the surveyed area. By combining the different photogrammetric processing outcomes with image-processing techniques, we proved the possibility of automatically estimating vineyard geometric and volumetric parameters. Multi-temporal analysis of vineyard vegetation development enabled monitoring vineyard growth. We observed both volume and area growth until the period were the in-field grapevine canopy management operations were carried out for leaf removal, decreasing from that moment until the grape harvesting season. Inter-row vegetation decreased as the campaign progressed due to the high air temperatures and the almost absent precipitation during the summer period. These results were corroborated by a thorough validation using ground-truth data. The proposed method provided height estimations with a mean RMSE of 0.13 m, corresponding to an error of less than 10% in the row height, even considering the most complex scenarios of vegetation development (projected branches in the side and in the top of the row). After canopy management operations, the method's effectiveness improves, benefiting from row shape regularity (RMSE ~0.10 m). Regarding the area evaluation, we validated that the overall method's effectiveness was over 90% for all the flight campaigns.

This study provides a more valuable and less complex crop-related data acquisition method for farmers and winegrowers. The acquisition of other UAV-based data from different sensors can also be employed to estimate other grapevine parameters, such as for multispectral and thermal infrared sensors. These sensors, despite being less cost-effective and sometimes requiring, more expensive UASs, can estimate other important parameters, such as vineyard water status by estimating crop water stress for decision support in irrigation management, LAI estimation from vegetation indices, which can also support canopy management operations, and estimate the presence of potential phytosanitary problems in vineyards.

In the near future, the growing attention given by UAS manufacturers to both PA and PV markets will provide new technology in these fields by designing sensors adaptable for different UAS. It is expected that cloud-based photogrammetric processing solutions and geographic information system (GIS)-based web platforms for data analysis and results interpretation will contribute to an easier and more flexible method of acquiring and interpreting crop-related UAV-based data.

## Acknowledgements

This work was financed by the European Regional Development Fund (ERDF) through the Operational Programme for Competitiveness and Internationalisation - COMPETE 2020 under the PORTUGAL 2020 Partnership Agreement, and through the Portuguese National Innovation Agency (ANI) as a part of project “PARRA - Plataforma integrAda de monitoRização e avaliação da doença da flavescência douRada na vinhA” (Nº 3447) and supported by the ERDF and North 2020 - North Regional Operational Program, as part of project “INNOVINEandWINE - Vineyard and Wine Innovation Platform” (NORTE–01–0145–FEDER–000038).

# Chapter 8.

## Vineyard Variability Analysis through UAV-Based Vigour Maps to Assess Climate Change Impacts

*Agronomy*, 2019, *9*(10), 581

Journal Impact Factor – 2019: 2.603

5 Year Impact Factor – 2019: n/a

**Luís Pádua**, Pedro Marques, Telmo Adão, Nathalie Guimarães,
António Sousa, Emanuel Peres and Joaquim J. Sousa

Refer to https://doi.org/10.3390/agronomy9100581 for online published version

# 8.1. Introduction

About 70% of the available worldwide clean water is used in agriculture (Gilbert, 2012). Moreover, by the year 2050, there will have to be an estimated 70% increase in food production (Gilbert, 2012) to sustain Earth's population. Therefore, to attain a sustainable agriculture, it is essential to ensure proper water management. Global warming evolution throughout the years means these phenomena is one of the major threats to agricultural production, also with effects on society (Asseng et al., 2015; C et al., 2009; Lobell & Gourdji, 2012; Jinxia Wang et al., 2009). Less precipitation, associated with more frequent and longer drought periods (Schmidhuber & Tubiello, 2007), ultimately leads to an increase in the use of water in agricultural activity. To improve water usage efficiency, the United Nations (UN) set sustainable development goals with the aim to create an expected increase in efficiency in all sectors by the year 2030. This will ensure sustainable extractions and the implementation of integrated water resources management (United Nations, 2015). It is crucial that the agricultural sector contributes to this effort by developing and implementing controlled irrigation management systems (Cancela et al., 2017; Gago et al., 2015). As such, it is necessary to have an efficient analysis of crops' water status.

The enduring search for resource use optimization, risks reduction, and minimizing environmental impacts led to the emergence of precision agriculture (PA) (Gebbers & Adamchuk, 2010). To understand both spatial and temporal variabilities of a production unit, PA's tools and technologies enable the acquisition and processing of large data volumes (e.g., image processing techniques, geo-statistical methods) (Gebbers & Adamchuk, 2010; Pablo J Zarco-Tejada et al., 2014). The precision viticulture (PV) concept derived from PA involves applying different technologies to vineyard management and grape production (Alessandro Matese et al., 2015; Morais et al., 2008). However, grapevine (*Vitis vinifera* L.) development is strongly related to spatial heterogeneity, which depends on several factors to determine both its production and quality (A. P. B. Proffitt et al., 2006). Some of the more relevant factors are soil quality and type, vegetation management operations, irrigation systems, nutritional status, pest and disease control, air temperature, and precipitation levels (Alessandro Matese et al., 2015; Steyn et al., 2016). Changes in one of these factors may result in the occurrence of biotic and abiotic problems. Depending on its severity, it may result in a significant decrease in production or quality, and therefore, considerable economic losses (Baofeng et al., 2016). The Douro Demarcated Region (DDR, north-eastern Portugal) spatial variability is high due mainly to the terrain's topographic profile, climatic variations, and soil characteristics, which causes vineyards to be unique throughout the DDR (Morais et al., 2008).

In the last few years, due to their flexibility and efficiency in diverse environments, the use of unmanned aerial vehicles (UAVs) emerged in agriculture applications (Adão et al., 2017). UAVs can acquire georeferenced data with a high spatial resolution while using different types of sensors (RGB, near infrared, multi and hyper-spectral, thermal infrared (TIR) and LiDAR) (Pádua, Vanko, et al., 2017), which allow for the output of several digital products, such as ortho-rectified mosaics, digital elevation models (DEMs), land surface temperature, and vegetation indices (VIs) (Pádua, Vanko, et al., 2017). Indeed, their ability to carry different types of sensors make UAVs a suitable solution for agricultural applications. While multispectral sensors acquire data from the electromagnetic spectrum in the near and visible infrared region (400 to 1000 nm), thermal sensors can acquire data in the far infrared zone (5000 to 18,000 nm), where the reflection value of each pixel can be transformed into a temperature value (Pádua, Vanko, et al., 2017). Among the different VIs, which can be considered as a set of arithmetic operations applied in different bands used to extract different vegetation characteristics (Pádua, Vanko, et al., 2017), the normalized difference vegetation index (NDVI) (Rouse et al., 1974) must be highlighted as it is frequently used in agricultural applications to estimate different crop-related parameters: biomass (Bendig et al., 2015); canopy structure, leaf area index (LAI), crop management (Candiago et al., 2015); and mapping vigour zones (J. Primicerio et al., 2015). Moreover, it was found to correlate well with grape quality properties (Alessandro Matese & Di Gennaro, 2018). As for temperature-based indices, they constitute a quick and practical way to estimate crop water status, therefore indicating the plants' water content. The crop water stress index (CWSI) (Idso et al., 1981) is widely used in remote sensing to monitor plants' water status and consequent irrigation management (Alderfasi & Nielsen, 2001). TIR-based indices were employed to different crops, such as olives (Berni, Zarco-Tejada, Sepulcre-Cantó, et al., 2009), grapevines (Bellvert et al., 2013), cotton (D. G. Sullivan et al., 2007), wheat (Banerjee et al., 2018), rice (Liu et al., 2018), sugar-beet (Quebrajo et al., 2018) and maize (Romano et al., 2011). Remote sensing platforms can also be a helpful tool for a better understanding of spatial variability, which has a significant meaning in vineyard management activities. Actually, UAVs have already been used to, e.g., estimate the leaf area index (Kalisperakis et al., 2015; Mathews & Jensen, 2013), irrigation management and water stress mapping (Baluja et al., 2012; Bellvert et al., 2013; Romero et al., 2018), diseases detection and mapping (Albetis et al., 2017; A. Matese et al., 2013), and detection of nutritional deficiencies (Martín et al., 2015).

UAVs have already proved to be a cost-effective and flexible alternative for remote sensing, within a PA context. They present an improved decision-making process to the farmer and provide greater flexibility, when compared to other remote sensing platforms (Alessandro Matese et al., 2015).

As for PV, vineyards have significant areas occupied by elements other than grapevines (e.g., inter-row vegetation, man-made structures, vegetation that usually surrounds the plot, and grapevines' shadows) (Burgos et al., 2015; Alessandro Matese et al., 2015). These elements can be automatically identified by means of digital image processing methods. Indeed, several methods have been proposed to deal with UAV-based aerial imagery or with the resulting digital products from the photogrammetric processing. For example, grapevine segmentation (Comba et al., 2015; A. Nolan et al., 2015), supervised and unsupervised machine learning (Poblete-Echeverría et al., 2017), point clouds derived from photogrammetric processing (Comba et al., 2018; Weiss & Baret, 2017), and DEMs (Baofeng et al., 2016; Burgos et al., 2015; Kalisperakis et al., 2015). Regarding VIs, they are one of the most common segmentation techniques applied in remote sensing (Ponti, 2013), mainly to segment a given image into two classes: vegetation or non-vegetation (Peña-Barragán et al., 2011). However, when considering vineyard vegetation, VIs acknowledges all types of vegetation without distinguishing grapevines from non-grapevines (e.g., inter-row vegetation). By using the DEM—or more specifically, the canopy surface model (CSM), which can be obtained by subtracting the digital terrain model (DTM) from the digital surface model (DSM)—quantifying and removing non-grapevine vegetation in a vineyard's segmentation process can be done as plant height is provided (Jiménez-Brenes et al., 2019).

While different digital outputs can be generated from UAV-based imagery, the amount of data and its complexity can be overwhelming for the common farmer to interpret. Straightforward useful crop-related information is needed. Vigour maps are an example where by using the NDVI, vegetation is classified into different classes according to its characteristics. By applying it to PV, grapevines' vigour can be defined as the measure of the growth rate during a given time period (e.g., the growing season). This not only enables the classification of vineyard homogeneity zones (T. Proffitt & Turner, 2017), which is a way to represent the impact of both environmental conditions and soil fertility (van Leeuwen, 2010). There have been some related works done in this area. Khaliq et al. (2019) compared satellite imagery with UAV-based multispectral data in four different epochs of the grapevines' vegetative cycle. Different comparisons were made by considering: (i) the whole vineyard, (ii) only the grapevines' vegetation, and (iii) only inter-row areas. The authors reported that satellite multispectral imagery presented limitations due to the ground sampling distance (GSD, 10 m) and to the influence of inter-row information Primicerio et al. (2015) evaluated vigour maps produced for the whole vineyard and only encompassing grapevines' vegetation, by applying an automatic segmentation method (Comba et al., 2015). Campos et al. (2019) used UAV-based vigour maps to create prescription maps for vineyard spraying operations.

Studies supported by imagery acquired in one flight mission alone mainly focused on assessing non-grapevine vegetation removal when considering the whole vineyard, and in creating task-oriented vigour maps (Campos et al., 2019; Costa Ferreira et al., 2007; J. Primicerio et al., 2015; Rey-Caramés et al., 2015). With reference to multi-temporal studies, there are those whose aim is to compare different growing seasons by evaluating biophysical grapevines parameters (Bonilla et al., 2015; A. Matese et al., 2019; Rey-Caramés et al., 2015). Furthermore, studies utilizing intra-season multi-temporal data, considered the whole vineyard information (Marcal & Cunha, 2007), or vineyard changes were not the main focus (Khaliq et al., 2019). As found in Primicerio et al. (2015), vigour maps using only grapevines' vegetation showed a better representation of the variability within the vineyard. The spatial variability in grapevines' water status can be assessed thought both multispectral and TIR imagery, where TIR imagery serves as an immediate way to estimate crops' water status, while multispectral data can show cumulative water deficits (Baluja et al., 2012). As such, the TIR data has the potential to help understand water stress for near-real-time decision-making support (Espinoza et al., 2017). By integrating TIR and multispectral data, datasets to study grapevines' response to climate change (Di Gennaro et al., 2017) can be created.

This study aimed to evaluate vineyard vigour maps (NDVI) created using UAV-based multispectral imagery within a multi-temporal context and in different grapevines' phenological stages. The main goal was to study grapevines' vegetation dynamics during the growing season up until harvesting. Two approaches were used: (i) considering the whole vineyard area, and (ii) considering only automatically detected grapevines' vegetation. Spatial assessment between the generated vigour maps, and grapevines' canopy temperature and height data—obtained from UAV-based TIR and RGB imagery, respectively—were conducted with the objective to correlate vigour maps with potential grapevines' water stress and canopy height. This allowed for the assessment of non-grapevine features when analysing vigour maps.

The next section presents the study area and the methods used both for data acquisition and processing. Results are presented in Section 8.3 and discussed in Section 8.4. Lastly, the most significant conclusions are shown in Section 8.5.

## 8.2. Materials and methods

### 8.2.1. Study Area and Environmental Context

This study was conducted in a 0.30 ha vineyard located in the University of Trás-os-Montes e Alto Douro campus, Vila Real, Portugal (41°17'13.2" N 7°44'08.7" W WGS84, altitude: 462 m), in the DDR (Figure 8.1). The vineyard (*cv. Malvasia Fina*) is trained in a double Guyot system, where each row has grapevines 1.20 m apart and there is 1.80 m distance in between rows. There is a total of 22 rows with a NE–SW orientation. Furthermore, it is a rainfed vineyard, with fertilization applied using foliar spraying and with phytosanitary management operations taking place throughout the entire season. Inter-row areas are composed of spontaneous vegetation, which is managed using mechanical interventions at least twice per season.

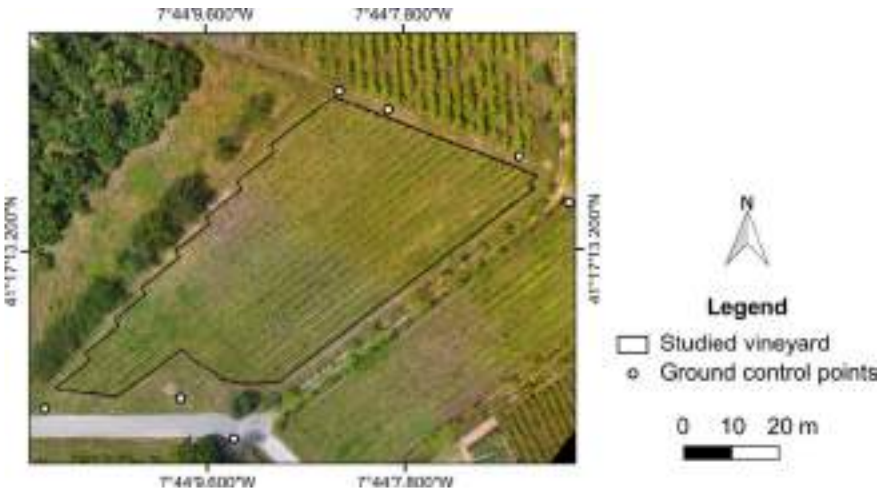


**Figure 8.1.** General overview of the studied area delimited by a polygon. Coordinates in WGS84 (EPSG:4326).

During the studied period (May to September 2018), a total of 170 mm of precipitation was registered, along with 590 mm of potential evapotranspiration. Mean values for maximum, mean, and minimum air temperatures were 29 °C, 20 °C, and 13 °C, respectively. Monthly values are presented in Figure 8.2. Higher air temperature values were observed in July, August, and September, while May and June presented higher precipitation values. In contrast, there was almost no precipitation in August. This environmental data was acquired using a weather station located some 400 m away from the study area.

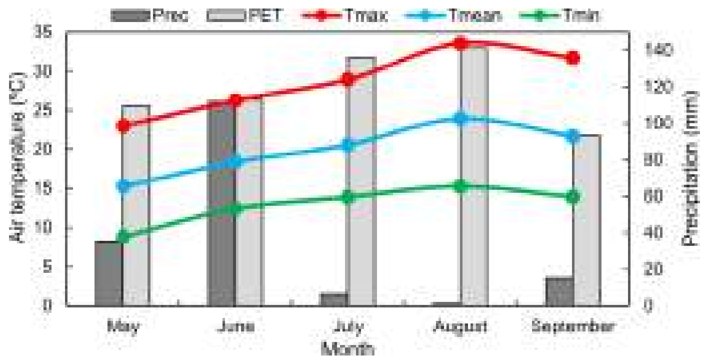


**Figure 8.2.** Monthly mean values for maximum (Tmax), mean (Tmean), and minimum (Tmin) air temperatures; precipitation (Prec); and potential evapotranspiration (PET) for the studied area in the period ranging from May to September 2018.

### 8.2.2. UAV-Based Data Acquisition

RGB, multispectral and TIR imagery were acquired using both a DJI Phantom 4 (DJI, Shenzhen, China) and a Sensefly eBee (senseFly SA, Lausanne, Switzerland). The former is a low-cost UAV equipped with an RGB sensor (12.4 MP resolution) attached to a three-axis electronic gimbal. For the purpose of this study, it was modified to support a multispectral sensor: the Parrot SEQUOIA (Parrot SA, Paris, France). This sensor consisted of a four-camera array, which was able to acquire data in the green (550 nm), red (660 nm), red-edge (735 nm), and near infrared (790 nm) parts of the electromagnetic spectrum, with a 1 MP resolution. Moreover, a Sunshine sensor (Parrot SA, Paris, France) was also added to the UAV's top. It is responsible for acquiring the irradiance conditions during the flight mission in the same spectral bands as the multispectral sensor and to geolocate the acquired imagery.

As for the Sensefly eBee, it is a fixed-wing UAV used to acquire TIR imagery with the thermoMAP (senseFly SA, Lausanne, Switzerland) sensor (between 7500 nm to 13,500 nm, with 640 × 512 pixels and a temperature resolution of 0.1 °C), with automatic in-flight thermal image-based calibration. Ground control points (GCPs), used for aligning the acquired imagery during the photogrammetric processing, were measured using a Global Navigation Satellite System (GNSS) receiver in real-time kinematic (RTK) mode based on the TM06/ETRS89 coordinate system (GCP's location in Figure 8.1). While the multi-rotor UAV was used mainly due to its capability to survey areas at lower flight heights, which provides higher spatial resolution (Pádua, Vanko, et al., 2017), the fixed-wing UAV surveyed a larger area, which included the studied area. Furthermore, the TIR sensor only operated as a fixed-wing UAV.

Data acquisition was conducted in five flight campaigns, from 17 May 2018 to 21 September 2018. Each flight campaign corresponded to distinct grapevine phenological stages: flowering (May and June), fruit set (July), veraison (August), and harvest (September). Details are presented in Figure 8.3. All flight campaigns were conducted near solar noon to minimize sun and shadow influences. Flights for both the RGB and multispectral sensors were done at a 40 m height, with a forward overlap of 80% and 70% side overlap between images. The GSD was approximately 1.8 cm for the RGB and of 4.4 cm for the multispectral imagery. Regarding flights for TIR imagery acquisition, they were carried out at a 75 m flight height, with a 90% forward overlap and 75% side overlap between images, resulting in an approximate 17.5 cm GSD. All flight campaigns utilized RGB and multispectral imagery, while TIR imagery was only acquired from F3 onward (see Figure 8.3), due to both in-field observations and the environmental context, since rainfall can induce an error in the remotely sensed grapevine water status in the subsequent days (Bellvert et al., 2016). Moreover, a radiometric calibration was performed prior to each flight for the multispectral imagery using a reflectance panel provided by the manufacturer, along with the irradiance data from the sunshine sensor. Irradiance and reflectance data enabled a reliable radiometric workflow for the collection of repeatable reflectance data over different flights, dates, and weather conditions.

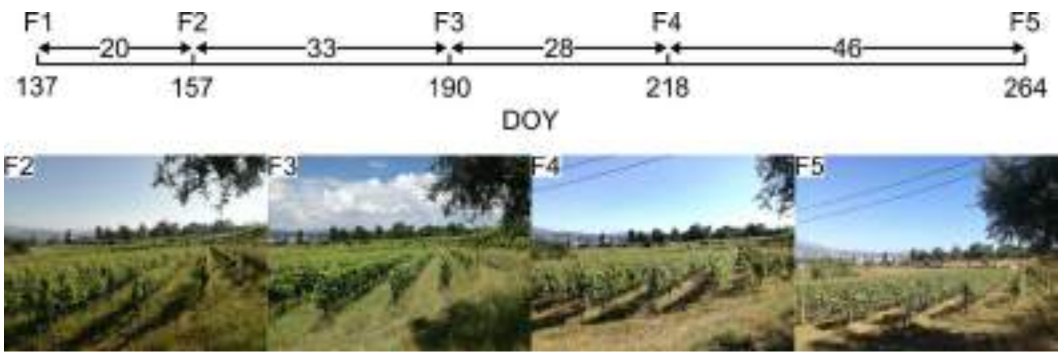


**Figure 8.3.** Flight campaigns' details: flight number (F#), Day of Year (DOY), and temporal difference (in days) between flights. Vineyard images in different flight campaigns are also shown.

### 8.2.3. Data Processing and Parameters Extraction

Imagery acquired in each flight campaign was processed using the Pix4Dmapper Pro (Pix4D SA, Lausanne, Switzerland). This software makes use of structure from motion (SfM) algorithms to identify common points in the images. It can create point clouds, and by interpolating them, generate different orthorectified outcomes depending on the sensor used. Imagery from each sensor was processed in different projects. The default processing options for each sensor were applied, but point clouds were generated with a high-point density. Point cloud interpolation was achieved using inverse distance weighting (IDW) and by applying noise filters. The generated digital outcomes were: (i) RGB–orthophoto mosaic, DSM, and DTM; (ii) multispectral–VIs; and (iii) TIR–land surface temperature. By subtracting the DTM from the DSM, the CSM was obtained. From the multispectral imagery, the NDVI (Rouse et al., 1974) was obtained using a normalization between the near-infrared (NIR) and red bands, as given in Equation (1).

$$\mathrm{NDVI} = \frac{\mathrm{NIR} - \mathrm{RED}}{\mathrm{NIR} + \mathrm{RED}} \tag{1}$$

The land surface temperature was used to compute the CWSI through the empirical model presented in Equation (2). It was based in the usage of canopy temperature, Tc, and the lower and upper canopy temperature limits ($T_{dry}$ and $T_{wet}$), corresponding, respectively, to well-watered and non-transpiring leaves. These values can be directly obtained in the field or by using UAV-based thermal infrared imagery (Alessandro Matese et al., 2018). CWSI values can vary between 0 (no stress signs) and 1 (high levels of stress). In this study, $T_{wet}$ and $T_{dry}$ values were obtained as described in the work of Matese and Di Gennaro (2018): $T_{wet}$ was obtained by wetting some leaves and immediately measuring their temperature, while $T_{dry}$ values were obtained by applying petroleum jelly in the leaves and registering their temperatures after some minutes had gone by. Temperature values were measured using a handheld infrared thermometer (Shenzhen Jumaoyuan Science and Technology Co., Ltd., Shenzhen, China), with a ±1.5 °C precision and operating between 8000 nm to 14,000 nm.

$$\mathrm{CWSI} = \frac{\mathrm{T_c} - \mathrm{T_{wet}}}{\mathrm{T_{dry}} - \mathrm{T_{wet}}} \tag{2}$$

To remove non-grapevine elements from the acquired imagery, segmentation was performed by using the method proposed in Pádua et al. (2018). Both the CSM and the G% index (Richardson et al., 2007), computed from the orthophoto mosaic, were used as inputs, and through thresholding, considering both vegetation and height thresholds, it identified all vegetation within a given height range. While G% was automatically obtained using Otsu's method for thresholding, CSM used a defined height range. An accurate grapevine segmentation was obtained, filtering out non-grapevine objects such as soil and inter-row vegetation.

This method has already been used in a multi-temporal analysis of grapevines' vegetation evolution throughout a season in two vineyard plots in Pádua et al. (2018). Similarly, in this study, the method to segment grapevines' vegetation (Pádua, Marques, Hruška, Adão, Bessa, et al., 2018) was applied to evaluate the multi-temporal vineyard evolution when regarding grapevine area and canopy volume, as well as the inter-row vegetation area. The grapevine canopy volume was computed according to Pádua et al. (2018), using the mean height of each cluster of pixels obtained during the segmentation process multiplied by its area, where the sum of the volume of each cluster represents the total vineyard volume.

As such, the orthorectified outputs from each flight campaign were used for different purposes. The grapevines' vegetation was detected and then CSM, NDVI, and CWSI values from the detected parts were considered, while non-grapevine pixels were discarded. Within the scope of this study, three different approaches were tested to create vigour maps. Figure 8.4 describes the main steps in each approach. Moreover, vigour classes were set to low, medium, and high. The workflow consisted in loading the orthorectified outcomes, followed by the vineyard segmentation method, depending on the used approach. Then, vigour maps were created by a applying a mean filter to the image, using a 2 × 2 m sliding window. Data could then be normalized before the vigour map creation. Again, this last step depended on the approach being used.

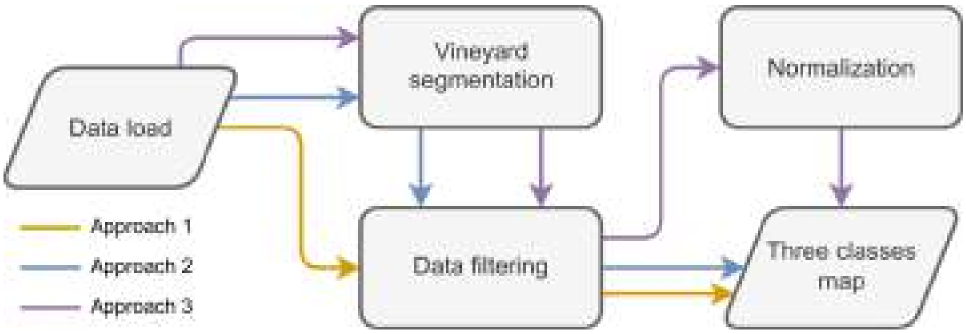


**Figure 8.4.** Approaches tested to produce vigour maps using three vigour classes.

The first approach relied on the usage of data from the whole vineyard. The outcome was directly smoothed and divided into three classes, using terciles. As for the second approach, it was similar to the first, but it only considered the grapevines' vegetation. Lastly, the third approach, similar to the second approach, considered only normalized grapevines' vegetation. Normalization was done based on the mean value of the 10% higher and lower values of the smoothed grapevines' vegetation values. Then, three vigour classes are created by dividing the values in the normalized raster according to fixed thresholds: (i) values lower or equal to 0.4 were considered low vigour; (ii) between 0.4 and 0.7 were considered medium vigour; (iii) and values above 0.7 were considered high vigour.

### 8.2.4. Vigour Maps versus Spatial Statistics

Vigour maps obtained from each flight campaign were compared with the CSM and the CWSI using statistical techniques that consider geospatial variability. This comparison was done by converting the three vigour classes maps to a 4 × 4 m grid. The grid size was selected by considering the studied vineyard's characteristics: each grid square was confined to two vine rows. This pipeline was proposed by Matese et al. (2019). Regarding the methods used in this comparison process, they were the local bivariate Moran's index (MI) and the bivariate local indicators of spatial association (LISA) (Anselin, 1995). Local MI (LMI) is based in the Moran's index (Moran, 1950), which measures the global data correlation. While a positive correlation represents similar values in the area's neighbourhood, a negative value represents the opposite, and zero represents a random spatial agreement. Regarding the LMI, a value is provided for each observation through permutation. The local bivariate MI was used in this study to assess the correlation between a defined variable and a different variable in the nearby areas. In turn, LISA measures the local spatial correlation, providing maps of local clusters with a similar behaviour, which is based on MI. This way, spatial clusters and its dispersion can be assessed. Bivariate LISA (BILISA) (Anselin, 1995) was used as in Anselin (2014) to examine the spatial relationship between the CSM and CWSI and the vigour maps. This comparison was made using GeoDa software (Anselin et al., 2006). Spatial weights were necessary to perform these analyses: an eight-connectivity approach (3 × 3 matrix) was used to create the weights map and BILISA was executed with 999 random permutations. The computed cluster maps and its significance were used. Cluster maps specify positive and negative spatial associations and are divided into four classes, based on the correlation of the value with its neighbourhood. The obtained associations are: (i) high–high (HH), where high values correlated with high values in the neighbourhood; (ii) low–low (LL), in which low values correlated with low values in the neighbourhood; (iii) high–low (HL); (iv) and low–high (LH). The three classes of vigour maps computed through the different approaches were compared with their correspondent vigour map in the following flight campaign, as well as with the CSM and CWSI three classes maps.

## 8.3. Results

This study yielded different digital products through the methods employed, from which it is important to highlight the vineyard status, vigour areas, potential water stress areas, and a multi-temporal vineyard characterization.

## 8.3.1. Multi-Temporal Vineyard Characterization

Figure 8.5 presents the orthorectified outcomes from the photogrammetric processing. There was a noticeable overall NDVI decline throughout the season (Figure 8.5a). However, grapevines' canopy height (Figure 8.5b) presented a growth from the first to the third flight campaign, while remaining constant from then on. As for the temperature (Figure 8.5c), a high temporal variability was observed due to both the day temperature and the inter-row vegetation. For example, in the third flight campaign, temperature differences between areas with or without grapevines' vegetation were smaller, about 1.0 °C, than in the other flight campaigns: approximately 2.2 °C for F4 and 1.4 °C for F5. Moreover, registered land surface temperatures presented the same behaviour as the maximum air temperature (Figure 8.2) registered in each month. Indeed, they were lower in July (followed by September), and higher in August.

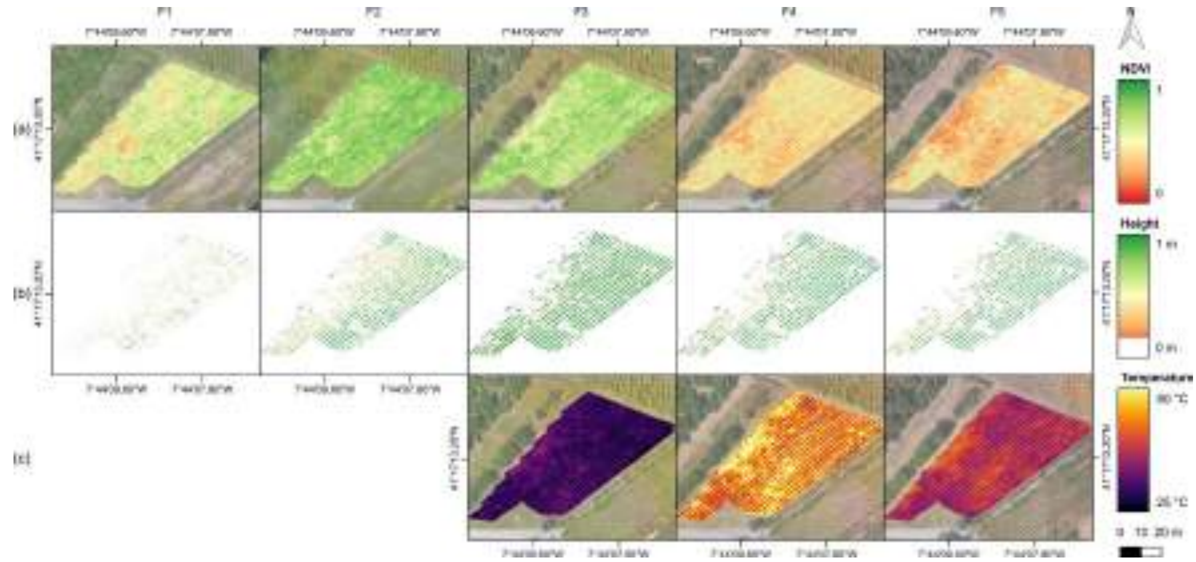

**Figure 8.5.** Orthorectified outcomes generated with data acquired in each flight campaign using a colour-code representation: (a) normalized difference vegetation index, (b) crop surface model, and (c) land surface temperature. Orthophoto mosaics are presented as the background of (a) and (c).

Due to early vegetation development in grapevines by the time the first flight campaign took place, the minimum height to consider as grapevines' vegetation was 0.2 m. As for the remainder of the flight campaigns, minimum and maximum heights were set to 0.5 and 1.9 m, respectively.

Table 8.1 presents the differences in NDVI, CSM, land surface temperature, and CWSI values when considering the whole vineyard plot and when analysing only detected grapevines' vegetation. Generally, mean and minimum NDVI values were higher when considering only grapevines' vegetation. As for maximum values, some high values were accounted for in areas other than with grapevines' vegetation. The same tendency was verified in the mean and minimum height values, obtained through the CSM. However, maximum values were practically similar, except for the first flight campaign. An inverse tendency was verified when analysing the land surface temperature and CWSI, i.e., higher values were found when analysing the whole vineyard plot.

**Table 8.1.** Maximum, mean, and minimum values of the normalized difference vegetation index (NDVI), crop surface model (CSM), surface temperature, and crop water stress index (CWSI) when considering the whole vineyard plot and only grapevines' vegetation in the five flight campaigns.

| Type | Outcome | Parameter | F1 | F2 | F3 | F4 | F5 |
|---|---|---|---|---|---|---|---|
| Whole area | NDVI | Max | 0.88 | 0.91 | 0.89 | 0.78 | 0.78 |
| | | Mean | 0.57 | 0.74 | 0.68 | 0.42 | 0.38 |
| | | Min | 0.13 | 0.26 | 0.27 | 0.17 | 0.01 |
| | CSM (m) | Max | 1.17 | 1.48 | 1.59 | 1.51 | 1.53 |
| | | Mean | 0.06 | 0.19 | 0.35 | 0.22 | 0.19 |
| | | Min | 0.00 | 0.00 | 0.00 | 0.00 | 0.00 |
| | Temp (°C) | Max | – | – | 38.74 | 59.90 | 45.84 |
| | | Mean | – | – | 29.89 | 44.35 | 37.20 |
| | | Min | – | – | 27.12 | 37.26 | 32.49 |
| | CWSI | Max | – | – | 1.00 | 1.00 | 1.00 |
| | | Mean | – | – | 0.60 | 0.83 | 0.78 |
| | | Min | – | – | 0.04 | 0.23 | 0.07 |
| Grapevines' vegetation only | NDVI | Max | 0.87 | 0.89 | 0.89 | 0.75 | 0.78 |
| | | Mean | 0.70 | 0.82 | 0.80 | 0.62 | 0.59 |
| | | Min | 0.41 | 0.59 | 0.64 | 0.37 | 0.25 |
| | CSM (m) | Max | 1.07 | 1.48 | 1.59 | 1.51 | 1.53 |
| | | Mean | 0.40 | 0.89 | 1.16 | 1.01 | 0.99 |
| | | Min | 0.20 | 0.47 | 0.52 | 0.27 | 0.20 |
| | Temp (°C) | Max | – | – | 31.20 | 47.81 | 39.36 |
| | | Mean | – | – | 28.92 | 42.17 | 35.84 |
| | | Min | – | – | 27.12 | 37.26 | 32.49 |
| | CWSI | Max | – | – | 0.82 | 1.00 | 0.91 |
| | | Mean | – | – | 0.38 | 0.68 | 0.48 |
| | | Min | – | – | 0.04 | 0.23 | 0.07 |

Extracted vineyard parameters allowed for a multi-temporal analysis of both grapevines' vegetation area and volume, as well as for other vegetation present in the studied area. Figure 8.6 contains these results. The first flight campaign presented the lower values for the grapevines' vegetation area: 82 m$^2$, representing 3% of the vineyard plot. The grapevines' vegetation area increased until the third flight campaign, from which a significant decline was verified in the following flight campaigns. The grapevines' canopy volume presented the same behaviour. As for inter-row vegetation, a growth happened between the first and the second flight campaigns, from 6% to 20% of the vineyard plot. After the fourth flight campaign, inter-row vegetation area decreased to 26 m$^2$ (1% of the vineyard plot), whilst a small increase was verified in the last flight campaign.

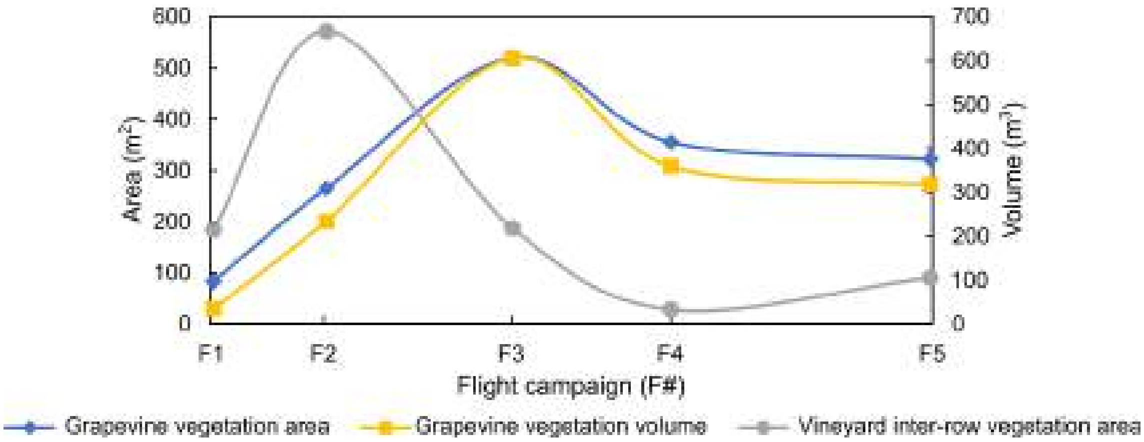


**Figure 8.6.** Estimated grapevines' vegetation area and volume, and inter-row vineyard vegetation, in each flight campaign.

## 8.3.2. Generated Vigour Maps

Vigour maps were generated as described in Section 8.2.3 and assessment values are presented in this section. Each map was classified as one of three classes, namely as a low, medium, or high vigour area.

### 8.3.2.1. Visual Assessment

Figure 8.7 presents the vigour maps generated using three approaches. When encompassing the whole vineyard (i.e., considering bare soil and all existing vegetation), as presented in Figure 8.7a, a perspective of the plot's homogeneity throughout the season was obtained. Approaches considering only detected vineyard vegetation presented a higher diversity, providing a deeper perspective on the grapevines' vegetation spatial variability (Figure 8.7b,c). Still, a tendency for a lower vigour classification in the left part of the studied area was noticeable in all approaches. The same situation was verified in the southern central part of the vineyard plot. This assessment was more pronounced in the first approach but had more detail in both the second and third approaches.

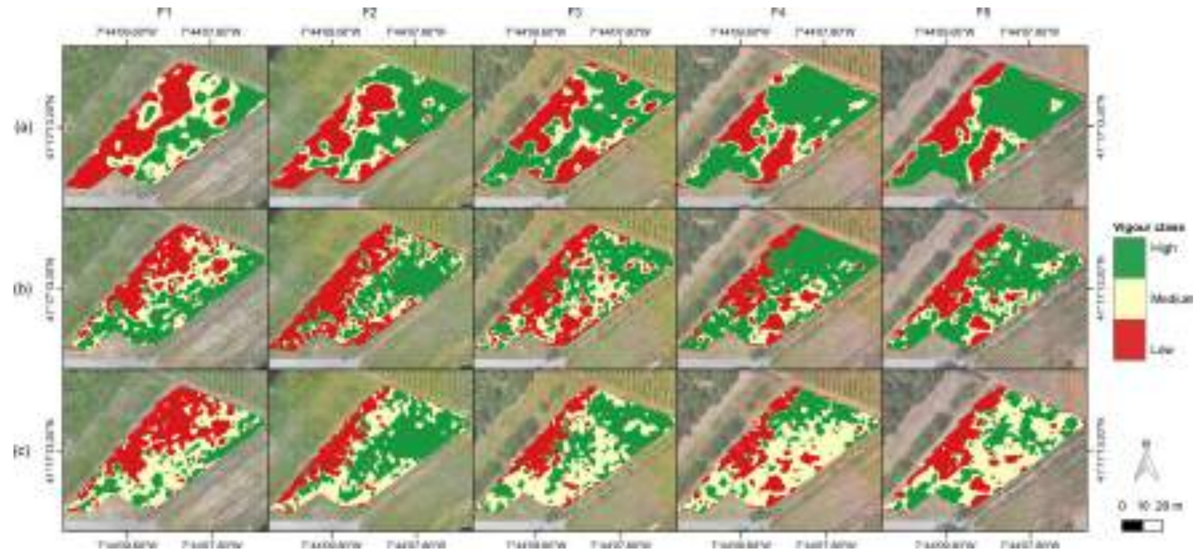


**Figure 8.7.** Generated vigour maps, based on the normalized difference vegetation index (NDVI), with three vigour classes (high, medium, and low) for each flight campaign, with the three evaluated approaches: (a) considering all vegetation present, (b) regarding only the grapevines' vegetation, and (c) considering only normalized grapevines' vegetation.

Vineyard areas classified with high, medium, or low vigour were evaluated in all flight campaigns. Their percentages are presented in Figure 8.8a. As for the first approach, the vineyard plot showed a higher percentage of vegetation in the high vigour class (mean overall percentage of 48%). However, in the first flight campaign, there was a higher area classified in the low vigour class (mean overall percentage of 31%). The medium vigour class presented the lower mean overall percentage (21%). As for the second approach, the overall mean area percentage was similar: 43% in the high vigour class, followed by 33% in the low vigour class and 24% in the medium vigour class. Regarding the third approach, the medium vigour class presented the higher mean overall occupation area (42%), followed by the high vigour class (31%) and the low vigour class (27%).

The vineyard vigour area behaviour may not correspond to the grapevines' vegetation. As such, Figure 8.8b shows the grapevines' canopy volume present in each class throughout all the flight campaigns. This was achieved by intercepting vigour classes with the detected grapevines' vegetation canopy volume. There were variations when comparing the applied approach and when analyzing the flight campaigns in the same approach: the overall value corresponded to the grapevines' canopy volume presented in Figure 8.6. When considering the NDVI values for the whole vineyard to generate a canopy map, the grapevines' canopy volume presented a higher predominance in the high vigour class. However, when comparing this with the approaches that consider only the grapevines' vegetation, the grapevines' canopy volume was significantly lower in the low vigour class for the latter approach. Regarding the approach where only grapevines' vegetation was considered, a clear distinction among the grapevines' vegetation volume was clear: the high vigour class had a greater grapevines' canopy volume, followed by the medium and low vigour classes. As for the third approach (normalized grapevines' vegetation), in the last two flight campaigns (F4 and F5), there was a higher volume in the medium vigour class, corresponding to the detected vineyard area (Figure 8.8a).

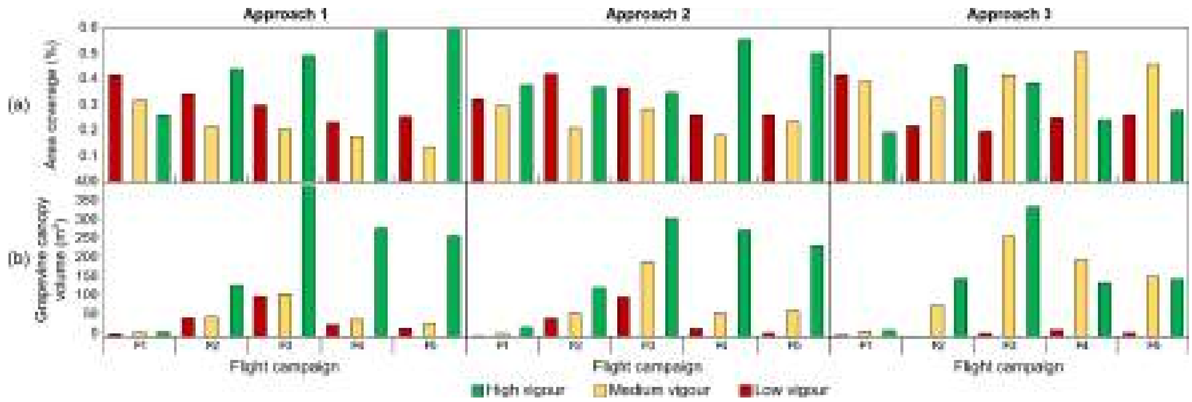


**Figure 8.8.** Vineyard area (a) and grapevines' canopy volume (b) per vigour class and approach in all flight campaigns (F#).

### 8.3.2.2. Spatial Correlations

To undergo a spatial assessment, the three approaches to generate vigour maps were applied to the CSM and CWSI outcomes of each flight campaign, when available. Ergo, maps with height values sorted in classes—low, medium and high height—could be obtained from the CSM. These results are presented in Figure 8.9. Height maps presented a high homogeneity among all approaches, especially from the third flight campaign onward.

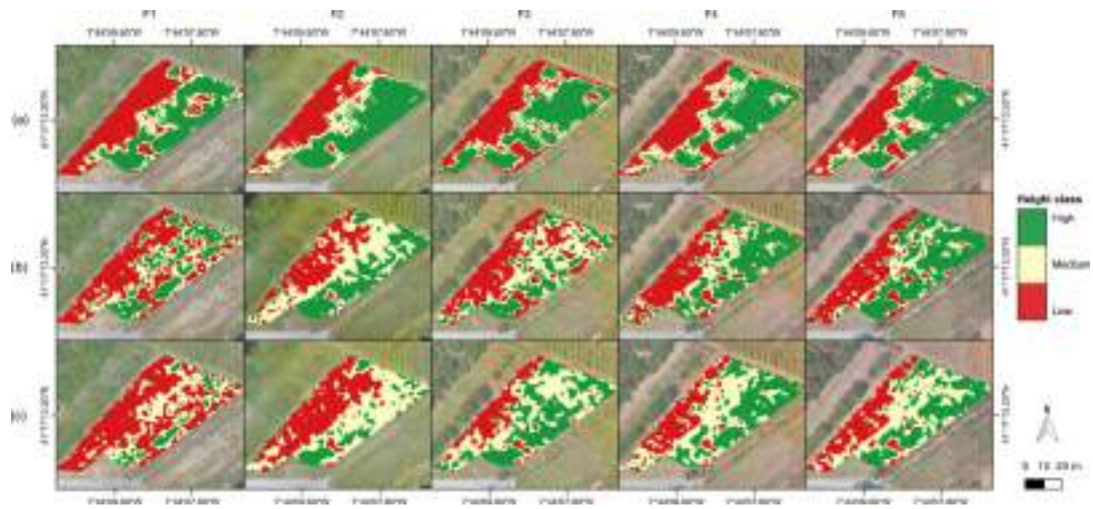

**Figure 8.9.** Generated height maps obtained from the crop surface models (CSM) for each flight campaign. Each height value was sorted into one of three height classes (low, medium, or high). The whole vineyard (a), grapevines' vegetation only (b), and normalized grapevines' vegetation (c) was considered.

From the CWSI, maps that could potentially point out grapevines' water stress were obtained. They are presented in Figure 8.10. Again, three classes were considered to sort out each value on every map: low, medium, and high water stress. Results from considering all vegetation present in the vineyard (Figure 8.10a) showed a high homogeneity across the plot for all flight campaigns. However, when considering only grapevines' vegetation (approaches two and three) the behaviour was different (Figure 8.10b,c).

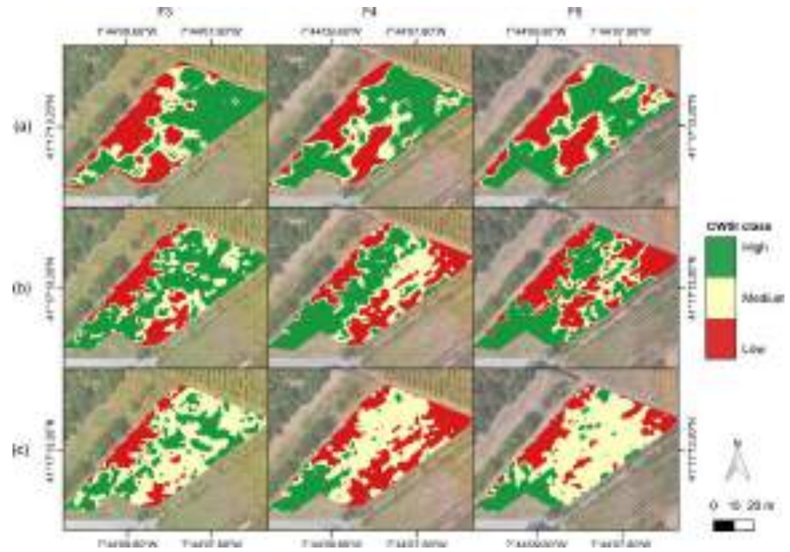


**Figure 8.10.** Generated crop water stress index (CWSI) maps for each flight campaign. Each CSWI value was sorted into one of three classes (low, medium, or high). The whole vineyard (a), grapevines' vegetation only (b), and normalized grapevines' vegetation (c) was considered.

Maps presented in Figures 8.9 and 8.10 were compared with the vigour maps presented in Figure 8.7 in a 4 × 4 m grid using the LMI to measure their spatial correlation. Table 8.2 presents these results. Considering all the vineyards' vegetation (first approach), stronger correlations were observed for the CSM. In turn, the other two approaches presented a more balanced trend for the CSM and CWSI. Stronger correlation values were found among vigour maps using data from the fourth flight campaign with the third approach (LMI = 0.70 for the CSM and LMI = 0.66 for the CWSI). Lower correlation values were observed in the height maps when considering all the vineyard's vegetation with data from the first flight campaign. The same was verified in the fourth flight campaign for the CWSI.

The local spatial autocorrelation enabled the creation of clusters maps using BILISA to evaluate HH, LL, LH, and HL patterns between vigour maps of the different flight campaigns and between vigour maps and their correspondent height and water stress maps.

**Table 8.2.** Quantitative comparison using the local Moran's index of the normalized difference vegetation index (NDVI) vigour classes in the three different approaches considered to the crop surface model (CSM) and crop water stress index (CWSI) classes with a *p*-value < 0.001, for each flight campaign (F#).

| Vigour map | Approach 1 | | Approach 2 | | Approach 3 | |
|---|---|---|---|---|---|---|
| F# | CSM | CWSI | CSM | CWSI | CSM | CWSI |
| 1 | 0.32 | – | 0.39 | – | 0.35 | – |
| 2 | 0.53 | – | 0.50 | – | 0.50 | – |
| 3 | 0.41 | 0.44 | 0.37 | 0.43 | 0.36 | 0.41 |
| 4 | 0.65 | 0.40 | 0.67 | 0.63 | 0.70 | 0.66 |
| 5 | 0.59 | 0.39 | 0.66 | 0.59 | 0.67 | 0.57 |

BILISA cluster map for the three evaluated vigour map approaches and its association with height maps is presented in Figure 8.11. As for the first approach (Figure 8.11a), there was a clear spatial correlation with a higher significance in the left and right sides of the vineyard plot, corresponding, respectively, to LL and HH associations. However, a smaller number of significant LH and HL clusters were detected. Regarding the other two approaches (Figure 8.11b,c) that considered only the grapevines' vegetation, similar spatial patters were found for HH and LL. Furthermore, a significant HL cluster could be found in the southwestern part of the vineyard plot in the fourth and fifth flight campaigns. Significant LH clusters were found in the south-eastern part of the vineyard in the second, third, and fourth flight campaigns for the second approach (Figure 8.11b).

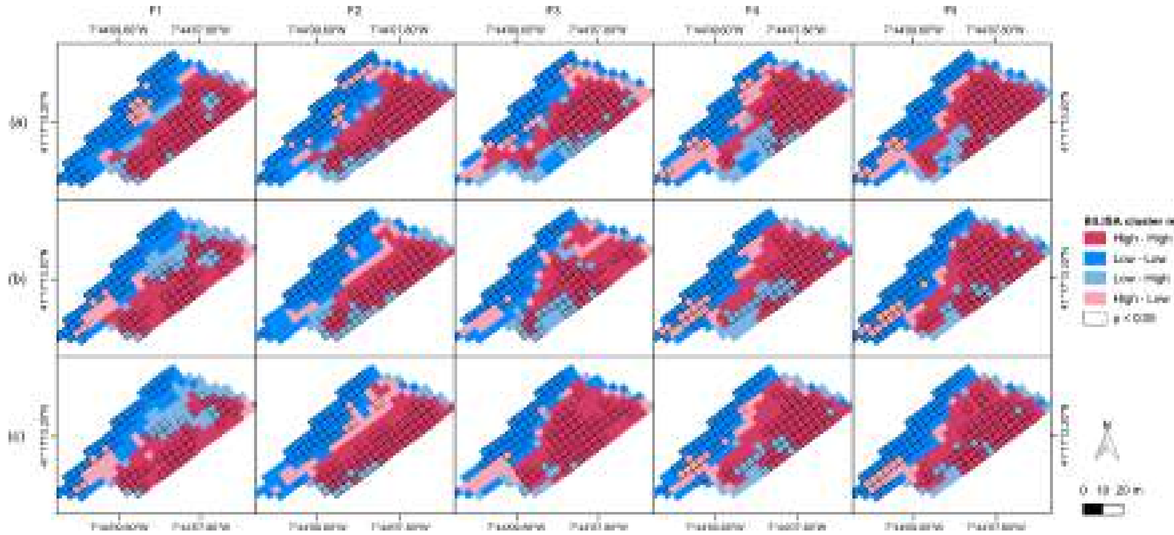

**Figure 8.11.** BILISA cluster maps between NDVI vigour maps and CSM height maps for the three evaluated approaches: (a) first approach, (b) second approach, and (c) third approach. Associations with a *p*-value < 0.05 are highlighted with a black border.

Figure 8.12 presents the BILISA cluster maps generated from the spatial associations among vigour maps and water stress maps (Figure 8.10). Significant associations were found when using the first approach, with a representative HH cluster present in the north-eastern region of the vineyard plot and a LL cluster in the vineyard's left side. When considering only the grapevines' vegetation, a similar behaviour was observed in the third flight campaign. In the remaining flight campaigns, a significant LL cluster existed in the left part of the vineyard, but a lower significance was found for HH in the north-eastern part. A high significance among the values was detected in the southern region, which presented HH and LH associations.

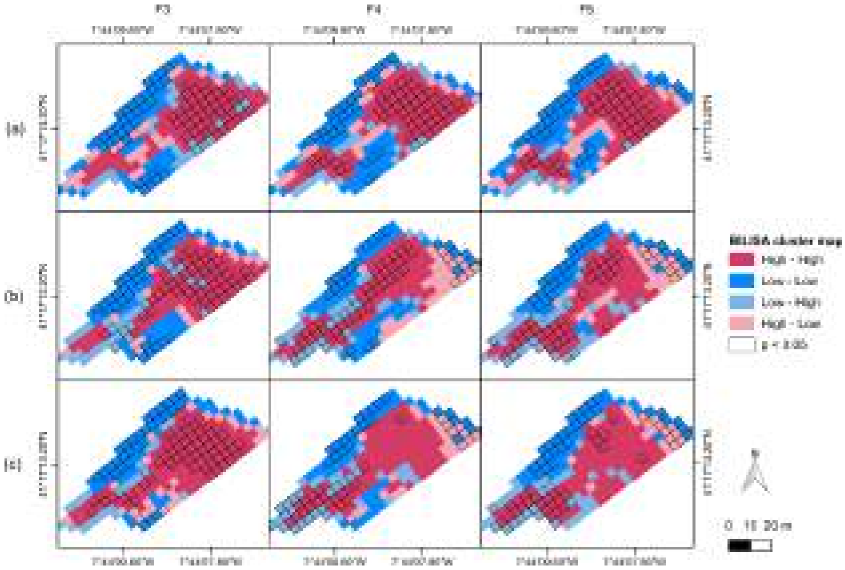

**Figure 8.12.** BILISA cluster maps between NDVI vigour maps and CWSI maps for the three evaluated approaches: (a) first approach, (b) second approach, and (c) third approach. Associations with a *p*-value < 0.05 are highlighted with a black border.

Considering the BILISA clusters maps from the vigour maps for each evaluated approach when comparing consecutive flight campaigns (Figure 8.13), similar patterns were observed in all approaches and significant LH clusters were identified when comparing the first and second flight campaigns considering only the grapevines' vegetation (Figure 8.13b,c).

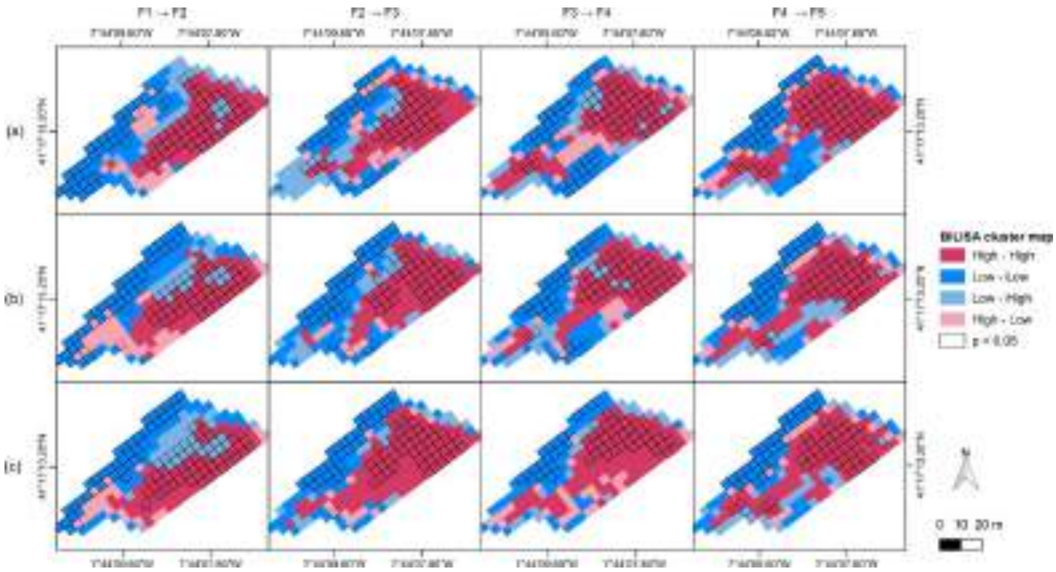

**Figure 8.13.** BILISA cluster maps between NDVI vigour maps of two consecutive flight campaigns for the three evaluated approaches: (a) first approach, (b) second approach, and (c) third approach. Associations with a *p*-value < 0.05 are highlighted with a black border.

## 8.4. Discussion

In this section the most meaningful results achieved in this study are discussed: (i) the multi-temporal analysis of the studied vineyard plot; (ii) the generated vigour maps; and (iii) spatial correlations between vigour maps, grapevines' height, and potential water stress.

### 8.4.1. Multi-Temporal Analysis

The vineyard multi-temporal dynamics can be better understood using the orthorectified results obtained via photogrammetric processing of the UAV-based imagery (Figure 8.5) though their visual inspection in a geographical information system (GIS) (Ozdemir et al., 2017).

Orthophoto mosaics can be used to detect missing grapevines and to manage vineyard in-field operations (Pádua, Marques, Hruška, Adão, Peres, et al., 2018). Vegetation indices (e.g., NDVI) can provide an overall assessment of vegetation vigour and potentially detect phytosanitary problems, such as *flavescence dorée* (Albetis et al., 2017) and esca (Gennaro et al., 2016). Leaf canopy temperature maps and CWSI can suppress the need to manually measure leaf water potential in the field (Baluja et al., 2012)—a time-consuming approach, usually not performed in the whole vineyard—as well as be used for irrigation management (Bellvert & Girona, 2012).

In this study, an overall NDVI decline was noticeable from the third flight campaign onward (Figure 8.5a F4, F5). This was related to the grapevines' vegetative cycle and to the decline of inter-row vegetation. Regarding height values obtained from each flight campaign's CSM (Figure 8.5b), a clear distinction existed between grapevine and non-grapevine vegetation (e.g., soil and inter-row vegetation), except for in the first flight campaign (Figure 8.5b F1). Land surface temperature (Figure 8.5c) was clear-cut between flight campaigns. In fact, in the fourth and fifth flight campaigns (Figure 8.5c F4 and F5), there were some signs of the grapevines' water stress.

Removing non-grapevine elements from the vineyard imagery provided a different perspective on the results, as confirmed in Table 8.1. Indeed, this enabled the production of estimate parameters such as the overall inter-row vegetation and the grapevines' area and volume (Figure 8.6). The estimated grapevines' vegetation area in the first flight campaign was 81 $m^2$ (3% of the vineyard plot) and in the second flight campaign, a 181 $m^2$ growth took place (262 $m^2$, 9% of the vineyard plot). As for the third flight campaign, there was a growth of 255 $m^2$ to 518 $m^2$ (18% of the vineyard plot). In the following flight campaigns, the grapevines' vegetation area was reduced by 199 $m^2$ (−38%) to 319 $m^2$. Regarding the grapevines' canopy volume, it was modified by +634%, +160%, −41%, and −12% in between each successive flight campaign, respectively. Concerning the inter-row vegetation area, it presented a behaviour consistent with the available precipitation data (Figure 8.2). Indeed, it had a 214% growth in between the first two flight campaigns (from 181 $m^2$ to 569 $m^2$), representing 20% of the vineyard plot area. A steep decline was noticeable in the third and fourth flight campaigns (a decline of 95% to 26 $m^2$), followed by a growth in the last flight campaign (88 $m^2$). As such, the vineyard inter-row vegetation was a good indicator of soil water status. The same tendency had already been verified in Pádua et al. (2018).

By comparing the mean, maximum, and minimum values observed in the different outcomes, either when considering the whole vineyard or only grapevines' vegetation (Table 8.1), there was a clear difference among the flight campaigns. Mean NDVI values were superior in all flight campaigns when considering only the grapevines' vegetation. The same tendency was verified in the CSM. This can be explained by the presence of a significant amount of lower values in the non-grapevine vegetation areas. However, the maximum NDVI values in the first, second, and fourth flight campaigns were registered in non-grapevine vegetation areas. Inter-row vegetation can account for this. Regarding maximum CSM values, they were similar in all flight campaigns, except for the first one, where the maximum height was detected in a non-grapevine area (probably a vineyard post). Minimum CSM and NDVI values were lower in non-grapevine areas. As for temperature-based outcomes (land surface temperature and CWSI), the opposite behaviour was found for the maximum values: they were located in non-grapevine vegetation areas. Mean temperature and CWSI values were lower in the grapevines' vegetation areas, as it was expected due to the existence of bare soil areas in the vineyard. Minimum temperature and CWSI values were similar in both approaches since they were found in the grapevines' vegetation areas. These results showed the importance of grapevines' vegetation segmentation when analysing a whole vineyard plot. The grapevines' vegetation segmentation could improve the results in studies where this operation was not automatically performed, which is beneficial for removing non-grapevine elements from the analysis. Such an automatic procedure could help in the evaluation of vegetation indices (Candiago et al., 2015), to detect *flavescence dorée* and grapevine trunk diseases (Albetis et al., 2019) and to estimate grapevines' biophysical and geometrical parameters (Caruso et al., 2017).

## 8.4.2. Vigour Maps

Vigour maps generated when considering the whole vineyard provided an overall perspective (Figure 8.7a) about the studied area. Indeed, influences from bare soil and especially inter-row vegetation were clearly noticeable. Generally, the medium vigour class had the smaller area (Figure 8.8a) and the high vigour class encompassed the majority of the grapevines' canopy volume (Figure 8.8b). The latter was, on average, 150% higher than the other vigour classes. A high homogeneity was verified for the last two flight campaigns. The same happened from the second to the last flight campaigns, when computing height maps from the CSM and all campaigns with CWSI. The whole vineyard was considered in both. Positive correlation values were found for the LMI (Table 8.2). Moreover, the verified homogeneity resulted in meaningful HH and LL areas when comparing vigour maps with CSM and CWSI in the same flight campaign.

Different results were obtained in the other two approaches, where only the grapevines' vegetation was considered to create vigour maps. The higher incidence of missing grapevine plants in the left area of the vineyard remained almost the same throughout all flight campaigns. This was not noticeable in the first two flight campaigns' vigour maps when considering the whole vineyard, probably due to an effect caused by inter-row vegetation. Other studies reported similar trends using vigour maps produced from the UAV-based NDVI (Khaliq et al., 2019; J. Primicerio et al., 2015), when excluding inter-row vegetation. Moreover, Vanegas et al. (2018) found positive correlations when comparing vigour maps created from UAV-based data and a vineyard expert assessment.

As for vineyard area, when considering only grapevine vegetation, it presented a more balanced behaviour. The third approach, normalized grapevines' vegetation, showed a considerable area of medium vigour class, particularly in the last three flight campaigns due to the fixed cut-off values to create vigour classes. Both approaches, grapevines' vegetation and normalized grapevines' vegetation, presented insignificant grapevines' canopy volume values in the lower classes. Moreover, when considering normalized grapevines' vegetation, canopy volume values were predominant in the medium vigour class, in agreement with the vineyard's overall vegetative growth and decline (growth from first to the third flight campaigns and decline onward). Similar relations between vigour and the grapevines' canopy volume were reported in other studies (Caruso et al., 2017; Alessandro Matese et al., 2016). A higher heterogeneity was verified when observing both the CSM and CWSI maps generated with the approach that considered the normalized grapevines' vegetation. In fact, when analysing the CWSI maps from the last two flight campaigns (Figure 8.10), a period of the grapevines' water stress was observed. However, this period was not clearly distinguishable in a visual map inspection based on data from the first approach (when the whole vineyard was considered). These correlations were observed in the BILISA cluster maps (Figure 8.12b,c), where areas with a high vigour showed a HL relationship with the CWSI maps, and significant agreements could be observed in the third flight campaign. A similar trend was reported in Matese and Di Gennaro (2018). Significant spatial associations were found in all approaches—whole vineyard, grapevines' vegetation, and normalized grapevines' vegetation—when analysing the height class maps (Figure 8.11). Although lesser associations were found in the first flight campaign, this can be explained with the grapevines' growth cycle. In this case, significant HL areas were found in the approaches considering only the grapevine vegetation. Similarly, Matese et al. (2016) observed that some areas with a higher vigour were linked to areas with higher heights.

This study analysed a vineyard's behaviour throughout a season with a multi-temporal approach based on multispectral data acquired using a UAV. Furthermore, correlations between the different digital outcomes were found. This presents a potential tool for multi-temporal vineyard assessment and can serve as a base to provide prescription maps, similar to Campos et al. (2019), since they can be correlated with agronomical variables (e.g. yield, berry weight and total soluble solids), as shown in Matese et al. (2019). Indeed, patterns detected when comparing vigour maps from consecutive flight campaigns (Figure 8.13) highlighted differences in the multi-temporal data, which helps to understand local and spatial grapevines' vegetative development dynamics throughout the season. However, filtered data considering only values representing grapevines' vegetation, therefore representing the plants' physiological status, was proven to be more reliable when comparing the evaluated approaches (Table 8.2); that is to say, it had a higher overall correlation. As such, it stands to be an excellent tool for decision support systems within vineyard management processes.

## 8.5. Conclusions

Climate change can heighten key environmental vectors that negatively impact vineyards. Grapevines can be weakened by both water stress and exposure to higher temperatures, which will increase their vulnerability to phytosanitary issues. UAVs equipped with different sensors can be used to regularly monitor grapevines, documenting changes in the vegetation or signs of diseases/infestation, as well as any stress caused by environmental constraints.

In this context, the need to evaluate current vineyard behaviour is crucial to proceed toward PV. Vigour maps can help to provide relevant insights, helping farmers and/or winemakers to understand their vineyards status and enabling timely actions to tackle problematic areas or observing response to treatments. Furthermore, the methods employed in this study to filter out non-grapevine vegetation presented a better vineyard representation, which can be used to assess a vineyard's variability, but also to help in managing field-operations, such as those to inspect grapevines or to improve grapevines' physiological status.

The use of methods to compare spatial correlations allowed us to obtain a spatial distribution of significant clusters among the different approaches evaluated for creating vigour maps. The importance of using different UAV-based outcomes to estimate biophysical and geometrical parameters shows the suitability of UAVs as a remote sensing platform for vineyard multi-temporal monitoring operations. This study allowed us to conclude that the need for UAV-based data can be tracked according to a vineyard's phenology. Moreover, TIR data should be acquired in periods of higher temperatures to assess areas potentially affected by water stress. Nevertheless, the analysis presented in this study should be assessed in other vineyard types, such as those with irrigation systems, with a lower rate of missing grapevines, and in other wine producing regions with different grapevine training parameters.

## Acknowledgements

The authors would like to thank Miguel Fonseca for providing the photographs of the vineyard.

## Funding

The research activities of Luís Pádua were funded by the Portuguese Foundation for Science and Technology (SFRH/BD/139702/2018).

# Chapter 9.

## Individual grapevine analysis in a multi-temporal context using UAV-based multi-sensor imagery

---

*Remote Sensing*, 2020, *12*(1), 139

Journal Impact Factor – 2019: 4.509

5 Year Impact Factor – 2019: 5.001

**Luís Pádua**, Telmo Adão, António Sousa, Emanuel Peres and Joaquim J. Sousa

Refer to https://doi.org/10.3390/rs12010139 for online published version

## 9.1. Introduction

The need to assess vineyard spatiotemporal variability is crucial in viticulture, as it is directly related to grapevine health status and yield (A. P. B. Proffitt et al., 2006), which can be achieved through precision viticulture (PV). Derived from precision agriculture concept (Pablo J Zarco-Tejada et al., 2014), in PV different technologies for vineyard management and grape production are employed for data acquisition and processing, aiming, among others, to maximize the oenological potential of vineyards, according to their spatiotemporal variability, by adopting site-specific management practices to increase both quality and yield (Alessandro Matese & Di Gennaro, 2015; Zhang & Kovacs, 2012). Thus, individual grapevines identification is important to precisely assess the vineyard status, by estimating several metrics for each plant. In this way, a better knowledge of grapevines (*Vitis vinifera* L.) development and spatial heterogeneity within the vineyard (A. P. B. Proffitt et al., 2006) along with the factors influencing it (Steyn et al., 2016) can be reached enabling individual plant treatments.

Traditional airborne remote sensing platforms, as satellites and manned aircrafts, both suitable for applications requiring a regional coverage, were used in PV to, among others, detect grapevine varieties (Karakizi et al., 2015), vigour assessment (Martín et al., 2007; Tisseyre et al., 2007), vineyard disease mapping (Hall et al., 2002), and for leaf area index (LAI) and canopy density estimation (L. Johnson et al., 2003; L. F. Johnson et al., 2001). However, given their coarser spatial resolution, crop and non-crop data are often mixed or represent multiple plants, lacking of true individual grapevine information (A. Matese et al., 2013). Nevertheless, data from these platforms can still deliver a general overview of vineyards, at least at a plot level (Khaliq et al., 2019). To overcome this scale-related issue, some approaches rely in proximal remote sensing (Mendes et al., 2016; Milella et al., 2019; Rosell et al., 2009). However, these approaches are time-consuming, requiring a passage through the whole vineyard and some issues can occur due to terrains' topography and possible obstacles in between the vine rows (Morais et al., 2008). Vibrations induced by the vehicles can interfere in data quality and the high costs of LiDAR sensors constitutes a drawback to their widespread adoption.

In the other hand, unmanned aerial vehicles (UAVs) provide aerial remote sensed data, with high temporal and spatial resolutions, and at lower costs for small to medium area coverages when compared to traditional airborne platforms (Alessandro Matese et al., 2015). UAVs are capable to acquire high-resolution georeferenced data from different sensors exploring different parts of the electromagnetic spectrum (Pádua, Vanko, et al., 2017). The georeferenced images driven from these sensors can be used to compute orthorectified outcomes, through photogrammetric processing (Colomina & Molina, 2014): orthophoto mosaics, digital elevation models (DEM) and spectral indices (Pádua, Vanko, et al., 2017) are among the most used. The normalized difference vegetation index (NDVI) (Rouse et al., 1974) is a vegetation index widely used in different remote sensing platforms for different purposes (Pádua, Vanko, et al., 2017). In the scope of PV, it is known to be correlated with LAI (Caruso et al., 2017), vegetative vigour (Campos et al., 2019) and yield (A. Matese et al., 2019). In turn, the crop water stress index (CWSI) (Idso et al., 1981) is used in different studies to assess vineyard water status (Baluja et al., 2012; Bellvert et al., 2013, 2015; Santesteban et al., 2017). In PA crop surface model (CSM) were used in different annual crops (Bendig et al., 2014; Du & Noguchi, 2017; Li et al., 2016; Tilly et al., 2014), where good agreements with crop height and biomass were observed. CSMs were also used in olive groves (Díaz-Varela, De la Rosa, et al., 2015), chestnut trees (Marques et al., 2019) and lychee trees (Johansen et al., 2018). As for PV, CSMs demonstrated a high agreement with grapevines' height (Caruso et al., 2017; A. I. de Castro et al., 2018; Pádua, Marques, Hruška, Adão, Peres, et al., 2018), and with vineyard vigour (Alessandro Matese et al., 2016; Pádua, Marques, et al., 2019). Its usage also enabled the estimation of grapevine volume (Caruso et al., 2017; A. I. de Castro et al., 2018; A. Matese et al., 2019; Pádua, Marques, Hruška, Adão, Peres, et al., 2018). Regarding vineyard vegetation detection several methods were already proposed, based in different approaches using the photogrammetric outcomes from UAV-based imagery by applying image processing techniques, machine learning methods and by filtering dense point clouds and DEMs (Baofeng et al., 2016; Burgos et al., 2015; Comba et al., 2015, 2018; Kalisperakis et al., 2015; A. Nolan et al., 2015; Pádua, Marques, Hruška, Adão, Bessa, et al., 2018; Poblete-Echeverría et al., 2017; Weiss & Baret, 2017). Those are capable to distinguish grapevine from non-grapevine vegetation and to extract different vineyard macro properties such as the number of vine rows, row spacing, width and height, potential missing plants and vineyard vigour maps.

In what concerns UAV-based approaches for individual identification of plants, the published studies mostly focus in tree detection within both forest and agriculture contexts (Dempewolf et al., 2017; Pádua, Marques, Adáo, et al., 2018; Surový et al., 2018). The outcomes resulting from photogrammetric processing can be used to estimate individual geometrical and biophysical grapevine parameters, providing a plant-specific application for PV (Jacopo Primicerio et al., 2017). In this scope, De Castro et al. (2018) proposed an object-based image analysis (OBIA) method using very high-resolution vineyard DSMs (1 cm ground sample distance—GSD) to estimate grapevine vegetation within vineyard plots. The method is based in a chessboard algorithm to consider pixels as grapevine. Grapevines are then divided by considering the spacing between plants, wherein missing plants are also estimated. Different geometrical properties were extracted, per grapevine: area, height, width, length, and volume. Matese and Di Genaro (2018) assessed missing plant detection, in a semi-automatic procedure, by filtering the DSM (1 cm GSD) in an 40 × 60 m experimental vineyard plot and by manually placing polygons of 1.00 × 0.60 m, representing each grapevine plant and, then, analysing the number of pixels intercepted by each polygon by using a five-classes approach based in quantiles to verify the probability of a missing plant presence. Primicerio et al. (2017) used a Binary Multivariate-Logistic Regression model for the individual detection of grapevines, including missing grapevines, in orthophoto mosaics. Grapevine vegetation segmentation was addressed by the method proposed in Comba et al. (2015). While De Castro et al. (2018) only focused in the extraction of grapevine geometric parameters, Primicerio et al. (2017) and Matese and Di Genaro (2018) mainly relied in the detection of presence/absence of grapevines. In the previously mentioned studies, it is pointed out that the integration of data from other sensors can enable the extraction of single plant vigour, health and water status, allowing to solve some of the problems of correct representation of vigour zones within the vineyard. Usually vineyard vigour maps rely in the averaging and/or interpolation of vegetation indices values (Jacopo Primicerio et al., 2017). Moreover, De Castro et al. (2018) state that grapevine multi-temporal analysis would provide a rapid way to monitor its status when compared to time-consuming and inconsistent in-field observations.

In this study, it is intended to address the gaps that were not covered in those implementations, by performing an individual grapevine estimation for site-specific management in a multi-temporal context, helping winegrowers into fully explore the potential of the high-resolution data provided by UAVs and to combine data resultant from the different imagery sensors for a more precise decision support and a quick vineyard inspection. This way, grapevine biophysical and geometric parameters extraction is performed using UAV-based data from different imagery sensors, namely: RGB, for grapevine vegetation detection, and geometrical features extraction; multispectral, for feature extraction from vegetation indices; and thermal infrared (TIR) imagery for grapevine temperature and water status estimations.

Next section characterizes the study areas, describes the data acquisition and processing, presents the method used for vineyard, as well as the validation procedures. The obtained results are shown in Section 9.3, considering grapevine estimation accuracy and the multi-temporal analysis. Section 9.4 discusses this study's findings. Section 9.5 addresses the main conclusions and presents potential future developments using the proposed method.

## 9.2. Materials and Methods

Aerial surveys were conducted in different vineyards, in the context of this study, and the most significant of their characteristics are shown in Table 9.1. Except for vineyard B, the analysed plots are located in the campus of the University of Trás-os-Montes e Alto Douro (UTAD, Vila Real, Portugal), in the Douro Demarcated Region. They are rainfed irrigated and trained in double guyot system. Vineyard B is located at Quinta do Suco (Amares, Braga, Portugal), in the Vinhos Verdes Region, it is trained in a single cordon and is irrigated through an irrigation system. Both training systems are the most common in these wine regions (Costa et al., 2015). The selection of these vineyard plots was based on the fact they present different row orientation, diverse levels of missing grapevines (0% to 33%) and plant height. The surveyed vineyard plots are presented in Figure 9.1.

**Table 9.1.** Characteristics of the analysed vineyard plots, indicating the original number of grapevines and missing grapevines; its number of rows, spacing, and height.

| Vineyard plot | Coordinates (Lat., Lon.) | Area (ha) | Number of grapevines | | Rows | | |
|---|---|---|---|---|---|---|---|
| | | | Original | Missing | Number | Spacing (m) | Height (m) |
| A | 41°17'12.1"N 7°44'15.2"W | 0.36 | 1440 | 381 | 34 | 1.20 | 1.4—1.7 |
| B | 41°39'24.2"N 8°22'24.5"W | 0.19 | 234 | 0 | 7 | 2.00 | 2.8 |
| C | 41°17'08.6"N 7°44'13.6"W | 0.35 | 1439 | 448 | 36 | 1.20 | 1.4—1.7 |
| D | 41°17'13.2"N 7°44'08.7"W | 0.30 | 1228 | 320 | 22 | 1.20 | 1.4—1.7 |
| E | 41°17'08.1"N 7°44'09.9"W | 0.57 | 2266 | 416 | 55 | 1.25 | 1.4 |
| F | 41°17'09.5"N 7°44'09.1"W | 0.32 | 1224 | 405 | 45 | 1.25 | 1.4 |

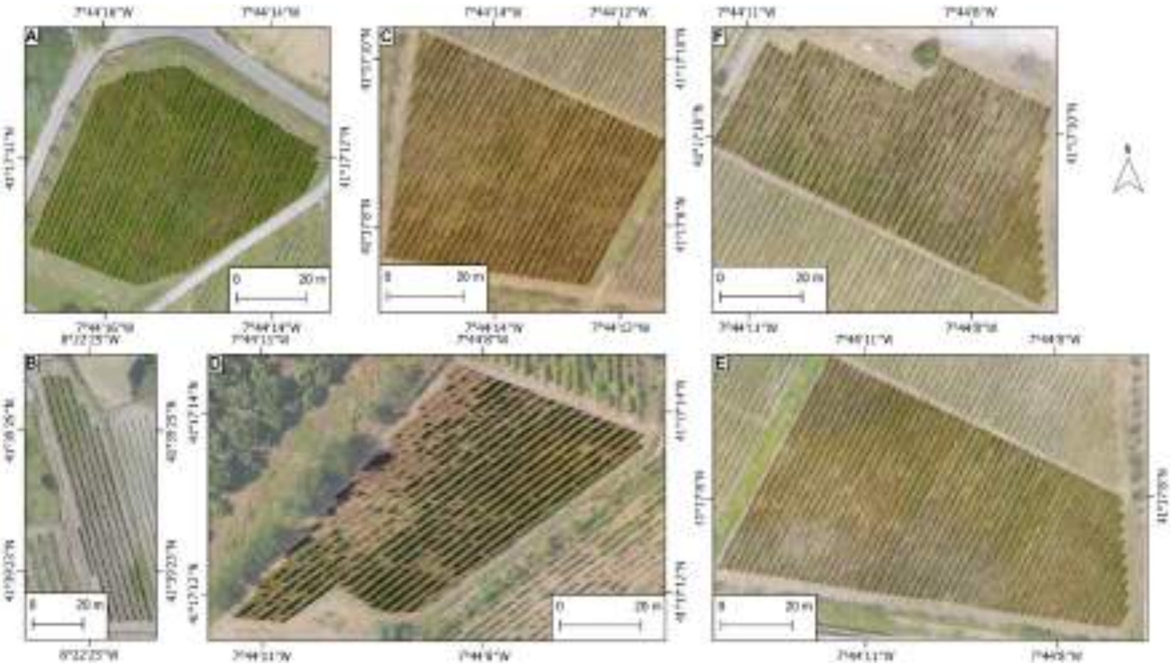

**Figure 9.1.** Analysed vineyard plots. The uppercase letter in the upper left corner represents each vineyard plot ID. Coordinates in WGS 84 (EPSG: 4326).

Aerial imagery acquisition was performed using two UAVs, a multi-rotor UAV, the DJI Phantom 4 (DJI, Shenzhen, China) and a fixed-wing UAV, the senseFly's eBee (senseFly SA, Lausanne, Switzerland). The Phantom 4 was used to acquire RGB and multispectral imagery at lower flight heights, whereas eBee was used to survey a larger area for TIR imagery acquisition, which included the studied areas. RGB imagery was acquired using Phantom 4 native camera, FCC 3 model, a CMOS sensor with 12.4 MP resolution mounted in a 3-axis electronic gimbal. Multispectral imagery acquisition was conducted using the Parrot SEQUOIA (Parrot SA, Paris, France), using green (550 nm), red (660 nm), red-edge (735 nm), and near infrared (790 nm) bands, with 1.2 MP resolution. The radiometric calibration is performed based on the irradiance measured by the sensor located at the top of the UAV and using the reflectance from calibration target (Airinov, Paris, France) prior to each flight. TIR imagery was acquired using thermoMAP (senseFly SA, Lausanne, Switzerland) which can acquire TIR data between 7500 nm to 13500 nm with 640 × 512 pixels and with a temperature resolution of 0.1 °C. The sensor's calibration is automatically performed in-flight.

UAV flight campaigns performed with the multi-rotor UAV were conducted with 80% front overlap and 70% side overlap at ≈40 m height from the take-off point in a double-grid configuration, resulting in GSDs of approximately 2 cm for RGB imagery and approximately 5 cm for multispectral imagery. While, the flights conducted with the fixed-wing UAV had 90% front overlap and 70% side overlap and were performed at 75 m height in a single grid, these specifications were selected according to manufacturer recommendations, obtaining an approximate GSD of 18 cm. The preparation and execution of flight campaigns of the multi-rotor UAV took 20 minutes, while the fixed-wing UAV took 30 minutes.

## 9.2.1. Data acquisition

### 9.2.1.1. Validation dataset

A validation dataset, composed of all the surveyed vineyard plots (A to F), was created for accuracy assessment of the individual grapevine detection procedure. Specifically, for the estimation of the number of grapevines and for canopy gaps detection, i.e. parts of vine rows where no grapevine canopy is present (missing plants). For this purpose, only RGB data was considered. The data was collected between May to August 2018 at the following at days of year (DOY):136 (vineyard plot B); 186 (vineyard plot A); 197 (vineyard plot D); 215 (vineyard plot C); and 219 (vineyard plots E and F).

### 9.2.1.2. Multi-temporal dataset

Vineyard plots A and B were used for multi-temporal analysis and were surveyed using different UAV-based sensors, namely, RGB, MSP and TIR. The context of these vineyard plots is different: vineyard plot A, located at UTAD campus, it is mainly used for experimental purposes, while plot B is a commercial vineyard. Vineyard plot B was selected to be surveyed throughout the vegetative growth cycle. It is composed by seven rows of two white grapevine varieties, four rows of cv. *Alvarinho* and three rows of cv. *Loureiro*. Vineyard plot A had a higher incidence of missing grapevines and suffered from powdery and downy mildew due to the conjugation of high air temperature and high humidity levels. These fungi affect the grapevines yield and leaves, causing potential losses (Maria do Carmo Val, 2013). It is composed by a collection of recommended Portuguese grapevine varieties.

In the case of vineyard plot A, flight campaigns were conducted in the first and fourth weeks of July and in the third week of August and September (2018), with an average time distance of approximately 26 days in between flight campaigns, covering most part of the fruit set and varaison phenological stages. As for vineyard B, the flight period is broader encompassing most part of grapevine’s phenological development, from the third week of May 2018 until the second week of October 2018, after grape harvesting. The remaining campaigns were performed at the third week of June and July, and at the second week of August 2018. The temporal mean distance between campaigns is 37 days.

For an accurate multi-temporal analysis, six ground control points (GCP) were acquired in different points from the surroundings of each analysed vineyard plot using a GNSS receiver in RTK mode in the TM06/ETRS89 coordinate system to perform imagery alignment during the photogrammetric processing. In order to ensure GCPs' recognition in TIR imagery, aluminium foil was used, as in Hartmann et al. (2012). Figure 9.2 presents an example of the aluminium target appearance thermal and RGB images.

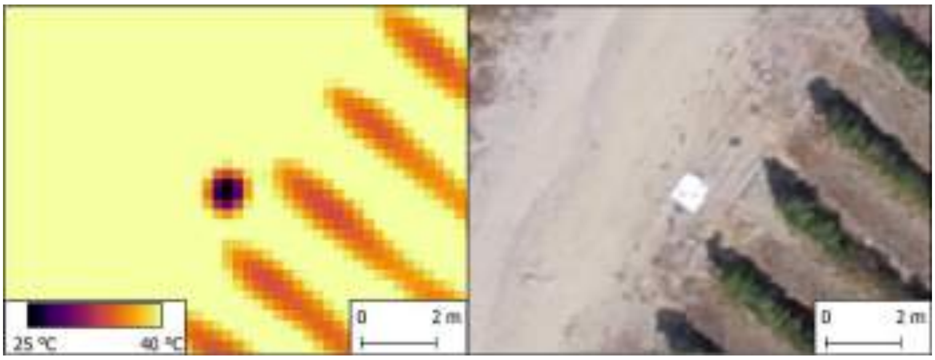


**Figure 9.2.** Thermal target, indicated by the arrow, used for data alignment: (a) its representation in thermal infrared imagery and (b) in RGB.

## 9.2.2. Data processing

The data acquired in each flight campaign passed through a pre-processing stage by means of photogrammetric processing for computation of different orthorectified outcomes. After this stage, the data was used as input for individual grapevine estimation and computation of different vineyard-related parameters.

### 9.2.2.1. Data pre-processing

Pix4Dmapper Pro (Pix4D SA, Lausanne, Switzerland) was used for photogrammetric processing. It supports the imagery from all the sensors used in this study, allowing to generate 3D point clouds using Structure from Motion (SfM) algorithms and, therefore, different orthorectified outcomes. However, depending on the source data, different outcomes were computed. This way, when processing RGB imagery, orthophoto mosaics, DSMs and DTMs were generated. Moreover, crop surface models (CSM) were computed subtracting the DTM altitude values from the DSM. The G% index (Richardson et al., 2007) was computed according to Pádua et al. (2018), from the RGB orthophoto mosaic, as in (1), by normalizing the green band with the sum of all bands. The data from other sensors used in this study can also generate CSM, but they suffer from smoothing effects, since they have less spatial resolution and, therefore, lack of detail (Alessandro Matese et al., 2016).

$$G\% = \mathrm{Green}/(\mathrm{Red} + \mathrm{Green} + \mathrm{Blue}) \quad (1)$$

The NDVI was computed using multispectral imagery. Using TIR imagery, the land surface temperature (LST) was computed. However, since crop temperature varies along the day and epoch of the year, it can penalize the multi-temporal data analysis representativeness (Bellvert et al., 2013). Thus, to ensure the most representative results from TIR data, LST from each flight campaign was used to compute the CWSI (Idso et al., 1981). This index relies in the usage of upper and lower temperature bounds ($T_{wet}$ and $T_{dry}$) which, respectively, correspond to the temperatures of well-watered leaf and a non-transpiring leaf. Since GSDs from different sensors were also different, to enable data integration, it was necessary to standardize the GSD. This operation was directly performed in the photogrammetric software, using the gaussian average, being the data resampled to 5 cm GSD. Obviously, this procedure did not improve the resolution of the thermal data, as in practice the original pixel was split divided allowing a direct comparison. This ensures the resolution of the remaining information is maintained and, at the same time, making the image processing stage quicker, and preserving all relevant information. This ensures the resolution of the remaining information is maintained and, at the same time, making the image processing stage quicker, preserving relevant information. CSM and G% were computed using QGIS software, an open source geographical information system (GIS).

#### 9.2.2.2. Vine rows estimation and individual grapevine estimation

The detection of vineyard vegetation and vine rows was accomplished using the method from Pádua et al. (2018). Figure 9.3 presents the main stages of the method for individual grapevines estimation and parameters extraction.

Vegetation detection relies on the combination of **CSM** and **G%** with image processing techniques for a given vineyard plot **P**. Both **CSM** and **G%** are binarized by thresholding, automatically using the Otsu's method (Otsu, 1979) for **G%**, and using a height range for the **CSM**. The resulting images are combined resorting in a new binary image **V** representing the estimated vineyard vegetation, forming different group of pixels (clusters). Then, the detected clusters are dilated according to their orientation resulting in the vine rows estimations. By eroding this image, a new image **S** with the rows central lines is obtained. Considering the equidistance space *d* between grapevines' trunks along with **S**, grapevine plants can be estimated. This is the common scenario in modern vineyards were grapevines are mechanically implanted (Jacopo Primicerio et al., 2017). This way points are positioned along the vine rows and, then, dilated with a morphological line structuring element with the same orientation as the vine rows. Depending on the vineyard training system trunk's position can vary, being in the middle or in edges of the grapevine area. Taking this into account, the grapevines are correctly positioned. The resulting binary image is subjected to a thickening morphological operation, by adding pixels to border of the clusters, but maintaining the clusters unconnected. The binary image **G** forms the area where vegetation from each grapevine is confined, since they are trained with wires to grow vertically and horizontally in between rows.

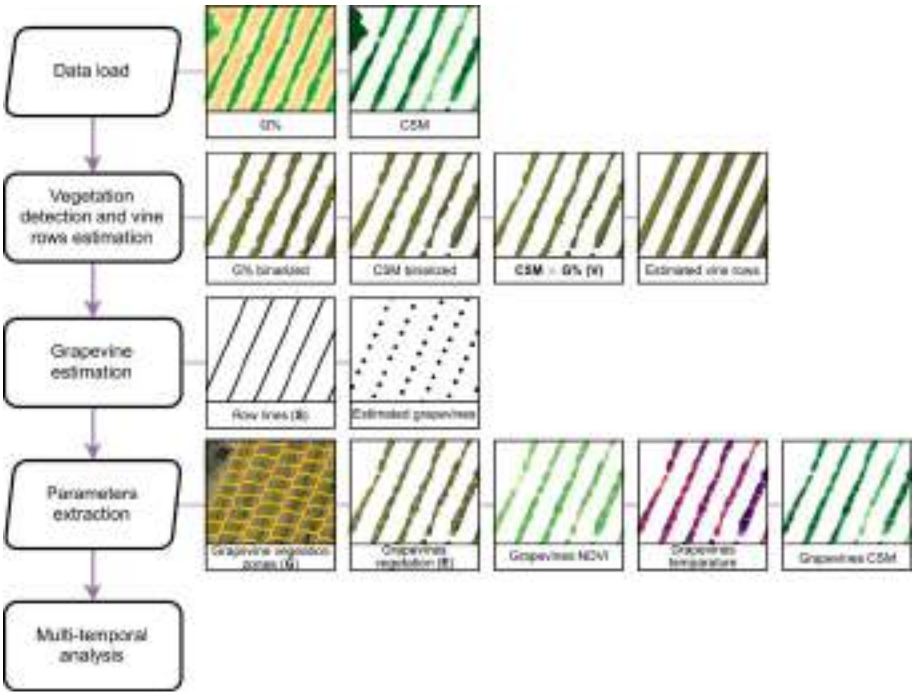


**Figure 9.3.** Main stages of individual grapevine estimation and its parameters extraction along with graphical examples of each step. Some graphical examples are presented in a colour-coded representation to highlight the different values. Binary images were used to mask the orthophoto mosaic.

### 9.2.2.3. Parameters extraction

By estimating the area of where each grapevine is present within a given plot, it is possible to individually estimate different parameters, from biological and physical characteristics. This way, the outcomes from different sensors can be useful to provide grapevine parameters.

This procedure uses the estimated grapevine vegetation **V** along with **G**, both are combined as in (2). The result of this combination in a new image **E,** representing the vegetation for each estimated grapevine, enabling the extraction of biophysical and geometric grapevine parameters from the UAV-based photogrammetric outcomes.

$$e_{i,j} = \begin{cases} 1, \text{if } v_{i,j} = 1 \land \ g_{i,j} = 1 \\ \quad \text{NaN, otherwise} \end{cases} \quad (2)$$

Depending on the available data, different parameters can be extracted for each grapevine, namely:

- the area of each grapevine, which is computed by the number of pixels present in each cluster from **E** multiplied by its squared GSD value;
- the grapevine height, these values are extracted from the CSM, only retrieved in the pixels of **E (**the remaining CSM pixels are not considered), mean, maximum and minimum values are estimated;
- the volume of grapevine, it is estimated using both height and area, the different height estimates (mean, maximum and minimum estimated height values) are used to calculate different volume values;
- features driven from multispectral and TIR imagery, in the case of this study, NDVI, LST and CWSI are masked according to **E** and its mean, maximum and minimum values are estimated.

Mean value refers to mean value of a given cluster, maximum and minimum values are estimated from the mean value of the higher/lower 10% values, this way, potential outlier pixels are discarded, independently from the area of the clusters. Since CWSI needs upper and lower bound temperature values, this was achieved by using the mean temperature values retrieved from LST, considering the mean temperature value of the 10% lowest and highest temperature values to compute $T_{dry}$ and $T_{wet}$, respectively. The estimation of other vegetation indices from different sensors is also supported. In the scope of this study only NDVI and CWSI are estimated. Still, other parts of the electromagnetic spectrum can also be used. The grapevine mask clusters are associated with the extracted grapevine parameters, which, in turn, are converted to a point shapefile or in a table format. Statistical parameters as standard deviation of the estimated values is also calculated, but such values are not in the scope of this study.

### 9.2.2.4. Multi-temporal analysis

The estimated grapevine positions enable its multi-temporal analysis which is crucial to track the grapevine vegetative development over time. This way, the analysis is performed by considering the position of each detected grapevine in a given flight campaign, aiming to individually monitor them regarding the various estimated parameters extracted from the multi-sensor data. This analysis is also performed at the vineyard plot scale, as proposed in Pádua et al. (2018).

Multi-temporal analysis is performed by using the detected grapevine estimation in each flight campaign. Using the mask created in **G** in the first flight campaign upon the estimated grapevine vegetation **V** from a flight campaign *k*, it is possible to estimate the different parameters from the available UAV-based data for *n* flight campaigns. Thus, data from flight campaign *k* can be used to evaluate the current vineyard status, by statistically assessing the distribution of the different extracted parameters, and to compare it with other flight campaigns. This enables to observe the grapevines vegetative evolution through the extracted biophysical and geometrical parameters.

### 9.2.3. Grapevine counting accuracy

For accuracy purposes, the number of estimated grapevines was evaluated. This process was conducted by counting the plants in the vineyard plots, in each vine row, and then different cases were evaluated:

1. the total number of estimated grapevines, this value helps to understand the robustness of the method, by considering the total number of grapevines for an analysed vineyard plot;
2. the number of existing plants, by cross-referring the actual number of plants observed in-field with the ones estimated from the method; and
3. the number of missing grapevines, i.e. grapevines that were missing causing a canopy gap in the vine row.

These values are compared at the vineyard plot level and at the row level.

Grapevine detection was evaluated based in true and false positives (TP/FP) which refer to the number of correct/incorrect estimated grapevines as real grapevines and, similarly, true and false negatives (TN/FN) for non-grapevines. For this purpose, different parameters were evaluated (equation presented in Table 9.2), namely:

- precision, the fraction of estimated grapevines that are correctly estimated (TP) rather than wrongly estimated (FP);
- recall, the fraction of grapevines that are correctly detected rather than wrongly estimated;
- false negative rate (FNR), percentage of grapevines falsely classified as being missing;
- $F_1$score, the harmonic mean of precision and recall measures; and

- overall accuracy, considering all correctly estimated grapevines and missing grapevines in all data.

**Table 9.2.** Evaluation parameters in grapevine vegetation classification

| Parameter | Equation |
|---|---|
| Precision | $Precision = \frac{TP}{TP + FP}$ |
| Recall | $Sensitivity = \frac{TP}{TP + FN}$ |
| False Negative Rate | $FNR = 1 - \frac{TP}{TP + FN}$ |
| F1score | $F_1 score = 2\left(\frac{Precision \times Recall}{Precision + Recall}\right)$ |
| Overall accuracy | $Accuracy = \frac{TP + TN}{TP + TN + FP + FN}$ |

### 9.2.4. Data alignment

Data alignment is crucial in multi-temporal analysis to accurately extract individual grapevine parameters with minor alignment errors. Thus, the photogrammetric processing of the UAV-based imagery from the different sensors was evaluated for each vineyard plot in the flight campaigns encompassed in the multi-temporal dataset. The mean error and root mean square error (RMSE) were used. RMSE equation is shown in (3), where $e_i$ is the error of each point in a given direction (X, Y, Z) and $n$ the total number of GCPs. This evaluation can further provide the deviation of the acquired UAV-based imagery from each sensor along the flight campaigns.

$$\mathrm{RMSE} = \sqrt{\frac{\sum_{i=1}^{n} {e_i}^2}{n}} \quad (3)$$

## 9.3. Results

### 9.3.1. Grapevine counting accuracy

Individual grapevine estimation for different plots of the study area is presented in Table 9.3. A perfect agreement was observed in vineyards A, B, D, and F, where the number of estimated grapevines per row matched with the ground-truth values. However, for vineyards C and E, the number of estimated vine rows differed in one in each vineyard plot, which was expectable since in these vine rows there were no grapevines, thus, these missing grapevines were discarded from further validation. The number of estimated grapevine plants differed in two for vineyard C and seven concerning vineyard E. Discarding the plants belonging to the undetected vine rows, the overall agreement was 99.88%, missing solely in nine plants (total: 7786, estimated: 7777).

**Table 9.3.** Number of estimated grapevines when compared to ground truth data observed in-field.

| Vineyard plot | Number of grapevines | | Percentage (%) |
|---|---|---|---|
| | Observed | Estimated | |
| A | 1436 | 1436 | 100.00 |
| B | 234 | 234 | 100.00 |
| C | 1369 | 1367 | 99.85 |
| D | 1238 | 1238 | 100.00 |
| E | 2279 | 2272 | 99.69 |
| F | 1230 | 1230 | 100.00 |
| Total | 7786 | 7777 | 99.88 |

Figure 9.4 presents the estimated grapevines in each vineyard plot, along with the corresponding numerical assessment shown in Table 9.4. The precision rate was above 99% (mean value of 99.59%), reaching 100% in vineyard B. Regarding recall, also quantifying FN; a mean value of 98.06% was obtained, being the lowest recall value obtained in vineyard C (93.98%). These cases reflect the number of grapevines that were incorrectly classified as missing grapevine (FN). Consequently, FNR was approximately 3% (vineyards C, D and F), while the mean FNR reached 1.94%. In what concerns the harmonic mean of precision and recall metrics (F1score) its mean value is above 98%. The lower value for this metric was observed for vineyard plot F (96.75%), in opposition to vineyards A and B (99%), which had the better ranks. For the remaining plots, F1score was within the range of 97-98%. Focusing on accuracy metrics, an overall value of 98% was obtained, with minimum occurrences above 96%. These results seem to represent a good overall agreement concerning individual grapevine classification.

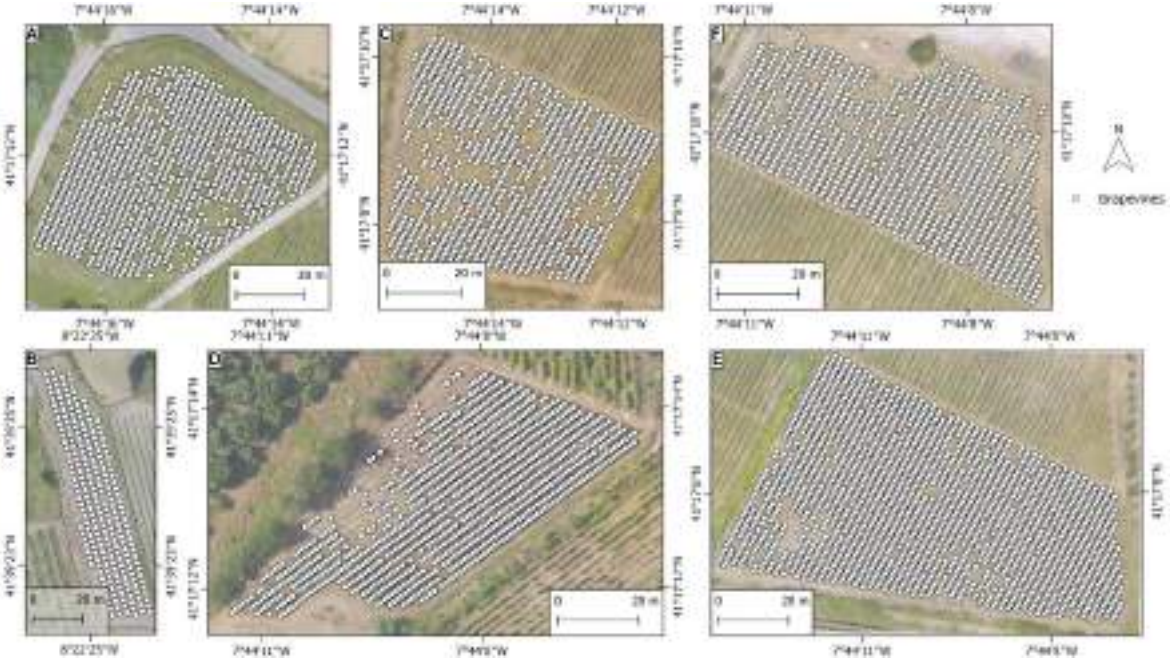

**Figure 9.4.** Estimated grapevine plants in the validation dataset. The uppercase letter in the upper left corner represents each vineyard plot ID. Coordinates in WGS 84 (EPSG: 4326).

**Table 9.4.** Evaluation of the proposed method in the grapevine's classification for the following parameters: precision, recall, F1score, false negative rate (FNR) and overall accuracy (OA).

| Vineyard plot | Precision (%) | Recall (%) | F1score (%) | FNR (%) | OA (%) |
|---|---|---|---|---|---|
| A | 99.22 | 98.71 | 98.96 | 1.29 | 98.33 |
| B | 100.00 | 100.00 | 100.00 | 0.00 | 100.00 |
| C | 100.00 | 93.98 | 96.90 | 6.02 | 95.17 |
| D | 99.90 | 96.62 | 98.23 | 3.38 | 97.09 |
| E | 99.71 | 97.67 | 98.68 | 2.33 | 97.58 |
| F | 99.00 | 97.07 | 98.03 | 2.93 | 96.75 |
| Mean | 99.64 | 97.34 | 98.47 | 2.66 | 97.49 |

## 9.3.2. Multi-temporal vineyard monitoring

Since the used methods anticipated a multi-temporal context application, supported through different photogrammetric outcomes from which individual grapevine parameters can be extracted, an analysis using UAV-based RGB, multispectral, and TIR imagery was conducted in vineyards A and B. Moreover, for this type of application, it is important to ensure a reliable imagery alignment, which was also evaluated.

### 9.3.2.1. Data alignment

The spatial accuracy of each orthorectified outcomes, generated from the photogrammetric processing, were evaluated in their mean spatial deviations (X, Y, Z) and mean RMSE. In this case, the UAV-based imagery acquired from RGB, multispectral and TIR sensors, with different spatial resolutions, were used along with georeferenced GCPs. The projection errors obtained in vineyards A and B for each sensor are presented in Table 9.5, for each flight campaign. Overall, the errors are lower for RGB, below 5 cm; followed by multispectral imagery, with errors ranging from 5 cm to 10 cm; and when processing TIR imagery higher error rates were obtained ranging from 10 cm to 20 cm. Pixel projection error was similar in all sensors, i.e., from approximately 0.5 to 1 pixel, being, generally, higher for RGB imagery. The overall mean RMSE values in vineyard A were 3.61 cm for the RGB imagery, 7.35 cm for the multispectral imagery, and 15.50 cm for the TIR imagery, while in vineyard B were, respectively, 2.24 cm, 4.84 cm, and 14.34 cm. The mean pixel projection error of all campaigns was lower than one pixel in all sensors; it was higher in the RGB, followed the multispectral and TIR imagery.

**Table 9.5.** Mean error, root mean square error (RMSE) and projection errors for the alignment of each project during photogrammetric processing in both analysed vineyard plots, at each flight campaign (F#).

| Vineyard plot | Sensor | F# | Mean (cm) | RMSE (cm) | Projection error (pixel) |
|---|---|---|---|---|---|
| A | RGB | F1 | -0.19 | 3.15 | 1.30 |
| | | F2 | -0.19 | 4.55 | 1.21 |
| | | F3 | 0.08 | 3.65 | 0.57 |
| | | F4 | 0.06 | 3.09 | 0.58 |
| | MSP | F1 | 0.78 | 5.47 | 0.71 |
| | | F2 | -0.40 | 5.90 | 0.43 |
| | | F3 | 0.41 | 8.22 | 1.25 |
| | | F4 | 0.24 | 9.82 | 0.51 |
| | TIR | F1 | 0.72 | 12.39 | 0.65 |
| | | F2 | -0.98 | 13.34 | 0.54 |
| | | F3 | 3.82 | 19.38 | 0.74 |
| | | F4 | 4.70 | 16.87 | 0.90 |
| B | RGB | F1 | -0.37 | 3.68 | 1.30 |
| | | F2 | 0.02 | 2.20 | 0.63 |
| | | F3 | 0.00 | 1.73 | 0.57 |
| | | F4 | -0.03 | 1.81 | 0.57 |
| | | F5 | -0.01 | 1.76 | 0.58 |
| | MSP | F1 | -0.63 | 4.66 | 0.50 |
| | | F2 | 0.24 | 4.38 | 0.85 |
| | | F3 | -1.16 | 3.84 | 0.93 |
| | | F4 | -0.76 | 4.99 | 0.53 |
| | | F5 | 0.11 | 6.35 | 0.75 |
| | TIR | F1 | 2.84 | 11.30 | 0.47 |
| | | F2 | 3.14 | 16.52 | 0.76 |
| | | F3 | 2.35 | 15.55 | 0.66 |
| | | F4 | 2.60 | 14.02 | 0.59 |
| | | F5 | 1.55 | 14.30 | 0.77 |

#### 9.3.2.2. Vineyard plot A

The applied method enables the estimation of vegetation (grapevine and. inter-row vegetation) present in the vineyard plot. In between the flight campaigns, an increment of grapevine vegetation area was observed from the first to the second flight campaign (from 675 $m^2$ to 782 $m^2$, corresponding to a 16% increase). From the second to the third flight campaign, there was a decline of 35% (-272 $m^2$). For the remaining flight campaigns, the grapevine vegetation area remained unchanged (around 500 $m^2$). The same behaviour was observed in grapevine volume, where 877 $m^3$ were estimated in the first flight campaign, 939 $m^3$ (growth of 7%) for the second flight campaign, followed by 619 $m^3$ (decline of 34%) and 610 $m^3$ (decline of 1%), for the third and fourth flight campaigns, respectively. Focusing in the inter-row vegetation, its area declined from the first to second flight campaigns (from 1221 $m^2$ to 6 $m^2$), and then remained unchanged on subsequent flights (lower than 90 $m^2$).

Figure 9.5 provides the distribution of the mean values of the different parameters extracted from the estimated grapevine plants. The flight campaigns were carried with a significant vegetation development from fruit set to harvest. This way, the height distribution in the different flight campaigns (Figure 9.5a) did not varied significantly, starting with a mean height of 1.23 m, in the first flight campaign, and stabilizing around 1.13 m, in the remaining campaigns. In what concerns the grapevine area and volume (Figure 9.5b and c) both parameters presented a similar behaviour, declining from the first to the last flight campaign. Grapevines mean area starts with 0.44 $m^2$ in the first campaign and a progressive decrease can be observed until the last campaign, in which grapevine mean area ends up with 0.32 $m^2$. In terms of the mean grapevine canopy volume, it is 0.69 $m^3$ in the first flight campaign, 0.58 $m^3$ in the second one and 0.50 $m^3$ in the remaining flight campaigns. Considering the distribution of the NDVI values (Figure 9.5d), a decline was verified when comparing the values of the previous campaigns sequence in which 0.80, 0.73, 0.66, and 0.55 of grapevine mean NDVI were respectively reached. Regarding the parameters extracted from the thermal infrared imagery, both grapevine temperature and CWSI (Figure 9.5e and f) presented distinct distributions. The temperature values were lower in the first flight campaign and higher in the third flight campaign. Despite the mean temperature variability through the flight campaigns, CWSI distribution is similar.

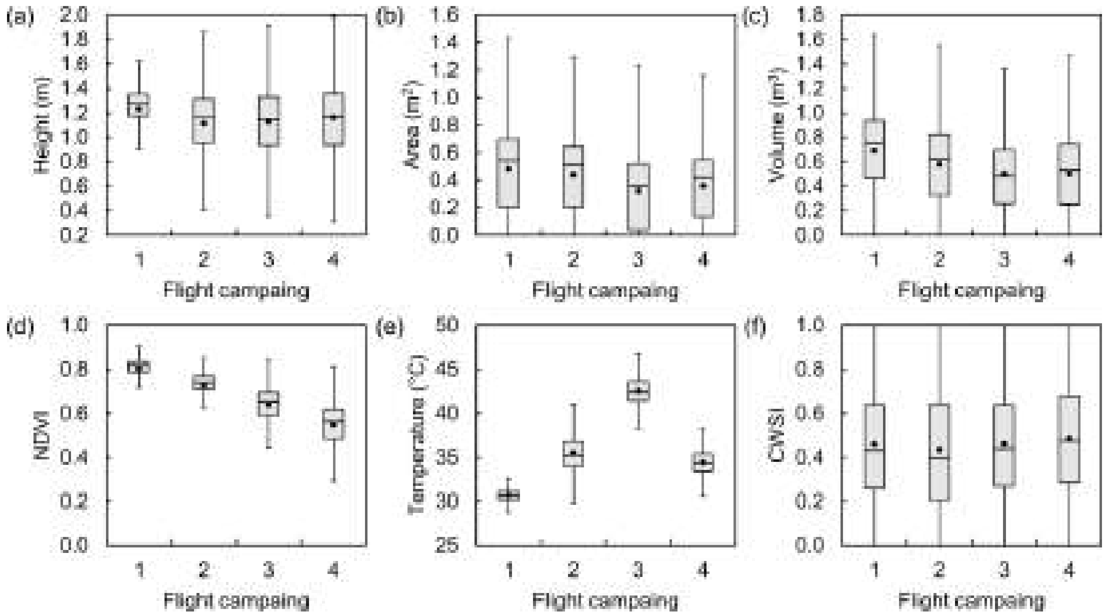


**Figure 9.5.** Boxplots of height (a), area (b), volume (c), normalized difference vegetation index (d), land surface temperature (e), and crop water stress index (f) of each flight campaign in vineyard A. Mean values are marked with •.

Figure 9.6 presents the main parameters extracted for the estimated grapevines. The grapevine's height distribution (Figure 9.6a) suffered a decline along the flight campaigns. In fact, 87% of estimated heights were higher than 1.0 m in the first flight campaign, falling to 77% in the second flight campaign, 64% in the third and 72% in the fourth flight campaign. Regarding plants with heights lower 0.5 m, no estimates were presented in the first flight campaign, whereas in the following campaigns this number represented 0.3%, 8% and 2%, of the total estimates. Individual grapevine canopy volume (Figure 9.6b) presented a similar trend. In the first flight campaign, 53% of the grapevines showed a volume greater than 0.75 $m^3$, while in the following flight campaigns only 39%, 24% and 19% where greater than 0.75$m^3$. Regarding plants with a volume greater than 1 $m^3$, they represented 19%, 10%, 6% and 4% of the estimated grapevines. Considering individual grapevine NDVI values (Figure 9.6c) bigger than 0.7, a total of 85% higher were identified in the first flight campaign, 60% in the second, 38% in the third, and 16% in fourth flight campaign. Focusing on the CWSI (Figure 9.6d), 75% of the grapevine plants were lower than 0.6 in the first three flight campaigns, while in the last flight campaign this value is 70%.

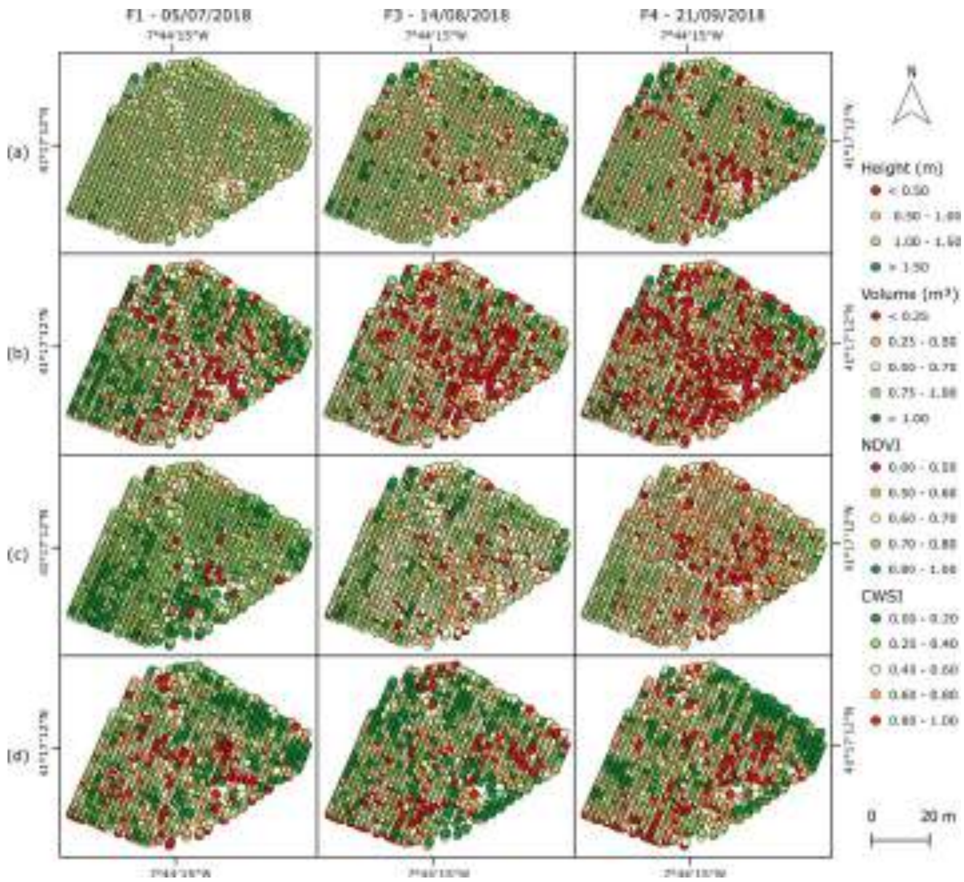


**Figure 9.6.** Estimated grapevine parameters in vineyard A, for three flight campaigns (DD/MM/YYYY): (a) height; (b) volume; (c) normalized difference vegetation index; (d) crop water stress index.

### 9.3.2.3. Vineyard plot B

In what concerns vineyard B, a broader period was analysed (from May to October 2018), encompassing most of the vineyard vegetative development, from flowering to harvesting. A growth trend of the grapevine vegetation area and volume is observed across the first four flight campaigns (growth of 218%, from 262 $m^2$ to 833 $m^2$ and 463%, from 339 $m^3$ to 1301 $m^3$). In the last campaign, a decline of 15% (–128 $m^2$) in area and 21% (–401 $m^3$) in volume was verified. From the second to third flight campaigns, there was a canopy management operation (leaf removal), due to the smaller growth area in between these flights (20% and 101 $m^2$). As for inter-row vegetation, this value increases until July (from 34 $m^2$ to 546 $m^2$) and decreases in August (34 $m^2$), whit a small growth in October (to 83 $m^2$).

The estimation of the individual grapevines position in the vineyard enabled to estimate several parameters. Their distribution is presented in Figure 9.7. Height distribution (Figure 9.7a) was lower in first flight campaign with a mean value of 1.24 m, which growth until the forth flight campaign and declined in the last one. Similar trends are observable in other geometrical parameters as area and volume (Figure 9.7b and c), as well as in the NDVI (Figure 9.7d). Indeed, from the first to the second flight campaigns, a significant growth was registered. The mean grapevine area increased almost to the double (from 1.10 $m^2$ to 2.12 $m^2$), and the mean grapevine volume increased 193% (from 1.38 $m^3$ to 4.04 $m^3$). In what respects the grapevines NDVI values, the mean value ranged from 0.56, in the first flight campaign, to 0.84 in the second, 0.86 in the third, 0.89 in the fourth and declined to 0.76 in the last flight one. As for LST (Figure 9.7e) and CWSI (Figure 9.7f), values a different trend was observed, the first flight campaign presented a higher temperature than the remaining ones (approximately 10 °C higher), while CWSI values spanned towards higher values in the first flight campaign and lower values in remaining flight campaigns, where most of the data is located below 0.5.

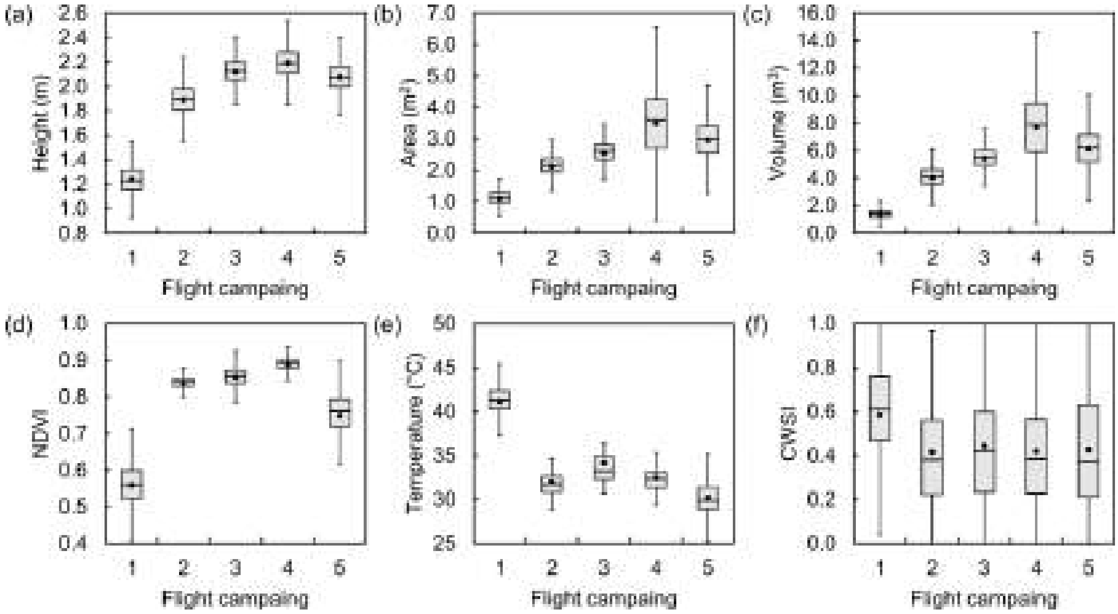


**Figure 9.7.** Boxplots for height (a), area (b), volume (c), normalized difference vegetation index (d), land surface temperature (e), and crop water stress index (f) of each flight campaign in vineyard B. Mean values are marked with •.

The individual grapevine values estimated for each parameter in the most representative flight campaigns is presented in Figure 9.8. From first to the reaming flight campaigns (Figure 9.8a, b and c), an overall numerical increase of assessed characteristics can be noted, while a decline from the fourth to fifth flight campaign is better observable in the NDVI, rather than with height or volume. Most of the height values (Figure 9.8a) in the first flight campaign are below 1.5 m, whereas in the remaining flight campaigns those are higher than 1.5 m. As for grapevine canopy volume (Figure 9.8b), in the first flight campaign all plants show a value below 4 $m^3$, estimations made upon data from the second flight campaign point out a rate of 57% of grapevine plants greater than 4 $m^3$, being above 94% in the remaining flight campaigns. NDVI values (Figure 9.8c) are lower than 0.7 in the first flight campaign (0.56 mean value) and higher than it in the remaining flight campaigns, excluding the last one where 82% of the grapevines were higher than 0.7. For CWSI, 53% of the grapevines presented a value higher than 0.6 in the first flight campaign, but in the remaining campaigns it is lower, as an example, it represents 21% and 28%, respectively, in the fourth and fifth campaigns.

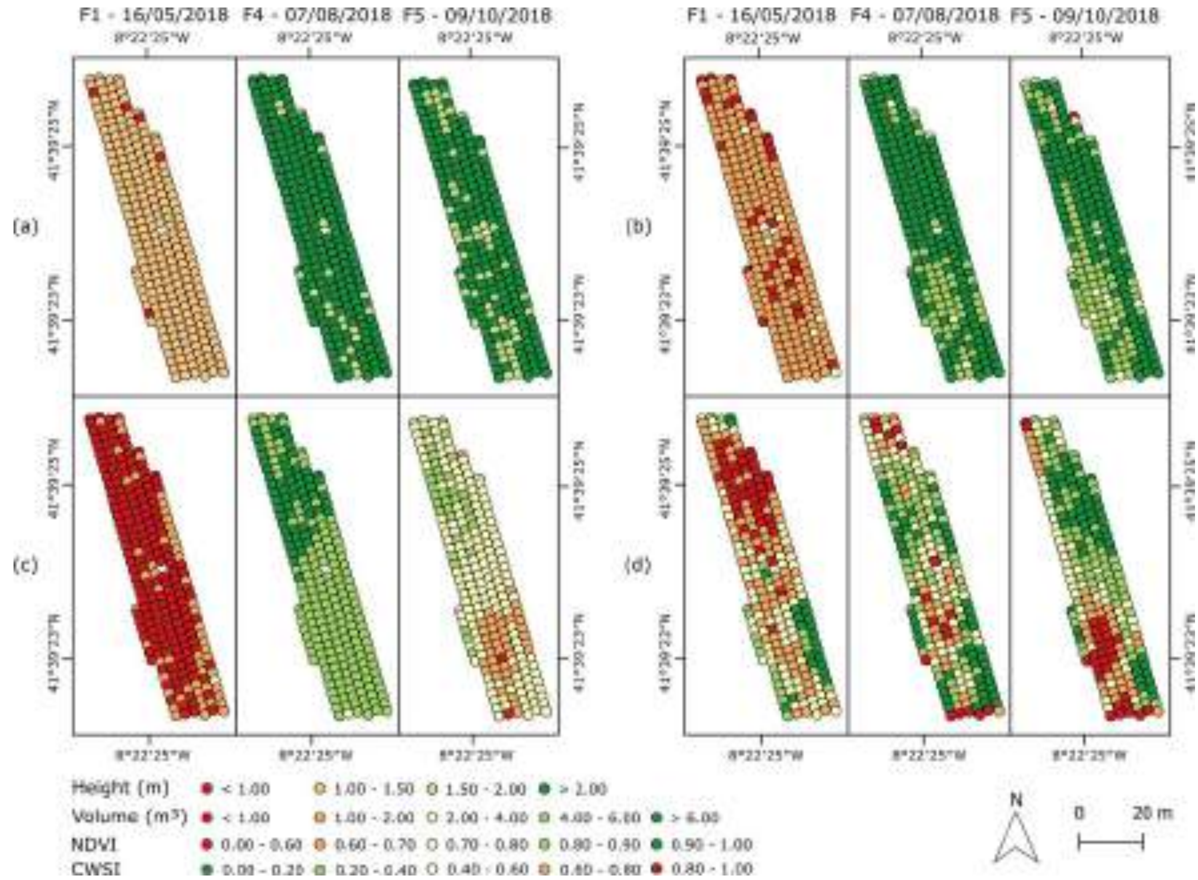


**Figure 9.8.** Estimated grapevine parameters in vineyard A, for three flight campaigns (DD/MM/YYYY): (a) height; (b) volume; (c) normalized difference vegetation index; (d) crop water stress index.

## 9.4. Discussion

### 9.4.1. Grapevine counting accuracy

The results presented in Section 9.3.1 document the method's effectiveness in the individual grapevine estimation using the six vineyard plots analysed. As for the number of grapevines presented in each vineyard plot (Table 9.3) the method showed 100% accuracy for vineyard plots A, B, D and F. However, for vineyard plots C and E, there was an under estimation in the number of grapevines, in both cases, due to the lack of one plant per vine row. Still, a mean accuracy value of 99.88% was achieved. This is related with the way that the vine rows were estimated, the distance of the rows were smaller than its ground-truth, possibly related to the automatic vine row orientation used during their estimation. Furthermore, as stated in the results section, there were two vine rows that were not detected, one in vineyard plot C (three grapevines) and another in vineyard D (five grapevines). However, since there were no grapevines present in those plots, they were discarded from this evaluation procedure.

As for grapevine identification, the results from the performed evaluation were slightly lower (Table 9.4), which is related with FP and FN estimations for grapevines. Nevertheless, a mean overall accuracy of 97.5% was achieved. It can be stated that the method tends to overestimate grapevines rather than underestimate, since more FN cases were identified (mean of 2.0% and mean of 0.4% FP). In vineyard A, the percentage of FP and FN was 1.6% representing, respectively, 8 and 10 cases. The higher number of FP was verified in vineyard F with 10 cases (1%), whereas the higher number of FN was reached in vineyard E with 49 cases (2.4%). However, vineyard F had the higher percentage of FN cases with 3% (30 occurrences). Cases of grapevines classified as being missing (FP) can be justified by erroneous three-dimensional reconstruction of the surveyed vineyard plots. Increasing the imagery overlap in the mission plan stage can help to mitigate this issue, since more common tie points will be found in correspondent images. The grapevine plants from the commercial vineyard (vineyard plot B) were correctly estimated, being this plot only composed by seven vine rows and with only two missing grapevine plants. In Primicerio et al. (2017), this issue was addressed by evaluating a total of 211 missing plants (incidence of 9.4%), in which the parameter found with most correlation was the grapevine area. Different area thresholds where considered, based in the cardinality of each cluster attributed to grapevine plants, wherein lower values showed to be more suitable for missing plants discrimination, but inducing the FP number growth, while higher values result in the inverse behaviour. In Matese and Di Genaro (2018), the results demonstrated 80% accuracy in missing plants detection with the application of their method. Authors stated that FP results (plants estimated as missing plant) were related to their low vegetative development, while FN results (missing plant classified as plant) were related to the high presence of weeds and overlap of adjacent plants. However, neither of these studies considered height properties. In De Castro et al. (2018) an overall accuracy of 95.3% was obtained in the analysis of three vineyard plots, in North-eastern Spain, at two different epochs (July and September). Similarly, to this study, according to the authors most of misclassification cases were related to grapevines lower vegetative development (thin branches and less leaves) which led to issues in the 3D canopy reconstruction through photogrammetric processing. Regarding FN cases, it can be justified by the growth of adjacent grapevines which tends to cover missing spots in the wires, making difficult to estimate missing plants. This way, as a future direction, machine learning classification should be considered to detect the number of missing grapevines. Moreover, as stated by Matese and Di Genaro (2018), by selecting an anticipated period to conduct this type of survey would increase the results accuracy, by having plants with less vegetative development, which would avoid the presence of adjacent grapevine vegetation in missing plant areas.

### 9.4.2. Data alignment

Since one of the main goals of this study is to extract grapevine properties from different outcomes through photogrammetric processing of UAV-based imagery from different sensors, a correct data alignment must be ensured to mitigate data alignment errors. Aiming to reduce geolocation errors from few metres to some centimetres (D. Turner et al., 2011). In Turner et al. (2014) the same tendency was inferred, when comparing with results obtained in this study. More specifically, the overall RMSE values were approximately 1.9 cm for RGB imagery (1 cm GSD), 6.4 cm for multispectral imagery (3 cm GSD), and 17.8 cm for TIR imagery (10 cm GSD). In their study, the authors used a higher number of GCPs along with a lower flight height and almost half of spatial resolution used in this study. The need of GCPs for multi-sensor data alignment will be mitigated by the technological development of sensors by combining visible, multispectral and TIR data into a single sensor, this is the case of the MicaSense Altum (MicaSense Inc., Washington, United States of America) which provides radiometrically corrected blue, green, red, red edge, NIR spectral bands along with TIR imagery. This way, in a single UAV flight all data is acquired and photogrammetric processing can be achieved in a single project.

### 9.4.3. Multi-temporal vineyard monitoring

By analysing the results obtained through the method application in both vineyards A and B (Sections 9.3.2.2 and 9.3.2.3) the spatial grapevine variability is noticeable. Furthermore, the multi-temporal analysis enabled to track the changes throughout the analysed periods.

In what concerns the experimental vineyard (vineyard A), it presented a higher incidence of missing grapevines, which is associated with the occurrence of phytosanitary problems and to the presence of different grapevine varieties wherein a higher data variability is clearly visible (Figure 9.6). Areas with better grapevine overall status are located in the upper right and bottom left parts of the vineyard. Higher NDVI values and grapevine volume were detected in those areas throughout the flight campaigns, being this more notorious in all flight campaigns for the estimated grapevine volume and in the first three flight campaigns for NDVI. With respect to CWSI, only in the first and last two flight campaigns highlighted this behaviour. On the other hand, the southern central part showed the lower results. The grapevines in this region presented lower volume—particularly in the last two flight campaigns—, along with higher CWSI values (potential water stress) and lower NDVI values.

The commercial vineyard plot (vineyard B) presented a high vegetative dynamic over the analysed period, its parameters growth throughout the flight campaigns and declined after the harvest season (Figure 9.7). Its geometrical features (height, area, and volume) along with NDVI showed a higher development from the first to second flight campaigns. These results are related to both phenological stages and training systems implemented in the Vinho Verde wine region. This vineyard presented overall good results as confirmed by the estimated grapevine values in the flight campaigns (Figure 9.8). The northern part presented higher grapevine volume, when analysing each flight campaign, while for NDVI this was only verified in the last two campaigns. The southern part presented some water stress signs (Figure 9.8d) in the last two flight campaigns, along with lower grapevine volume verified all flight campaigns, lower NDVI values were only observed in the last flight campaign. Regarding CWSI, the inferior grapevine vegetative development verified in the first flight campaign led to the estimation of potential water stress in the upper part of the vineyard, while in the last flight campaign the higher CWSI agreed with the lower NDVI values.

When comparing the commercial (vineyard B) and the experimental (vineyard A) vineyard, the former obtained better results in almost all parameters. A higher spatial heterogeneity was verified in vineyard A, while vineyard B presented a more homogeneous development, as can be seen when analysing the grapevine canopy volume and NDVI. However, some similar trends were detected in both vineyards, an overall decline of the NDVI values in the last flight campaigns and an agreement between NDVI with the estimated grapevine volume and with the CWSI values was observed. The decline of NDVI in the last flight campaigns can be related to the leaf senescence and, consequently, its discoloration (Junges et al., 2017, 2019). The relationships among the NDVI and volume relationships were verified in other studies (A. Matese et al., 2019) that shown that both of these parameters are related with LAI, which, in fact, is also verified in this study.

Grapevines located in the south parts (first plant of the rows) of the analysed vineyards presented potential water stress in the CWSI, an observation that gains meaning in the last two flight campaigns of vineyard B and in the first, third and fourth flight campaigns in vineyard A. This can be considered as outliers, since higher temperatures are observed due to heat advection from the soil in proximity of the edges of the rows to the grapevine canopy, which can affect in a significant manner the air temperature, with an increase of the loss of water by evapotranspiration (Yunusa et al., 2004). These results corroborated with Tucci et al. (2019) were external rows in a terrace vineyard presented higher temperatures due to solar exposition and shadowing effects when compared with internal vine rows. Although the individual grapevine temperature is estimated, this parameter shown to be ineffective to be evaluated in a multitemporal analysis. It is useful to understand the global temperature context in the flight campaign day. The CWSI trends shown a more stabilized distribution since this index represents a normalization throughout flight campaigns. Moreover, other TIR-based indices can be computed, as it is the case of stomatal conductance indices Ig and I3 (Jones, 1999), which, respectively, implicated in increases with stomatal conductance and correlates with stomatal resistance. The same applies to other multispectral-based vegetation indices and to hyperspectral data, as long as it comes in an orthorectified format. Usually, published studies resort to NDVI to produce vigour maps and use that information to improve the decision support at the vineyard plot scale (Campos et al., 2019; Khaliq et al., 2019; J. Primicerio et al., 2015). The approach proposed in this study provides a more incisive analysis. Multi-sensor parameters are extracted at the plant level, and are not exclusively relying on a qualitative analysis.

## 9.5. Conclusions

This study explores the usage of UAV-based photogrammetric outcomes to extract individual grapevine geometrical and biophysical parameters within vineyard plots. Missing plants and other vegetation are detected but not considered to perform multi-temporal analysis over a series of flight campaigns. Three different types of sensors (RGB, multispectral and TIR) were used. By estimating vine rows and, the individual position of each plant, several parameters can be extracted at the plot level, namely the: number of vine rows; number of plants; number of missing plants and grapevine vegetation area; and at the plant level the: position; length; width; area; volume; vigour (driven from NDVI); temperature from TIR and water status (driven from CWSI). The two multi-temporal analysis conducted in the two different vineyards presented in this study confirmed the method’s suitability for plant-specific analysis, allowing to assess the different estimated parameters and to establish relationships among them and between flight campaigns. This way, the methods employed in this study enable an overview of the current status of the grapevine plants and the monitoring of their evolution over time. The estimated geometrical and biophysical parameters can significantly help farmers and/or winemakers understanding the current vineyard overall status and can be used as a decision support tool to apply treatments in certain plants and to observe their response with multi-temporal analysis, helping to improve grapevines health. Moreover, it can be used to compare growth seasons from different years, by extending the flight campaigns.

The potential of the method can be extended for different applications, it can help in the decision support, by means of grapevine growth and status evaluation, and the individual grapevine water status estimation. Moreover, the different extracted parameters can be used to create datasets for supervised and unsupervised classification methods for disease detection and to improve the results in the detection of missing grapevines. The extracted individual grapevine parameters can be used for computation of prescription maps for individual grapevine treatment in PV plant-specific applications and to estimate individual grapevine production. The topographical data produced from the photogrammetric processing along with the position of each grapevine and its estimated parameters can be used to reproduce a 3D virtual vineyard environment. As such, this information can be used in augmented reality applications for easier vineyard in-field inspections.

## Acknowledgements

The authors would like to thank Miguel Fonseca for providing the photographs of the vineyard.

## Funding

Financial support provided by the FCT-Portuguese Foundation for Science and Technology (SFRH/BD/139702/2018) to Luís Pádua.

# Chapter 10.

## Conclusions and future perspectives

This thesis presents a series of contributions in the fields of computer vision, remote sensing, and precision agriculture. The multidisciplinary nature of the conducted research motivated the proposal of advances in different areas converging the novel approaches to assist farmers in decision support. This was reached allying data processing algorithms with very high resolution remote sensed data from multiple sensors, improving precision agriculture practices. The presented research work can be divided into two categories: (1) the proposal of new methods and approaches for multi-temporal data processing; and (2) the application of those methods to extract/estimate crop-related parameters.

The work chain was designed to answer the research questions (RQ):

**RQ1:** "Can multi-temporal data from multi-sources be combined to provide better management of agricultural and forest crops, in particular in vineyards and chestnut plantations?"

To answer this question, several algorithms/approaches were developed for the specific purpose of the detection of grapevines and chestnut trees which suffered an iterative process with the work progress. In fact, more features were added over time in an incremental logic, making it possible to respond to identified needs of farmers or winegrowers. The segmentation methods presented in Chapters 4 and 6 rely in the most cost-effective approach regarding UAV data acquisition, since it only relies in imagery from RGB sensors. Another aspect to consider is data extraction capabilities for multi-temporal analysis that was set to provide parcel-level and plant-level estimations. Moreover, the methods require few parameterization (depending on the level of analysis) and revealed potential to be applied in other crops with similar plantation styles (in rows or spaced).

By relying in the obtained results, it can be stated that multi-sensor data acquisition from unmanned aerial systems (UAVs) poses as an important process to substantially contribute for an improvement on crop analysis. The data obtained from each sensor proved to be useful for different or multiple tasks:

- the photogrammetric processing of RGB imagery leads to the computation of digital elevation models (DEM), which, in turn, can be used to detect crops and to retrieve geometrical features, this is particularly noticeable in crop height estimation on Chapter 4, grapevine volume and height estimation in Chapters 7 and 9, in a multi-temporal context can help to acknowledge the crop vegetative growth or decline;

- when using multispectral imagery for vegetation monitoring, the spectral response from other wavelengths can be considered (outside the visible spectrum)—particularly the near infrared region, where spectral differences among different crops and among crops with different health/vigour status are noticeable—this opens the possibility to monitor crops at an individual scale to estimate parameters that correlate with their biophysical status, in a multi-temporal context, enabling to extend the use of UAV multispectral data to understand the temporal dynamics of the crops along a growing season, to detect potential problematic areas (Chapters 8 and 9) and to estimate potential phytosanitary issues (Chapter 5);
- the use of thermal infrared imagery can help into the assessment of crop water status, which in a multi-temporal approach, is crucial for the maintenance and improvement or crops health status, and to provide a better water management efficiency (Chapter 9);
- when comparing data from different sensors, it is possible to notice common points highlighted areas, where crops tend to be less and more vigorous, as the comparison of a multispectral outcome with thermal and geometrical data products performed in Chapter 8, but their complementarity usage provides a wider range of possibilities in both crop monitoring (Chapter 9) and disease detection.

So, it was possible to answer to the **RQ2**:

"Can the agriculture and forest management process be automated based on the developed algorithms specifically for the extraction of valid information from data acquired from different types of sensors?"

In fact, the automatization process that was achieved in the findings documented in the presented study, allows to save time and resources spent in field inspection activities by covering and analysing, in a faster and efficient manner, wider areas and providing warnings to only certain parts of the terrain (Chapter 8) or certain trees (Chapters 4 and 5). Thus, the ability of the developed algorithms to automatically detect anomalous situations is a key factor to reduce the time required to perform interventions and to allocate the necessary human resources. This way, it is possible to reach a controlled monitoring of problems affecting cultures, with the economic benefits that come from it, as well as the monitoring of vegetative development.

A general methodology for UAV-based high-resolution multi-temporal data analysis can be withdrawn from this work. The methodology relies in five main steps: (1) UAV data acquisition, by planning multi-temporal campaigns for crucial stages of the growing season and ensuring the data alignment/co-registration, among sensors and flight campaigns; (2) data pre-processing, by means of photogrammetric processing or using a specific software for UAV data processing, depending on the used sensors; (3) vegetation segmentation, for an accurate detection of the crop or tree under analysis; (4) parameters extraction, depending on the data availability, can be adapted. Data from different sensors is not always needed, for example, the usage of thermal infrared imagery can be discarded when the weather is not propitious of water stress; and finally; (5) data from different periods will enable multi-temporal analysis through comparison over time. This methodology can be implemented in an agricultural management system to improve the support to the decision-making process.

Some paths can be taken as future research and development. The methods proposed in this thesis can be merged into a specific software for multi-temporal data analysis of a given crop providing the use with semi-automatic ways for quicker crop parameters estimation, and to adjust the results for more precise outcomes. The study of the correlation of the crop yields with parameters estimated from the UAV-based data products, can be of special interest for the wine section of the Douro Demarcated Region. This kind of approach can lead to a better harvest planning and resources allocation. In the field of crop phytosanitary monitorization, the aerial spectroscopy was not explored, in this work, and the availability of UAV hyperspectral sensors allows to cover a wider range of the electromagnetic spectrum, providing high spectral, spatial and temporal resolutions, supplying ways for early disease detection.

# References

Abdullahi, H. S., Mahieddine, F., & Sheriff, R. E. (2015). Technology Impact on Agricultural Productivity: A Review of Precision Agriculture Using Unmanned Aerial Vehicles. In P. Pillai, Y. F. Hu, I. Otung, & G. Giambene (Eds.), *Wireless and Satellite Systems: 7th International Conference, WiSATS 2015, Bradford, UK, July 6-7, 2015. Revised Selected Papers* (pp. 388–400). Springer International Publishing. https://doi.org/10.1007/978-3-319-25479-1_29

Aber, J. S., Marzolff, I., & Ries, J. (2010). *Small-Format Aerial Photography: Principles, Techniques and Geoscience Applications*. Elsevier Science. https://books.google.pt/books?id=TX2BsDMnLhEC

Adão, T., Hruška, J., Pádua, L., Bessa, J., Peres, E., Morais, R., & Sousa, J. J. (2017). Hyperspectral Imaging: A Review on UAV-Based Sensors, Data Processing and Applications for Agriculture and Forestry. *Remote Sensing*, *9*(11), 1110. https://doi.org/10.3390/rs9111110

Aebi, A., Schönrogge, K., Melika, G., Alma, A., Bosio, G., Quacchia, A., Picciau, L., Abe, Y., Moriya, S., Yara, K., Seljak, G., & Stone, G. N. (2006). Parasitoid Recruitment to the Globally Invasive Chestnut Gall Wasp Dryocosmus kuriphilus. In K. Ozaki, J. Yukawa, T. Ohgushi, & P. W. Price (Eds.), *Galling Arthropods and Their Associates* (pp. 103–121). Springer Japan.

Agüera-Vega, F., Carvajal-Ramírez, F., & Martínez-Carricondo, P. (2017). Assessment of photogrammetric mapping accuracy based on variation ground control points number using unmanned aerial vehicle. *Measurement*, *98*, 221–227. https://doi.org/10.1016/j.measurement.2016.12.002

Akar, Ö. (2016). *The Rotation Forest algorithm and object-based classification method for land use mapping through UAV images: Geocarto International: Vol 33, No 5*. https://www.tandfonline.com/doi/abs/10.1080/10106049.2016.1277273

Akar, Özlem. (2018). The Rotation Forest algorithm and object-based classification method for land use mapping through UAV images. *Geocarto International*, *33*(5), 538–553. https://doi.org/10.1080/10106049.2016.1277273

Akcay, H., Kaya, S., Sertel, E., & Alganci, U. (2019). Determination of Olive Trees with Multi-sensor Data Fusion. *2019 8th International Conference on Agro-Geoinformatics (Agro-Geoinformatics)*, 1–6.

Albetis, J., Duthoit, S., Guttler, F., Jacquin, A., Goulard, M., Poilvé, H., Féret, J.-B., & Dedieu, G. (2017). Detection of Flavescence dorée Grapevine Disease Using Unmanned Aerial Vehicle (UAV) Multispectral Imagery. *Remote Sensing*, *9*(4), 308. https://doi.org/10.3390/rs9040308

Albetis, J., Jacquin, A., Goulard, M., Poilvé, H., Rousseau, J., Clenet, H., Dedieu, G., & Duthoit, S. (2019). On the Potentiality of UAV Multispectral Imagery to Detect Flavescence dorée and Grapevine Trunk Diseases. *Remote Sensing*, *11*(1), 23. https://doi.org/10.3390/rs11010023

Alderfasi, A. A., & Nielsen, D. C. (2001). Use of crop water stress index for monitoring water status and scheduling irrigation in wheat. *Agricultural Water Management*, *47*(1), 69–75. https://doi.org/10.1016/S0378-3774(00)00096-2

Al-Samarrai, G., Singh, H., & Syarhabil, M. (2012). Evaluating eco-friendly botanicals (natural plant extracts) as alternatives to synthetic fungicides. *Annals of Agricultural and Environmental Medicine*, *19*(4).

Ambrosia, V. G., Wegener, S., Zajkowski, T., Sullivan, D. V., Buechel, S., Enomoto, F., Lobitz, B., Johan, S., Brass, J., & Hinkley, E. (2011). The Ikhana unmanned airborne system (UAS) western states fire imaging missions: From concept to reality (2006–2010). *Geocarto International*, *26*(2), 85–101. https://doi.org/10.1080/10106049.2010.539302

Ambrosini, I., Gherardi, L., Viti, M. L., Maresi, G., & Turchetti, T. (1997). Monitoring diseases of chestnut stands by small format aerial photography. *Geocarto International*, *12*(3), 41–46. https://doi.org/10.1080/10106049709354595

Anderson, K., & Gaston, K. J. (2013). Lightweight unmanned aerial vehicles will revolutionize spatial ecology. *Frontiers in Ecology and the Environment*, *11*(3), 138–146. https://doi.org/10.1890/120150

Anselin, L. (1995). Local indicators of spatial association—LISA. *Geographical Analysis*, *27*(2), 93–115.

Anselin, L. (2014). *Modern spatial econometrics in practice: A guide to GeoDa, GeoDaSpace and PySAL*. Geoda Press LLC.

Anselin, L., Syabri, I., & Kho, Y. (2006). GeoDa: An Introduction to Spatial Data Analysis. *Geographical Analysis*, *38*(1), 5–22. https://doi.org/10.1111/j.0016-7363.2005.00671.x

Regulamento nº 1093/2016, Pub. L. No. Regulamento nº 1093/2016, Diário da República n.º 238/2016, Série II 1093/2016 36613 (2016). https://dre.pt/application/conteudo/105362832

Asseng, S., Ewert, F., Martre, P., Rötter, R. P., Lobell, D. B., Cammarano, D., Kimball, B. A., Ottman, M. J., Wall, G. W., White, J. W., Reynolds, M. P., Alderman, P. D., Prasad, P. V. V., Aggarwal, P. K., Anothai, J., Basso, B., Biernath, C., Challinor, A. J., De Sanctis, G., … Zhu, Y. (2015). Rising temperatures reduce global wheat production. *Nature Climate Change*, *5*(2), 143–147. https://doi.org/10.1038/nclimate2470

Atzberger, C. (2013). Advances in Remote Sensing of Agriculture: Context Description, Existing Operational Monitoring Systems and Major Information Needs. *Remote Sensing*, *5*(2), 949–981. https://doi.org/10.3390/rs5020949

Austin, R. (2011). *Unmanned Aircraft Systems: UAVS Design, Development and Deployment*. John Wiley & Sons.

Balasundram, S. K., Golhani, K., Shamshiri, R. R., & Vadamalai, G. (2020). Precision Agriculture Technologies for Management of Plant Diseases. In I. Ul Haq & S. Ijaz (Eds.), *Plant Disease Management Strategies for Sustainable Agriculture through Traditional and Modern Approaches* (pp. 259–278). Springer International Publishing. https://doi.org/10.1007/978-3-030-35955-3_13

Ballesteros, R., Ortega, J. F., Hernández, D., & Moreno, M. Á. (2015). Characterization of Vitis vinifera L. Canopy Using Unmanned Aerial Vehicle-Based Remote Sensing and Photogrammetry Techniques. *American Journal of Enology and Viticulture*, ajev.2014.14070. https://doi.org/10.5344/ajev.2014.14070

Baluja, J., Diago, M. P., Balda, P., Zorer, R., Meggio, F., Morales, F., & Tardaguila, J. (2012). Assessment of vineyard water status variability by thermal and multispectral imagery using an unmanned aerial vehicle (UAV). *Irrigation Science*, *30*(6), 511–522. https://doi.org/10.1007/s00271-012-0382-9

Banerjee, K., Krishnan, P., & Mridha, N. (2018). Application of thermal imaging of wheat crop canopy to estimate leaf area index under different moisture stress conditions. *Biosystems Engineering*, *166*(Supplement C), 13–27. https://doi.org/10.1016/j.biosystemseng.2017.10.012

Baofeng, S., Jinru, X., Chunyu, X., Yulin, F., Yuyang, S., & Fuentes, S. (2016). Digital surface model applied to unmanned aerial vehicle based photogrammetry to assess potential biotic or abiotic effects on grapevine canopies. *International Journal of Agricultural and Biological Engineering*, *9*(6), 119.

Bareth, G., Bendig, J., Tilly, N., Hoffmeister, D., Aasen, H., & Bolten, A. (2016). A Comparison of UAV- and TLS-derived Plant Height for Crop Monitoring: Using Polygon Grids for the Analysis of Crop Surface Models (CSMs). *PFG Photogrammetrie, Fernerkundung, Geoinformation*, 85–94. https://doi.org/10.1127/pfg/2016/0289

Barnes, E., Clarke, T., Richards, S., Colaizzi, P., Haberland, J., Kostrzewski, M., Waller, P., Choi, C., Riley, E., & Thompson, T. (2000). *Coincident detection of crop water stress, nitrogen status and canopy density using ground based multispectral data*. *1619*.

Battisti, A., Benvegnù, I., Colombari, F., & Haack, R. A. (2014). Invasion by the chestnut gall wasp in Italy causes significant yield loss in Castanea sativa nut production. *Agricultural and Forest Entomology*, *16*(1), 75–79. https://doi.org/10.1111/afe.12036

Belgiu, M., & Drăguţ, L. (2016). Random forest in remote sensing: A review of applications and future directions. *ISPRS Journal of Photogrammetry and Remote Sensing*, *114*, 24–31. https://doi.org/10.1016/j.isprsjprs.2016.01.011

Bellvert, J., & Girona, J. (2012). The use of multispectral and thermal images as a tool for irrigation scheduling in vineyards. *Erena, M.; López-Francos, A.; Montesinos, S. y Berthoumieu, JF (2012):«The Use of Remote Sensing and Geographic Information Systems for Irrigation Management in Southwest Europe». Options Méditerranéennes. Serie B: Studies and Researchs*, *67*, 131–137.

Bellvert, J., Marsal, J., Girona, J., & Zarco-Tejada, P. J. (2015). Seasonal evolution of crop water stress index in grapevine varieties determined with high-resolution remote sensing thermal imagery. *Irrigation Science*, *33*(2), 81–93. https://doi.org/10.1007/s00271-014-0456-y

Bellvert, J., Zarco-Tejada, P. J., Girona, J., & Fereres, E. (2013). Mapping crop water stress index in a 'Pinot-noir' vineyard: Comparing ground measurements with thermal remote sensing imagery from an unmanned aerial vehicle. *Precision Agriculture*, *15*(4), 361–376. https://doi.org/10.1007/s11119-013-9334-5

Bellvert, J., Zarco-Tejada, P. J., Marsal, J., Girona, J., González-Dugo, V., & Fereres, E. (2016). Vineyard irrigation scheduling based on airborne thermal imagery and water potential thresholds. *Australian Journal of Grape and Wine Research*, *22*(2), 307–315. https://doi.org/10.1111/ajgw.12173

Bendig, J., Bolten, A., & Bareth, G. (2013). UAV-based Imaging for Multi-Temporal, very high Resolution Crop Surface Models to monitor Crop Growth Variability. *PFG Photogrammetrie, Fernerkundung, Geoinformation*, 551–562. https://doi.org/10.1127/1432-8364/2013/0200

Bendig, J., Bolten, A., Bennertz, S., Broscheit, J., Eichfuss, S., & Bareth, G. (2014). Estimating Biomass of Barley Using Crop Surface Models (CSMs) Derived from UAV-Based RGB Imaging. *Remote Sensing*, *6*(11), 10395–10412. https://doi.org/10.3390/rs61110395

Bendig, J., Yu, K., Aasen, H., Bolten, A., Bennertz, S., Broscheit, J., Gnyp, M. L., & Bareth, G. (2015). Combining UAV-based plant height from crop surface models, visible, and near infrared vegetation indices for biomass monitoring in barley. *International Journal of Applied Earth Observation and Geoinformation*, *39*, 79–87. https://doi.org/10.1016/j.jag.2015.02.012

Bergonoux, F., Verlhac, A., Breisch, H., & Chapa, J. (1978). *Le châtaignier, production et culture*. Comité National Interprofessionel de la Chataigne et du Marron.

Berni, J. A. J., Zarco-Tejada, P. J., Sepulcre-Cantó, G., Fereres, E., & Villalobos, F. (2009). Mapping canopy conductance and CWSI in olive orchards using high resolution thermal remote sensing imagery. *Remote Sensing of Environment*, *113*(11), 2380–2388. https://doi.org/10.1016/j.rse.2009.06.018

Berni, J. A. J., Zarco-Tejada, P. J., Suarez, L., & Fereres, E. (2009). Thermal and Narrowband Multispectral Remote Sensing for Vegetation Monitoring From an Unmanned Aerial Vehicle. *IEEE Transactions on Geoscience and Remote Sensing*, *47*(3), 722–738. https://doi.org/10.1109/TGRS.2008.2010457

Berni, J. A. J., Zarco-Tejada, P. J., Suárez, L., González-Dugo, V., & Fereres, E. (2009). Remote sensing of vegetation from UAV platforms using lightweight multispectral and thermal imaging sensors. *Int. Arch. Photogramm. Remote Sens. Spatial Inform. Sci*, *38*(6). https://www.ipi.uni-hannover.de/fileadmin/institut/pdf/isprs-Hannover2009/Jimenez_Berni-155.pdf

Bio, A., Bastos, L., Granja, H., Pinho, L., Gonçalves, J., Henriques, R., & Rodrigues, D. (2015). Methods for Coastal Monitoring and Erosion Risk Assessment: Two Portuguese Case Studies. *Journal of Integrated Coastal Zone Management*, *15*(1), 47–63. https://doi.org/DOI:10.5894/rgci490

Birth, G. S., & McVey, G. R. (1968). Measuring the Color of Growing Turf with a Reflectance Spectrophotometer 1. *Agronomy Journal*, *60*(6), 640–643. https://doi.org/10.2134/agronj1968.00021962006000060016x

Blaschke, T. (2010). Object based image analysis for remote sensing. *ISPRS Journal of Photogrammetry and Remote Sensing*, *65*(1), 2–16. https://doi.org/10.1016/j.isprsjprs.2009.06.004

Bobillet, W., Da Costa, J., Germain, C., Lavialle, O., & Grenier, G. (2003). Row detection in high resolution remote sensing images of vine fields. *Proceedings of the 4th European Conference on Precision Agriculture*, 81–87.

Bonilla, I., Toda, F. M. de, & Martínez-Casasnovas, J. A. (2015). Vine vigor, yield and grape quality assessment by airborne remote sensing over three years: Analysis of unexpected relationships in cv. Tempranillo. *Spanish Journal of Agricultural Research*, *13*(2), 0903. https://doi.org/10.5424/sjar/2015132-7809

Borges, O., Gonçalves, B., de Carvalho, J. L. S., Correia, P., & Silva, A. P. (2008). Nutritional quality of chestnut (Castanea sativa Mill.) cultivars from Portugal. *Food Chemistry*, *106*(3), 976–984. https://doi.org/10.1016/j.foodchem.2007.07.011

Bounous, G., & Conedera, M. (2014). *Il castagno: Risorsa multifunzionale in Italia e nel mondo* (first). Edagricole.

Bradley, D., & Roth, G. (2007). Adaptive thresholding using the integral image. *Journal of Graphics Tools*, *12*(2), 13–21.

Bramley, R. (2005). Understanding variability in winegrape production systems 2. Within vineyard variation in quality over several vintages. *Australian Journal of Grape and Wine Research*, *11*(1), 33–42.

Bramley, R. G. V. (2001). *Progress in the development of precision viticulture—Variation in yield, quality and soil properties in contrasting Australian vineyards*. https://publications.csiro.au/rpr/pub?list=BRO&pid=procite:3e137b02-855b-4023-ac50-41b8a484071d

Bramley, R., & Hamilton, R. (2004). Understanding variability in winegrape production systems. *Australian Journal of Grape and Wine Research*, *10*(1), 32–45.

Brito, D., Esteves, R., Ramos, S., Pinto, T., & Gomes-Laranjo, J. (2012). ColUTAD e Ca90, dois porta-enxertos para o combate à doença da tinta no castanheiro. *Frutas, Legumes e Flores*, *124*, 38–41.

Bruinsma, J. (2011). The resources outlook: By how much do land, water and crop yields need to increase by 2050? *Looking Ahead in World Food and Agriculture: Perspectives to 2050*, 233–278.

Burgos, S., Mota, M., Noll, D., & Cannelle, B. (2015). Use of very high-resolution airborne images to analyse 3D canopy architecture of a vineyard. *The International Archives of Photogrammetry, Remote Sensing and Spatial Information Sciences*, *40*(3), 399.

C, N., Gerald, W, R., Mark, Jawoo, K., Richard, R., Timothy, S., Tingju, Z., Claudia, R., Siwa, M., Amanda, P., Miroslav, B., Marilia, M., Rowena, V.-S., Mandy, E., & David, L. (2009). *Climate Change: Impact on Agriculture and Costs of Adaptation*. Intl Food Policy Res Inst.

Calderón, R., Navas-Cortés, J. A., Lucena, C., & Zarco-Tejada, P. J. (2013). High-resolution airborne hyperspectral and thermal imagery for early detection of Verticillium wilt of olive using fluorescence, temperature and narrow-band spectral indices. *Remote Sensing of Environment*, *139*(Supplement C), 231–245. https://doi.org/10.1016/j.rse.2013.07.031

Calderón, Rocío, Navas-Cortés, J. A., & Zarco-Tejada, P. J. (2015). Early Detection and Quantification of Verticillium Wilt in Olive Using Hyperspectral and Thermal Imagery over Large Areas. *Remote Sensing*, *7*(5), 5584–5610. https://doi.org/10.3390/rs70505584

Camisón, Á., Martín, M. Á., Oliva, J., Elfstrand, M., & Solla, A. (2019). Increased tolerance to Phytophthora cinnamomi in offspring of ink-diseased chestnut (Castanea sativa Miller) trees. *Annals of Forest Science*, *76*(4), 119. https://doi.org/10.1007/s13595-019-0898-8

Campos, J., Llop, J., Gallart, M., García-Ruiz, F., Gras, A., Salcedo, R., & Gil, E. (2019). Development of canopy vigour maps using UAV for site-specific management during vineyard spraying process. *Precision Agriculture*. https://doi.org/10.1007/s11119-019-09643-z

Cancela, J., Fandiño, M., Rey, B., Dafonte, J., & González, X. (2017). Discrimination of irrigation water management effects in pergola trellis system vineyards using a vegetation and soil index. *Agricultural Water Management*, *183*, 70–77.

Candiago, S., Remondino, F., De Giglio, M., Dubbini, M., & Gattelli, M. (2015). Evaluating Multispectral Images and Vegetation Indices for Precision Farming Applications from UAV Images. *Remote Sensing*, *7*(4), 4026–4047. https://doi.org/10.3390/rs70404026

Capolupo, A., Kooistra, L., Berendonk, C., Boccia, L., & Suomalainen, J. (2015). Estimating Plant Traits of Grasslands from UAV-Acquired Hyperspectral Images: A Comparison of Statistical Approaches. *ISPRS International Journal of Geo-Information*, *4*(4), 2792–2820. https://doi.org/10.3390/ijgi4042792

Carr, J. C., & Slyder, J. B. (2018). Individual tree segmentation from a leaf-off photogrammetric point cloud. *International Journal of Remote Sensing*, *39*(15–16), 5195–5210. https://doi.org/10.1080/01431161.2018.1434330

Caruso, G., Tozzini, L., Rallo, G., Primicerio, J., Moriondo, M., Palai, G., & Gucci, R. (2017). Estimating biophysical and geometrical parameters of grapevine canopies ('Sangiovese') by an unmanned aerial vehicle (UAV) and VIS-NIR cameras. *VITIS - Journal of Grapevine Research, Vol 56 No 2 (2017): Vitis*. https://doi.org/10.5073/vitis.2017.56.63-70

Castaldi, F., Pelosi, F., Pascucci, S., & Casa, R. (2017). Assessing the potential of images from unmanned aerial vehicles (UAV) to support herbicide patch spraying in maize. *Precision Agriculture*, *18*(1), 76–94. https://doi.org/10.1007/s11119-016-9468-3

Castro, J., Azevedo, J. C., & Martins, L. (2010). TEMPORAL ANALYSIS OF SWEET CHESTNUT DECLINE IN NORTHEASTERN PORTUGAL USING GEOSTATISTICAL TOOLS. *Acta Horticulturae*, *866*, 405–410. https://doi.org/10.17660/ActaHortic.2010.866.53

Caturegli, L., Corniglia, M., Gaetani, M., Grossi, N., Magni, S., Migliazzi, M., Angelini, L., Mazzoncini, M., Silvestri, N., Fontanelli, M., Raffaelli, M., Peruzzi, A., & Volterrani, M. (2016). Unmanned Aerial Vehicle to Estimate Nitrogen Status of Turfgrasses. *PLOS ONE*, *11*(6), e0158268. https://doi.org/10.1371/journal.pone.0158268

CeSIA, A. dei G., Corti, L. U., & Firenze, I. (1997). A simple model for simulation of growth and development in grapevine (Vitis vinifera L.). I. Model description. *Vitis*, *36*(2), 67–71.

Chanussot, J., Bas, P., & Bombrun, L. (2005). Airborne remote sensing of vineyards for the detection of dead vine trees. *Proceedings of the Geoscience and Remote Sensing Symposium (IGARSS)*, *5*, 3090–3093. https://doi.org/10.1109/IGARSS.2005.1526490

Chen, J. S., Li, L., Wang, J. Y., Barry, D. A., Sheng, X. F., Gu, W. Z., Zhao, X., & Chen, L. (2004). Water resources: Groundwater maintains dune landscape. *Nature*, *432*(7016), 459–460. http://www.nature.com/nature/journal/v432/n7016/suppinfo/432459a_S1.html

Chisholm, R. A., Cui, J., Lum, S. K. Y., & Chen, B. M. (2013). UAV LiDAR for below-canopy forest surveys. *Journal of Unmanned Vehicle Systems*, *01*(01), 61–68. https://doi.org/10.1139/juvs-2013-0017

Cho, J., Lim, G., Biobaku, T., Kim, S., & Parsaei, H. (2015). Safety and Security Management with Unmanned Aerial Vehicle (UAV) in Oil and Gas Industry. *Procedia Manufacturing*, *3*, 1343–1349. http://dx.doi.org/10.1016/j.promfg.2015.07.290

Chu, T., Starek, M. J., Brewer, M. J., Masiane, T., & Murray, S. C. (2017). UAS imaging for automated crop lodging detection: A case study over an experimental maize field. *SPIE Commercial + Scientific Sensing and Imaging*, *10218*, 102180E-102180E. https://www.spiedigitallibrary.org/conference-proceedings-of-spie/10218/1/UAS-imaging-for-automated-crop-lodging-detection–a-case/10.1117/12.2262812.short?SSO=1

Chuvieco, E., Martín, M. P., & Palacios, A. (2002). Assessment of different spectral indices in the red-near-infrared spectral domain for burned land discrimination. *International Journal of Remote Sensing*, *23*(23), 5103–5110. https://doi.org/10.1080/01431160210153129

Cohen, Y., Alchanatis, V., Meron, M., Saranga, Y., & Tsipris, J. (2005). Estimation of leaf water potential by thermal imagery and spatial analysis. *Journal of Experimental Botany*, *56*(417), 1843–1852. https://doi.org/10.1093/jxb/eri174

Colomina, I., & Molina, P. (2014). Unmanned Aerial Systems for Photogrammetry and Remote Sensing: A Review. *ISPRS Journal of Photogrammetry and Remote Sensing*, *92*, 79–97. http://dx.doi.org/10.1016/j.isprsjprs.2014.02.013

Comba, L., Biglia, A., Ricauda Aimonino, D., & Gay, P. (2018). Unsupervised detection of vineyards by 3D point-cloud UAV photogrammetry for precision agriculture. *Computers and Electronics in Agriculture*, *155*, 84–95. https://doi.org/10.1016/j.compag.2018.10.005

Comba, L., Gay, P., Primicerio, J., & Ricauda Aimonino, D. (2015). Vineyard detection from unmanned aerial systems images. *Computers and Electronics in Agriculture*, *114*, 78–87. https://doi.org/10.1016/j.compag.2015.03.011

Costa Ferreira, A.-M., Germain, C., Homayouni, S., Da Costa, J.-P., Grenier, G., Marguerit, E., Roby, J.-P., & Van Leeuwen, C. (2007). Transformation of high resolution aerial images in vine vigour maps at intra-block scale by semi automatic image processing. *International Symposium of the GESCO*, 1372–1381. https://hal.archives-ouvertes.fr/hal-00169844

Costa, R., Fraga, H., Malheiro, A. C., & Santos, J. A. (2015). Application of crop modelling to portuguese viticulture: Implementation and added-values for strategic planning. *Ciência e Técnica Vitivinícola*, *30*(1), 29–42. https://doi.org/10.1051/ctv/20153001029

Cracknell, A. P., & Hayes, L. W. B. (2007). *Introduction to remote sensing*. Taylor & Francis.

D. M. Woebbecke, G. E. Meyer, K. Von Bargen, & D. A. Mortensen. (1995). Color Indices for Weed Identification Under Various Soil, Residue, and Lighting Conditions. *Transactions of the ASAE*, *38*(1), 259–269. https://doi.org/10.13031/2013.27838

Dandois, J. P., Olano, M., & Ellis, E. C. (2015). Optimal Altitude, Overlap, and Weather Conditions for Computer Vision UAV Estimates of Forest Structure. *Remote Sensing*, *7*(10), 13895–13920. https://doi.org/10.3390/rs71013895

de Castro, A. I., Jiménez-Brenes, F. M., Torres-Sánchez, J., Peña, J. M., Borra-Serrano, I., & López-Granados, F. (2018). 3-D Characterization of Vineyards Using a Novel UAV Imagery-Based OBIA Procedure for Precision Viticulture Applications. *Remote Sensing*, *10*(4), 584. https://doi.org/10.3390/rs10040584

Dempewolf, J., Nagol, J., Hein, S., Thiel, C., & Zimmermann, R. (2017). Measurement of Within-Season Tree Height Growth in a Mixed Forest Stand Using UAV Imagery. *Forests*, *8*(7), 231. https://doi.org/10.3390/f8070231

Di Gennaro, S. F., Matese, A., Gioli, B., Toscano, P., Zaldei, A., Palliotti, A., & Genesio, L. (2017). Multisensor approach to assess vineyard thermal dynamics combining high-resolution unmanned aerial vehicle (UAV) remote sensing and wireless sensor network (WSN) proximal sensing. *Scientia Horticulturae*, *221*, 83–87. https://doi.org/10.1016/j.scienta.2017.04.024

Di Gennaro, S. F., Nati, C., Dainelli, R., Pastonchi, L., Berton, A., Toscano, P., & Matese, A. (2020). An Automatic UAV Based Segmentation Approach for Pruning Biomass Estimation in Irregularly Spaced Chestnut Orchards. *Forests*, *11*(3), 308. https://doi.org/10.3390/f11030308

Díaz-Varela, R. A., De la Rosa, R., León, L., & Zarco-Tejada, P. J. (2015). High-Resolution Airborne UAV Imagery to Assess Olive Tree Crown Parameters Using 3D Photo Reconstruction: Application in Breeding Trials. *Remote Sensing*, *7*(4), 4213–4232. https://doi.org/10.3390/rs70404213

Díaz-Varela, R. A., de la Rosa, R., León, L., & Zarco-Tejada, P. J. (2015). High-Resolution Airborne UAV Imagery to Assess Olive Tree Crown Parameters Using 3D Photo Reconstruction: Application in Breeding Trials. *Remote Sensing*, *7*(4), 4213–4232. https://doi.org/10.3390/rs70404213

DJI Official. (n.d.). *DJI Phantom 4 – Specs, FAQ, Tutorials and Downloads*. DJI Phantom 4 – Specs, FAQ, Tutorials and Downloads. Retrieved 3 September 2020, from https://www.dji.com/pt/phantom-4/info

Dobrowski, S. Z., Ustin, S. L., & Wolpert, J. A. (n.d.). Remote estimation of vine canopy density in vertically shoot-positioned vineyards: Determining optimal vegetation indices. *Australian Journal of Grape and Wine Research*, *8*(2), 117–125. https://doi.org/10.1111/j.1755-0238.2002.tb00220.x

Dong, X., Yu, B., Shi, Z., & Zhong, Y. (2015). Time-Varying Formation Control for Unmanned Aerial Vehicles: Theories and Applications. *IEEE Transactions on Control Systems Technology*, *23*(1), 340–348. https://doi.org/10.1109/TCST.2014.2314460

Dooly, G., Omerdic, E., Coleman, J., Miller, L., Kaknjo, A., Hayes, J., Braga, J., Ferreira, F., Conlon, H., Barry, H., Marcos-Olaya, J., Tuohy, T., Sousa, J., & Toal, D. (2016). Unmanned Vehicles for Maritime Spill Response Case Study: Exercise Cathach. *Marine Pollution Bulletin*, *110*(1), 528–538. http://dx.doi.org/10.1016/j.marpolbul.2016.02.072

DRAPN. (2014). *Plano de ação nacional para o controlo do inseto Dryocosmus kuriphilus YASUMATSU (Vespa das galhas do castanheiro)* [Report]. Direção Regional de Agricultura e Pescas do Norte. http://www.drapn.min-agricultura.pt/drapn/PLANO_A%C3%A7%C3%A3o-dryocosmusFinal.pdf

DroneDeploy. (2016, August). *Commercial Drone Industry Trends*. DroneDeploy's Commercial Drone Industry Trends. http://info.dronedeploy.com/commercial-drone-industry-trends/

Drummond, C. D., Harley, M. D., Turner, I. L., A Matheen, A. N., & Glamore, W. C. (2015). UAV applications to coastal engineering. *Australasian Coasts & Ports Conference*, 267–272.

Du, M., & Noguchi, N. (2017). Monitoring of Wheat Growth Status and Mapping of Wheat Yield's within-Field Spatial Variations Using Color Images Acquired from UAV-camera System. *Remote Sensing*, *9*(3), 289. https://doi.org/10.3390/rs9030289

Duchêne, E., & Schneider, C. (2005). Grapevine and climatic changes: A glance at the situation in Alsace. *Agronomy for Sustainable Development*, *25*(1), 93–99.

Ercin, A. E., & Hoekstra, A. Y. (2014). Water footprint scenarios for 2050: A global analysis. *Environment International*, *64*, 71–82.

Ermacora, G., Toma, A., Rosa, S., Bona, B., Chiaberge, M., Silvagni, M., Gaspardone, M., & Antonini, R. (2014). A Cloud Based Service for Management and Planning of Autonomous UAV Missions in Smart City Scenarios. In J. Hodicky (Ed.), *Modelling and Simulation for Autonomous Systems: First International Workshop, MESAS 2014, Rome, Italy, May 5-6, 2014, Revised Selected Papers* (pp. 20–26). Springer International Publishing. https://doi.org/10.1007/978-3-319-13823-7_3

Espinoza, C. Z., Khot, L. R., Sankaran, S., & Jacoby, P. W. (2017). High Resolution Multispectral and Thermal Remote Sensing-Based Water Stress Assessment in Subsurface Irrigated Grapevines. *Remote Sensing*, *9*(9), 961. https://doi.org/10.3390/rs9090961

Eysn, L., Hollaus, M., Lindberg, E., Berger, F., Monnet, J.-M., Dalponte, M., Kobal, M., Pellegrini, M., Lingua, E., Mongus, D., & Pfeifer, N. (2015). A Benchmark of Lidar-Based Single Tree Detection Methods Using Heterogeneous Forest Data from the Alpine Space. *Forests*, *6*(5), 1721–1747. https://doi.org/10.3390/f6051721

Falkowski, M. J., Gessler, P. E., Morgan, P., Hudak, A. T., & Smith, A. M. S. ; (2005). *Characterizing and mapping forest fire fuels using ASTER imagery and gradient modeling*. http://www.treesearch.fs.fed.us/pubs/23874

Felderhof, L., & Gillieson, D. (2012). Near-infrared Imagery From Unmanned Aerial Systems and Satellites Can Be Used to Specify Fertilizer Application Rates in Tree Crops. *Canadian Journal of Remote Sensing*, *37*(4), 376–386. https://doi.org/10.5589/m11-046

Feng, Q., Liu, J., & Gong, J. (2015). UAV Remote Sensing for Urban Vegetation Mapping Using Random Forest and Texture Analysis. *Remote Sensing*, *7*(1), 1074–1094. https://doi.org/10.3390/rs70101074

Fladeland, M., Sumich, M., Lobitz, B., Kolyer, R., Herlth, D., Berthold, R., McKinnon, D., Monforton, L., Brass, J., & Bland, G. (2011). The NASA SIERRA science demonstration programme and the role of small–medium unmanned aircraft for earth science investigations. *Geocarto International*, *26*(2), 157–163. https://doi.org/10.1080/10106049.2010.537375

Flener, C., Vaaja, M., Jaakkola, A., Krooks, A., Kaartinen, H., Kukko, A., Kasvi, E., Hyyppä, H., Hyyppä, J., & Alho, P. (2013). Seamless Mapping of River Channels at High Resolution Using Mobile LiDAR and UAV-Photography. *Remote Sensing*, *5*(12), 6382–6407. https://doi.org/10.3390/rs5126382

Floros, J. D., Newsome, R., Fisher, W., Barbosa-Cánovas, G. V., Chen, H., Dunne, C. P., German, J. B., Hall, R. L., Heldman, D. R., & Karwe, M. V. (2010). Feeding the world today and tomorrow: The importance of food science and technology: An IFT scientific review. *Comprehensive Reviews in Food Science and Food Safety*, *9*(5), 572–599.

Fraga, H., & Santos, J. A. (2017). Daily prediction of seasonal grapevine production in the Douro wine region based on favourable meteorological conditions. *Australian Journal of Grape and Wine Research*, *23*(2), 296–304. https://doi.org/10.1111/ajgw.12278

Fraga, Helder, Amraoui, M., Malheiro, A. C., Moutinho-Pereira, J., Eiras-Dias, J., Silvestre, J., & Santos, J. A. (2014). Examining the relationship between the Enhanced Vegetation Index and grapevine phenology. *European Journal of Remote Sensing*, *47*(1), 753–771. https://doi.org/10.5721/EuJRS20144743

Fraga, Helder, Malheiro, A. C., Moutinho-Pereira, J., Cardoso, R. M., Soares, P. M. M., Cancela, J. J., Pinto, J. G., & Santos, J. A. (2014). Integrated Analysis of Climate, Soil, Topography and Vegetative Growth in Iberian Viticultural Regions. *PLOS ONE*, *9*(9), e108078. https://doi.org/10.1371/journal.pone.0108078

Frankenberger, J. R., Huang, C., & Nouwakpo, K. (2008). Low-Altitude Digital Photogrammetry Technique to Assess Ephemeral Gully Erosion. *IGARSS 2008 - 2008 IEEE International Geoscience and Remote Sensing Symposium*, *4*, IV-117-IV–120. https://doi.org/10.1109/IGARSS.2008.4779670

Fraser, R. H., Olthof, I., Lantz, T. C., & Schmitt, C. (2016). UAV photogrammetry for mapping vegetation in the low-Arctic. *Arctic Science*, *2*(3), 79–102. https://doi.org/10.1139/as-2016-0008

Fryskowska, A., Kedzierski, M., Grochala, A., & Braula, A. (2016). Calibration of low cost RGB and NIR UAV cameras. *The International Archives of the Photogrammetry, Remote Sensing and Spatial Information Sciences*, *XLI-B1*, 817–821. https://doi.org/doi:10.5194/isprsarchives-XLI-B1-817-2016

Funaki, M., Higashino, S.-I., Sakanaka, S., Iwata, N., Nakamura, N., Hirasawa, N., Obara, N., & Kuwabara, M. (2014). Small Unmanned Aerial Vehicles for Aeromagnetic Surveys and Their Flights in The South Shetland Islands, Antarctica. *Polar Science*, *8*(4), 342–356. http://dx.doi.org/10.1016/j.polar.2014.07.001

Gago, J., Douthe, C., Coopman, R. E., Gallego, P. P., Ribas-Carbo, M., Flexas, J., Escalona, J., & Medrano, H. (2015). UAVs challenge to assess water stress for sustainable agriculture. *Agricultural Water Management*, *153*, 9–19. https://doi.org/10.1016/j.agwat.2015.01.020

Galiano, S. G. (2012). Assessment of vegetation indexes from remote sensing: Theoretical basis. *Paseo Alfonso XIII*, *52*, 65–75.

Garcia-Torres, L., Caballero-Novella, J. J., Gómez-Candón, D., & De-Castro, A. I. (2014). Semi-Automatic Normalization of Multitemporal Remote Images Based on Vegetative Pseudo-Invariant Features. *PLOS ONE*, *9*(3), e91275. https://doi.org/10.1371/journal.pone.0091275

Gatziolis, D., Lienard, J. F., Vogs, A., & Strigul, N. S. (2015). 3D Tree Dimensionality Assessment Using Photogrammetry and Small Unmanned Aerial Vehicles. *PLOS ONE*, *10*(9), e0137765. https://doi.org/10.1371/journal.pone.0137765

Gebbers, R., & Adamchuk, V. I. (2010). Precision Agriculture and Food Security. *Science*, *327*(5967), 828–831. https://doi.org/10.1126/science.1183899

Gehring, E., Pezzatti, G. B., Krebs, P., Mazzoleni, S., & Conedera, M. (2015). On the applicability of the pipe model theory on the chestnut tree (Castanea sativa Mill.). *Trees*, *29*(2), 321–332.

Geipel, J., Peteinatos, G. G., Claupein, W., & Gerhards, R. (2013). Enhancement of micro Unmanned Aerial Vehicles for agricultural aerial sensor systems. In J. V. Stafford (Ed.), *Precision agriculture '13* (pp. 161–167). Wageningen Academic Publishers. https://doi.org/10.3920/978-90-8686-778-3_18

Gennaro, S. F. D., Battiston, E., Marco, S. D., Facini, O., Matese, A., Nocentini, M., Palliotti, A., & Mugnai, L. (2016). Unmanned Aerial Vehicle (UAV)-based remote sensing to monitor grapevine leaf stripe disease within a vineyard affected by esca complex. *Phytopathologia Mediterranea*, *55*(2), 262–275. https://doi.org/10.14601/Phytopathol_Mediterr-18312

George, E. A., Tiwari, G., Yadav, R. N., Peters, E., & Sadana, S. (2013). UAV systems for parameter identification in agriculture. *2013 IEEE Global Humanitarian Technology Conference: South Asia Satellite (GHTC-SAS)*, 270–273. https://doi.org/10.1109/GHTC-SAS.2013.6629929

Gertler, J. (2012). *U.S. Unmanned Aerial Systems* (U.S. Unmanned Aerial Systems; R42136, p. 55). Congressional Research Service.

Getzin, S., Wiegand, K., & Schöning, I. (2012). Assessing biodiversity in forests using very high-resolution images and unmanned aerial vehicles. *Methods in Ecology and Evolution*, *3*(2), 397–404. https://doi.org/10.1111/j.2041-210X.2011.00158.x

Gevaert, C. M., Persello, C., Sliuzas, R., & Vosselman, G. (2017). Informal settlement classification using point-cloud and image-based features from UAV data. *ISPRS Journal of Photogrammetry and Remote Sensing*, *125*, 225–236. http://dx.doi.org/10.1016/j.isprsjprs.2017.01.017

Gilbert, N. (2012). Water under pressure. *Nature*, *483*(7389), 256–257.

Gini, R., Sona, G., Ronchetti, G., Passoni, D., & Pinto, L. (2018). Improving Tree Species Classification Using UAS Multispectral Images and Texture Measures. *ISPRS International Journal of Geo-Information*, *7*(8), 315. https://doi.org/10.3390/ijgi7080315

Gitelson, A. A., Kaufman, Y. J., & Merzlyak, M. N. (1996). Use of a green channel in remote sensing of global vegetation from EOS-MODIS. *Remote Sensing of Environment*, *58*(3), 289–298. https://doi.org/10.1016/S0034-4257(96)00072-7

Gitelson, A. A., Kaufman, Y. J., Stark, R., & Rundquist, D. (2002). Novel algorithms for remote estimation of vegetation fraction. *Remote Sensing of Environment*, *80*(1), 76–87. https://doi.org/10.1016/S0034-4257(01)00289-9

Gnyp, M. L., Bareth, G., Li, F., Lenz-Wiedemann, V. I. S., Koppe, W., Miao, Y., Hennig, S. D., Jia, L., Laudien, R., Chen, X., & Zhang, F. (2014). Development and implementation of a multiscale biomass model using hyperspectral vegetation indices for winter wheat in the North China Plain. *International Journal of Applied Earth Observation and Geoinformation*, *33*, 232–242. https://doi.org/10.1016/j.jag.2014.05.006

Gobron, N., Pinty, B., Verstraete, M. M., & Widlowski, J. L. (2000). Advanced vegetation indices optimized for up-coming sensors: Design, performance, and applications. *IEEE Transactions on Geoscience and Remote Sensing*, *38*(6), 2489–2505. https://doi.org/10.1109/36.885197

Gomes-Laranjo, J., Dinis, L.-T., Martins, L., Portela, E., Pinto, T., Ara, M. C., Díaz, I. F., Majada, J., Peixoto, F., Lorenzo, S. P., & others. (2012). Characterization of Chestnut Behavior with Photosynthetic Traits. In *Applied Photosynthesis*. InTech.

Gómez-Candón, D., Castro, A. I. D., & López-Granados, F. (2013). Assessing the accuracy of mosaics from unmanned aerial vehicle (UAV) imagery for precision agriculture purposes in wheat. *Precision Agriculture*, *15*(1), 44–56. https://doi.org/10.1007/s11119-013-9335-4

Gómez-Candón, David, Virlet, N., Labbé, S., Jolivot, A., & Regnard, J.-L. (2016). Field phenotyping of water stress at tree scale by UAV-sensed imagery: New insights for thermal acquisition and calibration. *Precision Agriculture*, *17*(6), 786–800. https://doi.org/10.1007/s11119-016-9449-6

Gonçalves, J. A., Bastos, L., Pinho, J. L., & Granja, H. (2011). Digital Aerial Photography to Monitor Changes in Coastal Areas Based on Direct Georeferencing. *5th EARSeL Workshop on Remote Sensing of the Coastal Zone*, 1–10. http://www.conferences.earsel.org/abstract/show/2689

Gonçalves, J. A., & Henriques, R. (2015). UAV Photogrammetry for Topographic Monitoring of Coastal Areas. *ISPRS Journal of Photogrammetry and Remote Sensing*, *104*, 101–111. http://dx.doi.org/10.1016/j.isprsjprs.2015.02.009

Gonzalez-Dugo, V., Zarco-Tejada, P., Nicolás, E., Nortes, P. A., Alarcón, J. J., Intrigliolo, D. S., & Fereres, E. (2013). Using high resolution UAV thermal imagery to assess the variability in the water status of five fruit tree species within a commercial orchard. *Precision Agriculture*, *14*(6), 660–678. https://doi.org/10.1007/s11119-013-9322-9

Goodbody, T. R. H., Coops, N. C., Hermosilla, T., Tompalski, P., & Crawford, P. (2018). Assessing the status of forest regeneration using digital aerial photogrammetry and unmanned aerial systems. *International Journal of Remote Sensing*, *39*(15–16), 5246–5264. https://doi.org/10.1080/01431161.2017.1402387

Granitto, P. M., Furlanello, C., Biasioli, F., & Gasperi, F. (2006). Recursive feature elimination with random forest for PTR-MS analysis of agroindustrial products. *Chemometrics and Intelligent Laboratory Systems*, *83*(2), 83–90. https://doi.org/10.1016/j.chemolab.2006.01.007

Grenzdörffer, G. J., Engel, A., & Teichert, B. (2008). The photogrammetric potential of low-cost UAVs in forestry and agriculture. *The International Archives of the Photogrammetry, Remote Sensing and Spatial Information Sciences*, *31*(B3), 1207–1214.

Guerra-Hernández, J., Cosenza, D. N., Rodriguez, L. C. E., Silva, M., Tomé, M., Díaz-Varela, R. A., & González-Ferreiro, E. (2018). Comparison of ALS- and UAV(SfM)-derived high-density point clouds for individual tree detection in Eucalyptus plantations. *International Journal of Remote Sensing*, *39*(15–16), 5211–5235. https://doi.org/10.1080/01431161.2018.1486519

Guerra-Hernández, J., González-Ferreiro, E., Monleón, V. J., Faias, S. P., Tomé, M., & Díaz-Varela, R. A. (2017). Use of Multi-Temporal UAV-Derived Imagery for Estimating Individual Tree Growth in Pinus pinea Stands. *Forests*, *8*(8), 300. https://doi.org/10.3390/f8080300

Guerrero, J. M., Pajares, G., Montalvo, M., Romeo, J., & Guijarro, M. (2012). Support Vector Machines for crop/weeds identification in maize fields. *Expert Systems with Applications*, *39*(12), 11149–11155. https://doi.org/10.1016/j.eswa.2012.03.040

Gutiérrez, P. A., López-Granados, F., Peña-Barragán, J. M., Jurado-Expósito, M., & Hervás-Martínez, C. (2008). Logistic regression product-unit neural networks for mapping Ridolfia segetum infestations in sunflower crop using multitemporal remote sensed data. *Computers and Electronics in Agriculture*, *64*(2), 293–306. http://dx.doi.org/10.1016/j.compag.2008.06.001

Guyon, I., Weston, J., Barnhill, S., & Vapnik, V. (2002). Gene Selection for Cancer Classification using Support Vector Machines. *Machine Learning*, *46*(1), 389–422. https://doi.org/10.1023/A:1012487302797

Haboudane, D., Miller, J. R., Pattey, E., Zarco-Tejada, P. J., & Strachan, I. B. (2004). Hyperspectral vegetation indices and novel algorithms for predicting green LAI of crop canopies: Modeling and validation in the context of precision agriculture. *Remote Sensing of Environment*, *90*(3), 337–352. https://doi.org/10.1016/j.rse.2003.12.013

Hague, T., Tillett, N. D., & Wheeler, H. (2006). Automated Crop and Weed Monitoring in Widely Spaced Cereals. *Precision Agriculture*, *7*(1), 21–32. https://doi.org/10.1007/s11119-005-6787-1

Hall, A., Lamb, D. w., Holzapfel, B., & Louis, J. (2002). Optical remote sensing applications in viticulture—A review. *Australian Journal of Grape and Wine Research*, *8*(1), 36–47. https://doi.org/10.1111/j.1755-0238.2002.tb00209.x

Hancock, D. W., & Dougherty, C. T. (2007). Relationships between Blue- and Red-based Vegetation Indices and Leaf Area and Yield of Alfalfa. *Crop Science*, *47*(6), 2547–2556. https://doi.org/10.2135/cropsci2007.01.0031

Hardin, P. J., & Jensen, R. R. (2011). Small-Scale Unmanned Aerial Vehicles in Environmental Remote Sensing: Challenges and Opportunities. *GIScience & Remote Sensing*, *48*(1), 99–111. https://doi.org/10.2747/1548-1603.48.1.99

Hartmann, W., Tilch, S., Eisenbeiss, H., & Schindler, K. (2012). Determination of the UAV position by automatic processing of thermal images. *International Archives of the Photogrammetry, Remote Sensing and Spatial Information Sciences*, *39*, B6.

Hernandez, J. G., Gonzalez-Ferreiro, E., Sarmento, A., Silva, J., Nunes, A., Correia, A. C., Fontes, L., Tomé, M., & Diaz-Varela, R. (2016). Using high resolution UAV imagery to estimate tree variables in Pinus pinea plantation in Portugal. *Forest Systems*, *25*(2), 09. https://doi.org/10.5424/fs/2016252-08895

Herwitz, S. R., Johnson, L. F., Dunagan, S. E., Higgins, R. G., Sullivan, D. V., Zheng, J., Lobitz, B. M., Leung, J. G., Gallmeyer, B. A., Aoyagi, M., Slye, R. E., & Brass, J. A. (2004). Imaging from an unmanned aerial vehicle: Agricultural surveillance and decision support. *Computers and Electronics in Agriculture*, *44*(1), 49–61. https://doi.org/10.1016/j.compag.2004.02.006

Hill, R. A., Wilson, A. K., George, M., & Hinsley, S. A. (2010). Mapping tree species in temperate deciduous woodland using time-series multi-spectral data. *Applied Vegetation Science*, *13*(1), 86–99. https://doi.org/10.1111/j.1654-109X.2009.01053.x

Hodgson, A., Kelly, N., & Peel, D. (2013). Unmanned Aerial Vehicles (UAVs) for Surveying Marine Fauna: A Dugong Case Study. *PLOS ONE*, *8*(11), e79556. https://doi.org/10.1371/journal.pone.0079556

Holman, F. H., Riche, A. B., Michalski, A., Castle, M., Wooster, M. J., & Hawkesford, M. J. (2016). High Throughput Field Phenotyping of Wheat Plant Height and Growth Rate in Field Plot Trials Using UAV Based Remote Sensing. *Remote Sensing*, *8*(12), 1031. https://doi.org/10.3390/rs8121031

Honkavaara, E., Kaivosoja, J., Mäkynen, J., Pellikka, I., Pesonen, L., Saari, H., Salo, H., Hakala, T., Marklelin, L., & Rosnell, T. (2012). HYPERSPECTRAL REFLECTANCE SIGNATURES AND POINT CLOUDS FOR PRECISION AGRICULTURE BY LIGHT WEIGHT UAV IMAGING SYSTEM. *ISPRS Annals of Photogrammetry, Remote Sensing and Spatial Information Sciences*, *I–7*, 353–358. https://doi.org/10.5194/isprsannals-I-7-353-2012

Honkavaara, Eija, Kaivosoja, J., Mäkynen, J., Pellikka, I., Pesonen, L., Saari, H., Salo, H., Hakala, T., Marklelin, L., Rosnell, T., & others. (2012). Hyperspectral reflectance signatures and point clouds for precision agriculture by light weight UAV imaging system. *ISPRS Ann. Photogramm. Remote Sens. Spatial Inf. Sci. I-7*, 353–358.

Honkavaara, Eija, Saari, H., Kaivosoja, J., Pölönen, I., Hakala, T., Litkey, P., Mäkynen, J., & Pesonen, L. (2013). Processing and Assessment of Spectrometric, Stereoscopic Imagery Collected Using a Lightweight UAV Spectral Camera for Precision Agriculture. *Remote Sensing*, *5*(10), 5006–5039. https://doi.org/10.3390/rs5105006

Howden, S. M., Soussana, J.-F., Tubiello, F. N., Chhetri, N., Dunlop, M., & Meinke, H. (2007). Adapting agriculture to climate change. *Proceedings of the National Academy of Sciences*, *104*(50), 19691–19696.

Huete, A. R. (1988). A soil-adjusted vegetation index (SAVI). *Remote Sensing of Environment*, *25*(3), 295–309. https://doi.org/10.1016/0034-4257(88)90106-X

Hunt, E. R., Doraiswamy, P. C., McMurtrey, J. E., Daughtry, C. S. T., Perry, E. M., & Akhmedov, B. (2013). A visible band index for remote sensing leaf chlorophyll content at the canopy scale. *International Journal of Applied Earth Observation and Geoinformation*, *21*, 103–112. https://doi.org/10.1016/j.jag.2012.07.020

ICNF. (2010). *Relatório Final IFN5—FloreStat* (Vol. 2014). http://www.icnf.pt/portal/florestas/ifn/ifn5/rel-fin

Idso, S. B., Jackson, R. D., Pinter, P. J., Reginato, R. J., & Hatfield, J. L. (1981). Normalizing the stress-degree-day parameter for environmental variability. *Agricultural Meteorology*, *24*, 45–55. https://doi.org/10.1016/0002-1571(81)90032-7

Iizuka, K., Yonehara, T., Itoh, M., & Kosugi, Y. (2018). Estimating Tree Height and Diameter at Breast Height (DBH) from Digital Surface Models and Orthophotos Obtained with an Unmanned Aerial System for a Japanese Cypress (Chamaecyparis obtusa) Forest. *Remote Sensing*, *10*(1), 13. https://doi.org/10.3390/rs10010013

Inglada, J., & Christophe, E. (2009). The Orfeo Toolbox remote sensing image processing software. *2009 IEEE International Geoscience and Remote Sensing Symposium*, *4*, IV-733-IV–736. https://doi.org/10.1109/IGARSS.2009.5417481

Instituto Nacional de Estatística, I. P. (2016). *Estatísticas Agrícolas 2015*. Instituto Nacional de Estatística, I.P.

Instituto Nacional de Estatística, I. P. (2017). *Estatísticas Agrícolas 2016*. Instituto Nacional de Estatística, I.P.

Instituto Nacional de Estatística, I. P. (2019). *Estatísticas Agrícolas 2018*. Instituto Nacional de Estatística, I.P. https://www.ine.pt/xportal/xmain?xpid=INE&xpgid=ine_publicacoes&PUBLICACOESpub_boui=358629204&PUBLICACOESmodo=2

Israel, M. (2011). A UAV-based roe deer fawn detection system. *International Archives of Photogrammetry and Remote Sensing*, *38*, 1–5.

James, M. R., & Robson, S. (2014). Mitigating Systematic Error in Topographic Models Derived from UAV and Ground-based Image Networks. *Earth Surface Processes and Landforms*, *39*(10), 1413–1420. https://doi.org/10.1002/esp.3609

Järnstedt, J., Pekkarinen, A., Tuominen, S., Ginzler, C., Holopainen, M., & Viitala, R. (2012). Forest variable estimation using a high-resolution digital surface model. *ISPRS Journal of Photogrammetry and Remote Sensing*, *74*, 78–84. https://doi.org/10.1016/j.isprsjprs.2012.08.006

Jenkins, D., & Vasigh, B. (2013). *The economic impact of unmanned aircraft systems integration in the United States*. Association for Unmanned Vehicle Systems International (AUVSI).

Jenks, C. (2009). Law from above: Unmanned aerial systems, use of force, and the law of armed conflict. *NDL Rev.*, *85*, 649.

Jha, A. R. (2016). *Theory, Design, and Applications of Unmanned Aerial Vehicles*. CRC Press. https://books.google.pt/books?id=guGVDQAAQBAJ

Jia, Y., Su, Z., Shen, W., Yuan, J., & Xu, Z. (2016). UAV Remote Sensing Image Mosaic and Its Application in Agriculture. *International Journal of Smart Home*, *10*(5), 159–170. https://doi.org/10.14257/ijsh.2016.10.5.15

Jiménez-Brenes, F. M., López-Granados, F., Torres-Sánchez, J., Peña, J. M., Ramírez, P., Castillejo-González, I. L., & Castro, A. I. de. (2019). Automatic UAV-based detection of Cynodon dactylon for site-specific vineyard management. *PLOS ONE*, *14*(6), e0218132. https://doi.org/10.1371/journal.pone.0218132

Johansen, K., Raharjo, T., & McCabe, M. F. (2018). Using Multi-Spectral UAV Imagery to Extract Tree Crop Structural Properties and Assess Pruning Effects. *Remote Sensing*, *10*(6), 854. https://doi.org/10.3390/rs10060854

Johnson, L. F., Roczen, D., & Youkhana, S. (2001). *Vineyard canopy density mapping with IKONOS satellite imagery*. Proc. of 3rd International Conference on Geospatial Information in Agriculture and Forestry.

Johnson, L., Roczen, D., Youkhana, S., Nemani, R., & Bosch, D. (2003). Mapping vineyard leaf area with multispectral satellite imagery. *Computers and Electronics in Agriculture*, *38*(1), 33–44.

Jomaa, I., Auda, Y., Abi Saleh, B., Hamzé, M., & Safi, S. (2008). Landscape spatial dynamics over 38 years under natural and anthropogenic pressures in Mount Lebanon. *Landscape and Urban Planning*, *87*(1), 67–75. http://dx.doi.org/10.1016/j.landurbplan.2008.04.007

Jones, H. G. (1999). Use of infrared thermometry for estimation of stomatal conductance as a possible aid to irrigation scheduling. *Agricultural and Forest Meteorology*, *95*(3), 139–149. https://doi.org/10.1016/S0168-1923(99)00030-1

Junges, A. H., Fontana, D. C., Anzanello[1], R., & Bremm, C. (2017). Normalized difference vegetation index obtained by ground-based remote sensing to characterize vine cycle in Rio Grande do Sul, Brazil. *Ciência e Agrotecnologia*, *41*(5), 543–553. https://doi.org/10.1590/1413-70542017415049016

Junges, A. H., Fontana, D. C., Lampugnani, C. S., Junges, A. H., Fontana, D. C., & Lampugnani, C. S. (2019). Relationship between the normalized difference vegetation index and leaf area in vineyards. *Bragantia*, *78*(2), 297–305. https://doi.org/10.1590/1678-4499.2018168

Justice, C. O., Vermote, E., Townshend, J. R. G., Defries, R., Roy, D. P., Hall, D. K., Salomonson, V. V., Privette, J. L., Riggs, G., Strahler, A., Lucht, W., Myneni, R. B., Knyazikhin, Y., Running, S. W., Nemani, R. R., Wan, Z., Huete, A. R., Leeuwen, W. van, Wolfe, R. E., … Barnsley, M. J. (1998). The Moderate Resolution Imaging Spectroradiometer (MODIS): Land remote sensing for global change research. *IEEE Transactions on Geoscience and Remote Sensing*, *36*(4), 1228–1249. https://doi.org/10.1109/36.701075

Juul, M. (2015). *Civil drones in the European Union*. EPRS | European Parliamentary Research Service. http://www.europarl.europa.eu/thinktank/en/document.html?reference=EPRS_BRI(2015)571305

Kalisperakis, I., Stentoumis, C., Grammatikopoulos, L., & Karantzalos, K. (2015). Leaf area index estimation in vineyards from UAV hyperspectral data, 2D image mosaics and 3D canopy surface models. *The International Archives of Photogrammetry, Remote Sensing and Spatial Information Sciences*, *40*(1), 299.

Kankare, V., Holopainen, M., Vastaranta, M., Puttonen, E., Yu, X., Hyyppä, J., Vaaja, M., Hyyppä, H., & Alho, P. (2013). Individual tree biomass estimation using terrestrial laser scanning. *ISPRS Journal of Photogrammetry and Remote Sensing*, *75*, 64–75. https://doi.org/10.1016/j.isprsjprs.2012.10.003

Karakizi, C., Oikonomou, M., & Karantzalos, K. (2015). Spectral Discrimination and Reflectance Properties of Various Vine Varieties from Satellite, UAV and Proximate Sensors. *The International Archives of Photogrammetry, Remote Sensing and Spatial Information Sciences*, *40*(7), 31.

Karpina, M., Jarząbek-Rychard, M., Tymków, P., & Borkowski, A. (2016). UAV-BASED AUTOMATIC TREE GROWTH MEASUREMENT FOR BIOMASS ESTIMATION. *ISPRS - International Archives of the Photogrammetry, Remote Sensing and Spatial Information Sciences*, *XLI-B8*, 685–688. https://doi.org/10.5194/isprsarchives-XLI-B8-685-2016

Kawashima, S., & Nakatani, M. (1998). An Algorithm for Estimating Chlorophyll Content in Leaves Using a Video Camera. *Annals of Botany*, *81*(1), 49–54. https://doi.org/10.1006/anbo.1997.0544

Khaliq, A., Comba, L., Biglia, A., Ricauda Aimonino, D., Chiaberge, M., & Gay, P. (2019). Comparison of Satellite and UAV-Based Multispectral Imagery for Vineyard Variability Assessment. *Remote Sensing*, *11*(4), 436. https://doi.org/10.3390/rs11040436

Kiani, S., & Jafari, A. (2012). Crop detection and positioning in the field using discriminant analysis and neural networks based on shape features. *JOURNAL OF AGRICULTURAL SCIENCE AND TECHNOLOGY (JAST)*, *14*, 755–765.

Kim, D.-W., Yun, H. S., Jeong, S.-J., Kwon, Y.-S., Kim, S.-G., Lee, W. S., & Kim, H.-J. (2018). Modeling and Testing of Growth Status for Chinese Cabbage and White Radish with UAV-Based RGB Imagery. *Remote Sensing*, *10*(4), 563. https://doi.org/10.3390/rs10040563

Klemas, V. V. (2015). Coastal and Environmental Remote Sensing from Unmanned Aerial Vehicles: An Overview. *Journal of Coastal Research*, 1260–1267. https://doi.org/10.2112/JCOASTRES-D-15-00005.1

Lacar, F., Lewis, M., & Grierson, I. (2001). Use of hyperspectral imagery for mapping grape varieties in the Barossa Valley, South Australia. *Proceedings of the Geoscience and Remote Sensing Symposium (IGARSS)*, *6*, 2875–2877. https://doi.org/10.1109/IGARSS.2001.978191

Lagüela, S., Díaz−Vilariño, L., Roca, D., & Lorenzo, H. (2015). Aerial thermography from low-cost UAV for the generation of thermographic digital terrain models. *Opto-Electronics Review*, *23*(1), 78–84. https://doi.org/10.1515/oere-2015-0006

Laliberte, A. S., Herrick, J. E., Rango, A., & Winters, C. (2010). Acquisition, Orthorectification, and Object-based Classification of Unmanned Aerial Vehicle (UAV) Imagery for Rangeland Monitoring. *Photogrammetric Engineering & Remote Sensing*, *76*(6), 661–672. https://doi.org/10.14358/PERS.76.6.661

Laliberte, A. S., Winters, C., & Rango, A. (2011). UAS remote sensing missions for rangeland applications. *Geocarto International*, *26*(2), 141–156. https://doi.org/10.1080/10106049.2010.534557

Lamb, D. w., Weedon, M. m., & Bramley, R. g. v. (2004). Using remote sensing to predict grape phenolics and colour at harvest in a Cabernet Sauvignon vineyard: Timing observations against vine phenology and optimising image resolution. *Australian Journal of Grape and Wine Research*, *10*(1), 46–54. https://doi.org/10.1111/j.1755-0238.2004.tb00007.x

Lan, Y., Huang, Y., E. Martin, D., & C. Hoffmann, W. (2009). Development of an Airborne Remote Sensing System for Crop Pest Management: System Integration and Verification. *Applied Engineering in Agriculture*, *25*(4), 607–615. https://doi.org/10.13031/2013.27458

Lan, Yubin, Thomson, S. J., Huang, Y., Hoffmann, W. C., & Zhang, H. (2010). Current status and future directions of precision aerial application for site-specific crop management in the USA. *Computers and Electronics in Agriculture*, *74*(1), 34–38. https://doi.org/10.1016/j.compag.2010.07.001

Li, W., Niu, Z., Chen, H., Li, D., Wu, M., & Zhao, W. (2016). Remote estimation of canopy height and aboveground biomass of maize using high-resolution stereo images from a low-cost unmanned aerial vehicle system. *Ecological Indicators*, *67*, 637–648. https://doi.org/10.1016/j.ecolind.2016.03.036

Lim, Y. S., La, P. H., Park, J. S., Lee, M. H., Pyeon, M. W., & Kim, J.-I. (2015). Calculation of Tree Height and Canopy Crown from Drone Images Using Segmentation. *Journal of the Korean Society of Surveying, Geodesy, Photogrammetry and Cartography*, *33*(6), 605–614.

Lindberg, E., & Holmgren, J. (2017). Individual Tree Crown Methods for 3D Data from Remote Sensing. *Current Forestry Reports*, *3*(1), 19–31. https://doi.org/10.1007/s40725-017-0051-6

Lisein, J., Michez, A., Claessens, H., & Lejeune, P. (2015). Discrimination of Deciduous Tree Species from Time Series of Unmanned Aerial System Imagery. *PLOS ONE*, *10*(11), e0141006. https://doi.org/10.1371/journal.pone.0141006

Lisein, J., Pierrot-Deseilligny, M., Bonnet, S., & Lejeune, P. (2013). A Photogrammetric Workflow for the Creation of a Forest Canopy Height Model from Small Unmanned Aerial System Imagery. *Forests*, *4*(4), 922–944. https://doi.org/10.3390/f4040922

Liu, T., Im, J., & Quackenbush, L. J. (2015). A novel transferable individual tree crown delineation model based on Fishing Net Dragging and boundary classification. *ISPRS Journal of Photogrammetry and Remote Sensing*, *110*, 34–47. https://doi.org/10.1016/j.isprsjprs.2015.10.002

Liu, T., Li, R., Zhong, X., Jiang, M., Jin, X., Zhou, P., Liu, S., Sun, C., & Guo, W. (2018). Estimates of rice lodging using indices derived from UAV visible and thermal infrared images. *Agricultural and Forest Meteorology*, *252*, 144–154. https://doi.org/10.1016/j.agrformet.2018.01.021

Lobell, D. B., & Gourdji, S. M. (2012). The Influence of Climate Change on Global Crop Productivity. *Plant Physiology*, *160*(4), 1686–1697. https://doi.org/10.1104/pp.112.208298

Long, N., Millescamps, B., Guillot, B., Pouget, F., & Bertin, X. (2016). Monitoring the Topography of a Dynamic Tidal Inlet Using UAV Imagery. *Remote Sensing*, *8*(5), 1–18. https://doi.org/10.3390/rs8050387

López-López, M., Calderón, R., González-Dugo, V., Zarco-Tejada, P. J., & Fereres, E. (2016). Early Detection and Quantification of Almond Red Leaf Blotch Using High-Resolution Hyperspectral and Thermal Imagery. *Remote Sensing*, *8*(4), 276. https://doi.org/10.3390/rs8040276

Lucieer, A., Jong, S. M. de, & Turner, D. (2014). Mapping landslide displacements using Structure from Motion (SfM) and image correlation of multi-temporal UAV photography. *Progress in Physical Geography*, *38*(1), 97–116.

Lukas, V., Novák, J., Neudert, L., Svobodova, I., Rodriguez-Moreno, F., Edrees, M., & Kren, J. (2016). THE COMBINATION OF UAV SURVEY AND LANDSAT IMAGERY FOR MONITORING OF CROP VIGOR IN PRECISION AGRICULTURE. *ISPRS - International Archives of the Photogrammetry, Remote Sensing and Spatial Information Sciences*, *XLI-B8*, 953–957. https://doi.org/10.5194/isprsarchives-XLI-B8-953-2016

Ma, L., Fu, T., Blaschke, T., Li, M., Tiede, D., Zhou, Z., Ma, X., & Chen, D. (2017). Evaluation of Feature Selection Methods for Object-Based Land Cover Mapping of Unmanned Aerial Vehicle Imagery Using Random Forest and Support Vector Machine Classifiers. *ISPRS International Journal of Geo-Information*, *6*(2), 51. https://doi.org/10.3390/ijgi6020051

Madec, S., Baret, F., de Solan, B., Thomas, S., Dutartre, D., Jezequel, S., Hemmerlé, M., Colombeau, G., & Comar, A. (2017). High-Throughput Phenotyping of Plant Height: Comparing Unmanned Aerial Vehicles and Ground LiDAR Estimates. *Frontiers in Plant Science*, *8*. https://doi.org/10.3389/fpls.2017.02002

Magalhães, N. (2008). *Tratado de viticultura: A videira, a vinha eo terroir*. Chaves Ferreira.

Malinowski, R., Höfle, B., Koenig, K., Groom, G., Schwanghart, W., & Heckrath, G. (2016). Local-scale flood mapping on vegetated floodplains from radiometrically calibrated airborne LiDAR data. *ISPRS Journal of Photogrammetry and Remote Sensing*, *119*, 267–279. https://doi.org/10.1016/j.isprsjprs.2016.06.009

Mancini, F., Dubbini, M., Gattelli, M., Stecchi, F., Fabbri, S., & Gabbianelli, G. (2013). Using Unmanned Aerial Vehicles (UAV) for High-Resolution Reconstruction of Topography: The Structure from Motion Approach on Coastal Environments. *Remote Sensing*, *5*(12), 6880–6898. https://doi.org/10.3390/rs5126880

Marcal, A. R. S., & Cunha, M. (2007). Vineyard monitoring in Portugal using multi-sensor satellite images. In *GeoInformation in Europe* (Gomarasca, M.A., p. 704). Millpress.

Marchetti, F., Waske, B., Arbelo, M., Moreno-Ruíz, J. A., & Alonso-Benito, A. (2019). Mapping Chestnut Stands Using Bi-Temporal VHR Data. *Remote Sensing*, *11*(21), 2560. https://doi.org/10.3390/rs11212560

Marcial-Pablo, M. de J., Gonzalez-Sanchez, A., Jimenez-Jimenez, S. I., Ontiveros-Capurata, R. E., & Ojeda-Bustamante, W. (2019). Estimation of vegetation fraction using RGB and multispectral images from UAV. *International Journal of Remote Sensing*, *40*(2), 420–438.

Maria do Carmo Val. (2013). Technical Note 5—"Grapevine Powdery Mildew". In *ADVID Technical Notes*. ADVID - Associação para o Desenvolvimento da Viticultura Duriense. http://www.advid.pt/imagens/cadernos/1401354740109.pdf

Marques, P., Pádua, L., Adão, T., Hruška, J., Peres, E., Sousa, A., & Sousa, J. J. (2019). UAV-Based Automatic Detection and Monitoring of Chestnut Trees. *Remote Sensing*, *11*(7), 855. https://doi.org/10.3390/rs11070855

Martha, T. R., Kerle, N., van Westen, C. J., Jetten, V., & Vinod Kumar, K. (2010). Effect of Sun Elevation Angle on DSMs Derived from Cartosat-1 Data. *Photogrammetric Engineering & Remote Sensing*, *76*(4), 429–438. https://doi.org/10.14358/PERS.76.4.429

Martín, P., Zarco-Tejada, P., González, M., & Berjón, A. (2007). Using hyperspectral remote sensing to map grape quality inTempranillo'vineyards affected by iron deficiency chlorosis. *VITIS-GEILWEILERHOF-*, *46*(1), 7.

Martín, P., Zarco-Tejada, P. J., González, M. R., & Berjón, A. (2015). Using hyperspectral remote sensing to map grape quality in 'Tempranillo' vineyards affected by iron deficiency chlorosis. *VITIS - Journal of Grapevine Research*, *46*(1), 7.

Martins, L., Castro, J., Macedo, W., Marques, C., & Abreu, C. (2007). Assessment of The Spread of Chestnut Ink Disease Using Remote Sensing and Geostatistical Methods. *European Journal of Plant Pathology*, *119*(2), 159–164. https://doi.org/10.1007/s10658-007-9155-3

Martins, L., Castro, J., Marques, C., & Abreu, C. (2009). ASSESSMENT OF THE SPREAD OF CHESTNUT INK DISEASE FROM 1995 TO 2005 USING AERIAL PHOTOGRAPHY AND GEOSTATISTICAL METHODS. *Acta Horticulturae*, *844*, 349–354. https://doi.org/10.17660/ActaHortic.2009.844.48

Martins, L., Lufinha, M., Marques, C., & Abreu, C. (2001). Small Format Aerial Photography to Assess Chestnut Ink Disease. *Forest, Snow and Landscape Research*, *76*(3), 357–360.

Martins, L. M., Castro, J. P., Bento, R., & Sousa, J. J. (2015). Chestnut health monitoring by aerial photographs obtained by unnamed aerial vehicle. *Revista de Ciências Agrárias*, *38*(2), 184–190.

Martins, L. M., Lufinha, M. I., Marques, C. P., & Abreu, C. G. (2001). Small format aerial photography to assess chestnut ink disease. *Forest Snow and Landscape Research*, *73*, 357–360.

Martins, Luís, Castro, J. P., Bento, R., & Sousa, J. J. (2015). Monitorização da condição fitossanitária do castanheiro por fotografia aérea obtida com aeronave não tripulada. *Revista de Ciências Agrárias da Sociedade de Ciências Agrárias de Portugal*, *38*(2), 184–190.

Martins, Luís, Castro, J. P., & Gouveia, E. (2014). Biological control of chestnut blight in Portugal. *Acta Horticulturae*, *1043*, 51–56.

Martins, Luís, Castro, J. P., Macedo, F., Marques, C., & Abreu, C. (2005). Índices espectrais em fotografia aérea de infravermelho próximo na monitorização da doença tinta do castanheiro. *V Congresso Florestal Nacional*. V Congresso Florestal Nacional, Viseu. https://bibliotecadigital.ipb.pt/handle/10198/6038

Matese, A., Di Gennaro, S. F., & Santesteban, L. G. (2019). Methods to compare the spatial variability of UAV-based spectral and geometric information with ground autocorrelated data. A case of study for precision viticulture. *Computers and Electronics in Agriculture*, *162*, 931–940. https://doi.org/10.1016/j.compag.2019.05.038

Matese, A., Primicerio, J., Di Gennaro, F., Fiorillo, E., Vaccari, F. P., & Genesio, L. (2013). Development and Application of an Autonomous and Flexible Unmanned Aerial Vehicle for Precision Viticulture. *Acta Horticulturae*, *978*, 63–69. https://doi.org/10.17660/ActaHortic.2013.978.5

Matese, Alessandro, Baraldi, R., Berton, A., Cesaraccio, C., Di Gennaro, S. F., Duce, P., Facini, O., Mameli, M. G., Piga, A., & Zaldei, A. (2018). Estimation of Water Stress in Grapevines Using Proximal and Remote Sensing Methods. *Remote Sensing*, *10*(1), 114. https://doi.org/10.3390/rs10010114

Matese, Alessandro, & Di Gennaro, S. (2018). Practical Applications of a Multisensor UAV Platform Based on Multispectral, Thermal and RGB High Resolution Images in Precision Viticulture. *Agriculture*, *8*(7), 116. https://doi.org/10.3390/agriculture8070116

Matese, Alessandro, & Di Gennaro, S. F. (2015). Technology in precision viticulture: A state of the art review. *Int. J. Wine Res*, *7*, 69–81.

Matese, Alessandro, Di Gennaro, S. F., & Berton, A. (2016). Assessment of a canopy height model (CHM) in a vineyard using UAV-based multispectral imaging. *International Journal of Remote Sensing*, 1–11. https://doi.org/10.1080/01431161.2016.1226002

Matese, Alessandro, Toscano, P., Di Gennaro, S. F., Genesio, L., Vaccari, F. P., Primicerio, J., Belli, C., Zaldei, A., Bianconi, R., & Gioli, B. (2015). Intercomparison of UAV, Aircraft and Satellite Remote Sensing Platforms for Precision Viticulture. *Remote Sensing*, *7*(3), 2971–2990. https://doi.org/10.3390/rs70302971

Mathews, A. J. (2014). Object-based spatiotemporal analysis of vine canopy vigor using an inexpensive unmanned aerial vehicle remote sensing system. *Journal of Applied Remote Sensing*, *8*(1), 085199. https://doi.org/10.1117/1.JRS.8.085199

Mathews, A. J. (2015). A Practical UAV Remote Sensing Methodology to Generate Multispectral Orthophotos for Vineyards: Estimation of Spectral Reflectance Using Compact Digital Cameras. *International Journal of Applied Geospatial Research*, *6*(4), 65–87. https://doi.org/10.4018/ijagr.2015100104

Mathews, A. J., & Jensen, J. L. R. (2013). Visualizing and Quantifying Vineyard Canopy LAI Using an Unmanned Aerial Vehicle (UAV) Collected High Density Structure from Motion Point Cloud. *Remote Sensing*, *5*(5), 2164–2183. https://doi.org/10.3390/rs5052164

Maurer, C. R., & Raghavan,  and V. (2003). A linear time algorithm for computing exact Euclidean distance transforms of binary images in arbitrary dimensions. *IEEE Transactions on Pattern Analysis and Machine Intelligence*, *25*(2), 265–270. https://doi.org/10.1109/TPAMI.2003.1177156

McHugh, M. L. (2012). Interrater reliability: The kappa statistic. *Biochemia Medica: Biochemia Medica*, *22*(3), 276–282.

McKinsey, S. (2009). *Charting our water future: Economic framework to inform decision-making. 2030 Water Resources Group*.

Mejias, L., Lai, J., & Bruggemann, T. (2015). Sensors for Missions. In K. P. Valavanis & G. J. Vachtsevanos (Eds.), *Handbook of Unmanned Aerial Vehicles* (pp. 385–399). Springer Netherlands. http://link.springer.com/10.1007/978-90-481-9707-1_6

Melville, B., Lucieer, A., & Aryal, J. (2019). Classification of Lowland Native Grassland Communities Using Hyperspectral Unmanned Aircraft System (UAS) Imagery in the Tasmanian Midlands. *Drones*, *3*(1), 5. https://doi.org/10.3390/drones3010005

Mendes, J., Santos, F. N. d, Ferraz, N., Couto, P., & Morais, R. (2016). Vine Trunk Detector for a Reliable Robot Localization System. *2016 International Conference on Autonomous Robot Systems and Competitions (ICARSC)*, 1–6. https://doi.org/10.1109/ICARSC.2016.68

Merino, L., Caballero, F., Martínez-de-Dios, J. R., Maza, I., & Ollero, A. (2011). An Unmanned Aircraft System for Automatic Forest Fire Monitoring and Measurement. *Journal of Intelligent & Robotic Systems*, *65*(1–4), 533–548. https://doi.org/10.1007/s10846-011-9560-x

Messinger, M., & Silman, M. (2016). Unmanned Aerial Vehicles for The Assessment and Monitoring of Environmental Contamination: An Example From Coal Ash Spills. *Environmental Pollution*, *218*, 889–894. http://dx.doi.org/10.1016/j.envpol.2016.08.019

Meyer, F. (1994). Topographic distance and watershed lines. *Signal Processing*, *38*(1), 113–125. https://doi.org/10.1016/0165-1684(94)90060-4

Meyer, G. E., & Neto, J. C. (2008). Verification of color vegetation indices for automated crop imaging applications. *Computers and Electronics in Agriculture*, *63*(2), 282–293. https://doi.org/10.1016/j.compag.2008.03.009

Michel, J., Youssefi, D., & Grizonnet, M. (2014). Stable mean-shift algorithm and its application to the segmentation of arbitrarily large remote sensing images. *IEEE Transactions on Geoscience and Remote Sensing*, *53*(2), 952–964.

Michez, A., Piégay, H., Lisein, J., Claessens, H., & Lejeune, P. (2016). Classification of riparian forest species and health condition using multi-temporal and hyperspatial imagery from unmanned aerial system. *Environmental Monitoring and Assessment*, *188*(3), 146. https://doi.org/10.1007/s10661-015-4996-2

Milella, A., Marani, R., Petitti, A., & Reina, G. (2019). In-field high throughput grapevine phenotyping with a consumer-grade depth camera. *Computers and Electronics in Agriculture*, *156*, 293–306. https://doi.org/10.1016/j.compag.2018.11.026

Mirijovský, J., & Langhammer, J. (2015). Multitemporal Monitoring of the Morphodynamics of a Mid-Mountain Stream Using UAS Photogrammetry. *Remote Sensing*, *7*(7), 8586–8609. https://doi.org/10.3390/rs70708586

Moeckel, T., Dayananda, S., Nidamanuri, R. R., Nautiyal, S., Hanumaiah, N., Buerkert, A., & Wachendorf, M. (2018). Estimation of Vegetable Crop Parameter by Multi-temporal UAV-Borne Images. *Remote Sensing*, *10*(5), 805. https://doi.org/10.3390/rs10050805

Mohan, M., Silva, C. A., Klauberg, C., Jat, P., Catts, G., Cardil, A., Hudak, A. T., & Dia, M. (2017). Individual Tree Detection from Unmanned Aerial Vehicle (UAV) Derived Canopy Height Model in an Open Canopy Mixed Conifer Forest. *Forests*, *8*(9), 340. https://doi.org/10.3390/f8090340

Montagnoli, A., Fusco, S., Terzaghi, M., Kirschbaum, A., Pflugmacher, D., Cohen, W. B., Scippa, G. S., & Chiatante, D. (2015). Estimating forest aboveground biomass by low density lidar data in mixed broad-leaved forests in the Italian Pre-Alps. *Forest Ecosystems*, *2*(1), 10. https://doi.org/10.1186/s40663-015-0035-6

Morais, R., Fernandes, M. A., Matos, S. G., Serôdio, C., Ferreira, P. J. S. G., & Reis, M. J. C. S. (2008). A ZigBee multi-powered wireless acquisition device for remote sensing applications in precision viticulture. *Computers and Electronics in Agriculture*, *62*(2), 94–106. https://doi.org/10.1016/j.compag.2007.12.004

Moran, P. a. P. (1950). NOTES ON CONTINUOUS STOCHASTIC PHENOMENA. *Biometrika*, *37*(1–2), 17–23. https://doi.org/10.1093/biomet/37.1-2.17

Mozas-Calvache, A. T., Pérez-García, J. L., Cardenal-Escarcena, F. J., Mata-Castro, E., & Delgado-García, J. (2012). Method for photogrammetric surveying of archaeological sites with light aerial platforms. *Journal of Archaeological Science*, *39*(2), 521–530. http://dx.doi.org/10.1016/j.jas.2011.10.007

Muchiri, N., & Kimathi, S. (2016). A Review of Applications and Potential Applications of UAV. *Proceedings of Sustainable Research and Innovation Conference*, *0*(0), 280–283.

Naidu, R. A., Perry, E. M., Pierce, F. J., & Mekuria, T. (2009). The potential of spectral reflectance technique for the detection of Grapevine leafroll-associated virus-3 in two red-berried wine grape cultivars. *Computers and Electronics in Agriculture*, *66*(1), 38–45. https://doi.org/10.1016/j.compag.2008.11.007

Näsi, R., Honkavaara, E., Lyytikäinen-Saarenmaa, P., Blomqvist, M., Litkey, P., Hakala, T., Viljanen, N., Kantola, T., Tanhuanpää, T., & Holopainen, M. (2015). Using UAV-Based Photogrammetry and Hyperspectral Imaging for Mapping Bark Beetle Damage at Tree-Level. *Remote Sensing*, *7*(11), 15467–15493. https://doi.org/10.3390/rs71115467

Navia, J., Mondragon, I., Patino, D., & Colorado, J. (2016). Multispectral mapping in agriculture: Terrain mosaic using an autonomous quadcopter UAV. *2016 International Conference on Unmanned Aircraft Systems (ICUAS)*, 1351–1358. http://ieeexplore.ieee.org/xpls/abs_all.jsp?arnumber=7502606

Nebiker, S., Annen, A., Scherrer, M., & Oesch, D. (2008). A light-weight multispectral sensor for micro UAV—Opportunities for very high resolution airborne remote sensing. *The International Archives of the Photogrammetry, Remote Sensing and Spatial Information Sciences*, *37*(B1), 1193–1199.

Nebiker, S., Lack, N., Abächerli, M., & Läderach, S. (2016). Light-weight multispectral UAV sensors and their capabilities for predicting grain yield and detecting plant diseases. *ISPRS - International Archives of the Photogrammetry, Remote Sensing and Spatial Information Sciences*, *XLI-B1*, 963–970. https://doi.org/10.5194/isprsarchives-XLI-B1-963-2016

Nevalainen, O., Honkavaara, E., Tuominen, S., Viljanen, N., Hakala, T., Yu, X., Hyyppä, J., Saari, H., Pölönen, I., Imai, N. N., & Tommaselli, A. M. G. (2017). Individual Tree Detection and Classification with UAV-Based Photogrammetric Point Clouds and Hyperspectral Imaging. *Remote Sensing*, *9*. https://doi.org/10.3390/rs9030185

Nex, F., & Remondino, F. (2013). UAV for 3D mapping applications: A review. *Applied Geomatics*, *6*(1), 1–15. https://doi.org/10.1007/s12518-013-0120-x

Niethammer, U., James, M. R., Rothmund, S., Travelletti, J., & Joswig, M. (2012). UAV-based Remote Sensing of The Super-Sauze Landslide: Evaluation and Results. *Engineering Geology*, *128*, 2–11. http://dx.doi.org/10.1016/j.enggeo.2011.03.012

Nolan, A. P., Park, S., O'Connell, M., Fuentes, S., Ryu, D., & Chung, H. (2015, December 4). *Automated detection and segmentation of vine rows using high resolution UAS imagery in a commercial vineyard*. 21st International Congress on Modelling and Simulation, Gold Coast, Australia. https://www.researchgate.net/profile/Mark_Oconnell/publication/284206199_Automated_detection_and_segmentation_of_vine_rows_using_high_resolution_UAS_imagery_in_a_commercial_vineyard/links/566e1c9f08ae1a797e405f39.pdf

Nolan, A., Park, S., Fuentes, S., Ryu, D., & Chung, H. (2015). *Automated detection and segmentation of vine rows using high resolution UAS imagery in a commercial vineyard*. *29*, 1406–1412.

Ok, A. O., & Ozdarici-Ok, A. (2017). 2-D delineation of individual citrus trees from UAV-based dense photogrammetric surface models. *International Journal of Digital Earth*, *0*(0), 1–26. https://doi.org/10.1080/17538947.2017.1337820

Oleire-Oltmanns, S., Marzolff, I., Peter, D. K., & Ries, B. J. (2012). Unmanned Aerial Vehicle (UAV) for Monitoring Soil Erosion in Morocco. *Remote Sensing*, *4*(11), 3390–3416. https://doi.org/10.3390/rs4113390

Otsu, N. (1979). A Threshold Selection Method from Gray-Level Histograms. *IEEE Transactions on Systems, Man, and Cybernetics*, *9*(1), 62–66. https://doi.org/10.1109/TSMC.1979.4310076

Ozdemir, G., Sessiz, A., & Pekitkan, F. G. (2017). Precision viticulture tools to production of high quality grapes. *Scientific Papers-Series B-Horticulture*, *61*, 209–218.

Pádua, L., Adão, T., Hruška, J., Sousa, J. J., Peres, E., Morais, R., & Sousa, A. (2017). Very high resolution aerial data to support multi-temporal precision agriculture information management. *Procedia Computer Science*, *121*, 407–414. https://doi.org/10.1016/j.procs.2017.11.055

Pádua, L., Guimarães, N., Adão, T., Marques, P., Peres, E., Sousa, A., & Sousa, J. J. (2019). Classification of an Agrosilvopastoral System Using RGB Imagery from an Unmanned Aerial Vehicle. In P. Moura Oliveira, P. Novais, & L. P. Reis (Eds.), *Progress in Artificial Intelligence* (pp. 248–257). Springer International Publishing. https://doi.org/10.1007/978-3-030-30241-2_22

Pádua, L., Hruška, J., Bessa, J., Adão, T., Martins, L. M., Gonçalves, J. A., Peres, E., Sousa, A. M. R., Castro, J. P., & Sousa, J. J. (2017). Multi-Temporal Analysis of Forestry and Coastal Environments Using UASs. *Remote Sensing*, *10*(1), 24. https://doi.org/10.3390/rs10010024

Pádua, L., Marques, P., Adão, T., Guimarães, N., Sousa, A., Peres, E., & Sousa, J. J. (2019). Vineyard Variability Analysis through UAV-Based Vigour Maps to Assess Climate Change Impacts. *Agronomy*, *9*(10). https://doi.org/10.3390/agronomy9100581

Pádua, L., Marques, P., Adáo, T., Hruška, J., Peres, E., Morais, R., Sousa, A., & Sousa, J. J. (2018). UAS-based Imagery and Photogrammetric Processing for Tree Height and Crown Diameter Extraction. *Proceedings of the International Conference on Geoinformatics and Data Analysis*, 87–91. https://doi.org/10.1145/3220228.3220241

Pádua, L., Marques, P., Hruška, J., Adão, T., Bessa, J., Sousa, A., Peres, E., Morais, R., & Sousa, J. J. (2018). Vineyard properties extraction combining UAS-based RGB imagery with elevation data. *International Journal of Remote Sensing*, *39*(15–16), 5377–5401. https://doi.org/10.1080/01431161.2018.1471548

Pádua, L., Marques, P., Hruška, J., Adão, T., Peres, E., Morais, R., & Sousa, J. J. (2018). Multi-Temporal Vineyard Monitoring through UAV-Based RGB Imagery. *Remote Sensing*, *10*(12), 1907. https://doi.org/10.3390/rs10121907

Pádua, L., Vanko, J., Hruška, J., Adão, T., Sousa, J. J., Peres, E., & Morais, R. (2017). UAS, sensors, and data processing in agroforestry: A review towards practical applications. *International Journal of Remote Sensing*, *38*(8–10), 2349–2391. https://doi.org/10.1080/01431161.2017.1297548

Pajares, G. (2015). Overview and Current Status of Remote Sensing Applications Based on Unmanned Aerial Vehicles (UAVs). *Photogrammetric Engineering & Remote Sensing*, *81*(4), 281–329. https://doi.org/10.14358/PERS.81.4.281

Panagiotidis, D., Abdollahnejad, A., Surový, P., & Chiteculo, V. (2017). Determining tree height and crown diameter from high-resolution UAV imagery. *International Journal of Remote Sensing*, *38*(8–10), 2392–2410. https://doi.org/10.1080/01431161.2016.1264028

Pappalardo, J. (2003). Unmanned aircraft roadmap reflects changing priorities. *National Defense*, *87*(392), 30.

Park, S., Nolan, A., Ryu, D., Fuentes, S., Hernandez, E., Chung, H., & O'Connell, M. (2015). Estimation of crop water stress in a nectarine orchard using high-resolution imagery from unmanned aerial vehicle (UAV). *International Congress on Modelling and Simulation (MODSIM)(Tony Weber and Malcolm McPhee 29 November 2015 to 04 December 2015)*, 1413–1419. https://www.researchgate.net/profile/Sigfredo_Fuentes/publication/298070136_park/links/56e5daa008ae68afa112b648.pdf

Peña, J. M., Torres-Sánchez, J., Castro, A. I. de, Kelly, M., & López-Granados, F. (2013). Weed Mapping in Early-Season Maize Fields Using Object-Based Analysis of Unmanned Aerial Vehicle (UAV) Images. *PLOS ONE*, *8*(10), e77151. https://doi.org/10.1371/journal.pone.0077151

Peña-Barragán, J. M., Ngugi, M. K., Plant, R. E., & Six, J. (2011). Object-based crop identification using multiple vegetation indices, textural features and crop phenology. *Remote Sensing of Environment*, *115*(6), 1301–1316. https://doi.org/10.1016/j.rse.2011.01.009

Pereira, E., Bencatel, R., Correia, J., xe, lix, L., Gon, xe, alves, G., Morgado, J., & Sousa, J. (2009). Unmanned Air Vehicles for Coastal and Environmental Research. *Journal of Coastal Research*, 1557–1561.

Pereira, M., Caramelo, L., Gouveia, C., Gomes-Laranjo, J., Magalhães, M., Tarquis, M., Moratiel, R., & Vázquez, E. V. (2011). Assessment of weather-related risk on chestnut productivity. *Natural Hazards & Earth System Sciences*, *11*(10).

Pettorelli, N., Laurance, W. F., O'Brien, T. G., Wegmann, M., Nagendra, H., & Turner, W. (2014). Satellite remote sensing for applied ecologists: Opportunities and challenges. *Journal of Applied Ecology*, *51*(4), 839–848. https://doi.org/10.1111/1365-2664.12261

Poblete-Echeverría, C., Olmedo, G. F., Ingram, B., & Bardeen, M. (2017). Detection and Segmentation of Vine Canopy in Ultra-High Spatial Resolution RGB Imagery Obtained from Unmanned Aerial Vehicle (UAV): A Case Study in a Commercial Vineyard. *Remote Sensing*, *9*(3), 268. https://doi.org/10.3390/rs9030268

Pölönen, I., Saari, H., Kaivosoja, J., Honkavaara, E., & Pesonen, L. (2013). Hyperspectral imaging based biomass and nitrogen content estimations from light-weight UAV. *SPIE Remote Sensing*, 88870J-88870J. http://proceedings.spiedigitallibrary.org/proceeding.aspx?articleid=1757263

Ponti, M. P. (2013). Segmentation of Low-Cost Remote Sensing Images Combining Vegetation Indices and Mean Shift. *IEEE Geoscience and Remote Sensing Letters*, *10*(1), 67–70. https://doi.org/10.1109/LGRS.2012.2193113

Popescu, S. C., Wynne, R. H., & Nelson, R. F. (2003). Measuring individual tree crown diameter with lidar and assessing its influence on estimating forest volume and biomass. *Canadian Journal of Remote Sensing*, *29*(5), 564–577. https://doi.org/10.5589/m03-027

Portela, E., Roboredo, M., & Louzada, J. (2003). Assessment and Description of Magnesium Deficiencies in Chestnut Groves. *Journal of Plant Nutrition*, *26*(3), 503–523. https://doi.org/10.1081/PLN-120017662

Poulton, C. V., & Watts, M. R. (2016, August 4). *MIT and DARPA Pack Lidar Sensor Onto Single Chip*. IEEE Spectrum: Technology, Engineering, and Science News. http://spectrum.ieee.org/tech-talk/semiconductors/optoelectronics/mit-lidar-on-a-chip

Prabhakar, M., Prasad, Y. G., & Rao, M. N. (2012). Remote Sensing of Biotic Stress in Crop Plants and Its Applications for Pest Management. In B. Venkateswarlu, A. K. Shanker, C. Shanker, & M. Maheswari (Eds.), *Crop Stress and its Management: Perspectives and Strategies* (pp. 517–545). Springer Netherlands. https://doi.org/10.1007/978-94-007-2220-0_16

Primicerio, J., Gay, P., Ricauda Aimonino, D., Comba, L., Matese, A., & di Gennaro, S. f. (2015). NDVI-based vigour maps production using automatic detection of vine rows in ultra-high resolution aerial images. In *Precision agriculture '15* (Vol. 1–0, pp. 465–470). Wageningen Academic Publishers. https://doi.org/10.3920/978-90-8686-814-8_57

Primicerio, Jacopo, Caruso, G., Comba, L., Crisci, A., Gay, P., Guidoni, S., Genesio, L., Aimonino, D. R., & Vaccari, F. P. (2017). Individual plant definition and missing plant characterization in vineyards from high-resolution UAV imagery. *European Journal of Remote Sensing*, *50*(1), 179–186. https://doi.org/10.1080/22797254.2017.1308234

Primicerio, Jacopo, Di Gennaro, S. F., Fiorillo, E., Genesio, L., Lugato, E., Matese, A., & Vaccari, F. P. (2012). A flexible unmanned aerial vehicle for precision agriculture. *Precision Agriculture*, *13*(4), 517–523. https://doi.org/10.1007/s11119-012-9257-6

Proffitt, A. P. B., Bramley, R., Lamb, D., & Winter, E. (2006). *Precision viticulture: A new era in vineyard management and wine production*. Winetitles.

Proffitt, T., & Turner, N. (2017). Reducing vineyard management overheads from above. *Australian and New Zealand Grapegrower and Winemaker*, *647*(647), 46.

Puletti, N., Perria, R., & Storchi, P. (2014). Unsupervised classification of very high remotely sensed images for grapevine rows detection. *European Journal of Remote Sensing*, *47*(1), 45–54. https://doi.org/10.5721/EuJRS20144704

Puliti, S., Orka, O. H., Gobakken, T., & Næsset, E. (2015). Inventory of Small Forest Areas Using an Unmanned Aerial System. *Remote Sensing*, *7*(8), 9632–9654. https://doi.org/10.3390/rs70809632

Qi, J., Chehbouni, A., Huete, A. R., Kerr, Y. H., & Sorooshian, S. (1994). A modified soil adjusted vegetation index. *Remote Sensing of Environment*, *48*(2), 119–126. https://doi.org/10.1016/0034-4257(94)90134-1

Quater, P. B., Grimaccia, F., Leva, S., Mussetta, M., & Aghaei, M. (2014). Light Unmanned Aerial Vehicles (UAVs) for Cooperative Inspection of PV Plants. *IEEE Journal of Photovoltaics*, *4*(4), 1107–1113. https://doi.org/10.1109/JPHOTOV.2014.2323714

Quebrajo, L., Perez-Ruiz, M., Pérez-Urrestarazu, L., Martínez, G., & Egea, G. (2018). Linking thermal imaging and soil remote sensing to enhance irrigation management of sugar beet. *Biosystems Engineering*, *165*, 77–87. https://doi.org/10.1016/j.biosystemseng.2017.08.013

Quiroz, R. (2015). *Remote sensing as a monitoring tool for cropping area determination in smallholder agriculture in Tanzania and Uganda*. https://cgspace.cgiar.org/handle/10568/69110

Ramasamy, S., Sabatini, R., Gardi, A., & Liu, J. (2016). LIDAR obstacle warning and avoidance system for unmanned aerial vehicle sense-and-avoid. *Aerospace Science and Technology*, *55*, 344–358. https://doi.org/10.1016/j.ast.2016.05.020

Rehak, M., & Skaloud, J. (2015). FIXED-WING MICRO AERIAL VEHICLE FOR ACCURATE CORRIDOR MAPPING. *ISPRS Annals of Photogrammetry, Remote Sensing and Spatial Information Sciences*, *II-1/W1*, 23–31. https://doi.org/10.5194/isprsannals-II-1-W1-23-2015

Rey-Caramés, C., Diago, M. P., Martín, M. P., Lobo, A., & Tardaguila, J. (2015). Using RPAS Multi-Spectral Imagery to Characterise Vigour, Leaf Development, Yield Components and Berry Composition Variability within a Vineyard. *Remote Sensing*, *7*(11), 14458–14481. https://doi.org/10.3390/rs71114458

Rhee, D. S., Kim, Y. D., Kang, B., & Kim, D. (2017). Applications of Unmanned Aerial Vehicles in Fluvial Remote Sensing: An Overview of Recent Achievements. *KSCE Journal of Civil Engineering*, 1–15. https://doi.org/10.1007/s12205-017-1862-5

Richards, J. A. (2013). *Remote Sensing Digital Image Analysis: An Introduction* (5th ed.). Springer-Verlag. https://doi.org/10.1007/978-3-642-30062-2

Richardson, A. D., Jenkins, J. P., Braswell, B. H., Hollinger, D. Y., Ollinger, S. V., & Smith, M.-L. (2007). Use of digital webcam images to track spring green-up in a deciduous broadleaf forest. *Oecologia*, *152*(2), 323–334. https://doi.org/10.1007/s00442-006-0657-z

Rigling, D., & Prospero, S. (2017). Cryphonectria parasitica, the causal agent of chestnut blight: Invasion history, population biology and disease control. *Molecular Plant Pathology*, n/a-n/a. https://doi.org/10.1111/mpp.12542

Robin, C., Lanz, S., Soutrenon, A., & Rigling, D. (2010). Dominance of natural over released biological control agents of the chestnut blight fungus Cryphonectria parasitica in south-eastern France is associated with fitness-related traits. *Biological Control*, *53*(1), 55–61. http://dx.doi.org/10.1016/j.biocontrol.2009.10.013

Rokhmana, C. A. (2015). The Potential of UAV-based Remote Sensing for Supporting Precision Agriculture in Indonesia. *Procedia Environmental Sciences*, *24*, 245–253. https://doi.org/10.1016/j.proenv.2015.03.032

Romano, G., Zia, S., Spreer, W., Sanchez, C., Cairns, J., Araus, J. L., & Müller, J. (2011). Use of thermography for high throughput phenotyping of tropical maize adaptation in water stress. *Computers and Electronics in Agriculture*, *79*(1), 67–74. https://doi.org/10.1016/j.compag.2011.08.011

Romero, M., Luo, Y., Su, B., & Fuentes, S. (2018). Vineyard water status estimation using multispectral imagery from an UAV platform and machine learning algorithms for irrigation scheduling management. *Computers and Electronics in Agriculture*, *147*, 109–117. https://doi.org/10.1016/j.compag.2018.02.013

Rondeaux, G., Steven, M., & Baret, F. (1996). Optimization of soil-adjusted vegetation indices. *Remote Sensing of Environment*, *55*(2), 95–107. https://doi.org/10.1016/0034-4257(95)00186-7

Rosell, J. R., Llorens, J., Sanz, R., Arnó, J., Ribes-Dasi, M., Masip, J., Escolà, A., Camp, F., Solanelles, F., Gràcia, F., Gil, E., Val, L., Planas, S., & Palacín, J. (2009). Obtaining the three-dimensional structure of tree orchards from remote 2D terrestrial LIDAR scanning. *Agricultural and Forest Meteorology*, *149*(9), 1505–1515. https://doi.org/10.1016/j.agrformet.2009.04.008

Roujean, J.-L., & Breon, F.-M. (1995). Estimating PAR absorbed by vegetation from bidirectional reflectance measurements. *Remote Sensing of Environment*, *51*(3), 375–384. https://doi.org/10.1016/0034-4257(94)00114-3

Rouse, J. W., Jr., Haas, R. H., Schell, J. A., & Deering, D. W. (1974). Monitoring Vegetation Systems in the Great Plains with Erts. *NASA Special Publication*, *351*, 309.

Saari, H., Pellikka, I., Pesonen, L., Tuominen, S., Heikkilä, J., Holmlund, C., Mäkynen, J., Ojala, K., & Antila, T. (2011). Unmanned Aerial Vehicle (UAV) operated spectral camera system for forest and agriculture applications. *Proc. SPIE*, *8174*, 81740H-81740H – 15. https://doi.org/10.1117/12.897585

Salamí, E., Barrado, C., & Pastor, E. (2014). UAV Flight Experiments Applied to the Remote Sensing of Vegetated Areas. *Remote Sensing*, *6*(11), 11051–11081. https://doi.org/10.3390/rs61111051

Salamí, E., Gallardo, A., Skorobogatov, G., & Barrado, C. (2019). On-the-Fly Olive Tree Counting Using a UAS and Cloud Services. *Remote Sensing*, *11*(3), 316. https://doi.org/10.3390/rs11030316

Sankey, T., Donager, J., McVay, J., & Sankey, J. B. (2017). UAV lidar and hyperspectral fusion for forest monitoring in the southwestern USA. *Remote Sensing of Environment*, *195*, 30–43. https://doi.org/10.1016/j.rse.2017.04.007

Sankey, T. T., McVay, J., Swetnam, T. L., McClaran, M. P., Heilman, P., & Nichols, M. (2018). UAV hyperspectral and lidar data and their fusion for arid and semi-arid land vegetation monitoring. *Remote Sensing in Ecology and Conservation*, *4*(1), 20–33.

Santesteban, L. G., Di Gennaro, S. F., Herrero-Langreo, A., Miranda, C., Royo, J. B., & Matese, A. (2017). High-resolution UAV-based thermal imaging to estimate the instantaneous and seasonal variability of plant water status within a vineyard. *Agricultural Water Management*, *183*(Supplement C), 49–59. https://doi.org/10.1016/j.agwat.2016.08.026

Santos, C., Zhebentyayeva, T., Serrazina, S., Nelson, C. D., & Costa, R. (2015). Development and characterization of EST-SSR markers for mapping reaction to Phytophthora cinnamomi in Castanea spp. *Scientia Horticulturae*, *194*, 181–187. http://dx.doi.org/10.1016/j.scienta.2015.07.043

Sartor, C., Dini, F., Marinoni, D. T., Mellano, M. G., Beccaro, G. L., Alma, A., Quacchia, A., & Botta, R. (2015). Impact of the Asian wasp Dryocosmus kuriphilus (Yasumatsu) on cultivated chestnut: Yield loss and cultivar susceptibility. *Scientia Horticulturae*, *197*, 454–460.

Schirrmann, M., Giebel, A., Gleiniger, F., Pflanz, M., Lentschke, J., & Dammer, K.-H. (2016). Monitoring Agronomic Parameters of Winter Wheat Crops with Low-Cost UAV Imagery. *Remote Sensing*, *8*(9), 706. https://doi.org/10.3390/rs8090706

Schmidhuber, J., & Tubiello, F. N. (2007). Global food security under climate change. *Proceedings of the National Academy of Sciences*, *104*(50), 19703–19708. https://doi.org/10.1073/pnas.0701976104

Shamshiri, R. R., Hameed, I. A., Balasundram, S. K., Ahmad, D., Weltzien, C., & Yamin, M. (2018). Fundamental research on unmanned aerial vehicles to support precision agriculture in oil palm plantations. *Agricultural Robots-Fundamentals and Application*.

Siebert, S., & Teizer, J. (2014). Mobile 3D mapping for surveying earthwork projects using an Unmanned Aerial Vehicle (UAV) system. *Automation in Construction*, *41*, 1–14. https://doi.org/10.1016/j.autcon.2014.01.004

Simelli, I., & Tsagaris, A. (2015). The Use of Unmanned Aerial Systems (UAS) in Agriculture. *7th International Conference of HAICTA*, 730–736. http://ceur-ws.org/Vol-1498/HAICTA_2015_paper83.pdf

Smart, R. E., Dick, J. K., Gravett, I. M., & Fisher, B. M. (2017). Canopy Management to Improve Grape Yield and Wine Quality—Principles and Practices. *South African Journal of Enology and Viticulture*, *11*(1), 3–17.

Smit, J., Sithole, G., & Strever, A. (2010). Vine signal extraction–an application of remote sensing in precision viticulture. *South African Journal of Enology and Viticulture*, *31*(2), 65–74.

Soares, A. (2000). *Geoestatística para as Ciências da Terra e do Ambiente*. IST - Instituto Superior Técnico.

Sousa, A., & Muge, F. (1990). *Elementos de Geoestatística*. IST - Instituto Superior Técnico.

Sripada, R. P., Heiniger, R. W., White, J. G., & Meijer, A. D. (2006). Aerial Color Infrared Photography for Determining Early In-Season Nitrogen Requirements in Corn. *Agronomy Journal*, *98*(4), 968–977. https://doi.org/10.2134/agronj2005.0200

Steyn, J., Tudó, J. L. A., & Benavent, J. L. A. (2016). *Grapevine vigour and within vineyard variability: A review*.

Sullivan, D. G., Fulton, J. P., Shaw, J. N., & Bland, G. (2007). Evaluating the sensitivity of an unmanned thermal infrared aerial system to detect water stress in a cotton canopy. *Transactions of the ASABE*, *50*(6), 1963–1969.

Sullivan, J. M. (2006). Evolution or revolution? The rise of UAVs. *IEEE Technology and Society Magazine*, *25*(3), 43–49. https://doi.org/10.1109/MTAS.2006.1700021

Suomalainen, J., Anders, N., Iqbal, S., Roerink, G., Franke, J., Wenting, P., Hünniger, D., Bartholomeus, H., Becker, R., & Kooistra, L. (2014). A Lightweight Hyperspectral Mapping System and Photogrammetric Processing Chain for Unmanned Aerial Vehicles. *Remote Sensing*, *6*(11), 11013–11030. https://doi.org/10.3390/rs61111013

Surový, P., Ribeiro, N. A., & Panagiotidis, D. (2018). Estimation of positions and heights from UAV-sensed imagery in tree plantations in agrosilvopastoral systems. *International Journal of Remote Sensing*. http://www.tandfonline.com/doi/abs/10.1080/01431161.2018.1434329

Tamminga, A., Hugenholtz, C., Eaton, B., & Lapointe, M. (2015). Hyperspatial Remote Sensing of Channel Reach Morphology and Hydraulic Fish Habitat Using an Unmanned Aerial Vehicle (UAV): A First Assessment in the Context of River Research and Management. *River Research and Applications*, *31*(3), 379–391. https://doi.org/10.1002/rra.2743

Tanteri, L., Rossi, G., Tofani, V., Vannocci, P., Moretti, S., & Casagli, N. (2017). Multitemporal UAV Survey for Mass Movement Detection and Monitoring. In M. Mikos, B. Tiwari, Y. Yin, & K. Sassa (Eds.), *Advancing Culture of Living with Landslides: Volume 2 Advances in Landslide Science* (pp. 153–161). Springer International Publishing. https://doi.org/10.1007/978-3-319-53498-5_18

Teodoro, A., Taveira-Pinto, F., & Santos, I. (2014). Morphological and statistical analysis of the impact of breakwaters under construction on a sand spit area (Douro River estuary). *Journal of Coastal Conservation*, *18*(3), 177–191.

Thenkabail, P. S., Smith, R. B., & De Pauw, E. (2000). Hyperspectral Vegetation Indices and Their Relationships with Agricultural Crop Characteristics. *Remote Sensing of Environment*, *71*(2), 158–182. https://doi.org/10.1016/S0034-4257(99)00067-X

Thiel, C., & Schmullius, C. (2017). Comparison of UAV photograph-based and airborne lidar-based point clouds over forest from a forestry application perspective. *International Journal of Remote Sensing*, *38*(8–10), 2411–2426. https://doi.org/10.1080/01431161.2016.1225181

Tilly, N., Hoffmeister, D., Cao, Q., Huang, S., Lenz-Wiedemann, V., Miao, Y., & Bareth, G. (2014). Multitemporal crop surface models: Accurate plant height measurement and biomass estimation with terrestrial laser scanning in paddy rice. *Journal of Applied Remote Sensing*, *8*(1), 083671.

Tisseyre, B., Ojeda, H., & Taylor, J. (2007). New technologies and methodologies for site-specific viticulture. *Journal International Des Sciences de La Vigne et Du Vin*, *41*(2), 63–76.

Torres-Sánchez, J., López-Granados, F., & Peña, J. M. (2015). An automatic object-based method for optimal thresholding in UAV images: Application for vegetation detection in herbaceous crops. *Computers and Electronics in Agriculture*, *114*, 43–52. https://doi.org/10.1016/j.compag.2015.03.019

Torres-Sánchez, J., Peña, J. M., de Castro, A. I., & López-Granados, F. (2014). Multi-temporal mapping of the vegetation fraction in early-season wheat fields using images from UAV. *Computers and Electronics in Agriculture*, *103*, 104–113. https://doi.org/10.1016/j.compag.2014.02.009

Torres-Sánchez, Jorge, López-Granados, F., Serrano, N., Arquero, O., & Peña, J. M. (2015). High-Throughput 3-D Monitoring of Agricultural-Tree Plantations with Unmanned Aerial Vehicle (UAV) Technology. *PLOS ONE*, *10*(6), e0130479. https://doi.org/10.1371/journal.pone.0130479

Troen, I., & Lundtang Petersen, E. (1989). *European Wind Atlas*. Riso National Laboratory. http://orbit.dtu.dk/files/112135732/European_Wind_Atlas.pdf

Tucci, G., Parisi, E. I., Castelli, G., Errico, A., Corongiu, M., Sona, G., Viviani, E., Bresci, E., & Preti, F. (2019). Multi-Sensor UAV Application for Thermal Analysis on a Dry-Stone Terraced Vineyard in Rural Tuscany Landscape. *ISPRS International Journal of Geo-Information*, *8*(2), 87. https://doi.org/10.3390/ijgi8020087

Tucker, C. J. (1979). Red and photographic infrared linear combinations for monitoring vegetation. *Remote Sensing of Environment*, *8*(2), 127–150. https://doi.org/10.1016/0034-4257(79)90013-0

Turner, D., Lucieer, A., & Watson, C. S. (2011). Development of an Unmanned Aerial Vehicle (UAV) for hyper-resolution vineyard mapping based on visible, multispectral and thermal imagery. *Proceedings of 34th International Symposium on Remote Sensing of Environment (ISRSE)*. 34th International Symposium on Remote Sensing of Environment (ISRSE), Sydney, Australia.

Turner, Darren, Lucieer, A., & de Jong, M. S. (2015). Time Series Analysis of Landslide Dynamics Using an Unmanned Aerial Vehicle (UAV). *Remote Sensing*, *7*(2), 1736–1757. https://doi.org/10.3390/rs70201736

Turner, Darren, Lucieer, A., Malenovský, Z., King, D. H., & Robinson, S. A. (2014). Spatial Co-Registration of Ultra-High Resolution Visible, Multispectral and Thermal Images Acquired with a Micro-UAV over Antarctic Moss Beds. *Remote Sensing*, *6*(5), 4003–4024. https://doi.org/10.3390/rs6054003

Turner, Darren, Lucieer, A., & Watson, C. (2012). An Automated Technique for Generating Georectified Mosaics from Ultra-High Resolution Unmanned Aerial Vehicle (UAV) Imagery, Based on Structure from Motion (SfM) Point Clouds. *Remote Sensing*, *4*(5), 1392–1410. https://doi.org/10.3390/rs4051392

Turner, I. L., Harley, M. D., & Drummond, C. D. (2016). UAVs for Coastal Surveying. *Coastal Engineering*, *114*, 19–24. http://dx.doi.org/10.1016/j.coastaleng.2016.03.011

Turner, W., Spector, S., Gardiner, N., Fladeland, M., Sterling, E., & Steininger, M. (2003). Remote sensing for biodiversity science and conservation. *Trends in Ecology & Evolution*, *18*(6), 306–314. https://doi.org/10.1016/S0169-5347(03)00070-3

United Nations. (2015). Transforming our world: The 2030 agenda for sustainable development. *Resolution Adopted by the General Assembly*.

Uto, K., Seki, H., Saito, G., & Kosugi, Y. (2013). Characterization of Rice Paddies by a UAV-Mounted Miniature Hyperspectral Sensor System. *IEEE Journal of Selected Topics in Applied Earth Observations and Remote Sensing*, *6*(2), 851–860. https://doi.org/10.1109/JSTARS.2013.2250921

Valverde, A., González-Tirante, M., Medina-Sierra, M., Rivas, R., Santa-Regina, I., & Igual, J. M. (2017). Culturable bacterial diversity from the chestnut (Castanea sativa Mill.) phyllosphere and antagonism against the fungi causing the chestnut blight and ink diseases. *Microbiology 2017, Vol. 3, Pages 293-314*. https://doi.org/10.3934/microbiol.2017.2.293

van Leeuwen, C. (2010). 9 - Terroir: The effect of the physical environment on vine growth, grape ripening and wine sensory attributes. In A. G. Reynolds (Ed.), *Managing Wine Quality* (pp. 273–315). Woodhead Publishing. https://doi.org/10.1533/9781845699284.3.273

Vance, A. J., Reeve, A. L., & Skinkis, P. A. (2013). *The role of canopy management in vine balance* (p. 12) [Technical Report]. Corvallis, Or. : Extension Service, Oregon State University. https://ir.library.oregonstate.edu/concern/open_educational_resources/q524jp028?locale=en

Vanegas, F., Bratanov, D., Powell, K., Weiss, J., & Gonzalez, F. (2018). A Novel Methodology for Improving Plant Pest Surveillance in Vineyards and Crops Using UAV-Based Hyperspectral and Spatial Data. *Sensors*, *18*(1), 260. https://doi.org/10.3390/s18010260

Vanham, D., Hoekstra, A. Y., & Bidoglio, G. (2013). Potential water saving through changes in European diets. *Environment International*, *61*, 45–56.

Vannini, A., Vettraino, A. M., Fabi, A., Montaghi, A., Valentini, R., & Belli, C. (2005). MONITORING INK DISEASE OF CHESTNUT WITH THE AIRBORNE MULTISPECTRAL SYSTEM A.S.P.I.S. *Acta Horticulturae*, *693*, 529–534. https://doi.org/10.17660/ActaHortic.2005.693.68

Vega, F. A., Ramírez, F. C., Saiz, M. P., & Rosúa, F. O. (2015). Multi-temporal imaging using an unmanned aerial vehicle for monitoring a sunflower crop. *Biosystems Engineering*, *132*, 19–27.

Vettraino, A. M., Morel, O., Perlerou, C., Robin, C., Diamandis, S., & Vannini, A. (2005). Occurrence and distribution of Phytophthora species in European chestnut stands, and their association with Ink Disease and crown decline. *European Journal of Plant Pathology*, *111*(2), 169. https://doi.org/10.1007/s10658-004-1882-0

Von Bueren, S., & Yule, I. (2013). Multispectral aerial imaging of pasture quality and biomass using unmanned aerial vehicles (UAV). *Accurate and Efficient Use of Nutrients on Farms, Occasional Report*, *26*.

Wagner, M. (2015). *Unmanned Aerial Vehicles* (SSRN Scholarly Paper ID 2584652). Social Science Research Network. http://papers.ssrn.com/abstract=2584652

Wallace, L. (2013). Assessing the stability of canopy maps produced from UAV-LiDAR data. *2013 IEEE International Geoscience and Remote Sensing Symposium - IGARSS*, 3879–3882. https://doi.org/10.1109/IGARSS.2013.6723679

Wallace, L., Lucieer, A., & Watson, C. S. (2014). Evaluating Tree Detection and Segmentation Routines on Very High Resolution UAV LiDAR Data. *IEEE Transactions on Geoscience and Remote Sensing*, *52*(12), 7619–7628. https://doi.org/10.1109/TGRS.2014.2315649

Wallace, L. O., Lucieer, A., Turner, D., & Watson, C. S. (2011, October 19). *Error assessment and mitigation for hyper-temporal UAV-borne LiDAR surveys of forest inventory*. SilviLaser 2011, Hobart, Tasmania. http://events.cdesign.com.au/ei/viewpdf.esp?id=297&file=P:/Eventwin/docs/pdf/silvi2011Abstract00033.pdf

Wallace, Luke, Lucieer, A., Malenovský, Z., Turner, D., & Vopěnka, P. (2016). Assessment of Forest Structure Using Two UAV Techniques: A Comparison of Airborne Laser Scanning and Structure from Motion (SfM) Point Clouds. *Forests*, *7*(3), 62. https://doi.org/10.3390/f7030062

Wallace, Luke, Lucieer, A., & Watson, C. S. (2014). Evaluating Tree Detection and Segmentation Routines on Very High Resolution UAV LiDAR Data. *IEEE Transactions on Geoscience and Remote Sensing*, *52*(12), 7619–7628. https://doi.org/10.1109/TGRS.2014.2315649

Wallace, Luke, Lucieer, A., Watson, C., & Turner, D. (2012). Development of a UAV-LiDAR System with Application to Forest Inventory. *Remote Sensing*, *4*(6), 1519–1543. https://doi.org/10.3390/rs4061519

Wang, Jianghao, Ge, Y., Heuvelink, G. B. M., Zhou, C., & Brus, D. (2012). Effect of the sampling design of ground control points on the geometric correction of remotely sensed imagery. *International Journal of Applied Earth Observation and Geoinformation*, *18*, 91–100. http://dx.doi.org/10.1016/j.jag.2012.01.001

Wang, Jinxia, Mendelsohn, R., Dinar, A., Huang, J., Rozelle, S., & Zhang, L. (2009). The impact of climate change on China's agriculture. *Agricultural Economics*, *40*(3), 323–337. https://doi.org/10.1111/j.1574-0862.2009.00379.x

Ward Jr, J. H. (1963). Hierarchical grouping to optimize an objective function. *Journal of the American Statistical Association*, *58*(301), 236–244.

Ward, S., Hensler, J., Alsalam, B., & Gonzalez, L. F. (2016, March 5). Autonomous UAVs wildlife detection using thermal imaging, predictive navigation and computer vision. *Australian Research Centre for Aerospace Automation; School of Electrical Engineering & Computer Science; Institute for Future Environments; Science & Engineering Faculty*. 2016 IEEE Aerospace Conference, Yellowstone Conference Center, Big Sky, Montana. http://eprints.qut.edu.au/92309/

Watts, A. C., Ambrosia, V. G., & Hinkley, E. A. (2012). Unmanned Aircraft Systems in Remote Sensing and Scientific Research: Classification and Considerations of Use. *Remote Sensing*, *4*(6), 1671–1692. https://doi.org/10.3390/rs4061671

Wehrhan, M., Rauneker, P., & Sommer, M. (2016). UAV-Based Estimation of Carbon Exports from Heterogeneous Soil Landscapes—A Case Study from the CarboZALF Experimental Area. *Sensors*, *16*(2), 255. https://doi.org/10.3390/s16020255

Wei, L., Yang, B., Jiang, J., Cao, G., & Wu, M. (2017). Vegetation filtering algorithm for UAV-borne lidar point clouds: A case study in the middle-lower Yangtze River riparian zone. *International Journal of Remote Sensing*, *38*(8–10), 2991–3002. https://doi.org/10.1080/01431161.2016.1252476

Weiss, M., & Baret, F. (2017). Using 3D Point Clouds Derived from UAV RGB Imagery to Describe Vineyard 3D Macro-Structure. *Remote Sensing*, *9*(2), 111. https://doi.org/10.3390/rs9020111

Whitehead, K., & Hugenholtz, C. H. (2014). Remote sensing of the environment with small unmanned aircraft systems (UASs), part 1: A review of progress and challenges. *Journal of Unmanned Vehicle Systems*, *02*(03), 69–85. https://doi.org/10.1139/juvs-2014-0006

Willkomm, M., Bolten, A., & Bareth, G. (2016). Non-destructive monitoring of rice by hyperspectral in-field spectrometry and UAV-based remote sensing: Case study of field-grown rice in north Rhine-Westphalia, Germany. *ISPRS - International Archives of the Photogrammetry, Remote Sensing and Spatial Information Sciences*, *XLI-B1*, 1071–1077. https://doi.org/10.5194/isprs-archives-XLI-B1-1071-2016

Woebbecke, D. M. (University of N., Meyer, G. E., Von Bargen, K., & Mortensen, D. A. (1995). Color indices for weed identification under various soil, residue, and lighting conditions. *Transactions of the ASAE (USA)*. http://agris.fao.org/agris-search/search.do?recordID=US9561468

Xiang, H., & Tian, L. (2011). Development of a low-cost agricultural remote sensing system based on an autonomous unmanned aerial vehicle (UAV). *Biosystems Engineering*, *108*(2), 174–190. http://dx.doi.org/10.1016/j.biosystemseng.2010.11.010

Xie, Y., Sha, Z., & Yu, M. (2008). Remote sensing imagery in vegetation mapping: A review. *Journal of Plant Ecology*, *1*(1), 9–23. https://doi.org/10.1093/jpe/rtm005

Yin, D., & Wang, L. (2019). Individual mangrove tree measurement using UAV-based LiDAR data: Possibilities and challenges. *Remote Sensing of Environment*, *223*, 34–49. https://doi.org/10.1016/j.rse.2018.12.034

Yu, X., Liang, X., Hyyppä, J., Kankare, V., Vastaranta, M., & Holopainen, M. (2013). Stem biomass estimation based on stem reconstruction from terrestrial laser scanning point clouds. *Remote Sensing Letters*, *4*(4), 344–353.

Yue, J., Yang, G., Li, C., Li, Z., Wang, Y., Feng, H., & Xu, B. (2017). Estimation of Winter Wheat Above-Ground Biomass Using Unmanned Aerial Vehicle-Based Snapshot Hyperspectral Sensor and Crop Height Improved Models. *Remote Sensing*, *9*(7), 708. https://doi.org/10.3390/rs9070708

Yunusa, I. A. M., Walker, R. R., & Lu, P. (2004). Evapotranspiration components from energy balance, sapflow and microlysimetry techniques for an irrigated vineyard in inland Australia. *Agricultural and Forest Meteorology*, *127*(1), 93–107. https://doi.org/10.1016/j.agrformet.2004.07.001

Zarco-Tejada, P., Berjón, A., & Miller, J. (2004). Stress detection in crops with hyperspectral remote sensing and physical simulation models. *Proceedings of the Airborne Imaging Spectroscopy Workshop-Bruges*. Proceedings of the Airborne imaging spectroscopy workshop-Bruges, Bruges, Belgium.

Zarco-Tejada, P. J., Berjón, A., López-Lozano, R., Miller, J. R., Martín, P., Cachorro, V., González, M. R., & de Frutos, A. (2005). Assessing vineyard condition with hyperspectral indices: Leaf and canopy reflectance simulation in a row-structured discontinuous canopy. *Remote Sensing of Environment*, *99*(3), 271–287. https://doi.org/10.1016/j.rse.2005.09.002

Zarco-Tejada, P. J., Camino, C., Beck, P. S. A., Calderon, R., Hornero, A., Hernández-Clemente, R., Kattenborn, T., Montes-Borrego, M., Susca, L., Morelli, M., Gonzalez-Dugo, V., North, P. R. J., Landa, B. B., Boscia, D., Saponari, M., & Navas-Cortes, J. A. (2018). Previsual symptoms of Xylella fastidiosa infection revealed in spectral plant-trait alterations. *Nature Plants*, *4*(7), 432–439. https://doi.org/10.1038/s41477-018-0189-7

Zarco-Tejada, P. J., Diaz-Varela, R., Angileri, V., & Loudjani, P. (2014). Tree height quantification using very high resolution imagery acquired from an unmanned aerial vehicle (UAV) and automatic 3D photo-reconstruction methods. *European Journal of Agronomy*, *55*, 89–99. https://doi.org/10.1016/j.eja.2014.01.004

Zarco-Tejada, P. J., Ustin, S. L., & Whiting, M. L. (2005). Temporal and Spatial Relationships between Within-Field Yield Variability in Cotton and High-Spatial Hyperspectral Remote Sensing Imagery. *Agronomy Journal*, *97*(3), 641. https://doi.org/10.2134/agronj2003.0257

Zarco-Tejada, Pablo J., González-Dugo, V., & Berni, J. A. (2012). Fluorescence, temperature and narrow-band indices acquired from a UAV platform for water stress detection using a micro-hyperspectral imager and a thermal camera. *Remote Sensing of Environment*, *117*, 322–337.

Zarco-Tejada, Pablo J, Hubbard, N., & Loudjani, P. (2014). *Precision Agriculture: An Opportunity for EU Farmers—Potential Support with the CAP 2014-2020* [Technical Report]. Joint Research Centre (JRC) of the European Commission Monitoring Agriculture ResourceS (MARS).

Zhang, C., & Kovacs, J. M. (2012). The Application of Small Unmanned Aerial Systems for Precision Agriculture: A Review. *Precision Agriculture*, *13*(6), 693–712. https://doi.org/10.1007/s11119-012-9274-5

Zhen, Z., Quackenbush, L. J., & Zhang, L. (2016). Trends in Automatic Individual Tree Crown Detection and Delineation—Evolution of LiDAR Data. *Remote Sensing*, *8*(4), 333. https://doi.org/10.3390/rs8040333

# Appendices

# Appendix A. Supplementary material for Chapter 4

This appendix presents a comparison of different segmentation approaches for chestnut trees segmentation. To identify the proper segmentation approach different techniques were considered, namely: thresholding techniques, the Otsu's method, and adaptive thresholding; unsupervised clustering based in K-means; colour spacing thresholding using the Hue Saturation and Value (HSV) colour space; and based in vegetation indices. This evaluation motivated the selection of the segmentation approach from the method presented in section 4.2.3.

To evaluate these approaches, the area presented in Figure A.1 was selected as reference. This area was selected based on the existence of other features than vegetation, as infrastructures, such as houses with different roofs, roads, bare soil, and shadows casted by trees canopy.

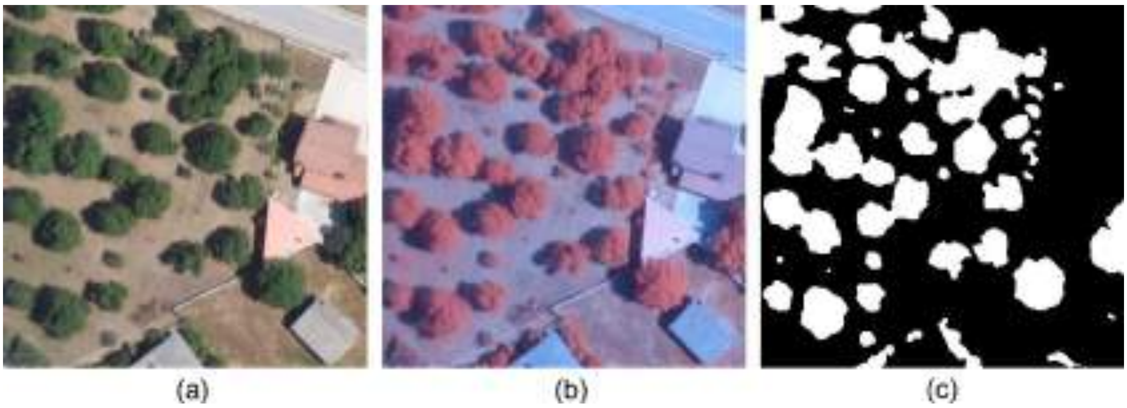


**Figure A.1.** Reference area used for the evaluation of the different segmentation approaches: (a) the RGB image; (b) colour infrared image; and (c) manually segmented image.

Otsu's method is a simple global thresholding technique. It assumes that the image contains two-pixel classes following a bi-modal histogram: one class is composed by the background pixels – corresponding, in this case, to non-vegetated areas – and the other class is composed by foreground pixels, corresponding to vegetation. In this evaluation the method was directly applied to the greyscale images of the RGB and CIR images obtaining a binary image after the method application. The adaptive thresholding technique differs from the Otsu's method in the number of used thresholds T. Whereas Otsu's method is globally applied to the image, this approach applies different thresholds to sub-regions of the image. Similarly, to the Otsu's method, this technique was applied to the RGB and CIR grayscale images, resulting in a binary image. K-means clustering is a non-supervised method that groups pixels in a K number of clusters in accordance with their likelihood. In this case the method was applied to the RGB and CIR images of the selected area and K was set to two, i.e. it was intended to divide the image into two distinct clusters, one representing vegetation and other non-vegetation, the vegetation cluster was then binarized for comparison against the manually segmented image. HSV is a colour space composed by Hue, Saturation and Value (or Bright), instead of the commonly used RGB colour space. This way, both RGB and CIR images were converted to HSV colour space, and the Hue band was used, it contains colour information, its thresholding was based in upper and lower limits, Hue values differ from zero to one, the values used for the RGB image were between 0.2 to 0.27, corresponding to the green colour, whereas, in the CIR case, as vegetation assumes a magenta colour the selected values where located between 0.85 to 1. The values within these ranges were then binarized (set to one) whereas other values where considered as background (set to zero). The last evaluated approach, which is commonly found in studies dealing with vegetation segmentation, is the usage of VI. This way, two different VI were applied, the RGBVI to the RGB image and the ExRE to the CIR imagery, these VIs were selected based in the results from the VI selection, see Appendix B for more information. To segment the vegetation the Otsu's method was applied to resulting VI images.

The evaluation of the different approaches was based in a pixel-wise comparison against the manually segmented image (Figure A.1c), and three classes were considered, exact detection, over detection and under detection. The obtained results applied to the RGB and CIR images from the reference scene are shown in Figure A.2.

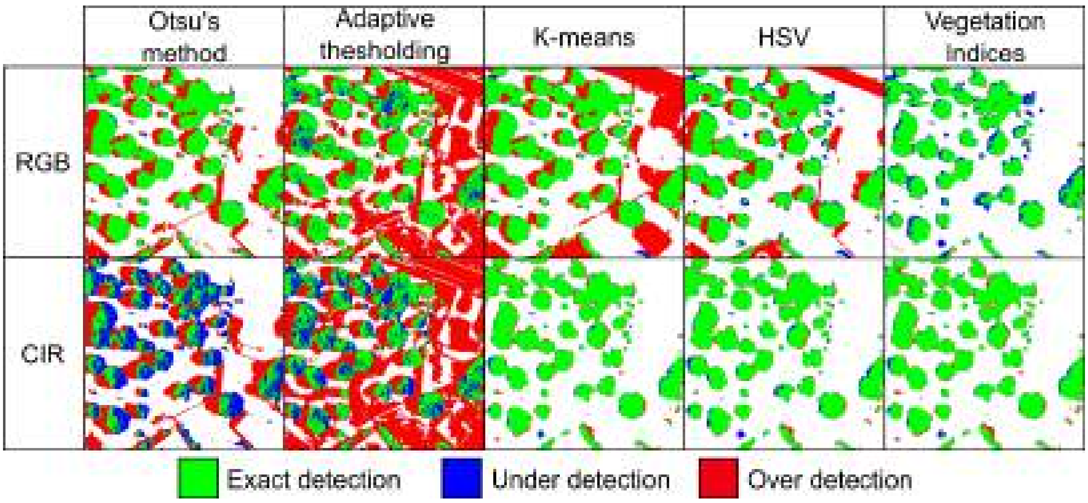


**Figure A.2.** Results obtained from the different segmentation approaches of the same area for the RGB and colour infrared (CIR) images. Exact detection of vegetation areas represented in green and exact detection of non-vegetation areas represented in black; red represents over detection; and blue signals under detection.

Table A.1 presents the percentage of exact, over and under detection, for each evaluated approach in the two tested images. According to the obtained results it is possible to conclude that K-means had a good performance in the CIR image with an exact detection rate of 96%. However, when applied to the RGB image this rate decreases to 74% with an over detection of 25%. The over detection mainly corresponds to infrastructures and shadows, being this approach not ideal to apply for vegetation detection in RGB images. As for the results obtained for the segmentation approach based in the Otsu's method, obtained a high over detection rate in the CIR image (18%), the same was verified for the under detection (17%). When analysing the results obtained from the RGB image the over detection rate decreases to 2%, however the under detection remains with a considerable percentage (16%). The adaptive thresholding approach did not provide satisfactory results for both images, the method obtained error rates higher than 40%. This is due to the method not being capable to discriminate between shadows and infrastructures from the vegetation since it is based in local threshold values. In what concerns the results obtained from the HSV-based technique, the results were acceptable in both tested images. The HSV conversion of the CIR image, showed an exact detection of 96%, although, in the case of the RGB image it decreased to 84%, being this a considerably acceptable value. However, the former, suffers from the same problem as other approaches, some outliers were wrongly classified (shadows and roads). The good detection accuracy in K-means and HSV-based techniques in CIR imagery can be explained due to the high reflection of the RedEdge in the vegetation, contributing for a clearer vegetation discrimination. The VI-based approach obtained the best overall results, with exact detection rates greater than 93%, being this value higher in the CIR image (96%), still the accuracy obtained in the RGB image was satisfactory (93%).

**Table A.1.** Results of the performance of the different methods classified in exact, over and under detection when compared to the manually segmented image of the same area for the RGB and colour infrared (CIR) images.

| Method | Image type | Exact detection (%) | Over detection (%) | Under detection (%) |
|---|---|---|---|---|
| Otsu | RGB | 82 | 16 | 2 |
| | CIR | 65 | 18 | 17 |
| Adaptive threshold | RGB | 59 | 38 | 3 |
| | CIR | 45 | 46 | 9 |
| K-means | RGB | 74 | 25 | 1 |
| | CIR | 96 | 3 | 1 |
| HSV | RGB | 84 | 13 | 3 |
| | CIR | 96 | 2 | 2 |
| Vegetation index | RGB | 93 | 1 | 6 |
| | CIR | 96 | 3 | 1 |

This way, when comparing the results of all approaches tested for vegetation segmentation the one based in VI was the one with the best overall performance for both types of images (94.5% mean value). The two evaluated thresholding methods (Otsu's and adaptive) were the approaches with lower exact detection accuracy with, respectively, 73.5% and 52% mean accuracy in vegetation detection. However, with image processing these methods provide more accuracy, as de case of the VI-based approach were the Otsu's method is applied to the images driven from the VI computation. The K-means and HSV-based segmentation approaches reached a reliable performance in the CIR image, which can be explained by the difference caused by the RE band where vegetation has higher pixel values, although when to the RGB image their performance decreases, their overall accuracy is 85% and 90%, respectively. Thus, the VI-based approach, more specifically using ExRE for CIR imagery and RGBVI in the case of RGB images (see Appendix B), corresponded to the selected approach for vegetation segmentation, since it had better behaviour, in both CIR and RGB images, thus providing a flexible and robust approach with respect to the type of image being used, with low error rates. These results motivated the selection of the VI-based approach for vegetation segmentation procedure of the method proposed in this study.

# Appendix B. Supplementary material for Chapter 4

To select the most suitable VI, a study was accomplished using the 17 VIs listed in Table B.1): six based exclusively on RGB bands and 11 VIs based on RGB and NIR/RE band combinations. These VIs were chosen due to their potential relevance in vegetation segmentation (highlighting vegetation areas). The validation was performed in the different areas, in the three epochs, presented in Figure 4.9 (location in Figure 4.1), selected to be representative: recent chestnut plantations, adult chestnut trees and both types, were included. The proximity between chestnut trees was also considered in the areas' selection: plantations with regular space between trees and trees with overlapping canopy areas. These areas were used as input of the proposed method and the first two phases of method's step one were performed (VI application and image thresholding). Results provided by the application of the VI-based segmentation (binary images) were compared with manual segmentation. To evaluate the segmentation accuracy, false negative and false positive rates of image pixels were calculated. False negatives are defined as vegetation pixels that were classified as background pixels (under detection). False positives are defined as background pixels that were classified as vegetation (over detection).

Over detection values correspond to false positives, i.e. values detected as vegetation but that are not classified as vegetation in the manual segmentation; and under detection values that correspond to false negatives, i.e. values that were classified as vegetation in the manual segmentation but were not detected as such by the applied VI.

**Table B.1.** List of broadband vegetation indices implemented and tested in the proposed method.

| Name | Equation | Reference |
|---|---|---|
| **Vegetation indices requiring NIR and RGB bands** | | |
| Blue Normalized Difference Vegetation Index | $\mathrm{BNDVI} = \frac{\mathrm{N-B}}{\mathrm{N+B}}$ | (Hancock & Dougherty, 2007) |
| Difference Vegetation Index | $\mathrm{DVI} = \mathrm{N} - \mathrm{R}$ | (Tucker, 1979) |
| Enhanced Vegetation Index | $\mathrm{EVI} = 2.5 \times \left(\frac{\mathrm{N} - \mathrm{R}}{\mathrm{N} + 6 \times \mathrm{R} - 7.5 \times \mathrm{B} + 1}\right)$ | (Justice et al., 1998) |
| Excess RedEdge | $\mathrm{ExRE} = 2 \times \mathrm{re_n} - \mathrm{g_n} - \mathrm{b_n}$ | Proposed in this study, derived from ExG |
| Green Difference Vegetation Index | $\mathrm{GDVI} = \mathrm{N} - \mathrm{G}$ | (Sripada et al., 2006) |
| Green Normalized Difference Vegetation Index | $\mathrm{GNDVI} = \frac{\mathrm{N} - \mathrm{G}}{\mathrm{N} + \mathrm{G}}$ | (Gitelson et al., 1996) |
| Green Soil-Adjusted Vegetation Index | $\mathrm{GSAVI} = \frac{\mathrm{N} - \mathrm{G}}{\mathrm{N} + \mathrm{G} + 0.5} \times 1.5$ | (Sripada et al., 2006) |
| Modified Soil-Adjusted Vegetation Index | $\mathrm{MSAVI} = \frac{(\mathrm{N} - \mathrm{R}) \times 1.5}{\mathrm{N} + \mathrm{R} + 0.5}$ | (Qi et al., 1994) |
| Normalized Difference Vegetation Index | $\mathrm{NDVI} = \frac{\mathrm{N} - \mathrm{R}}{\mathrm{N} + \mathrm{R}}$ | (Rouse et al., 1974) |
| Optimized Soil-Adjusted Vegetation Index | $\mathrm{OSAVI} = \frac{1.5 \times (\mathrm{N} - \mathrm{R})}{\mathrm{N} + \mathrm{R} + 0.6}$ | (Rondeaux et al., 1996) |
| Soil-Adjusted Vegetation Index | $\mathrm{SAVI} = \frac{\mathrm{N} - \mathrm{R}}{\mathrm{N} + \mathrm{R} + 0.5} \times 1.5$ | (Huete, 1988) |
| **Vegetation indices requiring only RGB bands** | | |
| **Name** | **Equation** | **Reference** |
| Excess Green | $\mathrm{ExG} = 2 \times \mathrm{g_n} - \mathrm{r_n} - \mathrm{b_n}$ | (Woebbecke et al., 1995) |
| Green-Blue Vegetation Index | $\mathrm{GBVI} = \frac{\mathrm{G} - \mathrm{B}}{\mathrm{G} + \mathrm{B}}$ | (Kawashima & Nakatani, 1998) |
| Green-Red Vegetation Index | $\mathrm{GRVI} = \frac{\mathrm{G} - \mathrm{R}}{\mathrm{G} + \mathrm{R}}$ | (Tucker, 1979) |
| Modified Green Red Vegetation Index | $\mathrm{MGRVI} = \frac{\mathrm{G}^2 - \mathrm{R}^2}{\mathrm{G}^2 + \mathrm{R}^2}$ | (Bendig et al., 2015) |
| Red Green Blue Vegetation Index | $\mathrm{RGBVI} = \frac{\mathrm{G}^2 - (\mathrm{B} \times \mathrm{R})}{\mathrm{G}^2 + (\mathrm{B} \times \mathrm{R})}$ | (Bendig et al., 2015) |
| Vegetation Index Green | $\mathrm{VARIg} = \frac{\mathrm{G} - \mathrm{R}}{\mathrm{G} + \mathrm{R} - \mathrm{B}}$ | (Gitelson et al., 2002) |

where, the reflectance values of each band are represented by R: Red; G; Green; B: Blue; N: NIR; and $\mathrm{re_n} = \frac{\mathrm{R}}{(\mathrm{R+G+B})}$; $\mathrm{r_n} = \frac{\mathrm{R}}{(\mathrm{R+G+B})}$; $\mathrm{g_n} = \frac{\mathrm{G}}{(\mathrm{R+G+B})}$; $\mathrm{b_n} = \frac{\mathrm{B}}{(\mathrm{R+G+B})}$.

Figure B.1 presents the mean results of the performed validation, using the VIs listed in Table B.1. For a complete overview, the results are presented, per tested area, in Table B.2 which shows the exact detection percentage.

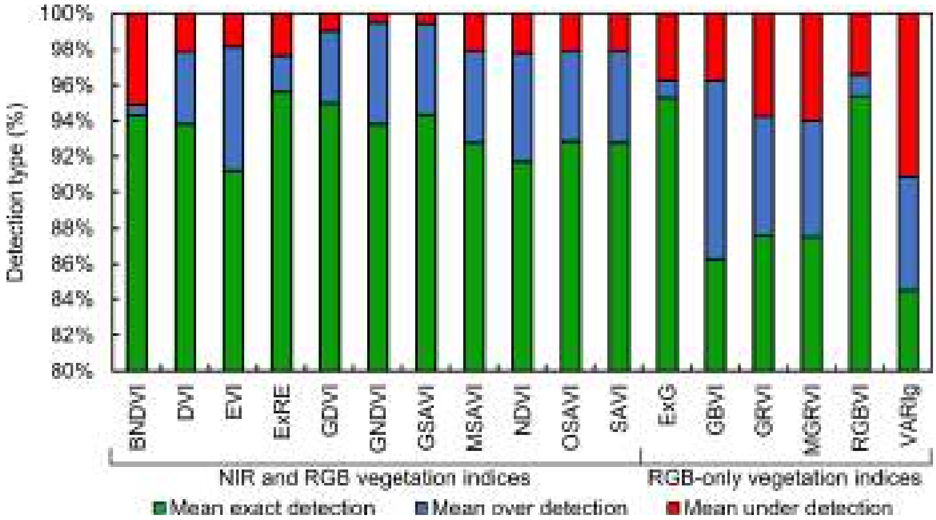


**Figure B.1.** Mean accuracy of exact, over and under detection in the evaluated vegetation indices from the comparison with manual segmentation masks from the seven evaluated areas.

**Table B.2.** Mean near-infrared (NIR) and RGB vegetation indices (VI) exact, over and under detection percentages for the evaluated chestnut plantations in epoch (year).

| VI | 2014 | | | 2015 | | | 2017 | | |
|---|---|---|---|---|---|---|---|---|---|
| | Exact (%) | Over (%) | Under (%) | Exact (%) | Over (%) | Under (%) | Exact (%) | Over (%) | Under (%) |
| **Vegetation indices requiring NIR and RGB bands** | | | | | | | | | |
| BNDVI | 94.9% | 0.8% | 4.3% | 94.4% | 0.2% | 5.4% | 93.7% | 0.7% | 5.6% |
| DVI | 94.2% | 3.7% | 2.1% | 92.8% | 4.8% | 2.4% | 94.4% | 3.6% | 2.0% |
| EVI | 92.1% | 6.1% | 1.7% | 89.9% | 7.8% | 2.3% | 91.6% | 6.9% | 1.4% |
| ExRE | 95.8% | 2.1% | 2.1% | 95.9% | 1.3% | 2.9% | 95.3% | 2.5% | 2.2% |
| GDVI | 94.7% | 4.4% | 0.8% | 95.8% | 2.9% | 1.3% | 94.3% | 4.9% | 0.8% |
| GNDVI | 93.8% | 5.8% | 0.4% | 95.1% | 4.0% | 0.9% | 92.5% | 7.2% | 0.3% |
| GSAVI | 94.2% | 5.3% | 0.5% | 95.5% | 3.5% | 0.9% | 93.2% | 6.4% | 0.3% |
| MSAVI | 93.5% | 4.5% | 2.0% | 91.8% | 5.8% | 2.4% | 93.1% | 5.1% | 1.7% |
| NDVI | 92.6% | 5.2% | 2.2% | 90.7% | 6.6% | 2.7% | 91.8% | 6.4% | 1.8% |
| OSAVI | 93.5% | 4.4% | 2.0% | 91.9% | 5.7% | 2.4% | 93.3% | 5.0% | 1.7% |
| SAVI | 93.5% | 4.5% | 2.0% | 91.8% | 5.8% | 2.4% | 93.1% | 5.1% | 1.7% |
| **Vegetation indices requiring only RGB bands** | | | | | | | | | |
| ExG | 95.8% | 0.9% | 3.3% | 95.2% | 1.2% | 3.5% | 94.9% | 0.9% | 4.3% |
| GBVI | 88.8% | 8.1% | 3.2% | 80.4% | 16.3% | 3.4% | 89.7% | 5.7% | 4.6% |
| GRVI | 89.5% | 5.1% | 5.4% | 85.5% | 8.6% | 5.9% | 87.7% | 6.2% | 6.0% |
| MGRVI | 89.4% | 5.1% | 5.5% | 85.4% | 8.3% | 6.3% | 87.6% | 6.2% | 6.2% |
| RGBVI | 95.9% | 1.1% | 3.0% | 95.2% | 1.4% | 3.3% | 95.1% | 1.1% | 3.9% |
| VARIg | 87.2% | 5.1% | 7.8% | 81.6% | 7.7% | 10.7% | 84.7% | 6.5% | 8.8% |

The results allow to conclude that, in general, NIR-based VIs presented a better overall performance, mean exact detection of 93% with a standard deviation of 0.7% considering the three flight campaigns. However, the performance achieved by RGB-based VIs presented an accuracy rate close to 90% (standard deviation of 1.6% in the three flight campaigns), if excluding VARIg. If discarding the less performant VIs (exact detection lower than 90%), the overall accuracy rate is around 94%.

The obtained results from the different VI motivated the selection of the ExRE as it was the VI with the best overall performance (mean accuracy of 96%). Despite the selection of ExRE, which is proposed in this study (being an adaptation of ExG to CIR imagery), as the VI of better performance, there were other NIR-based VIs with similar performance (~95%), therefore with equivalent results, namely: GDVI, GNDVI and GSAVI. However, if only RGB images are available, the method maintains its performance. Indeed, ExG and RGBVI reached an overall accuracy around 95%.

## Appendix C. Supplementary material for Chapter 5

This appendix contains the results of the RFE procedure presented in Section 5.3.3 (Table C.1). Moreover, boxplots of some of the vegetation indices used in this study (Figures Figure C.1 and Figure C.2) are also presented. These boxplots intend to depict the distribution of mean tree crown values when considering two or three classes: (i) with or without phytosanitary issues (Figure C.1); and (ii) affected by chestnut ink disease, nutritional deficiencies, or healthy (Figure C.2). Data dispersion trends throughout the season can be further studied to understand the multi-temporal variations of phytosanitary issues. The overall accuracy results from the prediction stage are presented in Figure C.3.

**Table C.1.** Recursive feature elimination results for each flight campaign, considering two classes (C2) and three classes (C3), and its overall rank. Top ten features are highlighted.

| Feature | May | | Jun | | Jul | | Aug | | Sep | | Oct | | Overall | |
|---|---|---|---|---|---|---|---|---|---|---|---|---|---|---|
| | C2 | C3 | C2 | C3 | C2 | C3 | C2 | C3 | C2 | C3 | C2 | C3 | C2 | C3 |
| **NDExNIR** | 1 | 2 | 2 | 4 | 2 | 2 | 1 | 1 | 4 | 4 | 2 | 2 | 1 | 1 |
| **EXNIR** | 3 | 3 | 3 | 3 | 3 | 3 | 3 | 3 | 2 | 3 | 3 | 3 | 2 | 2 |
| **GNDVI** | 4 | 1 | 1 | 1 | 4 | 5 | 2 | 4 | 3 | 2 | 4 | 5 | 3 | 3 |
| **NDRE** | 8 | 6 | 7 | 10 | 1 | 1 | 6 | 7 | 1 | 1 | 1 | 1 | 4 | 4 |
| **RVI** | 6 | 7 | 4 | 2 | 5 | 6 | 4 | 2 | 5 | 5 | 5 | 9 | 5 | 5 |
| **NDVI** | 2 | 4 | 5 | 5 | 6 | 9 | 5 | 5 | 6 | 9 | 9 | 10 | 6 | 7 |
| **RED** | 5 | 5 | 11 | 7 | 8 | 10 | 8 | 6 | 7 | 6 | 6 | 4 | 7 | 6 |
| **NDExRE** | 7 | 9 | 6 | 6 | 9 | 11 | 9 | 10 | 9 | 11 | 11 | 11 | 8 | 10 |
| **GRVI** | 11 | 11 | 12 | 12 | 7 | 4 | 10 | 8 | 10 | 7 | 8 | 6 | 9 | 8 |
| **EXRE** | 10 | 8 | 10 | 8 | 11 | 8 | 13 | 11 | 8 | 8 | 7 | 7 | 10 | 9 |
| **TCARI** | 9 | 12 | 9 | 9 | 12 | 12 | 7 | 9 | 13 | 10 | 10 | 14 | 11 | 12 |
| **SAVI** | 16 | 14 | 8 | 14 | 14 | 15 | 11 | 15 | 16 | 15 | 13 | 15 | 12 | 15 |
| **GREEN** | 13 | 10 | 13 | 11 | 13 | 7 | 14 | 13 | 11 | 12 | 16 | 8 | 13 | 11 |
| **NIR** | 12 | 13 | 14 | 13 | 10 | 13 | 15 | 12 | 14 | 13 | 15 | 13 | 14 | 13 |
| **RDVI** | 14 | 16 | 16 | 16 | 15 | 16 | 12 | 14 | 12 | 16 | 12 | 16 | 15 | 16 |
| **RE** | 15 | 15 | 15 | 15 | 16 | 14 | 16 | 16 | 15 | 14 | 14 | 12 | 16 | 14 |

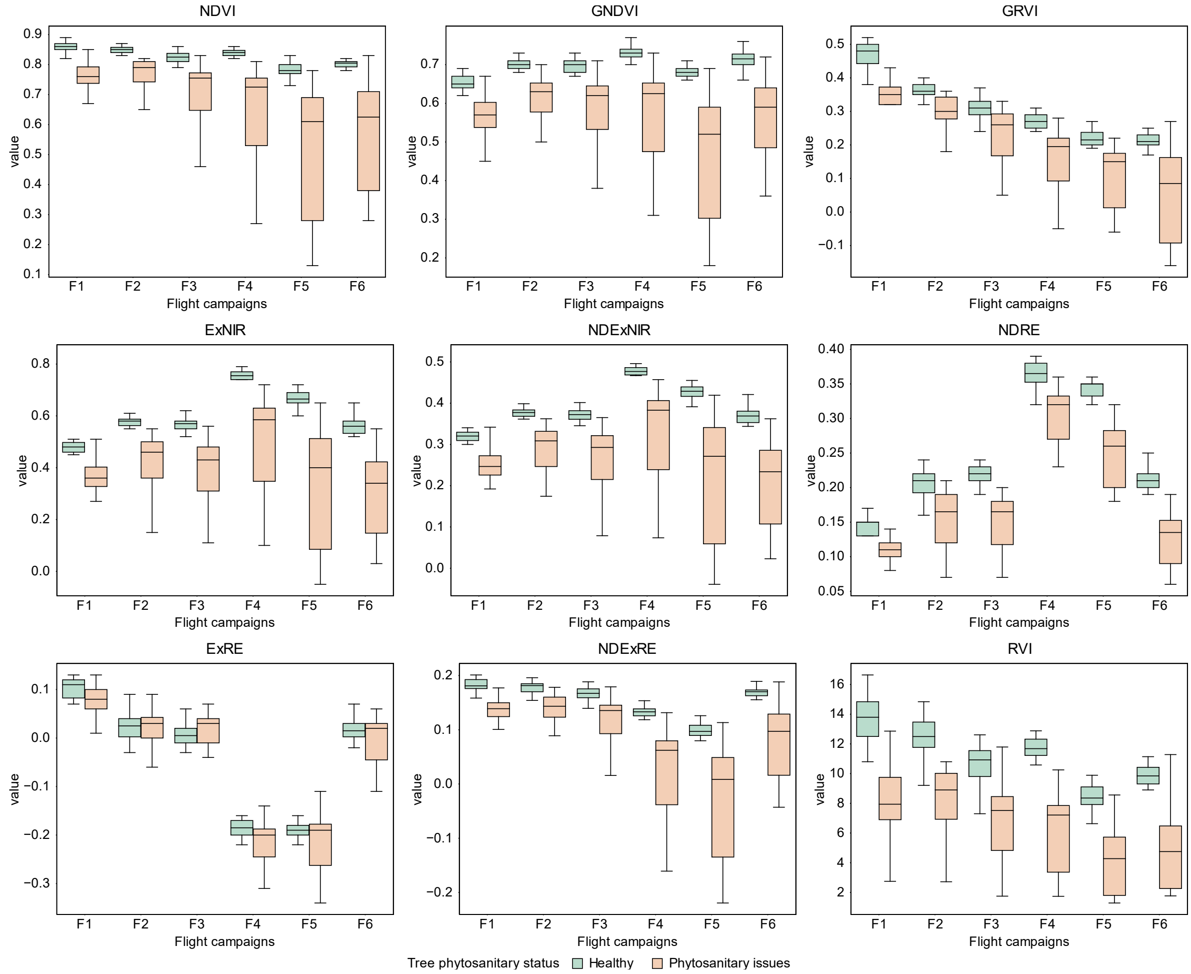


**Figure C.1.** Boxplots representing the distribution of tree crown mean values regarding the vegetation indices used for healthy chestnut trees and for those affected by phytosanitary issues.

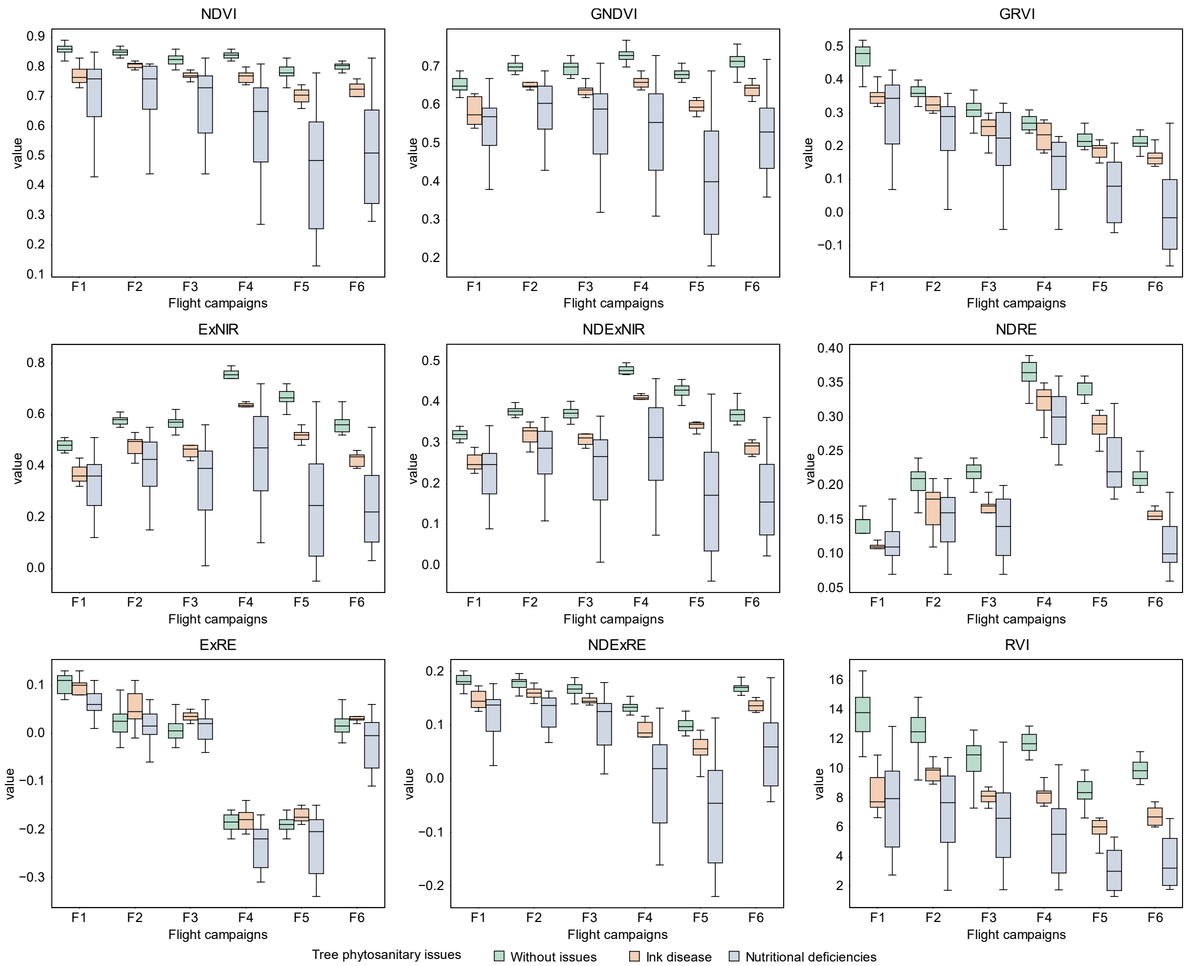


**Figure C.2.** Boxplots representing the distribution of tree crown mean values regarding the vegetation indices used for chestnut trees affected by ink disease, nutritional deficiencies, or healthy.

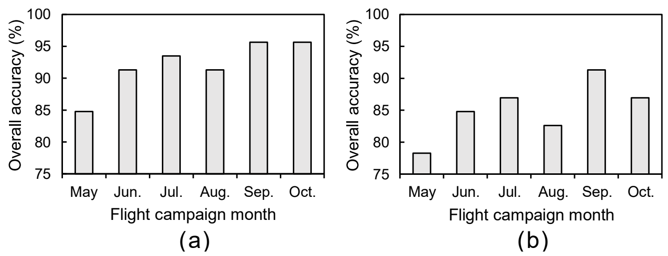


**Figure C.3.** Overall accuracy, per flight campaign, of the prediction for the presence of phytosanitary issues (a) and for phytosanitary issue detection (b).